Contribution à l'analyse multiphysique de la déformation d'assemblage

Stanislas de Lambert Des Champs de Morel

Thèse de doctorat

NNT : 2021UPAST035

université PARIS-SACLAY

Contribution à l'analyse multiphysique de la déformation d'assemblage

Contribution to the multiphysical analysis of fuel assembly bow

Thèse de doctorat de l'université Paris-Saclay

École doctorale n° 579, sciences mécaniques et énergétiques, matériaux et géosciences (SMEMAG)
Spécialité de doctorat : Énergétique
Unité de recherche : Université Paris-Saclay, CEA,
Service d'Études Mécaniques et Thermiques, 91191, Gif-sur-Yvette, France
Référent : ENS Paris-Saclay

Thèse présentée et soutenue à Paris-Saclay, le 03/03/2021, par

Stanislas de LAMBERT des CHAMPS de MOREL

Composition du Jury

Grégoire ALLAIRE Professeur, École polytechnique	Président
Pierre MOUSSOU Chercheur senior HDR, EDF R&D - IMSIA	Rapporteur
Marcus SEIDL Expert senior, PreussenElektra - TUM	Rapporteur
Elsa MERLE Professeur, Grenoble INP	Examinatrice
Éric DUMONTEIL Professeur, CEA - INSTN	Examinateur

Direction de la thèse

Vincent FAUCHER Expert senior HDR, CEA	Directeur de thèse
Jérome CARDOLACCIA Ingénieur-chercheur, CEA	Co-Encadrant
Guillaume CAMPIONI Ingénieur-chercheur, CEA	Co-Encadrant

"If it had been any different, if I had been born just one minute later, or been in the wrong pace at the right time or vice versa, the life that I've lived and come to love would not exist. And that is a situation that I would not want to consider in the slightest."

Slash.

À Jeannot.

Contents

Acknowledgment

Je profite de ces quelques mots en français pour pouvoir remercier les personnes qui ont (grandement) contribué à l'écriture de cette thèse.

Tout d'abord, je souhaiterais remercier Claire, ainsi que Valérie, pour m'avoir accueilli au sein de DYN et du SEMT. J'ai trouvé au sein du laboratoire une ambiance optimale pour suivre une thèse. Cette dernière a été grandement facilitée par la compagnie de mes collègues du BodyBuil'dyn ! Je remercie également Nicolas Dorville, Pierre Gavoille, Céline Guenaut et Loïc de Carlan pour m'avoir accueilli à divers moments au cours de la thèse au STMF et au SERMA.

Naturellement, je poursuis avec mon directeur de thèse, Vincent. Je le remercie pour sa gentillesse, sa réactivité, son écoute, et pour toutes nos conversations qui ont été productives. Ses diverses relectures, ainsi que ses conseils, ont été fort utiles. Je le salue également pour sa transmission de l'engouement pour la publication, qui, je pense, a plutôt bien fonctionné ! Promis, à l'avenir, j'éviterai de vouloir faire passer mes articles pour des flyers marketing d'une célèbre marque de latrines.

Vient ensuite mon encadrement de thèse, constitué d'une dreamteam qui a remarquablement supervisé ce projet de thèse. Premièrement, Jérome. Je pense lui devoir une grande partie du travail fait durant ces trois dernières années. De DIVA+G aux multiples propositions d'améliorations de modèles, jusqu'à l'idée même de Phorcys, cela a été une réelle force de l'avoir à mes côtés. Tes qualités humaines (tu es un brave gars) sont à la hauteur de tes qualités techniques, et franchement je te remercie pour ça, ce fut juste un véritable honneur et un immense plaisir de bosser avec toi ! Ensuite, Guillaume. Cela fait maintenant 5 ans que je le connais (déjà), et – rendons à César ce qui … - il fut l'un des piliers fondateurs de ce sujet. Je ne cesserai tout de même d'être surpris par les diverses qualités humaines de ce curieux gourou. Merci d'avoir été là, et de ne pas t'être perdu dans un occulte lieu péruvien en cours de route ! Complètent l'équipe Bertrand et Olivier, mécanicien et hydraulicien de la team IFS. Bertrand, je te remercie pour ta transmission de connaissances en mécanique, ainsi que pour le temps que tu as pris à modifier ton code pour le nourrir goulûment de sorties Phorcys. En plus d'être à la source du couplage IFS, cela a été un honneur d'être ton partenaire de bande-dessinée. Olivier je te remercie pour tes (très) nombreuses idées proposées, et ta bonne humeur ! Ta passion effrénée pour les sciences est rafraîchissante.

J'ai également une pensée pour toutes les personnes que j'ai pu torturer de questions (la liste n'est bien sûr pas exhaustive !). Au STMF je remercie André, Ulrich, et Yannick pour leurs collaborations sur la CFD et les maillages. Au SERMA je remercie notamment Karim, Nicolas, et François pour l'apprentissage d'AP3, d'Alamos et les débogages qu'ils ont pu entreprendre !

Cette thèse ne serait pas ce qu'elle est sans les diverses personnes qui ont rendu ces 3

années aussi agréables. Notamment mes collègues DYN, que je remercie pour leur accueil (je citerais volontiers l'intégralité du labo, mais ça serait long !), et les doctorants que j'ai pu rencontrer au cours de cette période et qui ont réussi à me supporter autant de temps (Roberto, Alexis, Huan, Gianluca, Alexandre, …).

I warmly acknowledge Pr. Grégoire Allaire who chaired the jury of my PhD defense. I also want to express my gratitude to Dr. Marcus Seidl and Dr. Pierre Moussou, who agreed to review my thesis. Last but not least, I thank Pr. Elsa Merle and Pr. Eric Dumonteil for accepting to investigate my work. It was a real pleasure and honor to discuss with you all.

J'accorderais une mention spéciale à mes partenaires de la section musique du CEA, avec qui nous avons partagé de longs (très longs) moments, et qui m'ont permis de jouer sur plein de concerts en parallèle de la thèse (Greg, Arnaud, Franz', Thom, …).

Je finirai par ma famille. Je ne saurai jamais les remercier assez pour leur soutien éternel et indéfectible. Ils ont toujours été là, dans les hauts, comme dans les bas. C'est une réelle chance de vous avoir, et pour cela : merci.

List of figures

List of tables

Nomenclature

Below we summed up the main notations which can be found in the manuscript.

Notation	Meaning (usual unit)
Q_i	Volumetric flow rate of section i ($m^3.s^{-1}$)
Q_i^0	Flow rate upstream from section i ($m^3.s^{-1}$)
K_i	Hydraulic resistance of section i ($Pa.m^{-6}.s^2$)
S_i	Upstream cross section of section i (m^2)
ρ	Density of the fluid ($kg.m^{-3}$)
λ	Minimum width of the water gap (m)
Λ	Width of the convergent-diffuser's base (m)
L	Depth of the convergent-diffuser (m)
α	Angle of the convergent-diffuseur (rad)
H	Length of the rectangular channel (m)
f	Darcy friction factor
ζ_1	Local coefficient due to convergent narrowing
ζ_3	Local coefficient due to diffuser enlargement
C_g	Loss coefficient of the grid
N	Number of crossed fuel rods rows
θ	Inclination of the flow with respect to the vertical direction
$\xi(\theta)$	Coefficient of the Eole correlation
β	Pitch-to-rod diameter ratio
h_l	Leaking length (m)
χ_i	Cross-sectional ratio of section i
p	Pressure (Pa)
P_i	Pressure at point i (Pa)
ΔP_i	Irreversible total pressure loss in section i (Pa)
v	Velocity distribution ($m.s^{-1}$)
V_i	Mean – bulk - velocity at point i ($m.s^{-1}$)
H_i	Head at point i (m)
F_Z	Lift force (N)
F_V	Lateral force induced by the difference of pressure around the grid (N)
F_{UP}	Lateral force induced by the flow being put in the upright position through the grid (N)
F_{Bu}, F_B	Lateral force induced by cross-flows through one bundle, mean of F_{Bu} upstream and downstream one grid
F_{M3_1}, F_{M3_2}	Forces on the rods (respectively at the left and right hand side) due to redistribution towards the gaps, upstream from the grids (N)
k_{eff}	Multiplication factor
ϕ	Flow angle of incidence with respect to the bundle horizontal plane (rad)
ψ	Angular flux ($cm^{-2}.MeV^{-1}.sr^{-1}.s^{-1}$)
Φ	Scalar flux ($cm^{-2}.MeV^{-1}.\ s^{-1}$)
σ_i	Microscopic cross-section for reaction i (barn)
Σ_i	Macroscopic cross-section for reaction i (cm^{-1})
τ_i	Reaction rate i ($cm^{-3}.\ s^{-1}$ if energy integrated, and s^{-1} if volume integrated)

Glossary

Name	Meaning
AP3	Abbreviation for APOLLO3®
APOLLO3®	Neutronic multi-purpose code (CEA, EDF, Framatome)
CASMO5	Lattice physics code for modeling PWR and BWR fuel (Studsvik)
Cast3M	Structural mechanics code (CEA)
CD	'Convergent-diffuser', geometrical space shaped by two adjacent spacer grids of a fuel assemly
CEA	The French Alternative and Atomic Energy Commission, French public government-funded research organization
CMSLINK5	Linking data code (Studsvik)
Code_Saturne	Computational Fluid Dynamics software (EDF)
DES	Division of Energies (CEA)
DIVA+G	Mock-up set up for the thesis, consisting in two 3D-printed grids facing each other in a middle of which lies a variable gap
DM2S	Systems and Structure Modeling Department (CEA)
DYN	Dynamics Studies Laboratory (CEA)
DYN3D	Code solving both neutron kinetics along with two-phase thermal hydraulics for LWR steady states and transients (HZDR)
EDF	Électricité de France, French multinational electricity utility company
EOLE	Test section with FA mock-up studied for losses due to cross-flow in bundles

FA	Fuel Assembly, component of a nuclear core made of subcomponents including fuel rods, guide tubes, grids, and nozzles
FLICA4	Sub channel, thermal-hydraulic code (CEA)
FR	Fuel Rod, element of a fuel assembly carrying the fuel pellets
Framatome	French nuclear reactor business
FSI	Fluid-Structure Interaction
Gen I, II, III, IV	Design generation of nuclear reactors, from the early prototypes (I) to the most advanced concepts (IV), most of them currently in service worldwide belong to Gen II
GT	Guide tube, element of a fuel assembly made for receiving the rod cluster control assembly
HERMES T	Hydraulic loop at the CEA Cadarache
MISTRAL	Mock-up regarding cross-flows in one FA
Paraview	Multi-platform data analysis and visualization application (Kitware)
PETER	Hydraulic loop used in Erlangen (Framatome)
Phorcys	Python library developed during the thesis, dedicated to solving hydraulic networks
RCCA	Rod Cluster Control Assembly
Salome	Post- and pre-processing platform for numerical simulations (CEA, EDF, Open Cascade)
SEMT	Mechanical and Thermal Studies Service (CEA)
SERMA	Reactor Studies and Applied Mathematics Service (CEA)

SERPENT	Multi-purpose three-dimensional continuous-energy Monte Carlo particle transport code (VTT)
SIMULATE5	3D steady-state multi-group code for the analysis of PWRs and BWRs (Studsvik)
STMF	Fluid Mechanics and Thermal Hydraulics Service (CEA)
T4	Abbreviation for TRIPOLI-4®
TrioCFD	Computational Fluid Dynamics software (CEA)
TRIPOLI-4®	Monte-Carlo neutronic code (CEA)
URANIE	Uncertainty analysis plateform (CEA)
VisIt	Interactive parallel visualization and graphical analysis tool (LLNL)

General introduction

1. Pressurized water reactors (PWR) and fuel assemblies (FA)

Nuclear power plants operation is basically the same as a thermal power station. In other words, electricity is obtained through heat energy. The latter is generated by nuclear fissions occurring in the nuclear reactor, and more specifically, in its core. Light-water reactors (LWR) are nuclear reactors using light water (ordinary water in comparison with heavy water – deuterium oxide) as both neutron moderator and coolant. The most common current types of LWR are the Pressurized Water Reactors (PWR) and the Boiling Water Reactor (BWR). In the BWRs, the coolant is heated and directly turned into steam inside the nuclear core. This steam is then used to drive the steam turbine. By rotating, the latter finally products electric power through a generator.

The PWRs are by far the most widespread type of reactor in the civilian nuclear world establishing a total net electrical capacity of about 300 GWe, and also constitute the whole French nuclear plants[1]. They differ from the BWRs in that the pressure inside the primary coolant loop (maintained through a pressurizer) is high enough to avoid boiling. Instead, the coolant after heating in the core flows into the steam generators. There, the water contained in a secondary circuit evaporates thanks to the heat exchange with the primary loop. The steam produced can finally drive the turbine. A third system cools the secondary coolant down with external water collected from the sea or a river. Its condenser turns the steam back to liquid. Figure 0-1 presents a schematic of a classical PWR.

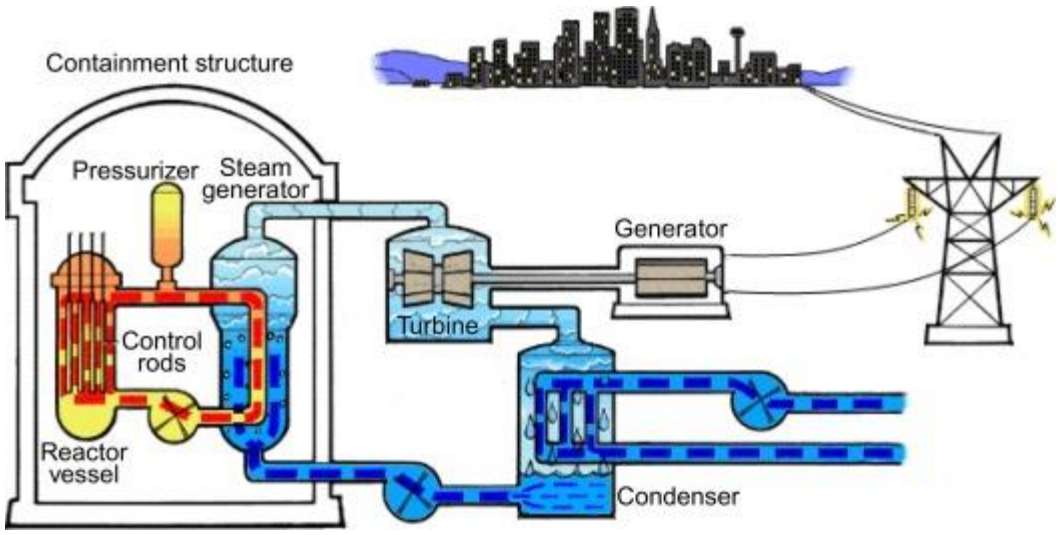

Figure 0-1 - Schematic of a PWR (source: [1])

If one focuses closely on the reactor pressure vessel (see Figure 0-2 for an exhaustive layout), the coolant is flowing from the *inlet nozzles* into the lower part of the core, below the *lower core plate* (*the lower plenum*). Then, it goes successively through the lower core plate, *the nuclear core*, and finally can exit the pressure vessel through the *outlet nozzles*

[1] https://pris.iaea.org/PRIS/WorldStatistics/OperationalReactorsByType.aspx

after passing the *upper core plate*.

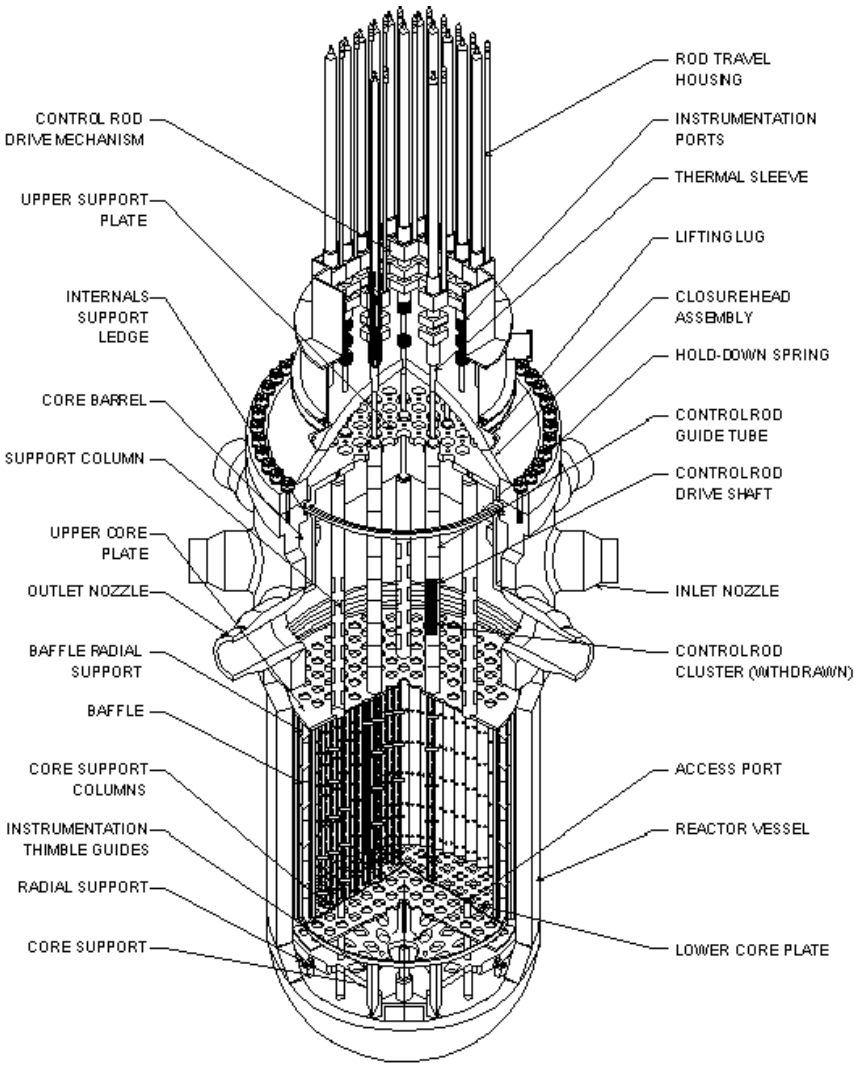

Figure 0-2 - Schematic of a reactor pressure vessel (source: [2])

The nuclear core itself is made of fuel assemblies (FA), where nuclear fission reactions produce heat. The latter is passed on the coolant thanks to convection (the coolant temperature rises by almost 30°C, from bottom to top of the core). The mean coolant velocity is around 5 m/s (Reynolds number of 5.10^5). Standing approximatively 4 meters high by 20 centimeters wide, the fuel assembly consists in a set of indivisible components (see Figure 0-3 for a schematic and photographs of components). The structure of the FA is made of the following elements. The *bottom nozzle* secures the connection with the lower core plate. The upper core plate is pressed against the *top nozzle springs* which guarantees a good support to the FA to counteract important axial fluid forces when the coolant flows from side to side. In the middle, guide tubes link both nozzles together. They permit the *rod cluster control assembly* (RCCA) insertion to monitor nuclear reactions. *Spacer grids*, also known as mixing grids, are distributed over the guide tubes every half meters approximately. Every spacer grid is connected to the guide tubes by means of spot-weld connections, except the bottom one which is directly supported by the nozzle. The grids have three features. First, they mechanically couple every guide tube in the FA, secondly they retain the fuel elements (fuel rods) spacing, and finally, they comprise mixing vanes which sharpens the coolant mixing downstream to improve the heat exchange between the fuel and the water

in the core.

Figure 0-3 - Left, schematic of a FA and its RCCA, middle, photo of a FA (source: World Nuclear Association[2]), right, grid zoom in (source: Framatome[3])

The structure of the FA supports a bundle of fuel rods, which are bound to the grids through the support of springs and dimples. Fuel rods are composed of an external cladding, the fuel pellets, and are filled with an inert gas like helium under pressure.

2. Phenomenology of fuel assembly bow in the PWR

The deformation of the assemblies, first noticed in 1994 after IRI (Incomplete control Rod Insertion, corresponding to the incomplete insertion of the RCCA) [3], is a problem for both exploitation (IRI, delicate removal of assemblies in the core ...) [4, 5, 3], but also for operation, because it has consequences on the power of the core [6]. Figure 0-4 shows a photo of a deformed assembly, and another which can no longer be inserted on the lower core plate due to its deformation. One has to know that fuel assembly bow is observed ex-core, and after handling, so that only a residue of the deformation can be noticed. Three phenomena are often reported to explain fuel assembly bow: the creep of the assembly and the guide tubes, the growth of the assembly under neutron flux, as well as hydraulic forces [3, 7, 8, 9, 10].

[2] https://www.world-nuclear.org/
[3] https://inis.iaea.org/collection/NCLCollectionStore/_Public/42/026/42026962.pdf

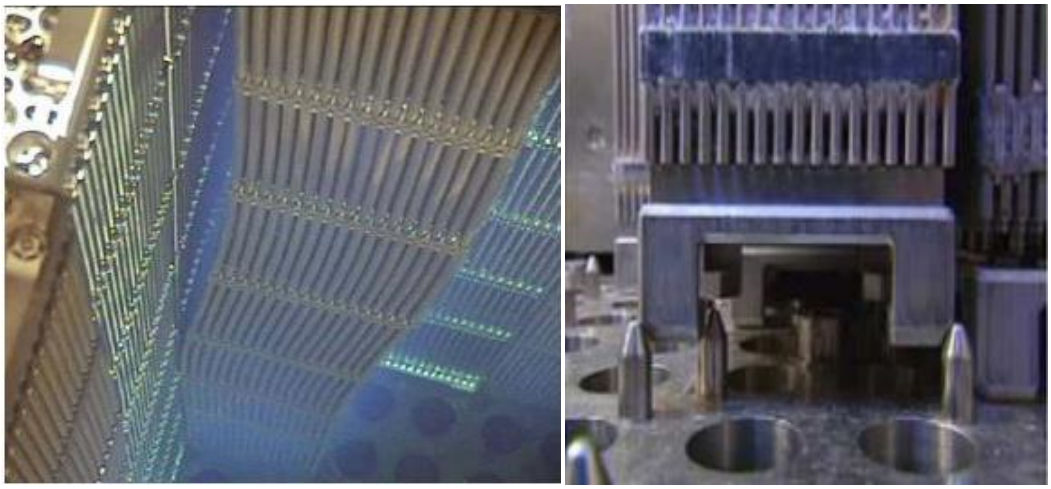

Figure 0-4 - Left, bowed fuel assembly (length of ~4m), right, dropped off fuel assembly (source: [11, 12])

One of the causes involved would therefore be the hydraulic forces exerted by the fluid circulating in the reactor primary circuit, and being applied to the fuel assemblies in the reactor core. Indeed, several reasons can a priori explain the origin of forces in the core, such as for example a theoretically axisymmetrical distribution of velocity at the core inlet [13, 14, 15], which can, under certain conditions (startup procedure, failure of a GMPP, downcomer eccentricity…) be asymmetrical [13], causing the appearance of cross velocities. It is also assumed that the outlet velocities are symmetrical with respect to an axial vertical plane, due to the position of the hot leg output nozzles [16, 8].

As we have said, several effects are involved in the multiphysics ecosystem of assembly bow. The diversity of deformations encountered in the core reflects the multitude of different causes that can impact the deformation. One observes in Figure 0-5 the numerous possibilities of deformation noted on a 1300 MWe nuclear core. Figure 0-5 (a) and (b) show the direction of the deformation at a given altitude (grid height). Figure 0-5 (c) represents all the deformation axially at the location of the corresponding assembly. In 4-loop reactors, the deformations are generally oriented radially at the bottom of the core, and follow two symmetrical directions at the top of the core [3].

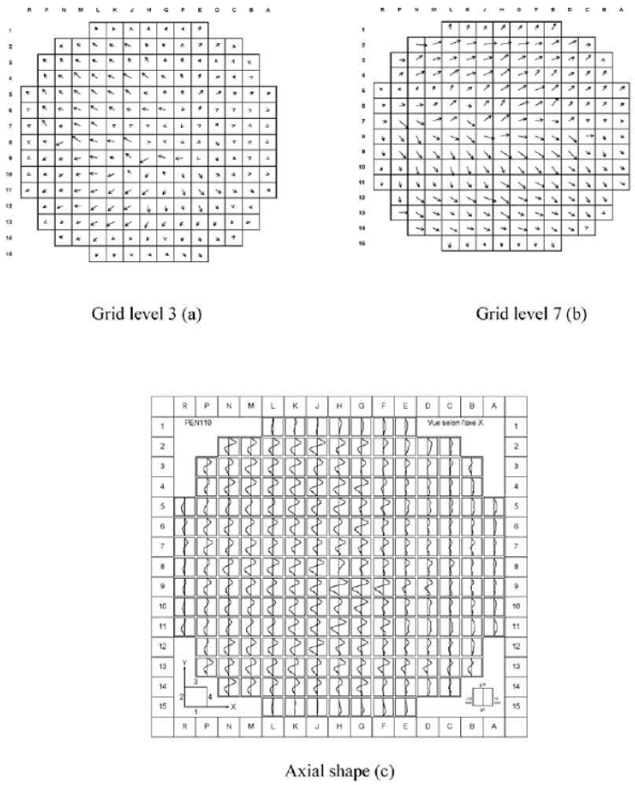

Figure 0-5 - Assemblies bow observed on an EDF's 1300MWe nuclear core [3]

This distribution of deformations can be explained by the distribution of lateral hydraulic forces in the core [3]. Indeed the radial (axisymmetric) distribution of the deformations at the bottom of the core, and plane symmetrical at the top of the core, corresponds to the velocity profiles generally given at the core inlet (axisymmetric) and outlet (symmetrical) core [13, 14, 15, 8, 17, 16]. Thus, the shape of the deformation of an assembly depends very much on its successive positions (cycle after cycle) in the core, and burnup has a very weak influence [8, 3]. The effect of burnup is felt locally at the level of the deformations generated on the guide tubes [3, 10, 12, 18]. New types of fuel assemblies and core loading maps tend to limit assembly bow [5, 3].

Figure 0-6 represents two deformations measured in the Ringhals-3 reactor. One "C" (right), and the other "S" (to the left). It is shown that these two types of deformation predominate in the core [3, 6, 19, 20].

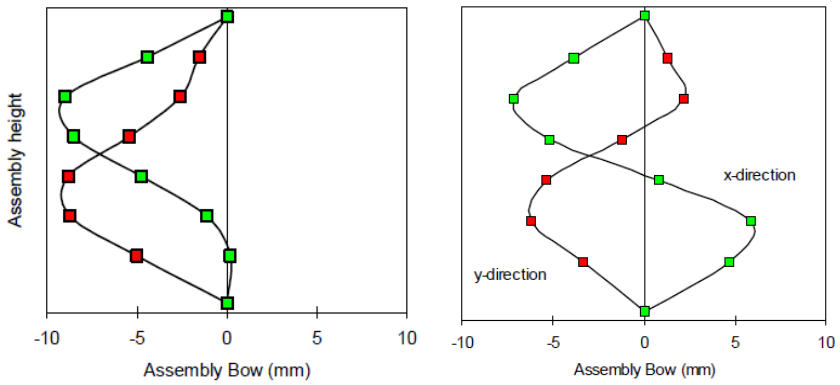

Figure 0-6 - C-shaped and S-shaped assembly bows observed at Ringhals [21]

We propose to classify through three scales (vessel, core, assembly) in Table 0-1 the proven effects/phenomena (in red) and plausible candidates, cause or consequence of the deformation (in black). The latter are found out in the literature. These can be either neutronic, mechanical or hydraulic effects. Among the proven effects, we find the bow-influencing mechanisms as reported in [22]. Among the candidates, we find various phenomena which can plausibly lead to an asymmetry in the core, including hydraulic forces.

Wanninger in [22] adapted an original background from [2] to highlight the main in-core fuel assembly bow influencing mechanisms through a very convenient representation (Figure 0-7).

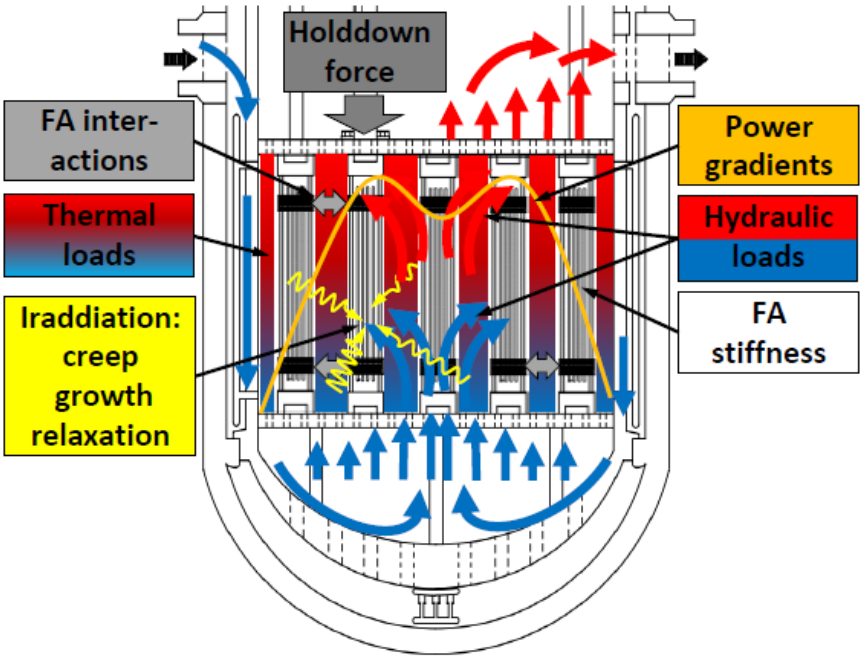

Figure 0-7 - In-reactor bow influencing mechanisms (from [22] and [2])

Scale	Effects or phenomena
Vessel	Transient / dysfunction of a primary circuit pump [23, 13, 4]
	Injection of the Chemical and Volumetric Control System [4]
	Influence of the downcomer – eccentricity defect? [13]
	Influence of the lower plenum – axisymmetric distribution of velocity profiles at the core inlet + plausible change of the velocity profile according to the downcomer geometry and the cold leg flow rates? [13, 8]
	Influence of the upper plenum – distribution of the velocity profile along a median plane (not axisymmetric) because of the hot leg nozzles position [8, 16, 17]
	Asymmetric transient of boron and neutronic consequences caused can be linked to assembly bow [6]
Core	Inter-assembly and wall gaps branches do not depict the same pressure loss [16]
	Baffle jetting [5, 24]
	Leak flow rates through the guide tubes dashpot [25]
	Irradiation growth [10, 7, 9, 22, 3]
	Assembly and guide tube creep [10, 7, 9, 22, 3]
	Thermal expansion [10, 22]
	Fuel assembly stiffness [22]
	Inter-assembly contacts [8, 22, 3]
	Hold-down forces and fuel assembly weight (~7kN) [26, 10]
	Handling related forces [8]
	Pre-existing bows coming from previous cycles [8, 16]
Assembly	Fuel rod – grid joints [22]
	Guide tube – grid joints [22]
	Grid spring relaxation [22, 9]
	Grid upstream flow redistributions depending on the grid design [27]
	Bundle cross-flows and thus flow inclination [28, 29, 8]
	Slanted flow put in the upright position across the grids [30, 9, 22]
	Neutronic consequences of the deformation and the associated boron concentration [6, 19, 20, 31, 32]

Table 0-1 - Phenomenology of the assembly bow - asymmetries, recognized causes and consequences

Amongst those effects, the author [22] reported on a couple of main bow influencing mechanisms and classified them between bow-enhancing mechanisms and bow-inducing

mechanisms. Bow-inducing mechanisms are those which are at the origin of bow by creating bending moments in the structure. Bow-enhancing mechanisms are those which cannot trigger the bow by themselves, but have an important influence on how and how fast it is promoted. The contribution of every single effect is drowned in the numerous interaction with every others. According to Wanninger, the coupling between all phenomena along with the in-core coupling of the fuel assemblies themselves potentially lead to counter-intuitive and self-amplifying effects and could explain the occurrences of strongly deformed cores with asymmetric bow patterns. The author classified the main mechanisms as follows:

- Thereby, **hold-down forces** constitute a *bow-enhancing* mechanism. In fact, the hold down force generates a compressive load on the fuel assembly, originated from the top nozzle springs compression against the upper core plate. This axial force reduces the lateral stiffness of the fuel assembly and thus enhances the lateral deformation provoked by external loads and the lateral creep rate. Those forces are too small compared to the critical buckling load to directly induce fuel assembly bow.
- **Structural irradiation growth** can be both *bow-enhancing* and *bow-inducing*. It is bow-enhancing as the fast neutron irradiation tends towards lengthening axially the guide tubes (in zircaloy) because of their anisotropic crystal lattice, and thus the whole fuel assembly. This growth can compress the top nozzle springs and thus increase the previous hold-down forces indirectly. However, it is also bow-inducing as fast neutron flux lateral gradients within one assembly can lengthen its guide tube unequally and thus cause bending moments in the structure leading to a deformation.
- **Structural creep** is a *bow-enhancing* and *bow-inducing* mechanism. It is a long-term time dependent plasticity effect like irradiation growth. In our context, creep is based on crystal lattices microscopic effects creating plastic strain in the same direction as a pre-existing stress, coming from external loads. Thus, creep is a mechanism which enhances a permanent deformation of the fuel assembly, but calls for external bow-inducing forces. As well as growth, flux gradients within one single assembly can induce a deformation.
- **Structural relaxation** is a *bow-enhancing* mechanism. In fact, the grid spring preload progresses during the fuel assembly operation. At the beginning of the life of the fuel assembly, the preload is high so that all fuel rods are held during handling, but it decreases all operation long. As a result, the coupling between the fuel rods and the fuel assembly structure is reduced as well as the fuel assembly stiffness. The creep deformation rate thus increases and enhances the whole bow. On the other side the relaxation breaks up the bow effect of the top nozzle springs by decreasing the hold down forces.
- **Thermal loads** are a *bow-inducing* effect as they create bending moments due to differential thermal expansion between the fuel assembly elements. Thermal expansion is a reversible effect, yet, it might introduce perturbations into the system of coupled fuel assemblies as stated by Wanninger. Otherwise, a gradient of temperature may also affect creep and relaxation processes. Because of a lateral power gradient -mostly regarding the fuel rods, the guide tubes are cooled

properly and put up with axial gradients-, fuel assemblies can undergo a permanent bow because of different creep strains. Also, the axial gradient of temperature regarding the coolant generates different grid spring relaxations along the assembly height. These are mainly *bow-enhancing* effects.

- **The inter-assembly contact** comes up several times. First, it couples the whole system of fuel assemblies so that the deformation of one assembly may propagate over the whole core. Secondly, it limits the permanent deformation. A contact of a bowed assembly against an unreformed one may reduce its permanent deformation in time. Thirdly, it restricts the maximal deflection. As said by Wanninger, within one row the deformation is limited to the cumulative gap sizes between the fuel assemblies in the row (which can evolve over the operation because of the growth of the spacer grids). As soon as a contact is established, one can say that this effect is *bow-inducing*.

The last effect are the **hydraulic forces**. The latter are obviously *bow-inducing* effects. They rely on a couple of intricate phenomena occurring in the core such as macroscopic flow redistributions brought in by inlet and outlet unalike behaviors, or local scale redistributions such as the massive redistributions in the grids upstream vicinity. Those effects are developed further in the thesis.

3. Role of this subject within the industrial context

As the previous section suggests, fuel assembly bow is an intricate multiphysical issue. All three classic fields of nuclear reactor physics are involved. To sum the problem up, Figure 0-8 illustrates the interactions occurring during the FA bow over its operation cycles.

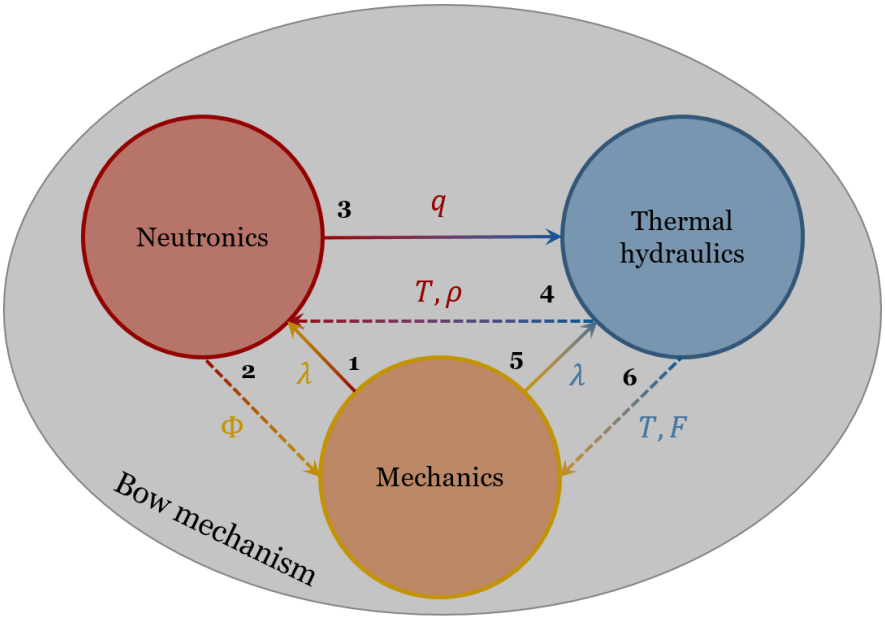

Figure 0-8 - Physical interactions during assembly bow

These interactions are:

- Interaction 1: the deformation (displacements and change of water gaps width λ) affects the core neutronics. Enlargement and reduction of gaps lead to a change in the power locally.
- Interaction 2: the flux affects the fuel assembly structure. It includes for instance the irradiaction creep and growth which evolve with the fluence Φ (time integration of the flux).
- Interaction 3: the power q generated in the fuel rods is transferred to the coolant.
- Interaction 4: the material density influences neutronics, and cross-sections depend on the material temperature T.
- Interaction 5: fuel assembly bow modifies the gaps width λ and thus the flow redistributions within the core.
- Interaction 6: fuel assembly structures are affected by the coolant temperature and hydraulic forces induced by the coolant.

We are interested in assembly deformation, which evolves on very long times (several days or months), dynamical effects are thus neglected. In addition, the FA displacement velocity is much lower than the fluid velocity in the cores, meaning that the interface velocity between the fluid and the structure is insignificant compared to the fluid velocity. In other words, the fluid system is characterized by motionless boundaries (which depend on the assembly position). This is the reason why those coupled coolant/assembly systems are considered as a quasi-static type of fluid-structure interactions. An equilibrium is thus to be found at every state point. As the fluid force over the FA is likely to be the main influencing parameter on the FA bow, especially for Beginning Of Life FAs (see the sensibility analysis Figure 0-9), interactions 6, and possibly 5 (for important returns of the FA bow on the redistributions – see [16]) are the most-studied interactions of the FA mechanics. In practice, temperature change due to bow is considered discretionary, first, because of the relatively low influence of the bow on the temperatures (see [6]), and second, because of the low impact of a temperature variation over the permanent deformation (see Figure 0-9). For these reasons interaction 3 is also not taken into account in the current work.

The mechanical constitutive equations of the FA depend on the fluence endured by the structures for a fast neutron flux. Characteristic times of neutronics are much lower than every other physics involved in the phenomenon. For this reason it is currently common to run independent neutronic simulations to track the fluence through time for a given loading pattern, or simply time integrate a constant fast neutron flux distribution (see [22]). In return, choosing not to upgrade the FA positions in the neutronic calculations in response to creep and growth parameters can be justified for simulation regarding a limited amount of time (e.g. a core starting), when the fluence is negligible. For longer times, the deformations might impact the flux distribution in theory and thus the mechanical constitutive laws. At this stage, as the deformation of the assembly does not seem quite sensitive to a slight macroscopic change of neutron flux level (see Figure 0-9) over one FA cycle, it can be accepted not to update FAs position. However, one has to study interaction 1 anyway. First, regarding large gaps which may come across in a PWR, the latter interaction 1 is still little studied in the literature. Second, it is necessary to undertake the spadework for interaction 1 to eventually

contemplating the return of mechanics over neutronics (interaction 2). Third, to have access to important information regarding related operational issues (for instance quadrant power tilt in the core, or even impact of FA-scaled flux gradients on the deformation).

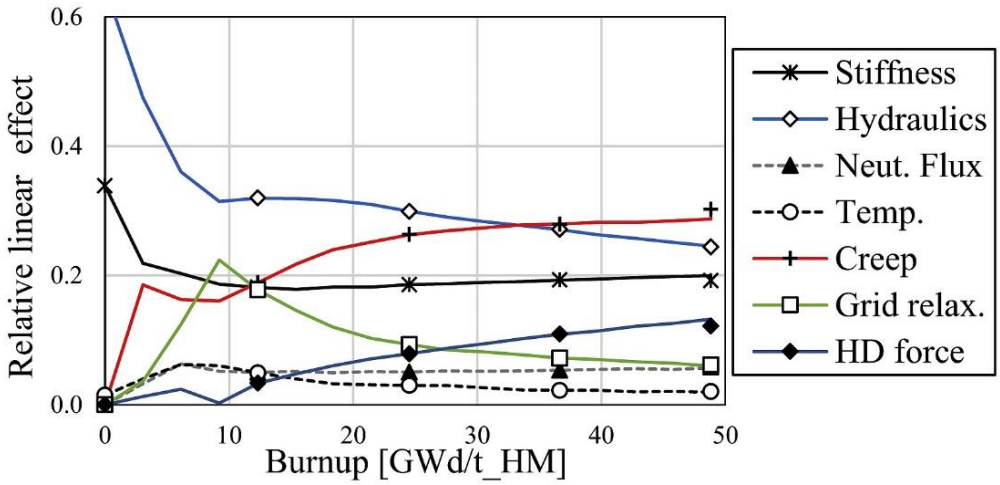

Figure 0-9 - Single assembly sensibility analysis for several values of burnup [9]

Interaction 4, resting upon the upgrade of fluid density and cross sections temperatures in the neutronics codes, has been compared in a previous study [6] and showed detectable effects. However, the latter seemed fully negligible compared to the effect related to the geometrical deformation (λ). For this reason, in a first attempt, this interaction is not considered as a matter of importance.

Finally, creep and hydraulic forces appear to be the principle driving parameters of the final FA bow. Growth and hold-down forces become important at End Of Life FAs. The stiffness of the FA depends on a set of FA structural parameters. Wanninger analyzed its impact on the FA bow through a change of several parameters including for instance the guide tubes diameters, or the grid springs and dimples stiffness. This effect is particularly strong when irradiation did not kick off.

Therefore, the role of this PhD thesis within this multiphysical environment is to investigate the remaining gray areas in the picture described above. Our involvement can thus be summed up through Figure 0-10.

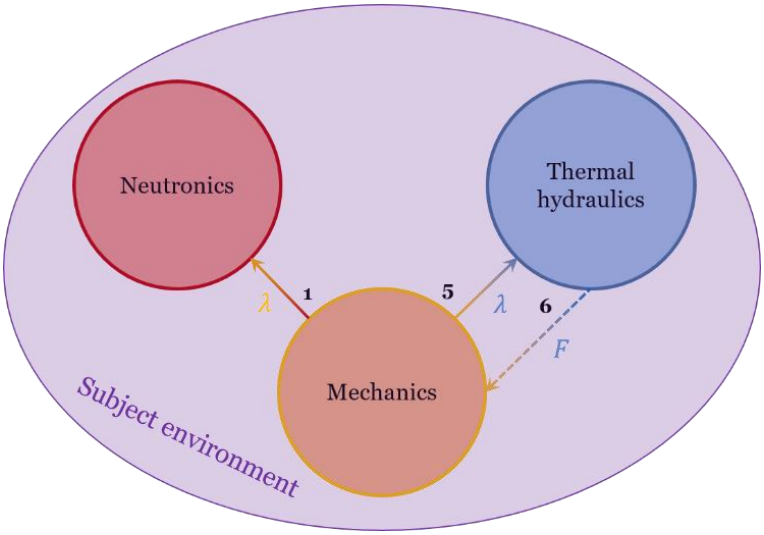

Figure 0-10 - Subjects of interest for our research area

In other words, a first part of this thesis will be dedicated to interactions 5 and 6 from chapters 1 to 4. We will look after the hydraulic redistributions mechanisms occurring in the core, especially the local scale redistributions upstream from the grids. In return, hydraulic forces, which seem to be a main driving effect of FA bow, are modelled on the basis of our own redistribution models. **Chapter 1** deals with the phenomena to take into account in terms of hydraulics. The next three chapters are organized by scales. **Chapter 2** dives deep into setting up models to depict local grid scale redistributions. **Chapter 3** deals with the extrapolation of the latter models up to the fuel assembly scale. Finally, **chapter 4** gives insights about core-related scales, including rows of FAs and the whole core. Further in the project, in chapters 5 and 6, we take an interest in strategies to study the impact of deformations onto the fuel assemblies neutronics (interaction 1). It is a worthy attempt as the change in water gaps surrounding the FA could properly estimate local neutronic features used for interaction 2. Also, as stated in [22], as the in-core neutron flux is measurable online, it could be an indirect way to confirm or deny the prediction of the core state of deformation which involves flux changes. **Chapter 5** deals with exact modelling of the FA curvature with Monte Carlo codes' native geometries at the FA and rod scales. **Chapter 6** follows introducing a deterministic scheme to depict deflections at a core scale.

Chapter 1: Review of fluid-structure interaction in a context of fuel assembly bow *(interactions 5 and 6)*

Highlights of the chapter

- We introduce hydraulic forces of interest, and the associated hydraulic effect.
- The grid design highly influences the flow in the vicinity of the grids.
- Water gaps enlargement and reduction have to be taken into account in a fuel assembly bow context.
- To depict redistributions at the grid scale, it is necessary to introduce a model depending on both the grid design and the bypass width.

It will be noted that 'transverse hydraulic forces' have not been listed as such in Table 0-1 of the previous chapter, whereas they seem to be a major cause of the deformation [3, 22]. Indeed, the efforts result from intricate in-core hydraulic redistributions, listed in the table: the axisymmetry of the inlet axial velocity profile, different gaps (inter-assembly/assembly-wall), as well as the state of deformation of the core are all candidates for the appearance of crosswise velocities in the core, and for the formation of forces, which are exerted on the assemblies.

Note that the thesis is concerned with a quasi-static context, in other words the deformation process is supposed to be long enough to be able to consider the evolution of the system as a succession of static states. The phenomena of vibration, occurring for example in a seismic setting [33], involving the speed and acceleration of the assembly, are therefore neglected.

1. Usual decomposition of the hydraulic forces

Two types of forces can be exerted on the assemblies, which are classically denoted axial and lateral at the fuel assembly scale. In the context of deformation, we are especially interested in lateral forces, that is to say lateral in relation to the axes of the core. We can see in Figure 1-1 what is meant by axial and lateral.

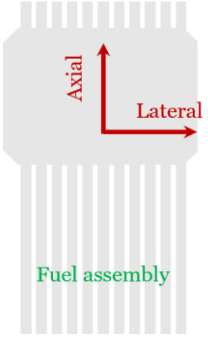

Figure 1-1 - Coordinate system for an unbowed FA

At the assembly level, there are therefore lateral forces on the grids, and lateral forces on the rods (see for example [16, 8, 22, 28]).

If the efforts are well distinguished, the way to compute them is not on the other hand always well highlighted. We will briefly present the idea for calculating the axial or lateral force associated with the assembly. We will then return in more depth to the different efforts in the suitable sections.

2. Axial forces

A force balance on a full FA highlight [26] that axial forces exerted by the flow above a cross-section of a FA are such that:

$$F_Z = F_N - A + G \qquad \text{(Eq. 1-1)}$$

Where F_N is the reaction forces, F_Z is the lift force stemming from the flow going from bottom to top in the FA. A stands for the buoyancy (hydrostatic force) and G for the FA weight. Contributions of axial fluid forces can reach the same order of magnitude than the weight of the FA (i.e. about 10^3 kg).

Figure 1-2 illustrates those forces.

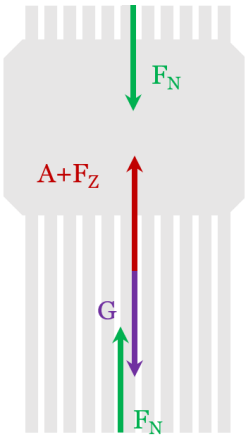

Figure 1-2 - Axial forces on a FA

3. Lateral forces due to cross-flows through the rod bundle

A couple of different authors were interested in the forces exerting on a single rod, and then on a bundle of rods through transposition. Among those authors we can quote [34] who showed that the normal force on a cylinder was proportional with respect to the drag coefficient multiplied by sinus squared of the angle of incidence. In other words, the force is carried by the crosswise component of the incident velocity, this is called the independence principle (Figure 1-3). [35, 36] noticed that this model has limits, in that it does not reproduce well the pressure distribution around the cylinder. In terms of effort, this model was validated for angles higher than 10°, but no experiment was run below. Consequently, the model is not considered validated for quasi-axial flows. Without any

experimental value, Taylor [37] clarifies the principle for small angles. When it comes to purely axial flow, the drag force is a friction force. Considering the latter as constant for small angles, he projected the force on the cylinder normal vector and highlighted a term proportional to the sinus of the angle of incidence. The rod normal force is thus a sum of the independence principle term due to the lateral component of the velocity, and a frictional term. Expanding the latter model with a Taylor series shows that the normal force is to be linear for very small angles. However, [38, 39, 40] showed that the force is indeed linear with respect to small angles, but the slope is too low to be only due to friction. Recently, Divaret [38, 39] pointed out that friction only made up 10% of the normal force. The main component of the force is actually due to lift, also linear with respect to the angle.

Divaret explains that it is possible to go from one single rod to a bundle of rods with the help of the Taylor model set up for a confined rod [37, 41]. The Taylor's friction term can be estimated through the Darcy-Weisbach equation, while the independence principle term is more complex. It previously stood for the drag of the unconfined rod in pure cross flow. Païdoussis chose an equivalent velocity to make the most of the independence principle: he focused on a bundle traveled along by a potential flow where cylinder X is missing, then he averaged the velocity around the missing cylinder X. Divaret noted that the latter model tends toward underestimating the measured force, and might be called into question.

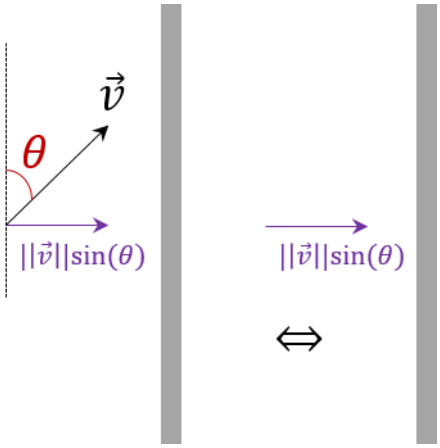

Figure 1-3 - The independence principle [42] [34], original inclined flow (left), force carried by the crosswise component of the flow (right)

More recently, Joly [43] went back over Divaret's works and implemented them in the TLP (Taylor-Lighthill-Païdoussis) model. The author also introduces the FICEL mock-up (cluster of 3x3 rods), and the related CFD simulations. Both experiment results and CFD simulations were in agreement, thus Joly considered that the numerical model was reliable enough to be compared with the TLP results. Aside from the rods at the bundle inlet and outlet, the simulation results validated his model.

The latter approaches are considered as 'single-rod based', as the transition toward the bundle is seen as an expansion from a single-rod to a bundle. Another approach is 'row – based'. In other words, hydraulic efforts are pulled out from an average behavior on the rows of rods within a bundle.

The 'row – based' approach is particularly based on the Peybernès' works [28] on inclined flows in fuel assemblies bundles. Here, the author took an interest in the pressure loss created by one whole row of fuel rods. To do so, he measured the loss induced by a 8 rods-bundle, over 4 rows, in the Eole mock-up (Figure 1-4). Then, he can deduce the pressure drop of a single row averaging the results on four rows (Eq. 1-2).

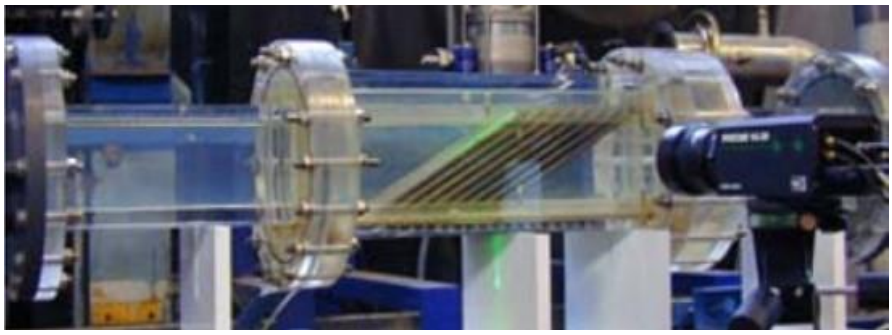

Figure 1-4 - The Eole mock-up (in [28])

$$\Delta P_{row}\left(V_{\text{gap}},\theta\right)=\frac{\Delta P_{8\text{rows}}-\Delta P_{4\text{rows}}}{4}=\frac{1}{2}\rho K_{\perp}\xi(\theta)V_{\text{gap}}^{2} \qquad \text{(Eq. 1-2)}$$

Where V_{gap} stands for the fluid velocity in the gaps between the rods, $K_{\perp}$ is the pressure drop coefficient for purely transverse flows ($\theta = 90°$) and $\xi(\theta)$ is an experimental correction factor depending on the flow inclination.

The main benefit of this method is to free ourselves from edge effects, and to probe the flow where it is not troubled. After a couple of measures with several velocities and angles, Peybernès found out a general correlation whatever the incident angle of the flow is (Eq. 1-3).

$$\xi(\theta)=\left(\frac{\sin(\theta)}{\cos\left(\frac{\pi}{4}-\frac{\theta}{2}\right)}\right)^{1.7} \qquad \text{(Eq. 1-3)}$$

This approach specifically deals with PWR FA bundles, and was validated in the MISTRAL mock-up. Although the boundary conditions of the experiment are called into question [30], the method is still used recently, particularly in the context of fuel assembly bow [22, 9]. Wanninger found satisfying results having implemented the Eole's correlation within the code *ANSYS CFX*.

As seen in Appendix B, the consequent force can be written as (Eq. 1-4) where N is the number of crossed rows, and S_B is the free lateral cross-section of the bundle (without rods).

$$F_{Bu}=\Delta P S_B=N\Delta P_{row}S_B \qquad \text{(Eq. 1-4)}$$

For our PWR operation context, the following Table 1-1 gives orders of magnitude according to different references.

Source	Position in-core or in a row	Force value (N)
[9]	Second bundle, assembly 5 (row of 15 FA)	5.10^{1}
[44]	Third bundle, assembly D9 (core)	2.10^{2}
[45]	Second bundle, assembly 2 (row of 15 FA)	5.10^{0}

Table 1-1 - Examples of bundle forces order of magnitude

4. Lateral forces due to inclined flows put in the upright position across the grids

Leaning on the works of U. Bieder focusing on flows across spacer grids [30] (see Figure 1-5), Wanninger [9, 22] assumes that inclined flows are totally made vertical downstream from the grids.

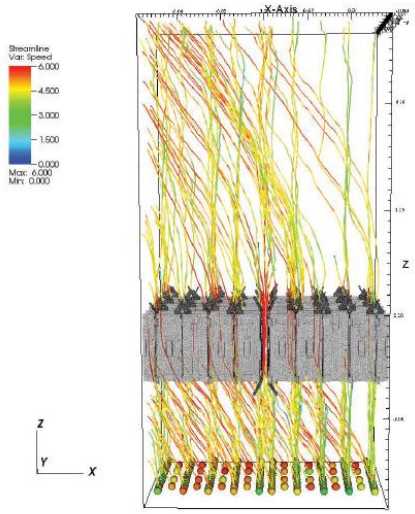

Figure 1-5 - Streamlines from a LES simulation [30]

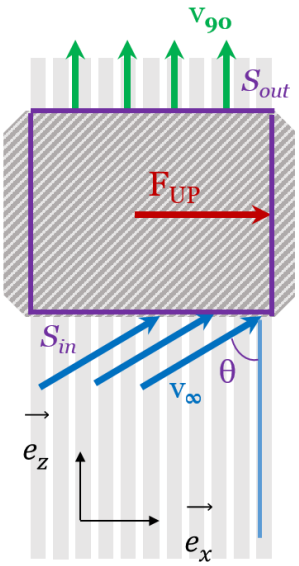

Figure 1-6 - Lateral force caused by the flow across the grid

The problem is presented in Figure 1-6, v_∞ is the incident mean fluid velocity forming an angle θ with the vertical axis. v_{90} is the velocity of the flow put in the upright position. S_{in} and S_{out} are respectively the grid upstream and downstream cross-section. S_g is the grid cross-section, such that $S_{in} = S_{out} = S_g$. Finally, F_{UP} is the lateral force due to the flow being put in the upright position inside the grid and F_z represents the axial force due to the grid pressure drop.

We can show that:

$$\begin{cases} F_{UP} = \frac{1}{2}\rho \sin(2\theta)\, S_{in} v_\infty^2 \\ F_z = \iint_{S_{in}} p dS - \iint_{S_{out}} p dS \end{cases} \qquad \text{(Eq. 1-5)}$$

The F_{UP} expression is obtained either through the Euler's momentum conservation equation considering the fluid as perfect (flat velocity profile i.e. no shear), or through the Navier-Stokes momentum equation in Appendix A with a set of reasonable assumptions. (Eq. 1-5) corresponds to the expression of the lateral force also given by Wanninger in [22].

We plot F_{UP} as as θ evolves in Figure 1-7 for θ between 0 and 2.3 degrees (order of magnitude taken from [28]), $\rho = 700\ kg.m^{-3}$ (order of magnitude of the density for an operating PWR whose pressure is set at 155 bar and temperature around 300°C), $v_\infty = 6\ m.s^{-1}$ (around the bulk velocity in the core). The force magnitude on this range is thus around 10^1 N.

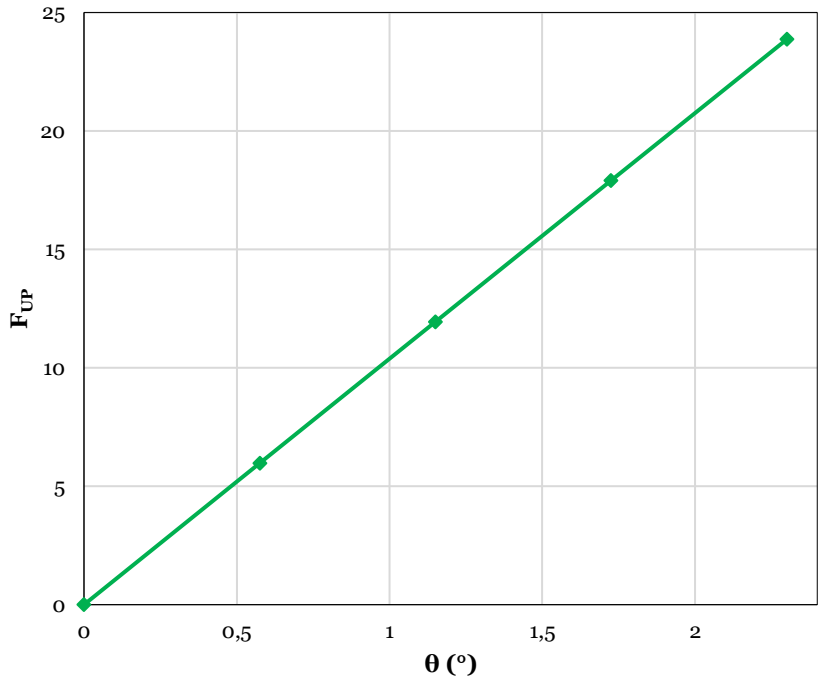

Figure 1-7 - F_{UP} according the angle of inclination

5. Lateral forces induced by the water gaps

In his works on the dynamical modeling of the fuel assembly [46], Ricciardi introduces a force induced by a pressure difference between the right and left side of the spacer grid. In fact, the author runs experimentations on a PWR fuel assembly within a hydraulic loop. To make his models fit better the tests results, Ricciardi introduces an added stiffness, in other words, a force whose value depends on the fuel assembly displacement and thus on the bypasses - also called water gap - thicknesses. As highlighted in Figure 1-8, this displacement is indeed directly related to the wall-assembly distances respectively named λ_1 and λ_2.

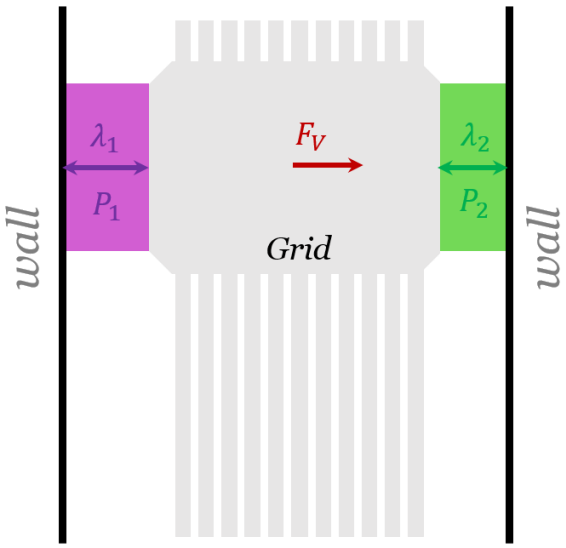

Figure 1-8 - Pressure deviation leading to a lateral force

This difference of water gap on each side of the spacer grid leads to a pressure difference

$P_2 - P_1$, which itself leads to a lateral force of the following form:

$$F_V = \Delta P S_{lat,g} \qquad \text{(Eq. 1-6)}$$

Where $S_{lat,g}$ is the area of the grid outer straps, and ΔP is the pressure difference $P_2 - P_1$ on each side of the grid, depending on both thicknesses λ_1 and λ_2. This force seemed of prime importance as it allowed Ricciardi to better fit his models compared to the tests he undertook. Joly [43], recently, also pointed out that adding an added stiffness term to the TLP model can improve the linear force distribution compared to an experiment run on a bowed fuel assembly. He also suspected the limit of extrapolating a cylinder behavior to a full bundle of rods, and especially invited the reader to take in interest in the grid role on the fluid forces distribution.

Table 1-2 gives some orders of magnitude of the total lateral force (which thus can include F_V and F_{UP}) that one can find out about the spacer grids.

Source	Position in-core or in a row	Force value (N)
[9]	First grid, assembly 3 (row of 15 FA)	1.10^1
[44]	Second grid, assembly H9 (core)	1.10^2
[45]	Second grid, assembly 2 (row of 15 FA)	5.10^0

Table 1-2 - Examples of lateral grid forces order of magnitude

The present Ricciardi's case deals with a specific case of bypasses located between a wall and a FA, and his approach simplifies several points. Among them we find the geometry considered as simple channel with frictional pressure loss and no fluid acceleration, as well as the equality of grid and bypasses pressure losses. In the next section we highlight that the grid geometry has a significate impact on redistributions occurring upstream from the grids, and has to be taken into account.

6. Fluid behavior in the water gap between adjacent grids

The last section establishes a connection with an important core effect: the coolant redistribution upstream from the spacer grids. In Figure 1-8 the axial flow which came up to a grid level had two choices: either going through the grid itself, or rather skirting it to the left or right hand side (in other words, in the water gap areas whose thicknesses are respectively λ_1 and λ_2). This redistribution is not trivial *a priori*, but can be modeled, like in [46], thanks to pressure loss coefficients regarding the three possible branches (grid and the two bypasses), and a simple hypothesis: the pressure losses of both branches are equal.

In the core, there is not one single assembly surrounded by walls, but rows of assemblies as for instance in Figure 1-9. The axial flow at a grid level has still two choices: either going through the grid, or in the bypass. However, the latter can be an inter-assembly bypass

located between two successive FAs (FA-FA bypass), or a bypass located between a FA and the core shroud (FA-wall bypass as shown in the previous section).

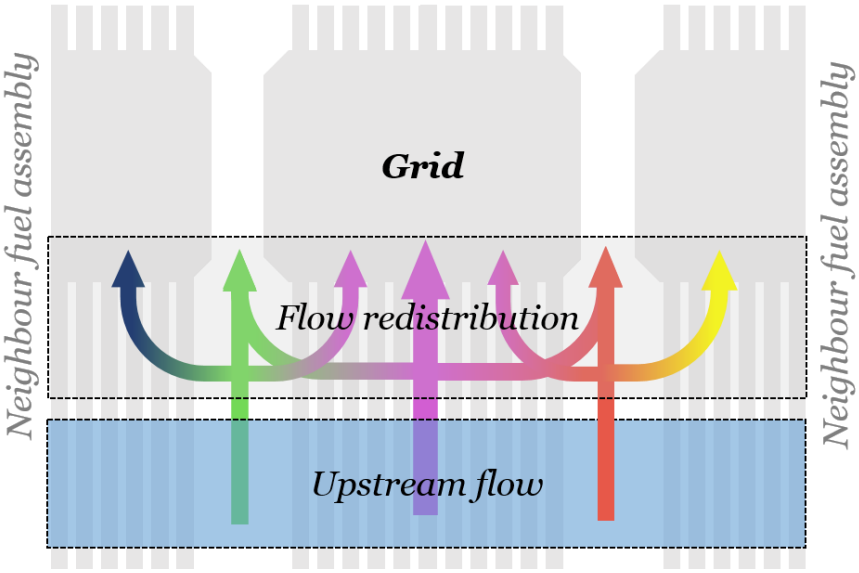

Figure 1-9 - Core redistributions upstream from the grids

As mentioned previously in Ricciardi's works, we can guess that this redistribution phenomenon depends on the pressure loss coefficient in each possible branch, i.e. grid or bypass, and thus on the geometry of the latter systems. Yet, the grid geometry, as well as the inter-grid geometry – outer straps geometry – whose designs comes under the jurisdiction of trade secret, is not evident. The grids comprise mixing vanes, springs, dimples and straps [47, 16]. A layout is available in Figure 1-10.

The grids external parts are composed of outer straps and vanes, as shown in Figure 1-11.

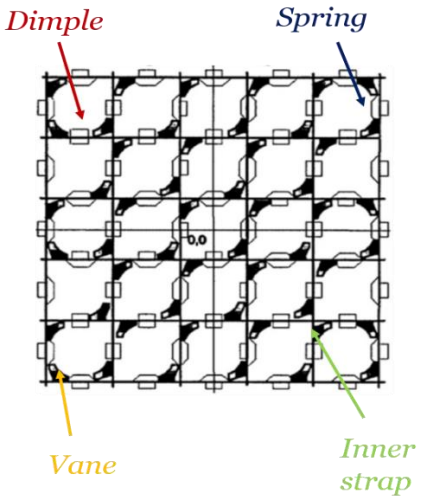

Figure 1-10 - Inner grid portion (adapted from [48])

The influence of this external geometry on redistributions occurring in the core has been raised in the literature [27, 16, 49]. Stabel also reported on the FA design impact on the full FA behavior [50]. In his publication [27], Yan pointed out a lack of research regarding the

grids outer straps. He undertook a study dealing with the sensibility of the outer straps design on the axial flow. Those designs are shown in Figure 1-11.

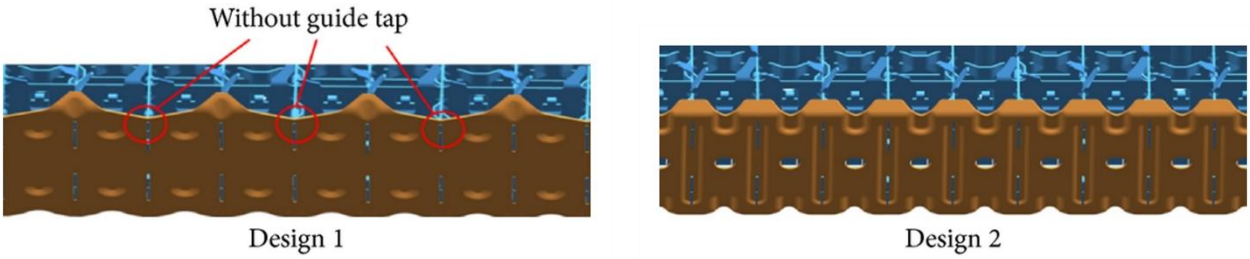

Figure 1-11 - Two different designs for outer straps (a) one vane in two fuel rods (b) one vane between each fuel rod (b) (figure from [27])

Yan considers a 2x2 cluster of fuel assemblies (Figure 1-12). He notices that pressure loss created by design 2 is 6.9% higher than the one created by design 1. Design 2 also leads to higher lateral velocities upstream from the grid, but less important downstream. In fact, we can observe in Figure 1-13 the cross flow rate evolution downstream from the grid which highly depends on the design studied. We can read into those results that the external geometry has an effect on the pressure drop along the water gap, and thus has an effect on the overall redistribution across the grid (Figure 1-13).

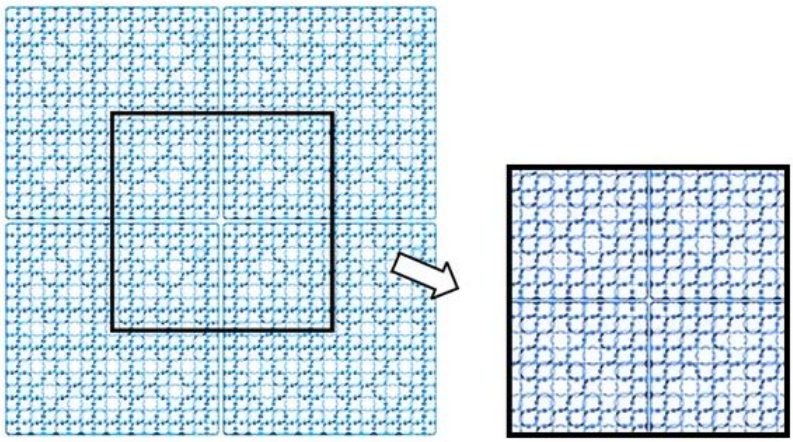

Figure 1-12 - Cluster 2x2 of FAs considered by Yan [27]

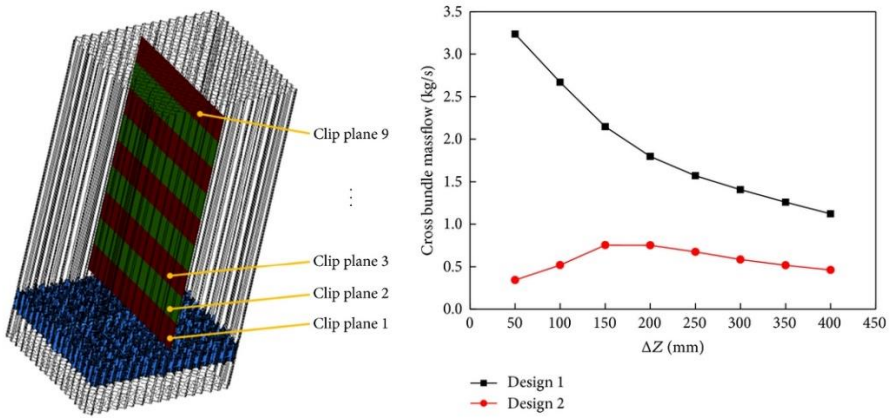

Figure 1-13 - (left) cross bundle mass flow at different axial levels, (right) associated evolution axially [27]

The lateral force due to a pressure difference around the grid depends on the pressure loss of the possible branches. The grid design and its external features are intricate by design. However, the geometry of the water gap has an important effect on the redistribution, and the associated pressure loss coefficient is not often studied (Wanninger, for instance, considers that it is zero [9, 22]).

The most important parameter to take into account is probably the width of this region. The deformation indeed leads to an increase or a decrease of those inter-grid areas [46]. As also remarked recently in [51, 52], the redistribution toward the bypasses depends on their width (and on the fluid velocity). Consequently, combining the grid external geometry as well as the distance between them (Figure 1-14), the coolant redistribution and the force associated could be estimated, *a posteriori*.

The latter phenomena, in view of the lack of references in the literature, embodies the basis of our future work in hydraulics.

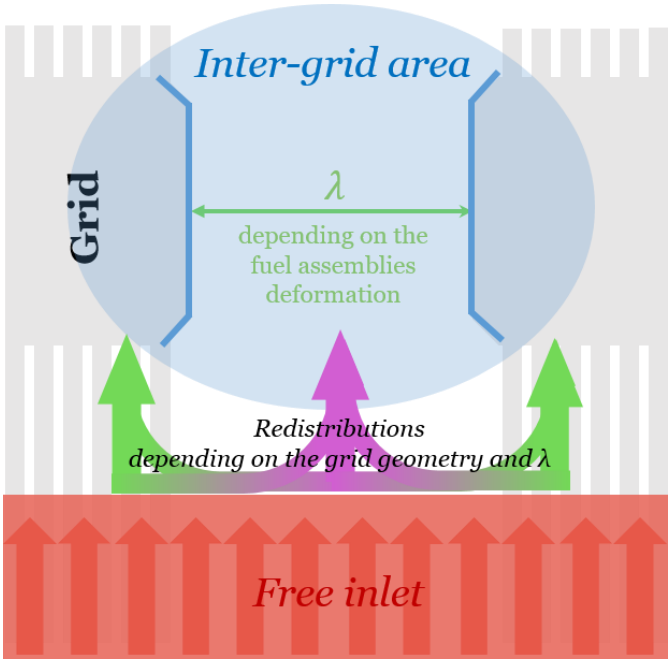

Figure 1-14 - Possible behaviors of the flow upstream from the grid

Chapter 2: Toward a water gap model to predict redistributions near the grids

Highlights of the chapter

- Flow redistribution near the grids is investigated in the context of fuel assembly bow.
- Semi-analytical models are built iteratively, their accuracy is assessed through comparisons with CFD and a dedicated experimental mock-up.
- Accounting for stagnation points below the water gap is important.
- Accounting for lateral friction across rods is recommended for narrow bypasses.
- Sensitivity analysis performed thanks to the computational efficiency of the models.

1. The inter-grid area seen as a simple channel flow

As mentioned above, the purpose of this section is twofold. On the one hand it aims at finding out the redistribution behavior upstream from the grid, on the other hand, it aims at estimating the related force F_V (chapter 1) through the pressure field. This chapter has been published in [53].

A natural 1D-approach consists in modelling the fluid flow through the *extended Bernoulli's principle*:

$$P_{\mathrm{A}} + \frac{1}{2}\rho V_{\mathrm{A}}^2 = P_{\mathrm{B}} + \frac{1}{2}\rho V_{\mathrm{B}}^2 + \Delta\mathbb{P} \qquad \text{(Eq. 2-1)}$$

Where P_{i} stands for the static pressure at point i, $\mathrm{V_i}$ stands for the bulk velocity (or mean velocity). A and B are points located respectively upstream and downstream of the water gap. ρ is still the fluid density, and finally $\Delta\mathbb{P} > 0$ is the irreversible pressure loss between A and B. This principle traces the mechanical energy all channel long. For the special case of a perfect fluid $\Delta\mathbb{P} = 0$, and energy conservation is reached. Appendix C derives the Bernoulli's principle. The expression of $\Delta\mathbb{P}$ is widely accepted as the following form [54]:

$$\Delta\mathbb{P} = KQ^a \qquad \text{(Eq. 2-2)}$$

Where K is an hydraulic resistance, Q is a volumetric flow rate, and a is an exponent whose value depends on the formula adopted. The general formula presented above covers the whole sum of both frictional losses (*i.e.* energy dissipation per unit length due to the fluid rubbing against the duct wall) and local losses (*i.e.* energy dissipation due to sharp changes of the duct geometry).

(Eq. 2-1) is a model of the bypass. This axial pathway is not evident, because the grid geometry is intricate, and depends on the core state of deformation - the closer the fuel assemblies get, the thinner the water gap is -. In order to simplify the real geometry of the

outer straps keeping in mind the general shape of the grids, we assimilate water gap as a 3D-extruded plane channel whose walls are flushed with the last rows of the two adjacent tube bundles. The guide vanes are represented by a bevel at both inlet and outlet of the latter channel. As seen before, the exact design of the vanes can vary, and the 3D extrusion does not account for the discontinuous, periodic, presence of guide vanes. Keeping those assumptions in mind, the angle and curvature of the adopted bevels are uncertain quantities.

The system is thus made of three parts: a convergent (C_1), a straight plane channel (C_2) and a diffuser (C_3). The whole region will often be referred as convergent-diffuser (CD) thereafter. The detail of this compound is shown in Figure 2-1.

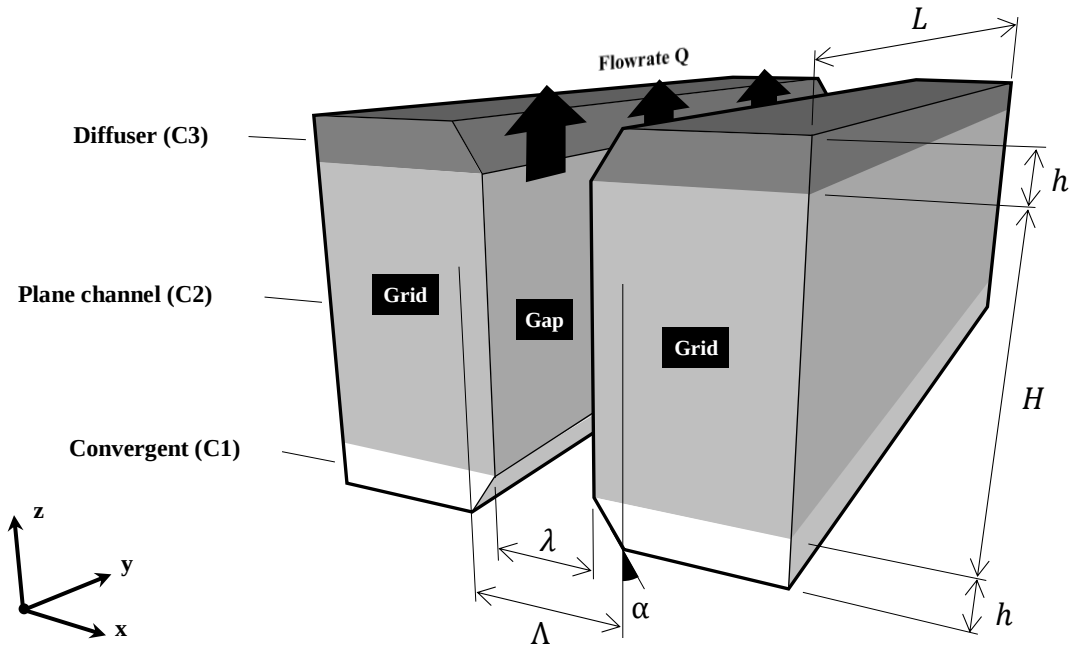

Figure 2-1 - Geometry considered for the area between two grids

The geometry is characterized by the channel width (in nominal conditions $\lambda \simeq 2.10^{-3}m$), which is the main parameter of the gap between fuel assemblies. Those kind of geometries depend very much on the geometrical dimensionless number Λ/λ where Λ is the width of both entrance and exit. The system is thus symmetric with respect to the horizontal and vertical mid-planes (so does design 2 in Figure 1-11). The latter two quantities are linked through:

$$\Lambda = \lambda + 2h \cdot \tan(\alpha) \qquad \text{(Eq. 2-3)}$$

Where h in the height of both the convergent (C_1) and the diffuser (C_3), α is the guide vanes angle. Those four parameters are such as $\Lambda\backslash\lambda$ equals more or less 4. H is the plane channel height, and finally L is the length of the system along the y-axis.

As the pressure drop induced by the latter geometry is not directly available in the literature, we decide to construct it.

1.1. *Pressure drop across C_1*

In the convergent C_1, we assume classically that the resistance is composed of both local and frictional parts. The total pressure loss across a "rectilinear converging bellmouth" is adapted from [55]:

$$\Delta\mathbb{P}_1 = \frac{1}{2}\rho\left[\frac{\zeta_1}{(L\lambda)^2}\left(1-\frac{\lambda}{\Lambda}\right)+\frac{1}{2L^2\cos(\alpha)}\int_0^h \frac{f(\ell_1(z_1),Q)}{\ell_1(z_1)^3}\,dz_1\right]Q^2 \qquad \text{(Eq. 2-4)}$$

Where ζ_1 and f are two coefficients for local and frictional losses respectively and ρ is the fluid density. The local gap width $\ell_1(z_1)$ is a linear map such that $\ell_1(0)=\Lambda$ and $\ell_1(h)=\lambda$. We considered that ζ_1 varied little enough on the range of commonly studied gap values $\lambda \in [0\text{ mm};\ 20\text{ mm}]$ so that it could be treated as a constant. Usually we assume that f is constant provided that the Reynolds number is high, however we chose not to make this unecessary assumption as Haaland came up with a computational-friendly correlation to assess f [56]. It led us to write the frictional part in Eq. 2-4 as the integration from $z_1=0$ to h of the Darcy-Weisbach equation applied to a pipe with a linearly varying hydraulic diameter (and thus linearly varying bulk velocity). One can check that taking f as a constant in Eq. 2-4 would have yielded the original Idel'Cik correlation [57].

1.2. *Pressure drop across C_2*

The middle part C_2 is a plane channel whose hydraulic diameter is 2λ. The flow resistance is then only due to friction. The Darcy-Weisbach equation directly gives the streamwise (linear) evolution of pressure loss in C_2:

$$\Delta\mathbb{P}_2 = \frac{\rho f H}{4\lambda}\left(\frac{Q}{L\lambda}\right)^2 \qquad \text{(Eq. 2-5)}$$

1.3. *Pressure drop across C_3*

Similarly to part C_1, this resistance in the diffuser C_3 depends on a local and a frictional part. The frictional resistance is equal to that of Eq. 2-4 for reasons of symmetry. We obtain in Eq. 2-6 the streamwise evolution of the pressure loss across C_3 in the same way as we did for C_1:

$$\Delta\mathbb{P}_3 = \frac{1}{2}\rho\left[\frac{\zeta_3}{(L\lambda)^2}\cdot\left(1-\frac{\lambda}{\Lambda}\right)^2+\frac{1}{2L^2\cos(\alpha)}\left(\int_0^h \frac{f(\ell_1(z_1),Q)dz_1}{\ell_1(z_1)^3}\right)\right]Q^2 \qquad \text{(Eq. 2-6)}$$

1.4. *Conclusion: total resistance coefficient - Model 0*

We derive the total pressure loss coefficient of what we call Model 0 from the summation of Eq. 4 to 8:

$$K_{\mathrm{CD}} = \frac{\Delta\mathbb{P}}{Q^2} = \frac{\rho}{2(L\lambda)^2}\left[\zeta_1 \cdot \left(1 - \frac{\lambda}{\Lambda}\right) + \frac{fH}{2\lambda} + \zeta_3 \cdot \left(1 - \frac{\lambda}{\Lambda}\right)^2 + \frac{\lambda^2}{\cos(\alpha)}\left(\int_0^h \frac{f(\ell_1(z_1), Q)dz_1}{\ell_1(z_1)^3}\right)\right] \qquad \text{(Eq. 2-7)}$$

First, to ensure that the total loss induced by this formula is coherent, we compared the latter with a simple, nominal, 1D channel case (Appendix D). The loss development with respect to λ is put to the test further below, when redistribution occurs.

Used to estimate lateral hydraulic forces due to pressure differences on each side of a spacer grid (see Appendix E), this initial model significantly overestimates the forces. This originates in the neglected, and unknown, fraction of the flow passing the grids level through the rod bundle rather than through the water gap, lowering the actual effect of the convergent-diffuser.

2. Step-by-step construction of an advanced model of the flow redistribution

2.1. *Model 1: distribution of the flow between the water gap and its surrounding grids*

In the Model 0, the flow is bound to circulate in separate domains, with some kind of impermeable boundary between the rod bundles and the water gap. Water particles initially inside one fuel assembly will go through the mixing grid and remain inside the assembly downstream of the grid. Water particles initally in the water gap between assemblies will go through the bypass between grids and continue along the water gap.

In reality, when the gap width λ decreases a lot, the flow in the bypass dries up. On the contrary, when the gap width increases enough, water rushes from the rod bundles and towards the gap. Model 1 is designed to account for these two phenomena in addition to the convergent-diffuser system of Model 0.

The grid is geometrically complex and modeling the behavior of the flow passing through it is a challenging task. Within this chapter, we stick to a simple expression of the irreversible pressure drop associated to the mixing grids in the following form Eq. 2-8:

$$\Delta\mathbb{P}_{\mathrm{g}} = \frac{1}{2}\rho C_{\mathrm{g}} V_{\mathrm{g}}^2 = K_{\mathrm{g}} Q_{\mathrm{g}}^2 \qquad \text{(Eq. 2-8)}$$

Where C_{g} is the coefficient of local resistance of the grid - values and experimental tests can be found in [58, 59, 60] -, V_{g} is the bulk velocity upstream of the half-grids, Q_{g} is the volumetric flow rate crossing one half-grid and K_{g} is the resistance given by Eq. 2-9:

$$K_{\mathrm{g}} = \frac{1}{2}\rho\frac{C_{\mathrm{g}}}{S_g^2} \qquad \text{(Eq. 2-9)}$$

With S_{g} being the flow cross-section upstream one half-grid.

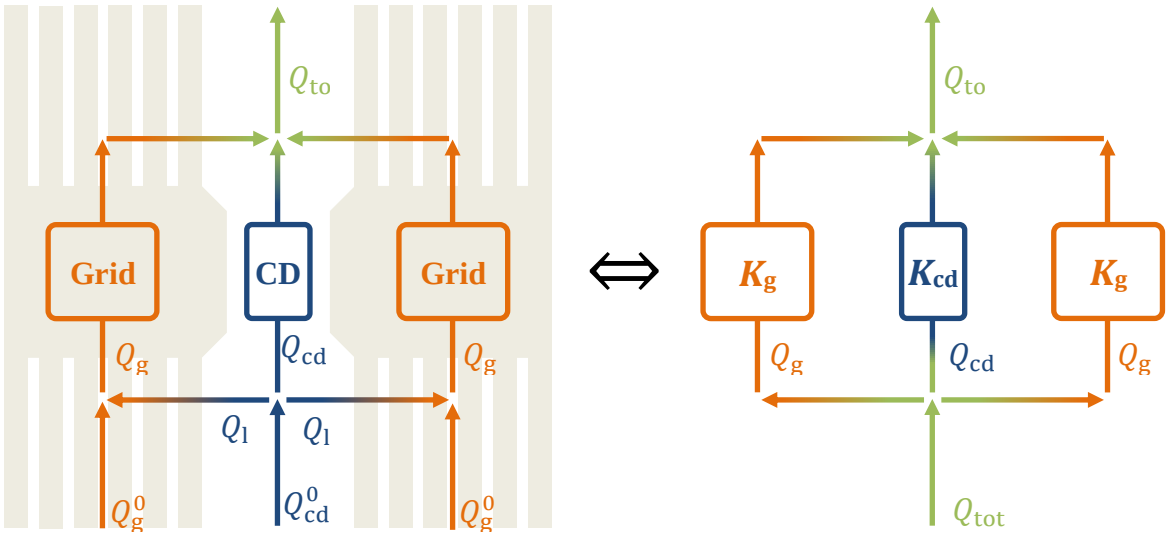

Figure 2-2 - Hydraulic network representing the possible pathways at the grids level (model 1)

Having developed adequate resistances for the convergent-diffuser (Eq. 2-7) and the grid (Eq. 2-9), we can set up a simple hydraulic network (Figure 2-2) representing the system of interest. It consists of two half-grids separated by a convergent-diffuser (meant for the water gap). Both half-grids are supplied with the same upstream flow rate noted Q_g^0 (symmetric system), while Q_{cd}^0 is the upstream flow rate feeding into the convergent-diffuser. The leaking flow rate between the grids and the convergent-diffuser is named Q_l. The effective flow rates crossing the grids and the convergent-diffuser are respectively named Q_g and Q_{cd}. The total outgoing flow rate leaving the system is named Q_{tot}. Applying the so-called *Kirchhoff hydraulic equations* [54], *i.e.* the network mass conservation and energy, we obtain the following system of equations (Eq. 2-10):

$$\begin{cases} \Delta P_{cd}(Q_{cd}) - \Delta P_g(Q_g) = 0 \\ Q_g^0 + Q_l = Q_g \\ Q_{cd}^0 = 2Q_l + Q_{cd} \end{cases} \qquad \text{(Eq. 2-10)}$$

By defining $Q_{tot} = 2Q_g^0 + Q_{cd}^0$, the system can be changed into Eq. 2-11:

$$\begin{cases} K_{cd}Q_{cd}^2 - K_gQ_g^2 = 0 \\ 2Q_g + Q_{cd} = Q_{tot} \end{cases} \qquad \text{(Eq. 2-11)}$$

Basically, Eq. 2-11 shows that the splitting of Q_{tot} into Q_{cd} and Q_g does not depend on individual inlet boundary conditions Q_g^0 and Q_{cd}^0 but on their sum only. In other words, the geometry upstream of the grids level has no influence on the redistribution computed in Model 1 (see the equivalent network in Figure 2-2). Practically, when modifying Q_{cd}^0 and Q_g^0 while keeping Q_{tot} constant, the leaking flow rate Q_l will adapt so that in the end Q_{cd} and Q_g remain the same (this is the meaning of the removed equation between Eq. 2-10 and Eq.

2-11).

One can notice that the final system depends on two functions $\Delta P_g(Q_g)$ and $\Delta P_{cd}(Q_{cd})$. It is non-linear in terms of unknowns Q_g and Q_{cd}, raised to the power of a in the energy equation ($a = 2$ in our case). While an advanced algorithm could be necessary for larger non-linear systems (see for instance [61, 62] or [63]), this small one can be solved easily using any root-finding algorithm. It is however shown below that the predictions of this model deteriorate when considering low values of λ. Indeed, when the CD's thickness tends towards zero, CFD simulations show that a stagnation point appears, increasing the pressure drop in a way this model cannot reproduce, yielding the need for a second improving step in the proposed modeling strategy.

2.2. *Model 2: stagnation point effect for thin water gaps*

When the CD gets very narrow ($\lambda \simeq 0$), it acts as an opaque obstacle to the fluid, thus producing a stagnation point: the flow flees towards the grids, the CD upstream velocity decreases down to almost zero and the kinetic energy turns into a pressure peak at the inlet of the CD (Figure 2-3).

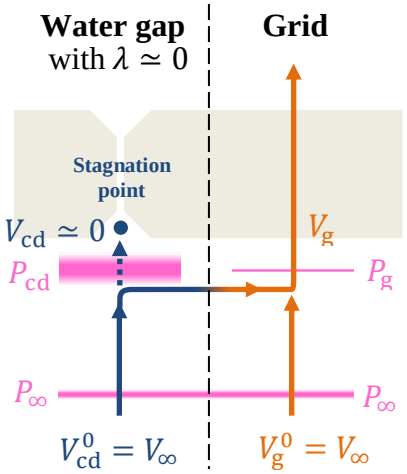

Figure 2-3 - Stagnation point setting up upstream from the convergent-diffuser

Therefore, we note that when λ is small enough, there is a conversion of the kinetic energy linked to V_{cd} into a kinetic energy linked to V_g. This observation introduces a 'branch-coupling' term in the energy equation.

Let us suppose that far from the obstacles, velocity V_∞ and pressure P_∞ are homogeneous (Figure 2-3). As explained above, in a stagnation point context, upstream grid pressure P_g and CD pressure P_{cd} are not equal anymore. Applying the Bernoulli equation along two distinct axial streamlines across the grid and across the convergent-diffuser, we obtain Eq. 2-12:

$$\begin{cases} P_\infty + \frac{1}{2}\rho V_\infty^2 = P_\mathrm{g} + \frac{1}{2}\rho V_\mathrm{g}^2 \\ P_\infty + \frac{1}{2}\rho V_\infty^2 = P_\mathrm{cd} + \frac{1}{2}\rho V_\mathrm{cd}^2 \end{cases} \quad \text{(Eq. 2-12)}$$

Which leads to:

$$\Delta P_\mathrm{c} = P_\mathrm{cd} - P_\mathrm{g} = \frac{1}{2}\rho\left(V_\mathrm{g}^2 - V_\mathrm{cd}^2\right) \quad \text{(Eq. 2-13)}$$

The 'branch-coupling' term named ΔP_c appears linking both grid and CD dynamic pressures. This additional term can be added to the equation energy (Eq. 2-11) in order to take into account that the pressure drops in grid and CD are no longer equal but are now shifted from each other by a value of ΔP_c:

$$\Delta P_\mathrm{cd} - \Delta P_\mathrm{g} = \Delta P_\mathrm{c} \quad \text{(Eq. 2-14)}$$

Introducing the flow rates Q_g and Q_cd, and the cross-section S_cd of the CD upstream of the grids, Eq. 2-14 becomes:

$$K_\mathrm{cd}Q_\mathrm{cd}^2 - K_\mathrm{g}Q_\mathrm{g}^2 = \frac{1}{2}\rho\left(\frac{Q_\mathrm{g}^2}{S_\mathrm{g}^2} - \frac{Q_\mathrm{cd}^2}{S_\mathrm{cd}^2}\right) \quad \text{(Eq. 2-15)}$$

We can then define the modified resistance coefficients as below:

$$\widetilde{K}_\mathrm{cd}(\lambda) = K_\mathrm{cd}(\lambda) + \frac{\rho}{2S_\mathrm{cd}^2(\lambda)} \quad \text{(Eq. 2-16)}$$

$$\widetilde{K}_\mathrm{g} = K_\mathrm{g} + \frac{\rho}{2S_\mathrm{g}^2} \quad \text{(Eq. 2-17)}$$

We thus obtain the final equation system for Model 2:

$$\begin{cases} \widetilde{K}_\mathrm{cd}Q_\mathrm{cd}^2 - \widetilde{K}_\mathrm{g}Q_\mathrm{g}^2 = 0 \\ 2Q_\mathrm{g} + Q_\mathrm{cd} = Q_\mathrm{tot} \end{cases} \quad \text{(Eq. 2-18)}$$

One can remark that Eq. 2-18 (Model 2) is formally identical to Eq. 2-11 (Model 1), except that both resistance coefficients are increased by distinct constant offsets, which entails that Eq. 2-11 and Eq. 2-18 will yield different solutions. This means that the flow rate redistribution is modified when the stagnation point in taken into account (the added pressure drop is not the only outcome).

2.3. *Model 3: lateral resistance due to the rods*

In the previous developments, the lateral obstruction due to the fuel rods presence was neglected and the fluid could switch among the grid and CD channels without any resistance. This means that in Models 1 and 2, the geometry upstream of the grids level has no actual influence on the flow redistribution.

In reality, an additional lateral resistance causes the total axial pressure drop to slightly increase. CFD simulations show in the next section that the bypass pressure drop is for instance underestimated by approximately 10% in the case of a 1mm-thin bypass without fuel rods. Practically, the next evolution of the model, *i.e.* Model 3, includes the resistance K_l for the leaking flow rate Q_l coming from the bypass and going to the grid through several rows of fuel rods (see Figure 2-4).

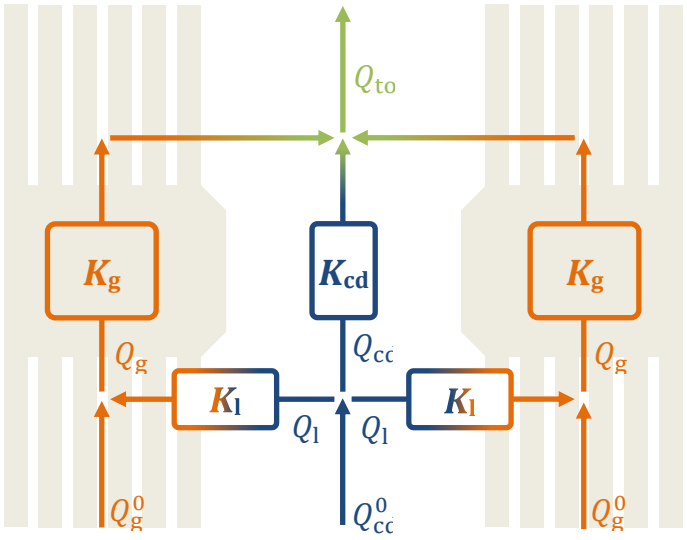

Figure 2-4 - Additional lateral resistance due to cross-flows through the rod bundle (model 3)

Quite intuitively, the coefficient K_l depends on the 3D incidence angle of the leaking flow rate in a very complicated way. To provide a first approximation of this contribution, a 2D representation is chosen (see Figure 2-5), so that some results are available in the literature. As we have seen in chapter 1, in his work, Peybernès [28, 30] came up with a correlation for the lateral pressure drop across an inclined rod bundle, based on the Eole experimental results. The same correlation has also been used recently in [9] in a more global effort to estimate the hydraulic forces on PWR fuel assemblies.

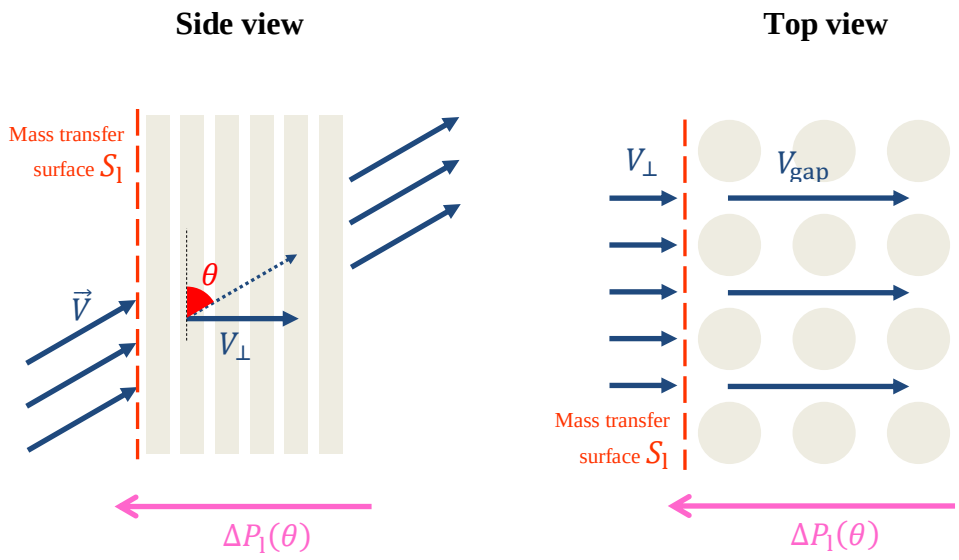

Figure 2-5 - General layout of an inclined flow passing through a rod bundle

As a reminder, the correlation states that the mean pressure drop per row is:

$$\Delta P_{\mathrm{row}}\left(V_{\mathrm{gap}},\theta\right)=\frac{1}{2}\rho K_{\perp}\xi(\theta)V_{\mathrm{gap}}^{2} \qquad \text{(Eq. 2-19)}$$

Where V_{gap} stands for the fluid velocity in the gaps between the rods, $K_{\perp}$ is the pressure drop coefficient for purely transverse flows ($\theta=90°$) and $\xi(\theta)$ is a correction factor stemming from the Eole installation operated at various incidence angles θ, given by Eq. 2-20 below:

$$\xi(\theta)=\left(\frac{\sin(\theta)}{\cos\left(\frac{\pi}{4}-\frac{\theta}{2}\right)}\right)^{1.7} \qquad \text{(Eq. 2-20)}$$

After some computations, the resulting lateral pressure drop across N rows of fuel rods is then given by:

$$\Delta P_{\mathrm{l}}(\theta)=\frac{\rho N K_{\perp}\xi(\theta)\beta^{2}}{2S_{\mathrm{l}}^{2}\sin^{2}(\theta)}Q_{\mathrm{l}}^{2}=K_{\mathrm{l}}(\theta)Q_{\mathrm{l}}^{2} \qquad \text{(Eq. 2-21)}$$

Where β is the geometrical ratio of the gap velocity to the pitch velocity and S_{l} the lateral rectangular surface over which the fluid transfer Q_{l} takes place.

Writing $S_{\mathrm{l}}=Lh_{\mathrm{l}}$ with L the total width of a fuel assembly (see Figure 2-1) and h_{l} the corresponding height, we eventually give the following expression for K_{l}:

$$K_{\mathrm{l}}(\theta)=\frac{\rho N K_{\perp}\xi(\theta)\beta^{2}}{2L^{2}h_{\mathrm{l}}^{2}\sin^{2}(\theta)} \qquad \text{(Eq. 2-22)}$$

In our context of multi-1D modeling, the incidence angle θ can be approximated from the ratio of the lateral velocity to the axial velocity in the upstream branch (*i.e.* grid or CD), which corresponds to the following expressions:

$$\theta=\begin{cases}\tan^{-1}\left(\dfrac{S_{\mathrm{g}}|Q_{\mathrm{l}}|}{S_{\mathrm{l}}|Q_{\mathrm{g}}|}\right) & \text{if } Q_{\mathrm{l}}<0\\ \tan^{-1}\left(\dfrac{S_{\mathrm{cd}}|Q_{\mathrm{l}}|}{S_{\mathrm{l}}|Q_{\mathrm{cd}}|}\right) & \text{if } Q_{\mathrm{l}}>0\end{cases} \qquad \text{(Eq. 2-23)}$$

Using the newly added resistance to lateral flow, system (Eq. 2-18) becomes:

$$\begin{cases}\widetilde{K}_{\mathrm{cd}}Q_{\mathrm{cd}}^{2}-\widetilde{K}_{\mathrm{g}}Q_{\mathrm{g}}^{2}-K_{\mathrm{l}}Q_{\mathrm{l}}^{2}=0\\ 2Q_{\mathrm{g}}+Q_{\mathrm{cd}}=Q_{\mathrm{tot}}\\ Q_{\mathrm{g}}^{0}+Q_{\mathrm{l}}=Q_{\mathrm{g}}\end{cases} \qquad \text{(Eq. 2-24)}$$

Unlike in previous models, the inlet flow rate Q_{g}^{0} (or Q_{cd}^{0}) now plays an important role in the redistribution of Q_{tot} between Q_{g} and Q_{cd}, due to the presence of Q_{l} in the first equation of system (Eq. 2-24). This means that in Model 3, the geometry of the fuel assemblies upstream of the grids does have an influence on the redistribution. In practice, this is shown by the appearance of several new geometrical parameters, notably β, h_{l} and N. The value of β can be easily calculated given the pitch and diameter of fuel rods. However, h_{l} and N characterize the dimensions of the region where cross-flows take place between the water gap and the grids. As such, those two parameters are complex to estimate and are likely to depend on the bypass thickness λ.

3. Comparison with local CFD simulations

3.1. *Presentation of the CFD models*

CFD simulations are carried out in order to validate our semi-analytical model. The local-scale solutions provided by two different programs, namely TrioCFD [64] and Code_Saturne [65], are cross compared to produce reliable reference data.

The geometry considered for the calculations is shown on Figure 2-6. It consists in two assemblies separated by a central bypass of adjustable thickness λ (1, 2, 3, 5, 10 and 20 mm). Two rods are represented along the y-axis while there are four and a half rods per assembly along the x-axis. The tube bundle regions use a rather fine mesh and the intricate geometry of the grids is not reproduced. Instead, we use a porous media approach with a coarser mesh and calibrate the source term in order to reach exactly the desired value of K_{g}. For the same reasons, some volume inside the grids close to the convergent-diffuser is not meshed (see again Figure 2-6), since it would bring unwanted recirculation in the flow, thus increasing artificially the value of K_{g}.

The mesh is unstructured, consisting in 3D tetrahedral elements with two prismatic layers applied on surfaces with a no-slip boundary condition (fuel rods and outward faces of the grids, see Figure 2-6). As TrioCFD does not allow prismatic volumes, a specific version of the mesh was created where the prisms near the walls are split into five tetrahedrons.

A mesh convergence study has been realized for the case $\lambda = 5\ \mathrm{mm}$. For both codes, four calculations have been run with various grid refinements whose y^{+} averaged on wall surfaces always laid in the $[30; 100]$ range required by the wall function. Volumetric flow rates in the water gap and pressure drop across the grid exhibited deviations of less than 6% between all the meshes. We selected the second thinnest mesh considering it was a fair trade-off between accuracy and performance. It contains approximately 5.10^{6} cells.

All meshes and geometries were run with the SALOME software [66].

Symmetry boundary conditions are applied on each lateral side of the fluid domain (see Figure 2-6). Inside the grids, a symmetry condition is applied on all the lateral surfaces (which are mainly fuel rods) in order to disable friction that would otherwise increase the pressure drop artificially (K_g is defined explicitly as a source term, see above). Outside of the grids, a no-slip condition is applied on the fuel rods and on the convergent-diffuser walls (Figure 2-6). An axial flow velocity of 6 m/s is imposed uniformly on the bottom inlet surface (the

Reynolds number based on bulk velocity and rod diameter is 10^5). Finally, a constant pressure is set on the top outlet surface (see Figure 2-6).

Turbulence is handled by a standard k-ε RANS model accompanied by a wall function (1-scale model - log law for Code_Saturne and Reichardt for TrioCFD). We aim at reaching a steady state.

Water density is 700 kg/m^3, close to the operating value in a PWR.

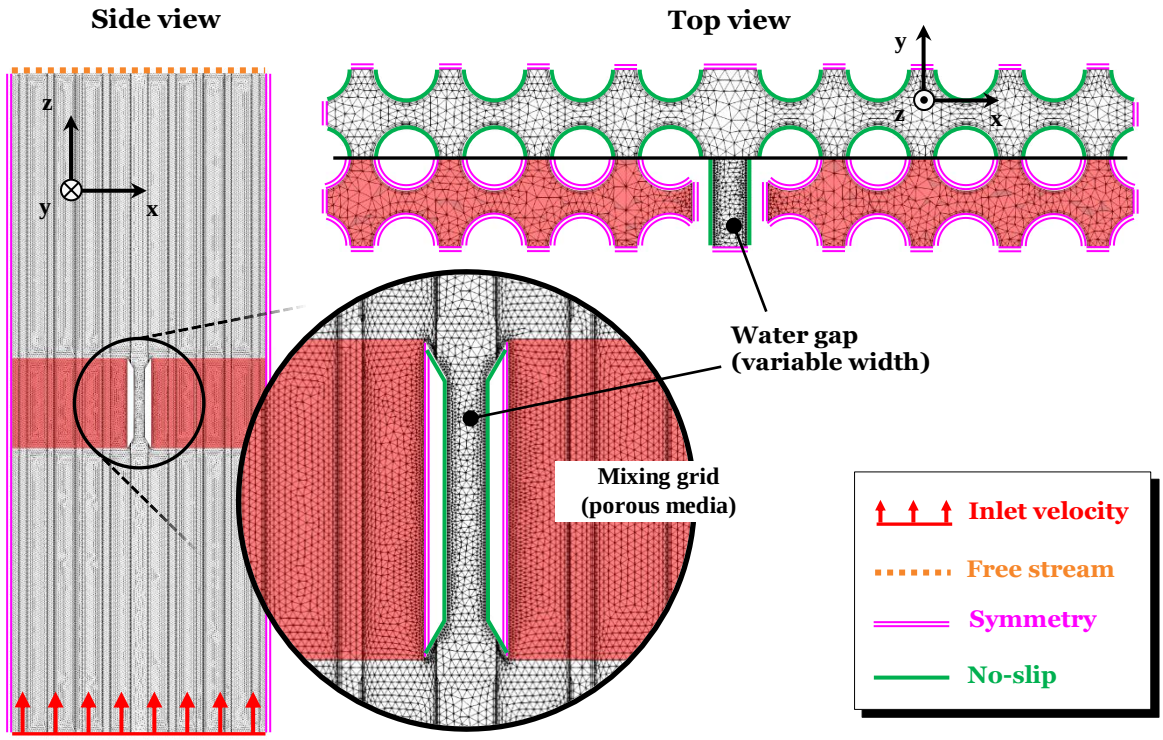

Figure 2-6 - Description of the mesh (λ = 5 mm here) and boundary conditions used in the CFD simulations

3.2. *Pressure drop across the grid*

The first physical value of interest is the pressure drop across the convergent-diffuser. Two different locations were probed, respectively called 'middle' and 'bevel' (Figure 2-7). The pressure drops obtained for the different CD thicknesses are plotted in Figure 2-8.

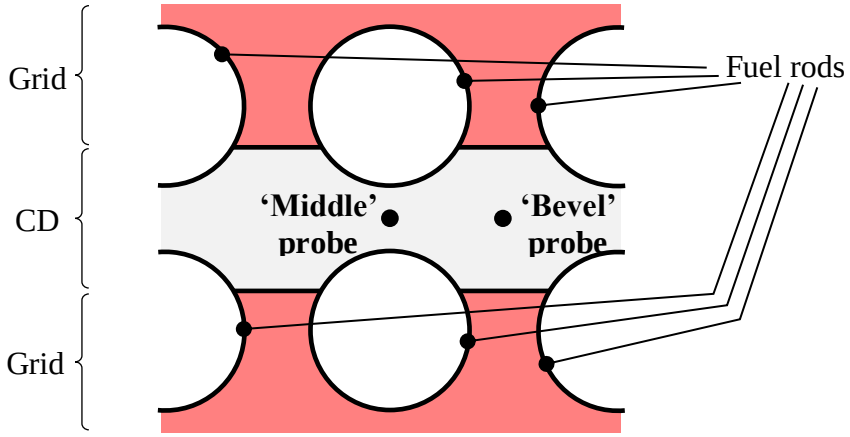

Figure 2-7 - Position of the probes of pressure drop

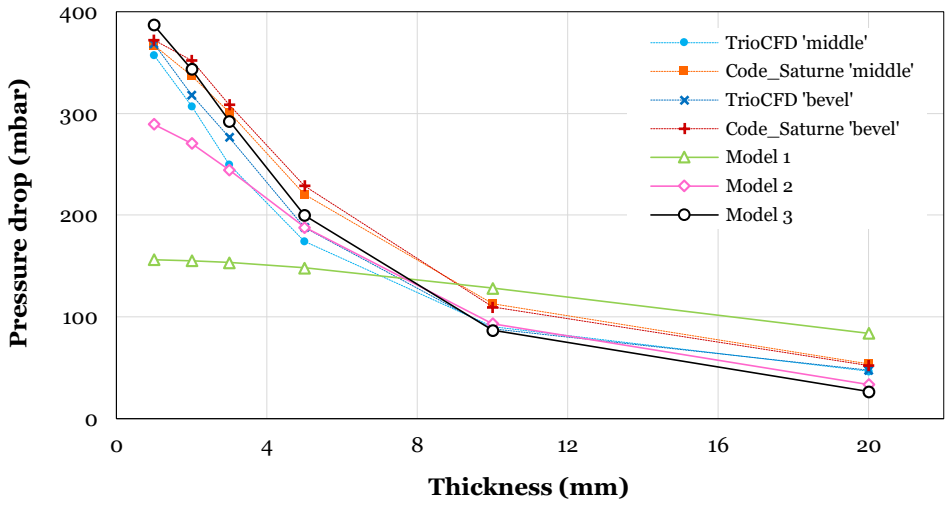

Figure 2-8 - Pressure drop as a function of the water gap thickness

Both CFD codes found that the pressure drop is almost the same for the 'middle' probe and for the 'bevel' probe. This means that the pressure hardly varies in the spanwise direction.

Compared to CFD, Model 1 shows poor results below $\lambda = 6$ mm. As mentioned in section 2, this discrepancy is related to the stagnation point at the entry of the CD, clearly visible in Figure 2-9 showing TrioCFD results in mid-plane for $\lambda = 1$ mm and not taken into account in the model. Model 2 logically performs better, with a relatively good agreement with both CFD reference results, even though a 25% deviation could be underlined for the smallest values of λ. Finally, Model 3 yields excellent results for all values of λ between 1 and 20 mm, with the internal parameters given in section 5.

It is worth putting emphasis on the CPU cost associated to one data point of Figure 2-8, reaching several days in the case of CFD versus a split second in the case of the semi-analytical Model 3 (for basically the same results).

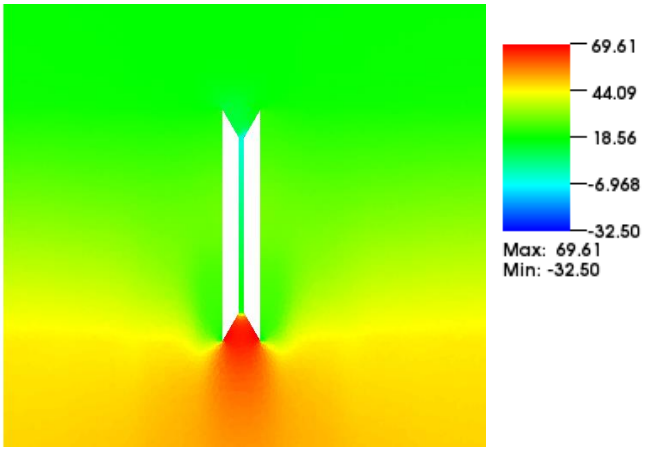

Figure 2-9 - Pressure peak underneath the CD for $\lambda = 1$ mm
Color map of pressure/density $(Pa.kg^{-1}.m^3)$

3.3. *Flow rate and mean axial velocity*

In this section, flow rate and velocity in the water gap obtained with CFD are compared to those given with the proposed semi-analytical models (see Figure 2-10). Since the mesh for CFD simulations only contains two rows of rods along the y-axis (see Figure 2-6), the flow rate must be rescaled to match the grid length L used in the models (see Figure 2-1).

Figure 2-10 (a) shows that Model 1 fails to reproduce the correct slope for the flow rate, but Models 2 and 3 give quantitatively accurate results. Model 3 stands out for its ability to stick to CFD curves even for the smallest values of λ (below 3 mm).

The bulk velocity in the bypass at mid-height is plotted in Figure 2-10 (b). When λ increases starting from very small values, a maximum is reached for $\lambda \simeq 3mm$ and the bulk velocity decreases thereafter. Model 1 does not reproduce this phenomenon as the bulk velocity keeps increasing with the bypass thickness. The modification brought in Model 2 (branch coupling term for capturing stagnation points) is the key to capturing the physics correctly. In this case, again Model 3 allows to further tune the solution for small values of λ to get very close to the reference curves.

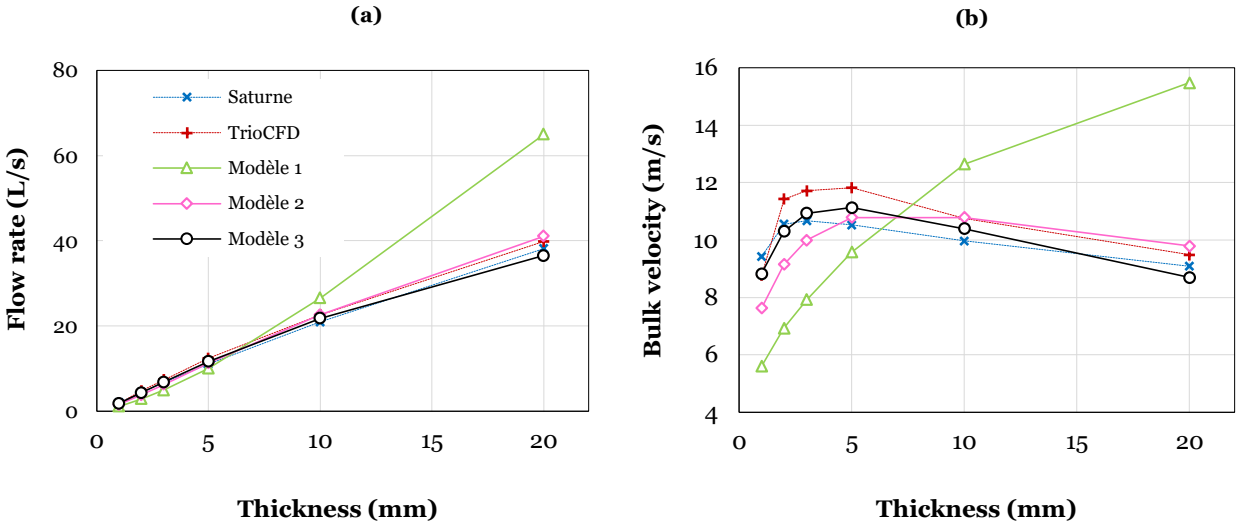

Figure 2-10 - Flow rate (a) and axial mean velocity (b) as a function of the water gap thickness

3.4. *Advanced calibration for parameters of Model 3*

As mentioned in section 2, Model 3 (*i.e.* integrating a resistance to the leaking flow Q_l) requires two empirical parameters to be set, namely the number of fuel rod rows N and the height h_l involved in the leak flow.

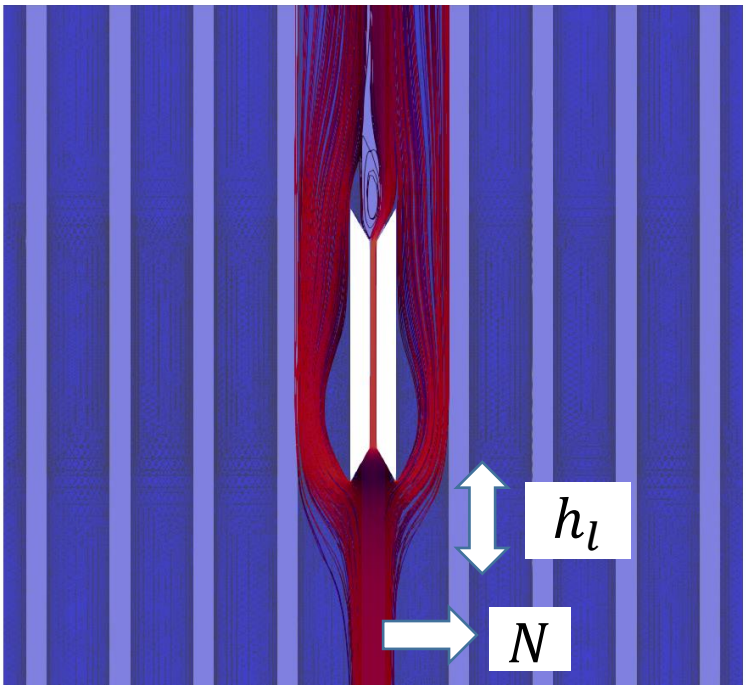

Figure 2-11 - Streamlines in the water gap for $\lambda = 1$ mm

First qualitative insights regarding these parameters are given by the streamlines in the vicinity of the grid for the flow coming initially from the water gap inlet boundary. An example is provided in Figure 2-11 for the streamlines obtained from the Code_Saturne simulation with a gap width $\lambda = 1$ mm. For this configuration, the redistribution (from the bypass to the grids) is initiated at a very small distance h_l upstream of the obstacle.

Furthermore, the fluid enters only the first row of the rod bundle inside the grids, yielding $N = 1$ in this particular case.

A more generic and quantitative approach is to calculate the lateral flow rate for successive rows upstream of the grids. The flow rates are calculated the same way as Yan [27]: clip planes are created parallel to the water gap for the first three rows and each of them is cut into several sub-surfaces along the bundle direction to estimate the evolution of the computed flow rates (see Figure 2-12 for the details). The first sub-surface is located between 0 and 5 mm upstream from the grids, and so on for the next 5 up to 30 mm upstream, with a 5 mm height each. The seventh and last sub-surface represents the lateral flow rate through the remaining geometry (between 30 mm and the 150 mm in the upstream direction).

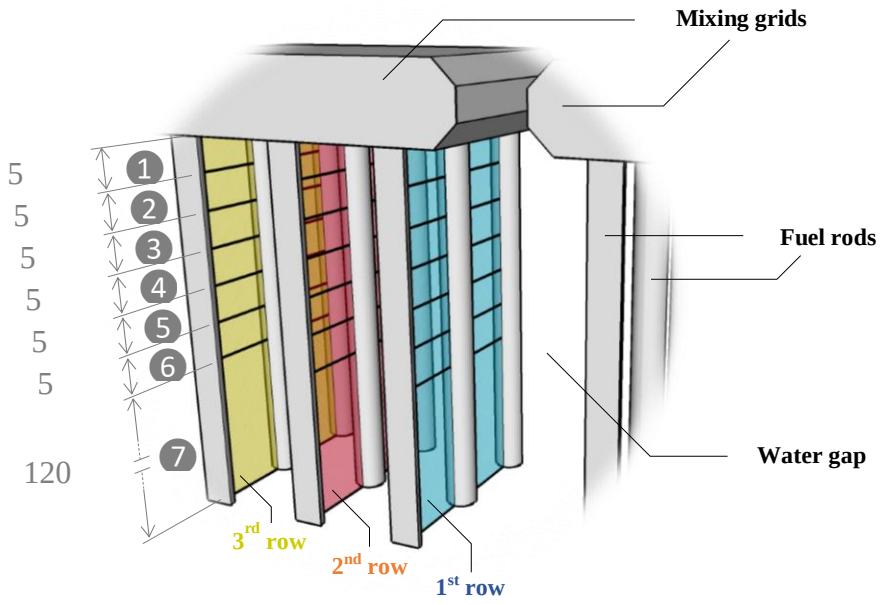

Figure 2-12 - Clip planes used for post-processing of local lateral flow rates and subdivision into sub-surfaces

This post-processing has been applied to the simulations performed with TrioCFD, for the two extremum values of CD's thicknesses (*i.e.* $\lambda = 1$ and $\lambda = 20$ mm) and the first three rows of fuel rods.

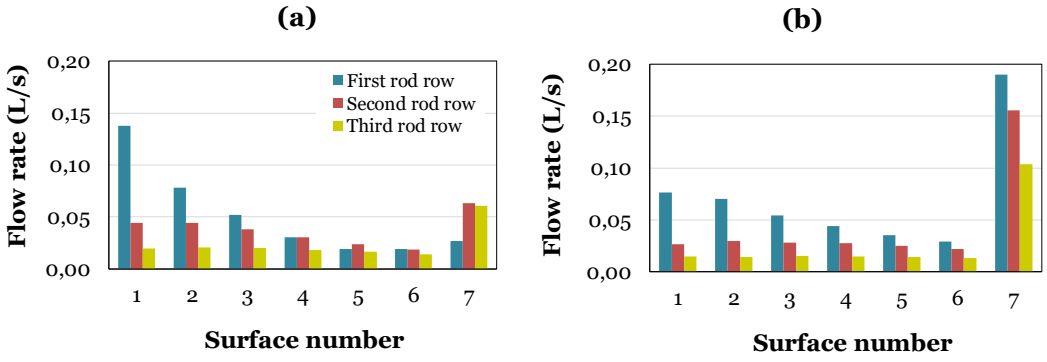

Figure 2-13 - Lateral flow rates calculated for a water gap width of (a) 1 mm and (b) 20mm

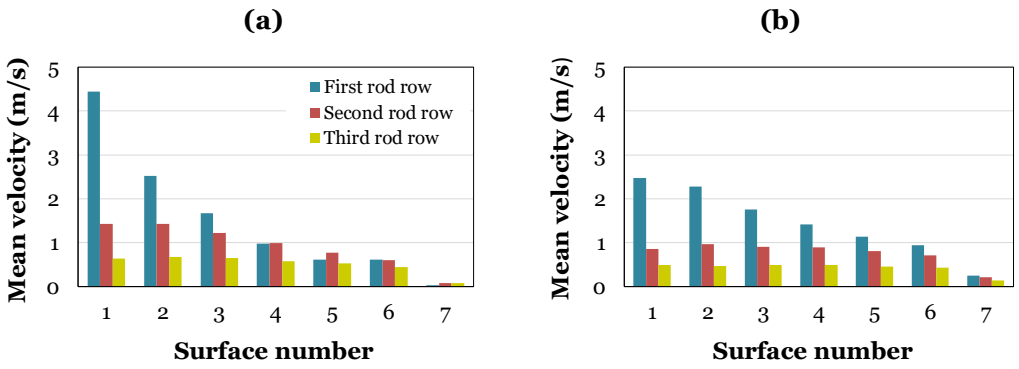

Figure 2-14 - Lateral average velocity for a water gap width of (a) 1 mm (b) 20 mm

Figure 2-13 and Figure 2-14 show the resulting flow rates and lateral average velocities respectively for both considered values of the water gap width. Absolute values are displayed for the sake of clarity in the comparisons, even though the fluid goes from the assembly to the bypass for the larger values of the water gap and in the opposite direction otherwise. The redistribution in the 1 mm-case (Figure 2-13 (a) and Figure 2-14 (a)) is strong near the grid (in agreement with what was observed on the streamlines of Figure 2-11), and for the first row of fuel rods. Actually, 60% of the total lateral flow rate occurs through surfaces 1 and 2 (*i.e.* within the first centimeter below the grid) and for the first rod row only. The lateral average velocity is also quite important within the first millimeters (almost the same order of magnitude as the axial velocity), but drops quickly under 1 m/s after only 1.5 cm. The 20 mm-case (Figure 2-13 (b) and Figure 2-14 (b)) shows smaller flow rates and they are more spread on all sub-surfaces. Only 30% of the total lateral flow rate is located within sub-surfaces 1 and 2 for the first row and the lateral velocity in the vicinity of the grid is again significantly larger for the first row of rods.

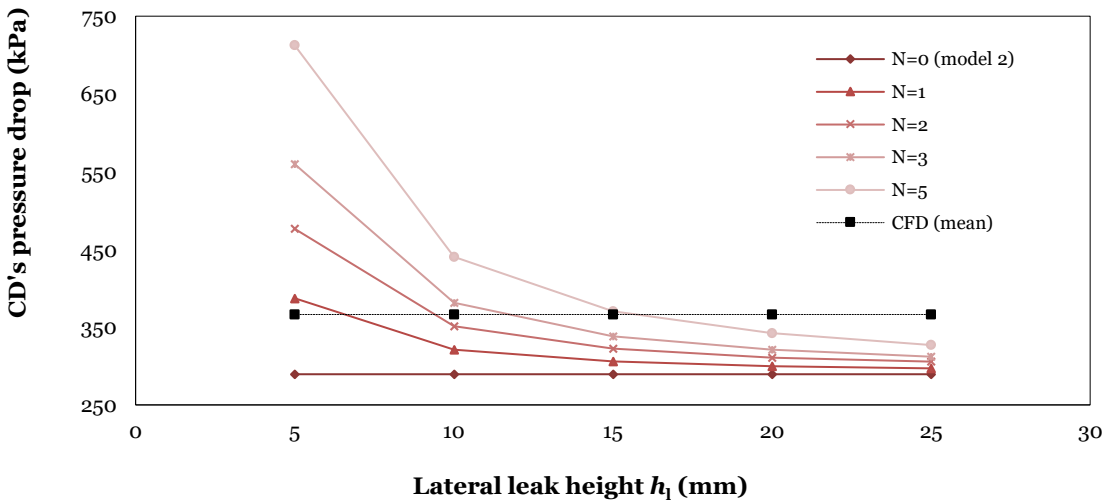

Figure 2-15 - Pressure drop as a function of leak length (for several row numbers) when λ = 1 mm

To close this section, it is noticeable that parameters h_l and N cannot be chosen independently. Figure 2-15 plots the pressure drops in the CD determined by Model 3 for many different combinations of leak height h_l and number of rows N, as well as the reference

value computed by CFD: several couples of values provide a good match, for instance $(h_l = 5\ \text{mm}\ ; N = 1)$, $(h_l = 10\ \text{mm}\ ; N = 3)$ or $(h_l = 15\ \text{mm}\ ; N = 5)$. The first one is probably the most relevant for small widths λ, while the second one best describes the configurations where λ is large. However, it is still possible to keep constant values for h_l and N for all values of λ. The sensitivity analysis in section 5 will help to assess the influence of these choices on the results produced by the semi-analytical models.

4. Comparison with dedicated experimental results

4.1. *Experimental mock-up*

In order to check that the previous semi-analytical models provide physically relevant results (in terms of pressure drop and flow rate distribution between the grids and the CD), a specific experimental setup was designed, named DIVA+G. Two half grids were 3D-printed in plastic material. They consist of a thick plate filled with numerous holes arranged in a triangular pattern, allowing a controlled pressure drop while maintaining flow conditions as homogeneous as possible. The space between the half-grids uses the same simplified geometry for the water gap as the theoretical model described in section 2 (Figure 2-1). Several shims of various thicknesses allow modifying the distance between the half-grids (*i.e.* the water gap). All these elements are placed in the test section of an hydraulic loop (Figure 2-16).

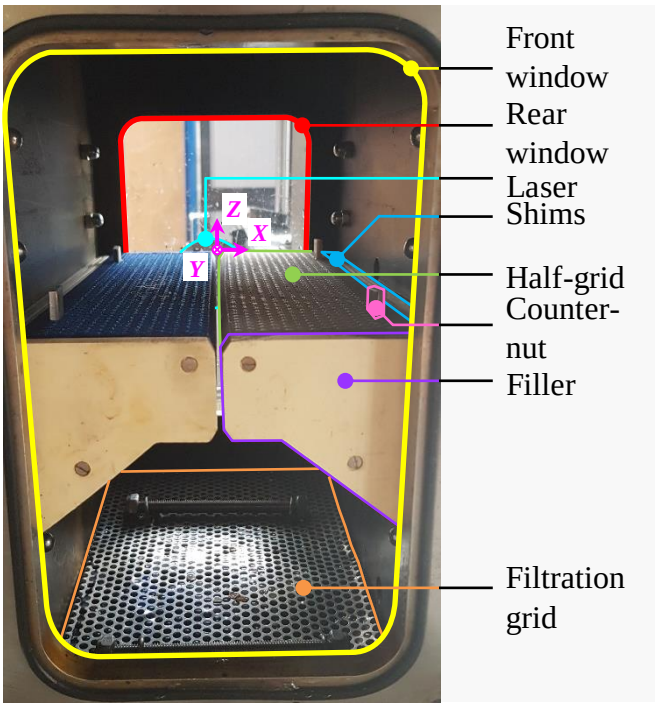

Figure 2-16 - The DIVA+G mock-up

Two differential pressure probes are located on a side wall at the base of one of the grids, above and below it. The local mean axial velocity is measured thanks to Laser Doppler Velocimetry. Between 60 and 340 locations are probed, according to the water gap width.

This allows determining accurately the flow rate through the gap, and therefore the flow rate within the grids by difference with the total flow rate. The reader could find further details of the mock-up in [67].

4.2. *Parameters for Models 1 and 2 for DIVA+G*

In DIVA+G, metallic shims are successively added aside to put grids closer. As a result, the ratio between flow cross-sections inside the grids and at the inlet decreases as the water gap goes thinner. Using the correlation in [55] for thickened grids, we are able to match the pressure drop measurement when the gap is closed ($\lambda = 0$). By extrapolation, it is possible to express the coefficient of local resistance C_g - defined in (Eq. 2-8) - with the following relation (Eq. 2-25):

$$C_g(\lambda) = 4.23 - 0.06\lambda \qquad \text{(Eq. 2-25)}$$

Here λ stands for the average width of the water gap, in millimeters. Likewise, the flow cross-section upstream of one half-grid S_g can be evaluated thanks to the following equation (Eq. 2-26):

$$S_g(\lambda) = \frac{1}{2}(S_0 - L\lambda) \qquad \text{(Eq. 2-26)}$$

where S_0 is the mock-up's cross-section (see Figure 2-16). As mentioned above in the chapter, the pressure loss associated to crossing the grids is thus given by (Eq. 2-27):

$$\Delta P_g = K_g(\lambda) Q_g^2 = \frac{1}{2}\rho C_g(\lambda)\frac{Q_g^2}{S_g(\lambda)^2} \qquad \text{(Eq. 2-27)}$$

Those functions are used to compute the solution for both Model 1 and Model 2. Model 3 is obviously out-of-scope in this section since no rods are included in the DIVA+G mock-up.

4.3. *Discussion of DIVA+G results*

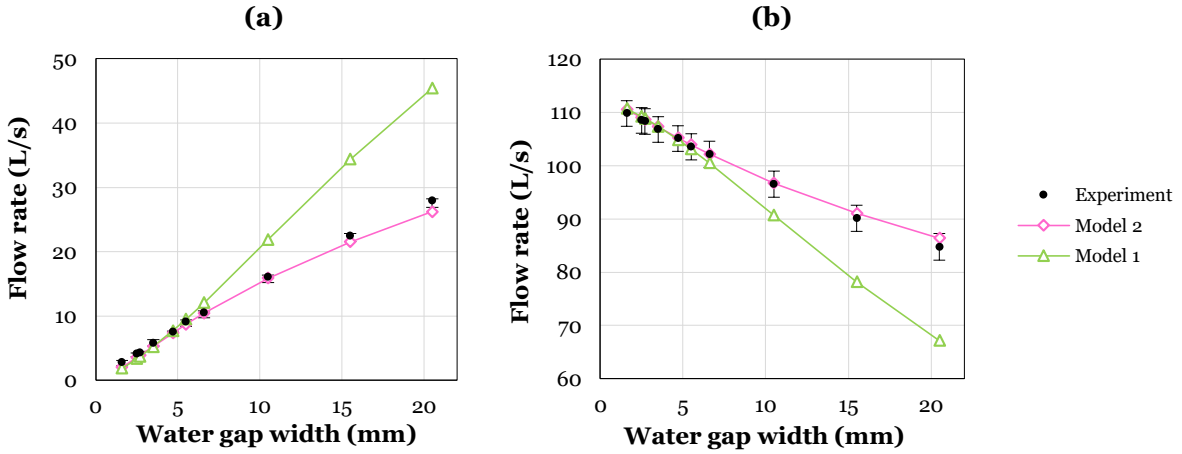

Figure 2-17 - Models vs DIVA+G: flow rates in (a) the water gap and (b) the grids (uncertainty ranges are plotted over experimental points)

Figure 2-17 represents the volumetric flow rate in the CD (a) and in the grids (b) as a function of λ. Model 2 is in very good agreement with experiments, whereas Model 1 shows significant discrepancies for larger gaps, confirming the importance of the stagnation point modeling to account for the heterogeneity of the pressure field.

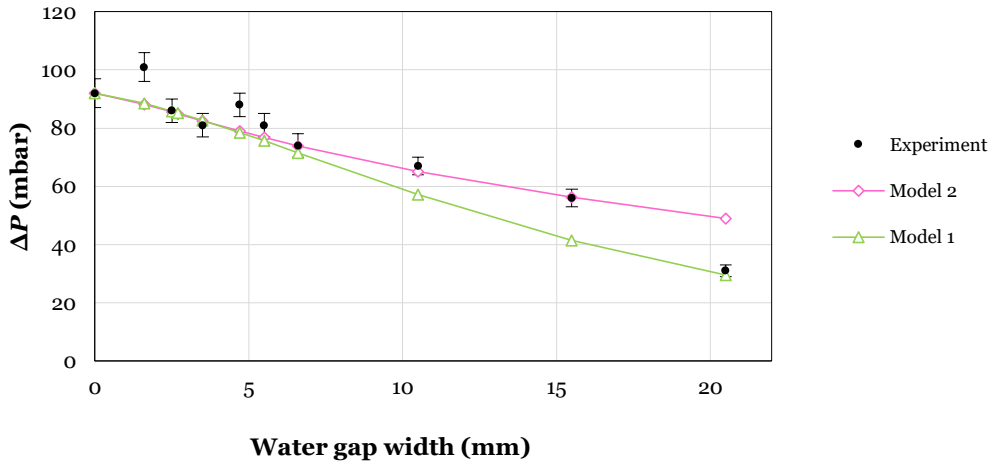

Figure 2-18 - Models vs DIVA+G: pressure drop, absolute uncertainties are indicated over measurements' points

Finally, Figure 2-18 presents the pressure drop through the grids. In DIVA+G, this value is obtained through the two pressure sensors placed on both sides of the right half-grid (see Figure 2-16). Experimental measurements are here subjected to additional uncertainties probably due to non-uniform operating conditions in the loop over the complete test sequence stretching over one week approximately (see for instance the points for values of λ of 1.6 mm, 4.5 mm and 20 mm). However, both Models 1 and 2 accurately reproduce the decrease of the pressure drop through the grid with the opening of the water gap.

As a conclusion, the very good match between Model 2 and DIVA+G experimental data

(in terms of pressure drop and flow rates) is remarkable, all the more so as this version of the semi-analytical model needs no empirical parameter at all. It shows that the physics of the redistribution upstream of the grids is correctly understood and well captured by our semi-analytical models.

5. Sensitivity analysis of the models

This last section provides some early work illustrating the potential of the proposed semi-analytical approach in terms of advanced sensitivity analysis, made possible by the balance between accuracy for the phenomena of interest and computational efficiency. Two case studies are considered: first, the sensitivity of Model 2 results to variations of its internal parameters together with some of the DIVA+G experimental inputs, and second, a deeper dive into the inner workings of the ΔP_c and ΔP_l corrective terms resulting from the stagnation point modeling, through compared sensitivity analyses of Model 2 and Model 3.

5.1. *Model 2 (applied to the DIVA+G experiment)*

In order to analyze the sensitivity of Model 2 and the experiment's parameters, 100 000 calculations were performed thanks to CEA's Uranie uncertainty platform [68] with different values of input parameters (see section 2) to estimate the Sobol Indexes [69, 70]. The sampling is operated by a Latin hypercube method [71]. The different inputs are drawn from uniform distributions whose bounds are detailed in Table 2-1. In section 4, it was explained why the grid coefficient C_g of the DIVA+G mock-up was a linear function of the water gap width λ. However, in order to make the sensitivity analysis simpler [69], we act as if these two variables were uncorrelated.

Input	Minimum	Maximum	Comments
$\boldsymbol{\lambda}$	0.1 mm	20.5 mm	
$\boldsymbol{H, h, \alpha}$	−10%	+10%	(Λ/λ) thus varies up to $\pm$20% for λ = 1 mm and $\pm$ 5% for λ = 20 mm (this ratio plays a major role on the flow redistribution, see (Eq. 2-7))
$\boldsymbol{\zeta_1}$	0.1	0.6	+20% upper margin w.r.t. the sudden contraction (ζ_1 = 0.5 when α = 90°)
$\boldsymbol{\zeta_3}$	1	1.3	ζ_1 = 1 is for a sudden expansion (α = 90°), ζ_1 = 1.15 the nominal value
$\boldsymbol{C_g}$	3.00	4.23	C_g depends on λ (see section 2)
$\boldsymbol{Q_{tot}}$	−10%	+10%	
$\boldsymbol{\rho}$	997 kg.m^{-3}	1000 kg.m^{-3}	Temperature variation between 5°C and 25°C
$\boldsymbol{\mu}$	8 × 10^{-4} Pa.s	1.5 × 10^{-4} Pa.s	Temperature variation between 5°C and 25°C
$\boldsymbol{\varepsilon}$	1 µm	100 µm	ε = 1 µm is typical steel, ε = 100 µm is an upper bound for 3D-printed PETG (ε is the wall rugosity, appearing in Haaland formula for f [56])
$\boldsymbol{S_0 = L \times W}$	−1 mm × −1 mm	+1 mm × +1mm	

Table 2-1 - Inputs for sensitivity analysis of Model 2 in the context of DIVA+G experiments

The chosen outputs of interest are the volumetric flow rate fraction going through the water gap, *i.e.* Q_{cd}/Q_{tot}, as well as the pressure drop divided by the square of total flow rate, *i.e.* $\Delta P_g/Q_{tot}^2$. Such nondimensionalization prevents any undesirable variation of Q_{cd} and Δp_g which would be imputed solely to an increase or decrease of the total flow rate Q_{tot} going into the system.

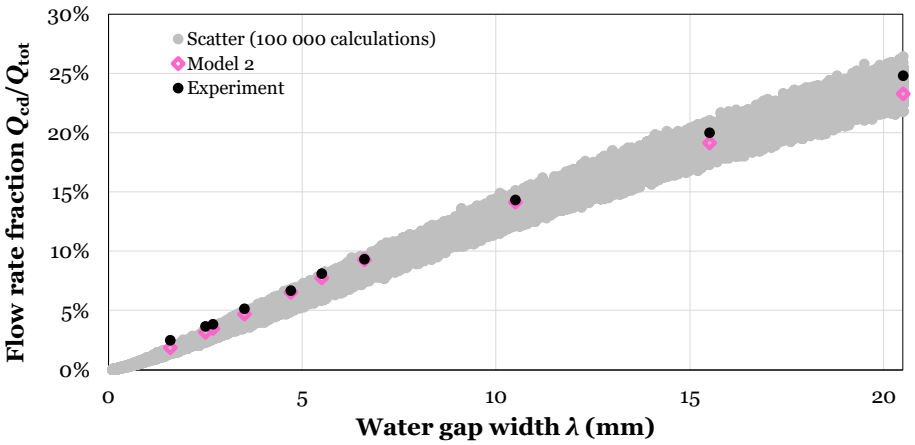

Figure 2-19 - Flow rate in the CD computed with perturbed input parameters

Figure 2-19 represents the nondimensional flow rate in the CD, for both experimental, initial Model 2 calculation (with nominal values), and the 100 000 calculations results. It highlights that whatever the draw, the maximal relative deviation towards experimentation is around 20%. Keeping in mind that every single possible input variable has been considered and that they have been drawn uniformly in the whole range of admissible values, this is a very satisfactory result. First, it shows that a rational change in the models' parameters will keep the solution (in terms of flow rate) in an acceptable range. Second, the distribution of the scattered results around the experimental values shows some robustness regarding the measurement errors. Finally, the shape of the scatter plot suggests that the flow rate is mostly a function of the thickness.

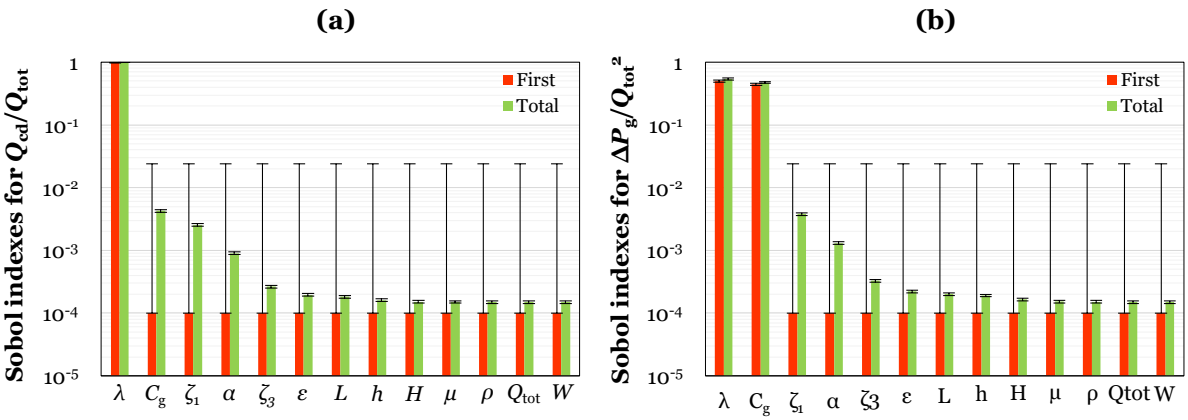

Figure 2-20 - Sobol indexes and 95% confidence intervals for Q_{cd}/Q_{tot} (a) and $\Delta P_g/Q_{tot}^2$ (b) obtained with 100 000 calculations with Model 2 in the context of DIVA+G experiments

To explicitly quantify the influence of the modelling parameters on the variation of Q_{cd}/Q_{tot}, first and total Sobol ([69] or [72] in English) are computed and displayed in Figure 2-20(a). The first index associated to the thickness λ is indeed around 1. It means as anticipated in Figure 2-19 that the output can be considered in first approximation as a function of λ only, neglecting some small interactions with other inputs. Confidence intervals of the other inputs for the first index are too large to be discussed. However, according to the total indexes (whose confidence intervals are small enough to allow interpretation), one could see that C_g, ζ_1 and α are the next three more influential inputs on the prescribed ranges, after the thickness λ. There is no way to tell if those parameters step in alone or through their interactions, but their total effect stands out from the others. More specifically, caution must be exercised with regards to C_g, as it was considered independent of λ to compute the Sobol indexes, whereas analyses from DIVA+G experimental campaign clearly concluded that these two parameters were strongly related (as such they should be considered as a same group of inputs [69]. Further correlation analyses could be performed to highlight this topic, but this goes beyond the scope of the current chapter.

Figure 2-20 (b) indicates the Sobol indexes calculated for the output $\Delta P_g/Q_{tot}^2$. The remarks pointed out above are still relevant, and the four more influential inputs are the same. The difference is that the effect of C_g is much more important in this case (see the total and first indexes) because the pressure drop is directly proportional to the loss coefficient.

5.2. *Model 3 (and comparison to the simpler Model 2)*

The common distinctive feature of Model 2 and Model 3 is held in the ΔP_c corrective term, and Model 3 then stands out from Model 2 for the additional parameters introduced by the lateral resistance K_l. It is interesting to analyze the sensitivity of $\Delta P_c = P_{cd} - P_g$ to different values of new inputs associated with K_l and to compare with Model 2's conclusions discussed above. Building on the results of Table 2-1, every parameter whose influence seemed negligible are now considered as constants. Simulations are otherwise analog to the ones performed in section 2. For Model 3, the inputs of the sensitivity analysis are listed in Table 2-2.

Input	Minimum	Maximum	Comments
$\boldsymbol{\lambda}^{(*)}$	1 mm	20 mm	
$\mathbf{C_g}^{(*)}$	0.9	1.3	
$\boldsymbol{\mu}$	10^{-5} Pa.s	10^{-4} Pa.s	Used to calculate the local Reynolds number in $K_\perp$ (Eq. 2-22)
N	1	3	See Figure 2-11
$\mathbf{h_l}$	1 mm	100 mm	Linear probability density function (instead of uniform) in order to promote low values of h_l (see Figure 2-11)

Table 2-2 - Inputs for sensitivity analysis of Model 2 ($*$ only) and 3 in the context of real PWR fuel assemblies

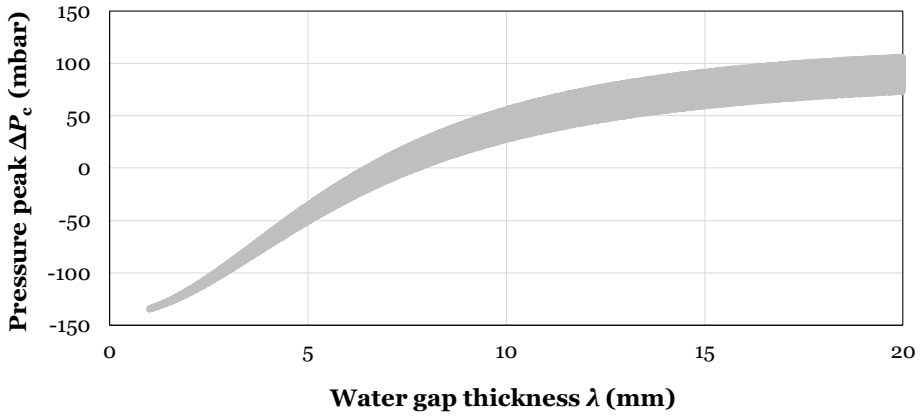

Figure 2-21 - Pressure peak term ΔP_c obtained by Model 2 when varying λ and C_g only

Figure 2-21 depicts the variance of ΔP_c obtained with Model 2 when varying λ and C_g only. One can notice that ΔP_c is either positive of negative according to the flow rate value in each branch. Thus, zero values obtained for λ around 7 mm correspond to equal velocities through the grid and the water gap (as shown by (Eq. 2-13)), which means a uniform flow. The dispersion induced by C_g clearly increases as the thickness λ grows larger. The Sobol indexes associated to this sensitivity analysis are given in Figure 2-22.

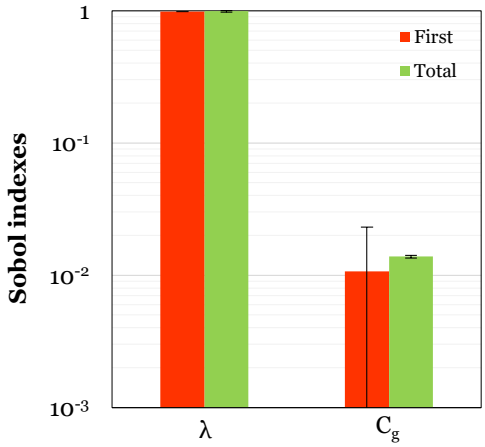

Figure 2-22 - Sobol indexes and 95% confidence intervals for ΔP_c obtained with 100 000 calculations with Model 2 in the context of real PWR fuel assemblies

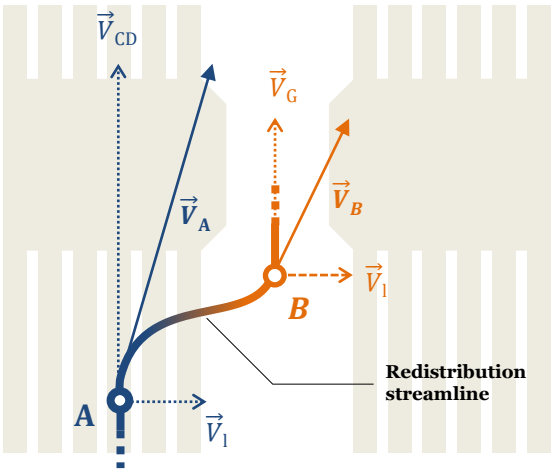

Figure 2-23 - Streamline upstream from the CD with fuel rods

In the case of Model 3, the quantity of interest is $\Delta P_{\mathrm{tot}} = \Delta P_{\mathrm{c}} + \Delta P_{\mathrm{l}}$. Indeed, two effects are now are involved in the upstream pressure drop. This can be shown by applying the generalized Bernoulli principle on a streamline following the flow redistribution (Figure 2-23) for instance from the grid (point A, velocity $\vec{V}_A = \vec{V}_{\mathrm{g}} + \vec{V}_{\mathrm{l}}$ and pressure $P_{\mathrm{A}} = P_{\mathrm{g}}$) to the water gap (point B, velocity $\vec{V}_B = \vec{V}_{\mathrm{cd}} + \vec{V}_{\mathrm{l}}$ and pressure $P_{\mathrm{B}} = P_{\mathrm{cd}}$). The sign convention for ΔP_{l} comes from (Eq. 2-24):

$$P_{\mathrm{A}} + \frac{1}{2}\rho V_{\mathrm{A}}^2 = P_{\mathrm{B}} + \frac{1}{2}\rho V_{\mathrm{B}}^2 - \Delta P_{\mathrm{l}} \qquad \text{(Eq. 2-28)}$$

which leads to the following formula for the total pressure drop:

$$\Delta P_{\mathrm{AB}} = P_{\mathrm{cd}} - P_{\mathrm{g}} = \frac{1}{2}\rho\left(V_{\mathrm{g}}^2 - V_{\mathrm{cd}}^2\right) + \Delta P_{\mathrm{l}} = \Delta P_{\mathrm{tot}} \qquad \text{(Eq. 2-29)}$$

(to be compared to (Eq. 2-13) which gives $P_{\mathrm{cd}} - P_{\mathrm{g}} = \Delta P_{\mathrm{c}}$ in the case of Model 2).

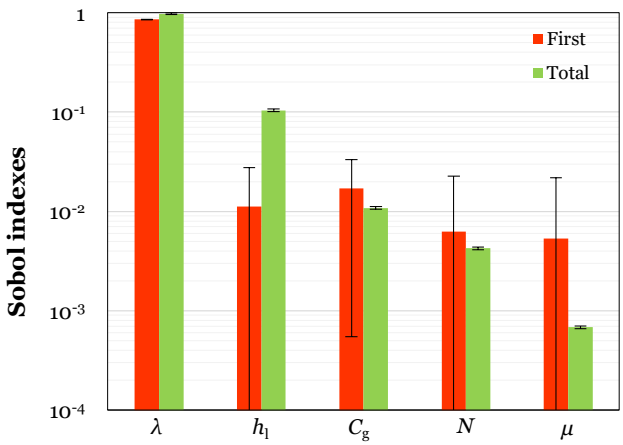

Figure 2-24 - Sobol indexes and 95% confidence intervals for ΔP_{tot} obtained with 100 000 calculations with Model 3 in the context of real PWR fuel assemblies

Figure 2-24 highlights Sobol indexes obtained for ΔP_{tot}. Once again, λ has by far the highest effect among all inputs. But in this new situation, the sum of all first indexes is not equal to 1, meaning that correlations exist between inputs. From h_l indexes, it can be inferred that this input is unimportant alone but has a significant impact through interactions, most probably with λ.

In order to grasp a better understanding of the roles of λ and h_l, the same calculations have been performed considering all the other inputs as constants with nominal values. Quantities of interest such as ΔP_c and ΔP_{tot} can therefore be visualized with smooth curves (instead of fuzzy scatter plots like in Figure 2-21 for instance). Figure 2-25 shows the evolution of Model 3 outputs along with h_l (for different values of λ) whereas Figure 2-26 and Figure 2-27 show their evolution along with λ (for different values of h_l).

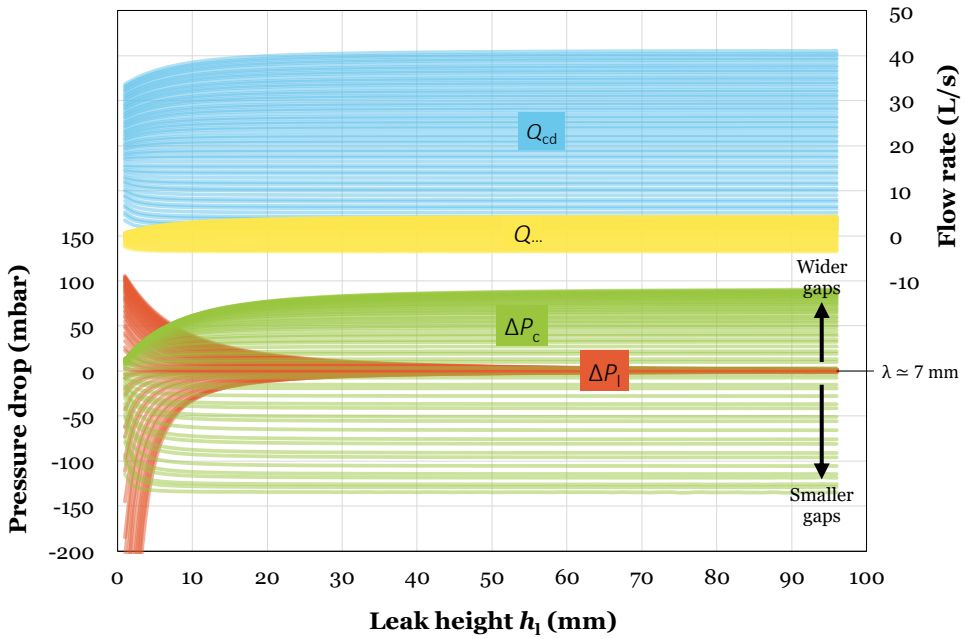

Figure 2-25 - Evolution of the flow rates and pressure drops along with h_l for different values of λ

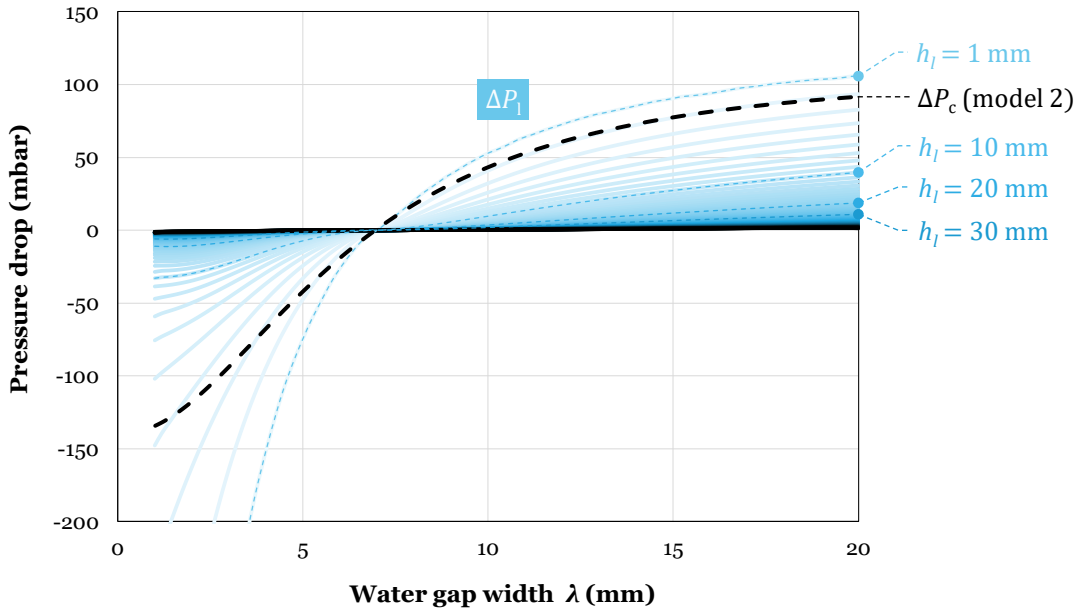

Figure 2-26 - Evolution of the lateral pressure drop along with λ for different values of h

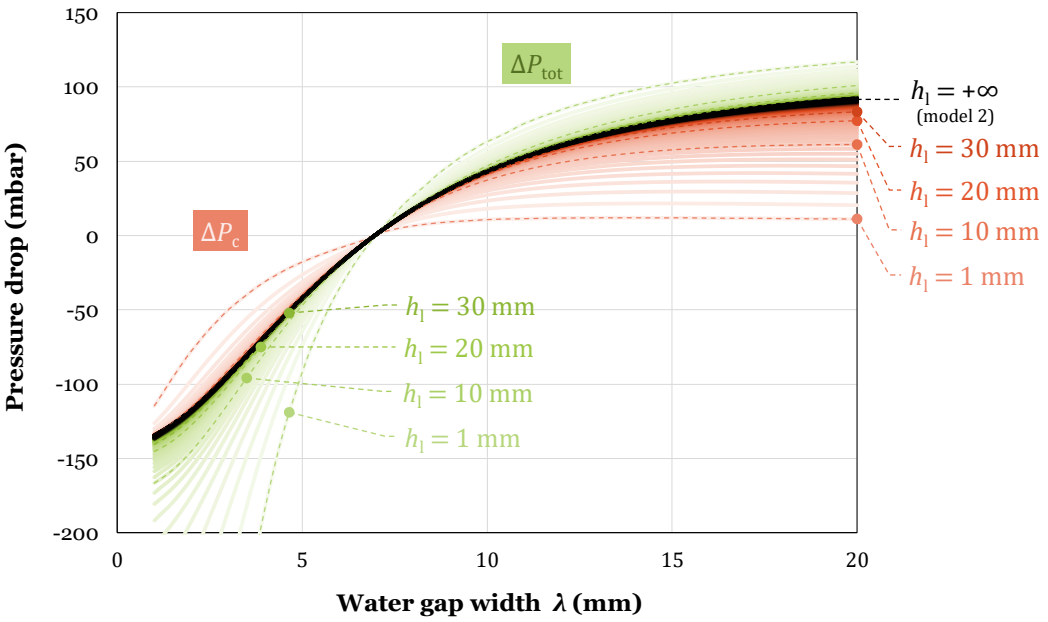

Figure 2-27 - Evolution of the upstream pressure drop along with λ for different values of h

One first observation is the presence of a singular point as both λ and h_l approch zero, for which the upstream pressure drop ΔP_{tot} associated to the redistribution becomes potentially infinite. Actually, the singular term is rather ΔP_l. It makes sense because that singular point corresponds to a situation where almost all the incoming flow would be forced towards the grids ($\lambda \simeq 0$) by going through an extremely thin horizontal slit ($h_l \simeq 0$). Hence, care must be taken so as not to choose too small a value for the h_l parameter. We suggest to keep h_l above 5 mm at the very least.

On the opposite, when h_l grows larger, Figure 2-25 and Figure 2-26 show that ΔP_l approach zero whatever the value of λ. In other words, Model 3 asymptotically tends towards Model 2 when h_l becomes infinite. Actually, it is possible to observe on Figure 2-25 that the

evolutions of flow rates and pressure drops become somewhat unaffected by increasing h_l beyond 3 cm.

The *loci* where pressure drop curves of Figure 2-26 and Figure 2-27 cross the horizontal axis is almost a single point near $\lambda \simeq 7$ mm. When the water gap has this width, the axial flow profile is flat ($V_{cd} = V_g$, with no cross-flow). Since it hardly depends on h_l at all, even Model 2 or a poorly calibrated Model 3 would be able to predict this equilibrium value accurately.

For intermediate values of h_l (in the "reasonable range" between 5 mm and 5 cm), one can wonder how the redistribution term of Model 2, namely ΔP_c, blends in the one of Model 3, namely $\Delta P_{tot} = \Delta P_c + \Delta P_l$. When h_l is between 5 and 50 mm, Figure 2-26 shows that the additional term ΔP_l increases (in absolute value) when h_l gets smaller, staying below the asymptotic value of ΔP_c curve for Model 2 even so. Conversely, Figure 2-27 shows that ΔP_c decreases (in absolute value) along with h_l, but not enough to compensate for the additional upstream pressure drop brought by ΔP_l. Everything boils down in the end to the total pressure drop ΔP_{tot} being slighted increased (in absolute value) when the length h_l becomes smaller. One worthy observation is that the flow rate Q_{cd} in the water gap shows little dependence on h_l. These results are the very purpose of Model 3 enhancements versus Model 2, aimed at tweaking the pressure axial profile without jeopardizing the good prediction of the flow rate redistribution, which was already validated for Model 2 by comparison to DIVA+G experimental data.

6. Partial conclusion

In this chapter, a series of different 1D hydraulic models of growing complexity were introduced to reproduce the flow redistribution upstream from the grids for two fuel assemblies separated by a water gap. All models are based on hydraulic networks, starting from the simple association of two pathways: one for the bypass, and one for the grids. The first model does not take into account the pressure peak which appears when the bypass is being closed, yielding a second model containing a modified energy equation to consider the effects of the identified stagnation point. Finally, a third model adds the lateral hydraulic resistance of the fuel rods, to further increase the accuracy of the network for small water gaps.

Although Model 1 turns out to be far too simplistic, both Model 2 and Model 3 are well-suited for reproducing the CFD results obtained with TrioCFD and Code_Saturne, with excellent agreement achieved by Model 3 even in the case of very narrow bypasses. Models 1 and 2 were also compared to a dedicated experiment called DIVA+G consisting in two 3D-printed porous grids facing each other, between which is located a bypass of varying thickness. Model 3 was not relevant in this case as there is no rod bundle in the mock-up. Model 2 accurately predicted flow rates and pressure losses measured in DIVA+G, validating the global strategy proposed to account for the flow redistribution upstream from the grids. As regards the improvements brought in Model 3 to account for the lateral obstruction due to the fuel rods, sensitivity analyses suggest that a particular attention should be paid to the choice of the h_l parameter, due to its significant influence on the pressure drop.

The next step of this work consists in building a model for the lateral forces acting on the fuel assembly, based on the computed flow rates and pressures.

Chapter 3: Construction of a fluid-structure model for a whole fuel assembly

Highlights of the chapter

- We compute the hydraulic forces F_V from the redistribution model of chapter 2.
- Their contribution at local scales are assessed by comparison with simulations and experiment.
- A hydraulic model of the FA is set up through a reunion with both bypasses and inner-FA redistributions and validated hydraulically by comparison with a CEA experimental mock-up.
- The coupling with an in-house mechanical code (using also forces described in chapter 1) produces an equilibrium state, validated by comparison with experiments.
- The lateral force F_V on the grid induced by redistribution has an important role on the final shape of the assembly.

1. Force model related to the pressure difference in surrounding water gaps

1.1. *Axial pressure profile in the water gap*

In the previous chapter, a model has been designed to depict fluid redistributions upstream from the spacer grids. As we said in the introduction, it is necessary to assess fluid forces onto the FA structure. Now, we will see how to take advantage of the network results (i.e. the flow rate Q in the CD) to run pressure forces calculations.

In what follows, we still consider the Bernoulli's principle in the CD (Eq. 2-1). The pressure evolution relies on geometrical effects (acceleration/deceleration of the fluid), and also on irreversible pressure losses (Eq. 2-7).The axial profile of pressure in the water gap, in the convergent (C_1), is modelled through the following equation (Eq. 3-1) ($z_1 \in [0, h]$):

$$p_{C_1}(z_1) = p_0 + \frac{1}{2}\rho\frac{Q^2}{S_{dyn}(0)^2}\left(1 - \frac{S_{dyn}(0)^2}{S_{dyn}(z_1)^2}\right) - \frac{1}{2}\rho\frac{1}{2L^2\cos(\alpha)}\int_0^{z_1}\frac{f(\ell_1, Q)}{\ell_1(z)^3}\,dz - \frac{1}{2}\rho\,\zeta_1\left(1 - \frac{\ell_1}{\Lambda}\right)\frac{Q^2}{(L\ell_1)^2} \quad \text{(Eq. 3-1)}$$

In the planar channel C_2, ($z_2 \in [0, H]$):

$$p_2(z_2) = p_{C_2}(0) - \frac{\rho f z_2}{4\lambda}\left(\frac{Q}{L\lambda}\right)^2 \quad \text{(Eq. 3-2)}$$

In the diffuser C_3, ($z_2 \in [0, h]$):

$$p_{C_3}(z_3) = p_{z_3}(0) + \frac{1}{2}\rho\frac{Q^2}{S_{dyn}(0)^2}\left(1 - \frac{S_{dyn}(0)^2}{S_{dyn}(z_3)^2}\right) - \frac{1}{2}\rho\frac{1}{2L^2\cos(\alpha)}\int_0^{z_3}\frac{f(\ell_3, Q)}{\ell_3(z)^3}\,dz - \frac{1}{2}\rho\,\zeta_3\left(1 - \frac{\lambda}{\Lambda}\right)\left(1 - \frac{\lambda}{\ell_3}\right)\frac{Q^2}{(L\lambda)^2} \quad \text{(Eq. 3-3)}$$

S_{dyn} is the real cross section of the fluid (keeping the fuel rods), at height z. We can analyze the difference between S_{dyn} and S_{cd}, which has been widely used before. Hydraulic resistances computed in the previous chapter are essentially based on idealized geometries. In that case, fuel rods were not considered in the cross sections used for the network calculation: the inter-grid area was thus a convergent-diffuser without any rods, it is S_{cd}. However, to better depict fuel assembly bow, the lateral forces acting on the spacer grids must be as reliable as possible. To do so, the pressure profiles must be representative. The dynamic pressure variation, which plays a role in the profile, is to be as close as possible to a real core context. S_{dyn}, introduced in this part, is thus a real cross section in that it equals S_{cd} at height z, but diminished by the appropriate portion of fuel rods. Figure 3-1 depicts the difference between both cross sections.

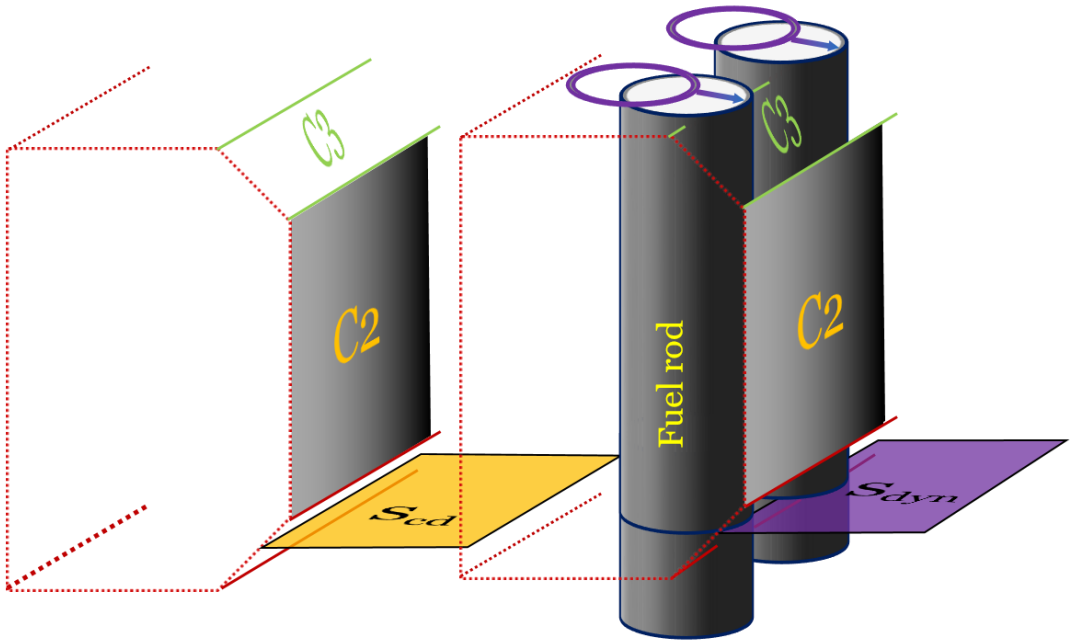

Figure 3-1 - Sketch of the difference between S_{cd} (left), and S_{dyn} (right) in the convergent C1

We can make another remark. The local pressure loss terms (last terms of (Eq. 3-1) and (Eq. 3-3)), are, as their names imply, local. The point here is to distribute them on a distance h.

Regarding the convergent, at a given height z, the local loss induced is chosen as equal to the one induced by a convergent of height z, with ζ_1 constant (see Figure 3-2).

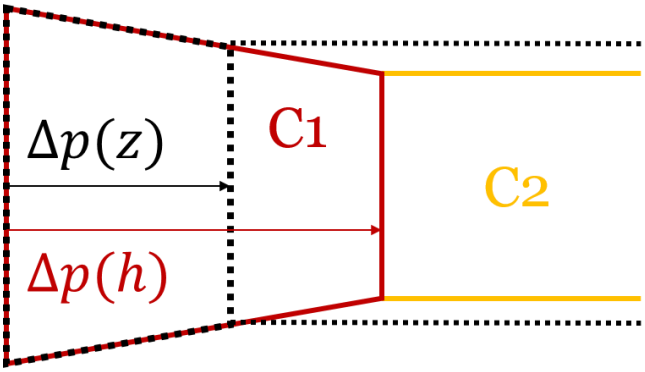

Figure 3-2 - Distribution of local loss in the convergent

This hypothesis expresses:

$$P_{C_1}^{local} = \frac{1}{2}\rho\zeta_1\left(1 - \frac{\ell_1(z_1)}{\Lambda}\right)\frac{Q^2}{\left(L\ell_1(z_1)\right)^2} \qquad \text{(Eq. 3-4)}$$

Incidentally, one can notice that when $z_1 = h$, we find back as in (Eq. 2-4):

$$P_{C_1}^{local}(z = h) = \frac{1}{2}\rho\zeta_1\left(1 - \frac{\lambda}{\Lambda}\right)\frac{Q^2}{(L\lambda)^2} \qquad \text{(Eq. 3-5)}$$

Which is the expression of the local loss used in the hydraulic resistance, for the whole height of C_1. For part C_3, regarding the strong detachments in the diffusers entrance (see section 5 of [55]), it is hard saying that the expression of the local loss at height z is the same as the one obtained with a diffuser of height z, because it would yield in a quadratic evolution of the loss coefficient. This is the reason why we will assume that its evolution is an analog of C_1's:

$$P_{C_3}^{local} = \frac{1}{2}\rho\zeta_3\left(1 - \frac{\lambda}{\Lambda}\right)\left(1 - \frac{\lambda}{\ell_3(z_3)}\right)\frac{Q^2}{(L\lambda)^2} \qquad \text{(Eq. 3-6)}$$

In that, if $z_3 = h$:

$$P_{C_3}^{local}(z = h) = \frac{1}{2}\rho\zeta_3\left(1 - \frac{\lambda}{\Lambda}\right)^2\frac{Q^2}{(L\lambda)^2} \qquad \text{(Eq. 3-7)}$$

Which is also the local loss used in the hydraulic resistance.

We can illustrate those dimensionless distributions of loss by plotting in Figure 3-3 the local pressure losses in C_1 and C_3 divided respectively by $L^2\lambda^2/2\rho\zeta_1 Q^2$ and $L^2\lambda^2/2\rho\zeta_3\left(1 - \frac{\lambda}{\Lambda}\right)Q^2$.

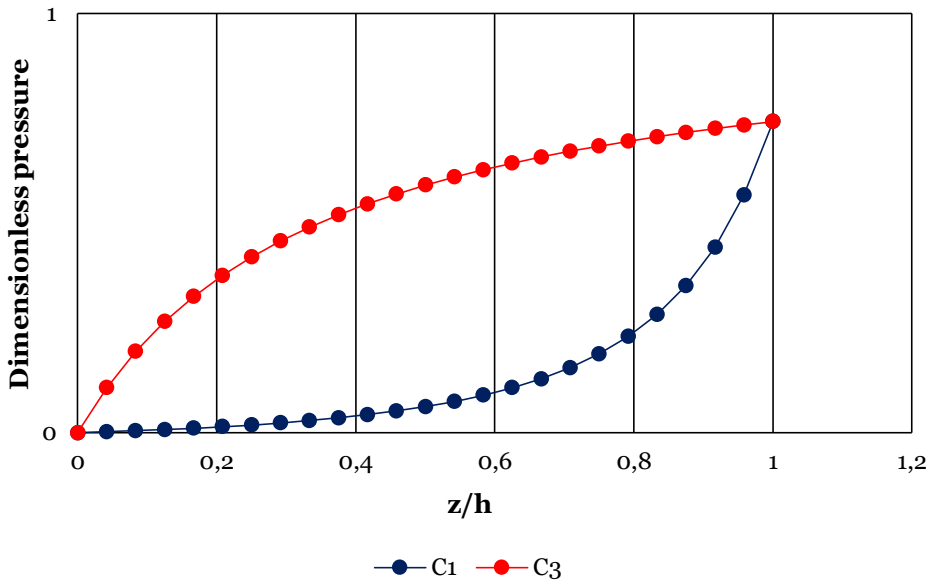

Figure 3-3 - Distribution of local pressure losses

The global static pressure in the CD thus writes:

$$p\colon z \to \begin{cases} p_{C_1}(z)\,, & \forall z \in [0,h] \\ p_{C_2}(z-h)\,, & \forall z \in [h,h+H] \\ p_{C_3}(z-h-H)\,, & \forall z \in [h+H,2h+H] \end{cases} \qquad \text{(Eq. 3-8)}$$

1.2. *Comparison of the pressure profiles with CFD simulations*

Our profiles, in C_1, C_2 and C_3 are compared with the same CFD simulations as presented in the previous chapter. We chose the 1, 5 and 20 mm cases, illustrating a wide range of water gaps widths. We inform the reader that the 'bevel' and 'middle' profiles were practically overlaid. The depth effect is thus almost nonexistent. For this reason, we only plotted the 'bevel' profiles in Figure 3-4. Model 3 is used with the parameters ($h_l = 5.10^{-3}$, $N = 1$).

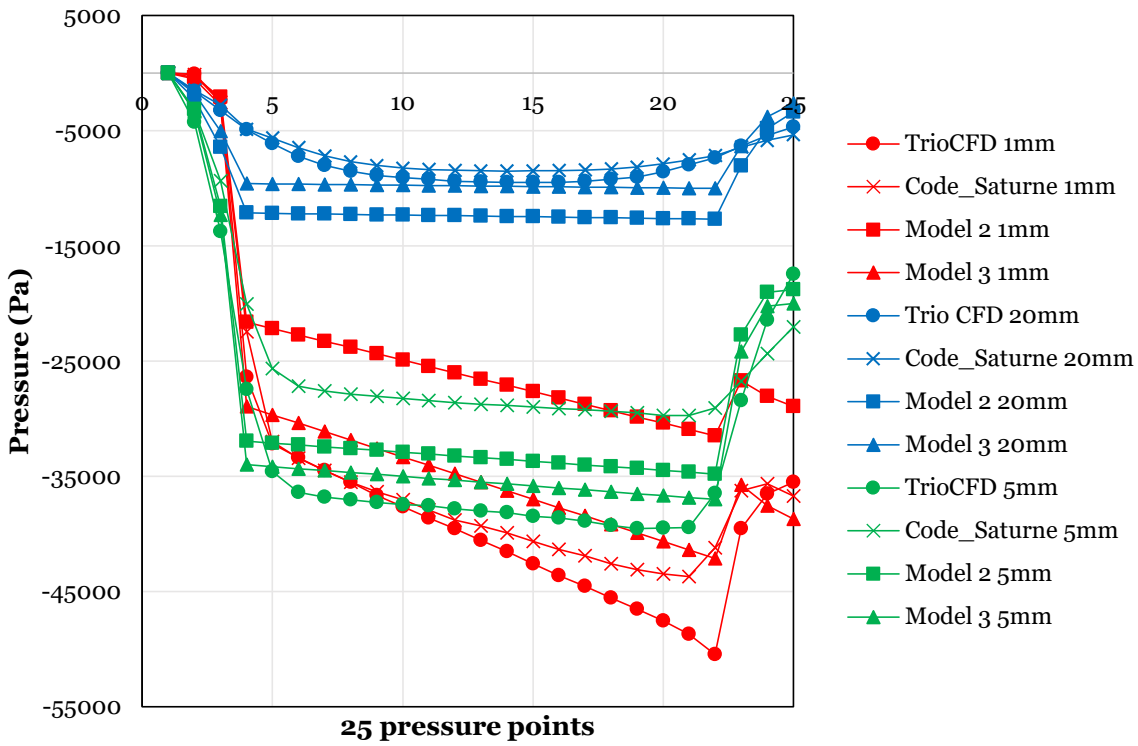

Figure 3-4 - Pressure profiles (Pa) drawn from CFD simulations and models, 25 pressure probes are used along the CD

We express the following remarks:

- For the 20 mm case, both models are close to the CFD simulations results, even though Model 2 slightly overestimates the pressure decrease by 16% when not corrected at all.
- For the 5 mm case, CFD simulations with TrioCFD and Code_Saturne give profiles with a deviation reaching 30% from each other. Yet, such a difference was already observed for bulk velocities between both two codes at 5 mm, which is the width for which they differ the most. Our two models are located between CFD results.
- For the 1 mm case, Model 2 underestimates importantly (by 40%) the pressure decrease. This is not surprising: we remind that Model 2 was superseded by Model 3 precisely for the thinnest gaps.

Generally, Model 3 gives a very good approximation of the pressure evolution in the convergent-diffuser. A compromise must be done before each calculation. Indeed, for larger gaps, Model 2 gives excellent results in terms of hydraulic redistribution (see DIVA+G for instance), but the calculation must be corrected all the same by Model 3 for improving the pressure profile.

1.3. *Lateral force on the grid due to pressure differences*

From pressure profiles, the lateral force due to redistribution exerting on the grid is the following:

$$\overrightarrow{F_V} = L\left(\int_0^{L_t}(p-\tilde{p})dz\right)\overrightarrow{e_x} \quad \text{(Eq. 3-9)}$$

Where $L_t = 2h + H$, p and $\tilde{p}$ being the static pressures at respectively the left and right hand side of the spacer grid. The integral in (Eq. 3-9), is not directly known. We rather have at our disposal the static pressure deviation between the two CD entrances (see Δp_{tot} in (Eq. 2-29)). We can observe that both profile can be written as follows (Eq. 3-10):

$$p(z) = p_0 + p_1(z), \;\; \tilde{p}(z) = \widetilde{p_0} + \widetilde{p_1}(z) \quad \text{(Eq. 3-10)}$$

Where p_0 and $\widetilde{p_0}$, correspond with the static pressure 'offsets'. p_1 and $\widetilde{p_1}$ contain dynamic pressure variations, frictions, and distributed local losses. (Eq. 3-9) can thus be rewritten:

$$F_V = L\left(\int_0^{L_t}(p_0-\widetilde{p_0})dz + \int_0^{L_t}(p_1-\widetilde{p_1})dz\right) \quad \text{(Eq. 3-11)}$$

In other words:

$$F_V = LL_t\Delta p_u + L\int_0^{L_t}(p_1-\widetilde{p_1})dz \quad \text{(Eq. 3-12)}$$

Where Δp_u is the total, upstream, static pressure deviation between both two convergent-diffusers surrounding one spacer grid.

We can make two comments:

- $LL_t\Delta p_u$ stands for the force component coming from the lateral static pressure deviation upstream from the grid, this term is related to lateral flows.
- $L\int_0^{L_t}(p_1-\widetilde{p_1})dz$ stands for the force component coming from the CD geometry. It will be particularly dependent on the cross section variation and thus the width λ.

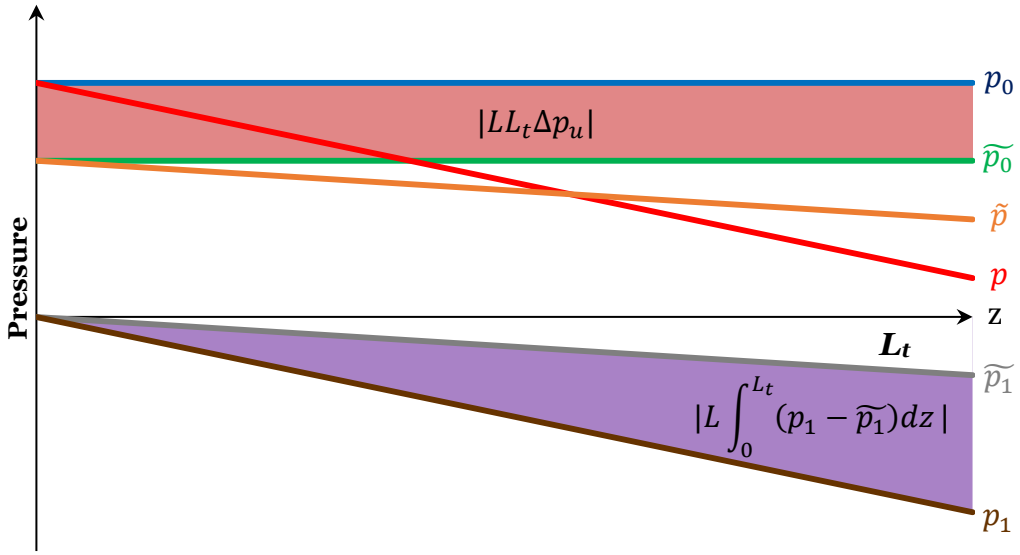

Figure 3-5 - Illustration of the $\overrightarrow{F_V}$ components

Figure 3-5 shows those notions, with simplified profiles. In this example, $LL_t\Delta p_u$ is positive, while $L\int_0^{L_t}(p_1-\widetilde{p_1})dz$ is negative.

1.4. Validation of F_V with CFD

The case of study is 3 fuel assemblies in a row over one span between successive grids. Ulrich Bieder in [49, 73] realized such CFD calculations. The gaps widths were changed in order to study the fluid behavior in the grids vicinity (respectively named A, B and C). We can observe this setup in Figure 3-6 and Figure 3-7, where there is a 2mm gap between A and B, and a 5mm gap between B and C. Symmetric boundary conditions impose a 2 mm gap at the left A and at the right of C.

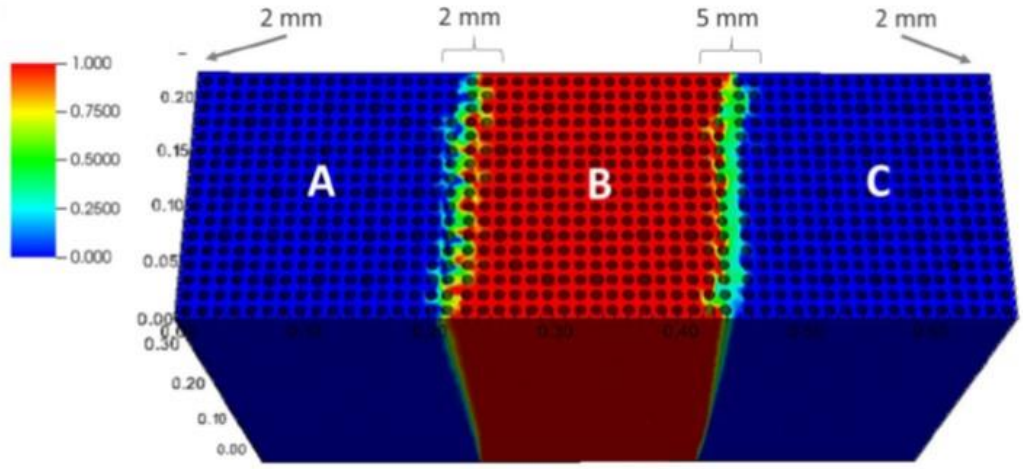

Figure 3-6 - CFD simulation with 3 FAs [49]
Central assembly marked by a red scalar

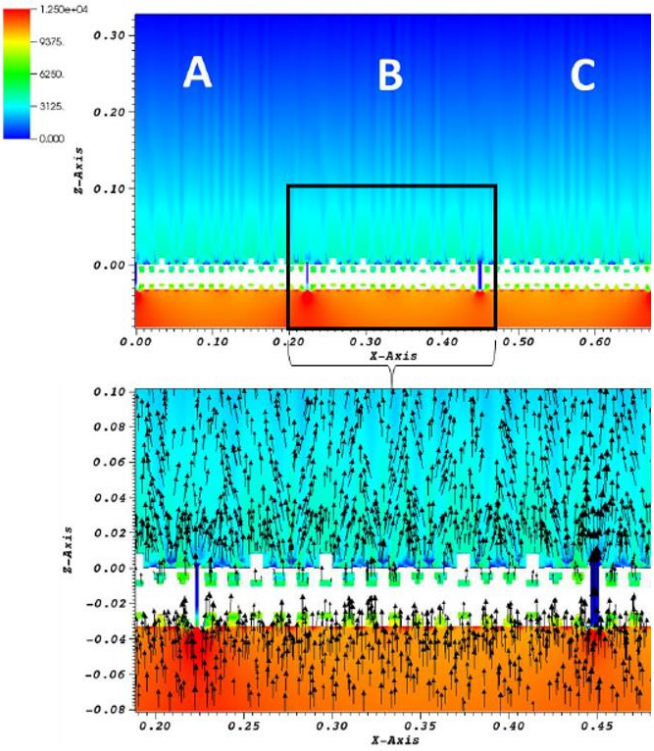

Figure 3-7 – Pressure (Pa) in the gaps [49]

Setup	*Gap A/B (mm)*	*Gap B/C (mm)*
Nominal	2	2
1	2	5
2	3	7

Table 3-1 - CFD setups

Table 3-1 sums up the different cases studied by Bieder.

From now on in the thesis, every network calculation is realized with Phorcys, a platform aiming at solving network-based formulations written in python. A detailed description of the code is available in Appendix F.

We can make the following remarks:

- The grid design as modelled by U. Bieder and C. Genrault comprises 'holes' across the outer straps (invisible on the figures). The latter, numbered 17 on every outer strap, aim at reducing pressure deviations on both sides of the grid. This geometry thus produces lower lateral forces compared to our semi-analytical 1D models, in which 'intra-grid' redistributions are not modelled.
- U. Bieder uses a periodic box at the geometry inlet to obtain an established profile [49]. In our case, we will choose an homogenous profile of velocity at the inlet with a whole axial span.
- In our network code Phorcys, the geometry could not be exactly the same as Bieder's, because the lateral symmetry boundary conditions applied in the CFD simulations are not reproducible. Instead, our three 2D FAs are bordered by two

nominal bypasses (whose $\lambda = 2mm$).

- ❖ As there is a difference of 10^3 to 10^4 between the viscous and pressure forces, only the pressure forces are presented, the viscous ones are openly negligible.

The network set up is shown in Figure 3-8, in which we can see a flow rates map. Each FA is composed of two axial branches (in orange), and surrounded by a bypass (in blue). Every axial elements are bound together at one at the outlet, which stands for a free outlet (same pressure). Also, between two axial elements lies an intra-assembly element whose height is $H_b \sim 0.5m$ (based on the Eole correlation as explained above). Between each bypass and axial elements are found Model 3's lateral elements also Eole-based (see the previous chapter). The latter are characterized by $N = 1$ and $h_l = 2.10^{-2}m$ being constant for every calculation set up, which seems to be a consistent compromise between having h_l low for the smallest λ, and $h_l \sim 3.10^{-2}m$ where the redistribution network studied in the previous chapter appeared to reach its asymptotic behavior for pressure and velocity (Model 2).

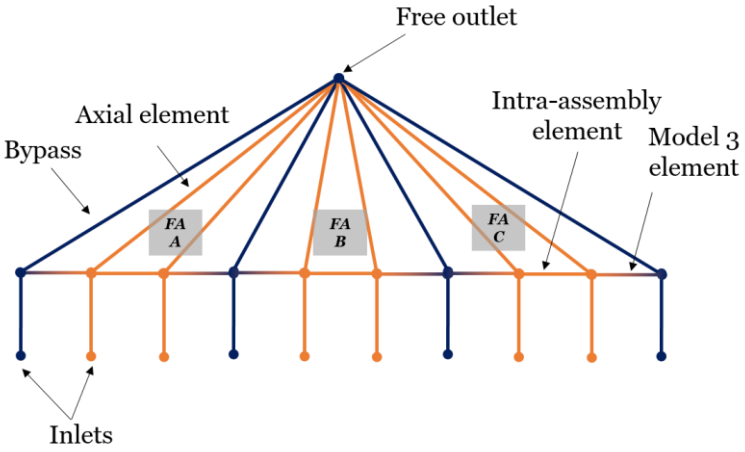

Figure 3-8 - Network set up for Bieder's calculations

1.5. *Results*

In Figure 2-9, we find the comparisons for lateral forces exerting on grids A, B and C.

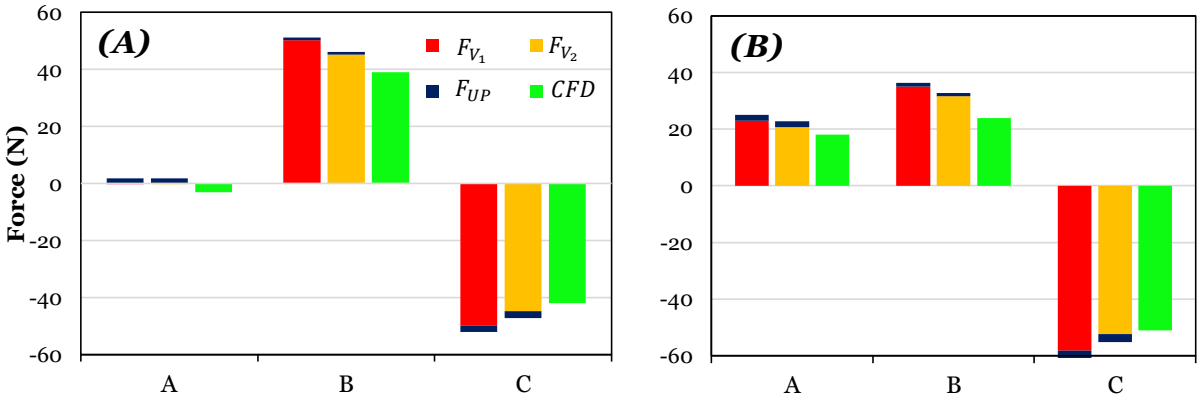

Figure 3-9 - Results of simulations with setups 1 (A) and 2 (B)

F_{V_1} is the force given by (Eq. 3-9). F_{V_2} is the same force as F_{V_1}, but diminished by the ratio of the grid lateral cross section without the holes, to the lateral cross section including the holes (it equals ~ 0.9). As said previously, the holes head toward decreasing the force equalizing the pressure on both sides of the grid. However, the 'intra-grid' redistribution is not taken into account in the models. The point is thus to figure out how close we can get to fine calculations (CFD) fiddling with the lateral cross section correction. This is a first step to a more global redistribution model of the grid, including intra-grid flows. F_{UP} stands for the upright position force presented in the hydraulic introduction (chapter 1) and used by some authors. In our model, it is estimated through lateral velocities in the intra-assembly lateral elements, axial velocities in the axial elements, and the grid cross section (Appendix F).

Regarding the first setup, the forces behavior is well depicted. Initial total forces (*i.e.* $F_{V_1} + F_{UP}$), have a consistent order of magnitude compared to Bieder's calculations (25% deviations), and are obviously overestimated as heralded above. Modified total forces (*i.e.* $F_{V_2} + F_{UP}$) are closer to the CFD results and thus lead to a better precision. In both cases, the force direction is correct for grids B and C (respectively positive and negative), but incorrect for grid A. Yet, the latter is insignificant; in fact it is lower than a residual force (a few Newtons) existing on an isolated grid in nominal conditions [49]. Consequently, discussing its direction makes no sense here.

Regarding setup 2, the same remarks can be made. Directions as well as orders of magnitude are respected. The change in water gaps width is thus well depicted by our model, and the results are very good for both values of 2/5 and 3/7 mm. Globally, in these configurations, F_{UP} seems to stay in the background compared to F_V. Apart from grid A in setup 1 where the whole effort is carried by F_{UP}, the latter equals 10% of the total force at the most.

Ulrich Bieder also plotted the lateral force with respect to a gap widening, benefiting from the symmetry conditions all around its geometry [73]. More specifically, regarding the two gaps surrounding the grid, one is locked with a nominal value of 2mm, while the other is equal to λ. The water gap widening is thus defined as $\Delta\lambda(mm) = \lambda - 2$. In concrete terms, to obtain $\Delta\lambda = 5\,mm$, the author considered the force exerting on grid C in setup 2 (bounded to 7 and 2 mm gaps). Computation times of our 1D models are very short, in other words it is easy to compute as many simulations as the amount of different $\Delta\lambda$. Thus, A/B has been fixed at nominal conditions (2 mm), whereas B/C was successively increased by a value $\Delta\lambda$. The comparison of the force behavior due to an enlargement of the right gap is shown in Figure 3-10.

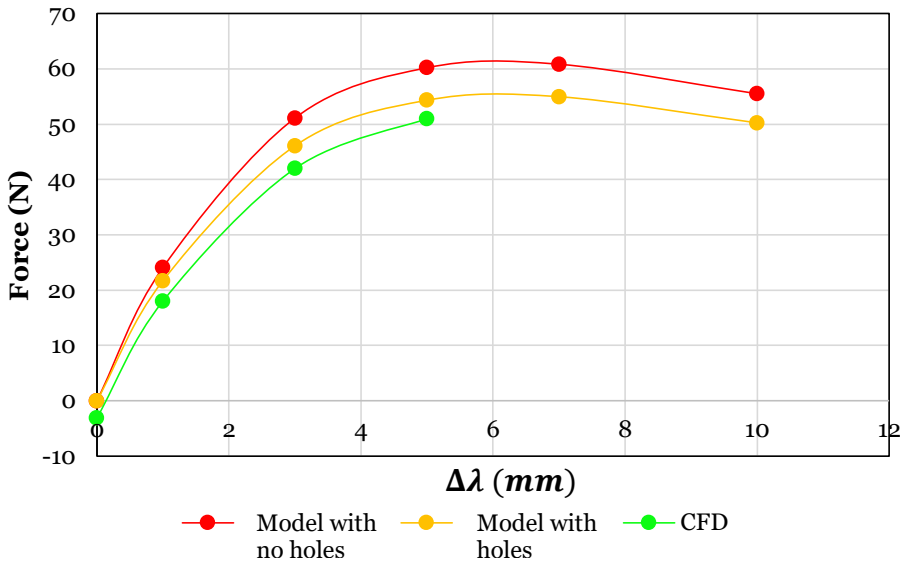

Figure 3-10 - Lateral force on a grid with respect to Δλ

At this time, we do not have access to $\Delta\lambda$ higher than 5 mm for CFD calculations, however one can notice that the three curves are very similar below. Our values are once again overestimated for the same reasons as above: lack of holes in the outer straps, and lack of residual effort when $\Delta\lambda = 0\ mm$, because of the mixing vanes.

Next, in Figure 3-11, we break down F_{V_1} which seems to be the main part of the total lateral force compared to F_{UP} The system is the same as the one studied above. The component $LL_t\Delta p_u$ expands continuously which is coherent with the fact that the wider the right gap is, the more important the flow is redistributed. On the other hand, the term related to the profiles $L\int_0^{L_t}(p_1 - \widetilde{p_1})dz$ is not that trivial. It is added to $LL_t\Delta p_u$ when $\Delta\lambda < 5\ mm$, and allays the total force when $\Delta\lambda > 5\ mm$. Thus, this term is the source of the bell behavior observed for F_{V_1}. Consequently, if ones does not take $L\int_0^{L_t}(p_1 - \widetilde{p_1})dz$ into account (which is not the case in the literature), it would lead in either underestimating F_{V_1} for the lowest variations of λ, or overestimating F_V for the highest variations of λ.

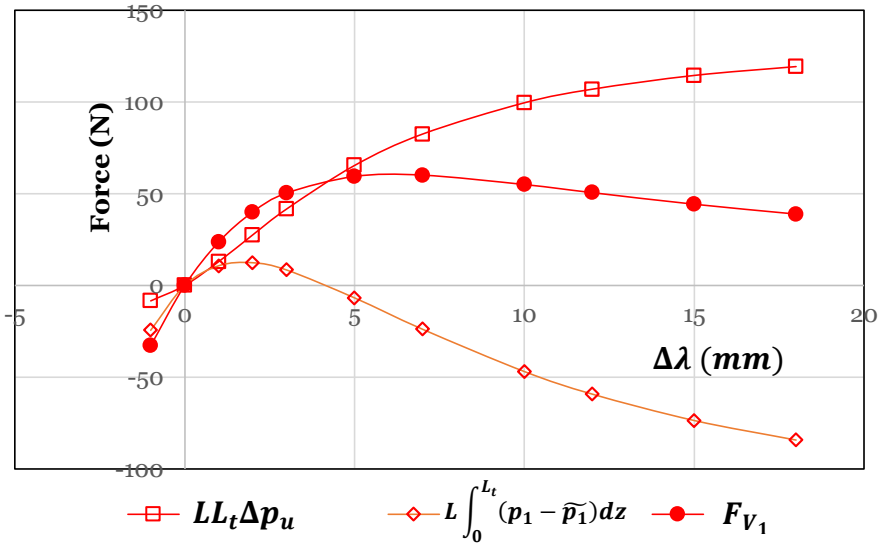

Figure 3-11 - F_{V_1} components (U. Bieder's case of study)

Another test, more realistic, can be simulated to deepen the behavior of the last few terms. It is about considering the same case (3x1 FAs), but this time, the central assembly is shifted between its two surrounding FAs. The structure displacement is thus limited to the two nominal values, *i.e.* -2/+2 mm. The results are given in Figure 3-12. In this case, the main part of the force is carried by the integral component. The strong fluid acceleration at low λ (the ratio Λ/λ is high) enhances indeed the CD profiles contribution – we remind that the ratio Λ/λ is the main factor influencing the pressure profiles -. Note that the order of magnitude of F_V is always around 10 to 100N. Also, as soon as $|\Delta x| = 1.9\ mm$, the Reynolds number within the C_2 channel section becomes lower than 5000: we can wonder about the consistency of the correlations (Haaland, convergent, diffuser) used for turbulent flows (we generally admit as valid our correlations when $R_e > 10^4$). In actual fact, a laminar flow, hardly predictable before the calculation, is likely to appear locally for very 'thin bypasses'. The fluid change of behavior is not taken into account in the code at the moment, we rather use the asymptotic behavior of turbulent flows correlations whose redistribution has been validated. We added a 'TDP' curve to the plot, standing for a third degree polynomial matching F_V with a coefficient of determination $r^2 = 1$.

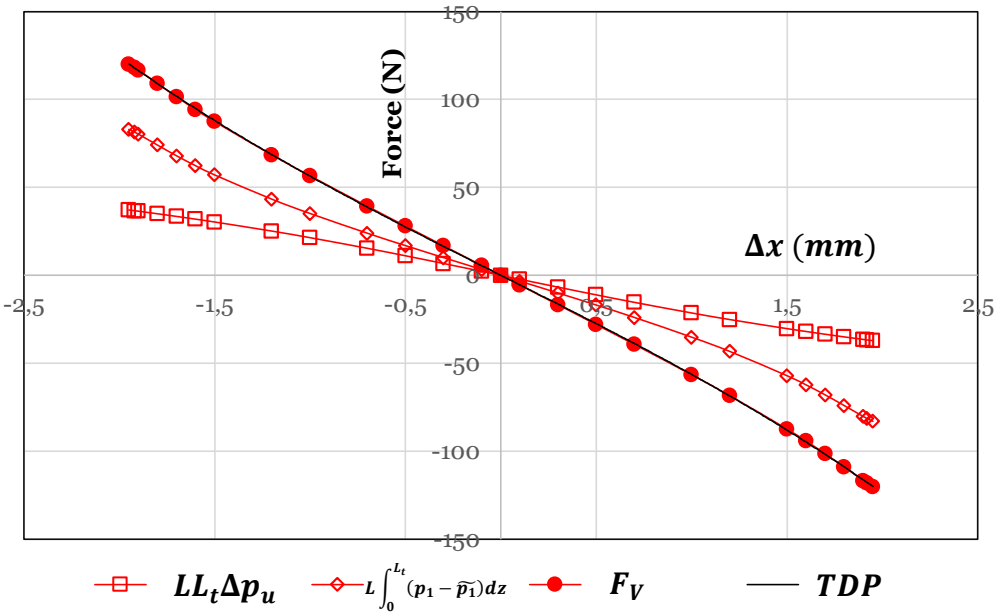

Figure 3-12 - Fv1 composition (test case)

2. Force model related to cross-flow inside the bundle

2.1. *Estimating the bundle force in a network*

Having considered the reliable results of a simple and fast network calculation (for the convergent-diffuser), we have chosen to adopt the same method thereafter. Because the row-based approach is clearly practicable in a network code (pressure drops), and its usage highlighted reliable results for FA bow, we will use it in our work. In fact, the same idea was undertaken for the Model 3 which also leant on the Eole's correlation to estimate the lateral loss induced by the rods coming up to the water gap. For this very reason, the equation

giving the loss across a bundle is reminded below (Eq. 3-13):

$$\Delta P_B(\theta) = \frac{\rho N K_\perp \xi(\theta) \beta^2}{2 S_B^2 \sin^2(\theta)} Q_B^2 = K_B(\theta) Q_l^2 \qquad \text{(Eq. 3-13)}$$

Where the Eole's correlation is:

$$\xi(\theta) = \left(\frac{\sin(\theta)}{\cos\left(\frac{\pi}{4} - \frac{\theta}{2}\right)} \right)^{1.7} \qquad \text{(Eq. 3-14)}$$

The main difference with Model 3 in terms of pressure drop lies in the expression of $S_B = H_B L$ (H_B being the bundle height) which stands for the full cross section of the bundle whereas it stood for the leak height related cross section for Model 3 ($S_l = h_l L$). Also, N, the number of rows, is explicitly defined as it now handles every single row crossed by the coolant (*i.e.* generally 17 for our designs, or 8 for a downscaled FA like the MISTRAL's, below).

The incident angle θ is chosen such as (Figure 3-13):

$$\theta = \begin{cases} \tan^{-1}\left(\frac{S_{g_1}|Q_B|}{S_B|Q_{g_1}|}\right) & \text{if } Q_B > 0 \\ \tan^{-1}\left(\frac{S_{g_2}|Q_B|}{S_B|Q_{g_2}|}\right) & \text{if } Q_B < 0 \end{cases} \qquad \text{(Eq. 3-15)}$$

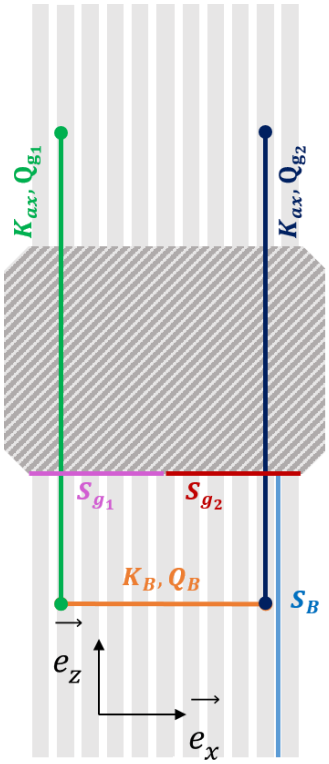

Figure 3-13 - Schema of the bundle flow in the FA

One can notice that the fuel assembly has been split into two axial elements by analogy with the CD redistribution model. K_{ax} is the axial hydraulic resistance associated with a full axial pathway from one assembly span to another (*i.e.* a friction loss term and the grid local term coefficient - K_g -). As seen in Appendix B the force is written as follows:

$$F_{Bu} = \Delta P_B(\theta) S_B = \frac{\rho N K_\perp \xi(\theta) \beta^2}{2 S_B \, sin^2(\theta)} Q_B^2 \qquad \text{(Eq. 3-16)}$$

In order to assess the relevance of the previous expression calculated in an operational network (which has not been assessed in the literature, unlike the correlation itself), we decide to redo the validation run by Wanninger [9], and Peybernès [28]. The two authors checked the correct implementation (respectively in *ANSYS CFX* and *FLICA4*) of the correlation through a test resting on the MISTRAL experiments (Figure 3-15).

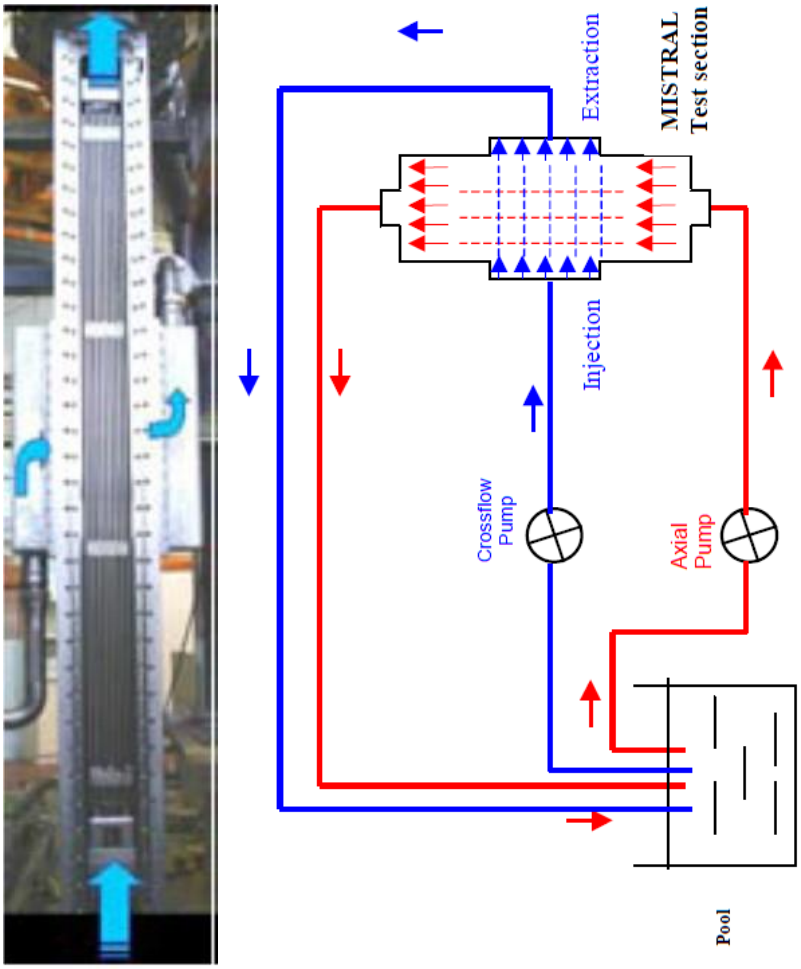

Figure 3-14 - The MISTRAL mock-up (left), associated hydraulic loops (right) (from [28])

The MISTRAL test section, within the THESEE hydraulic loop, aims at evaluating hydraulic efforts exerting on a 3 spans – 4 grids – nuclear fuel assembly made up of 8x8 fuel rods. An axial flow rate (further called Q_{ap}) is injected at the assembly foot, and a withdrawal flow rate

is extracted at the assembly top. Laterally, a cross flow rate is injected on the central bundle, and extracted on the other side. This way, the total lateral force is exerted on the central bundle, where a lateral inclination of the fluid is imposed.

Two experimental campaigns were run. The first (A) one consisted in maintaining the axial flow at $125\ m^3.h^{-1}$ which approximately matches an axial velocity of $5\ m.s^{-1}$ in the bundle, while the cross flow rate ranges from 0 to $40\ m^3.h^{-1}$, leading to cross velocities ranging from 0 to $0.2\ m.s^{-1}$. The latter are chosen so they are typical cross velocities found out in a bundle of fuel rods in operational conditions. The second campaign (B) maintained the ratio axial flow rate / cross flow rate at 3 with axial flow rates ranging from 50 to $125\ m^3.h^{-1}$. All tests are performed under ambient conditions.

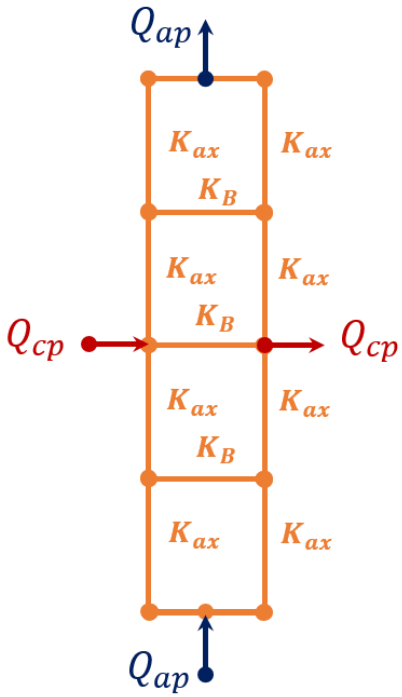

Figure 3-15 - Network of the MISTRAL experiment

Figure 3-15 highlights the hydraulic network built with the Phorcys code through a dedicated dataset. One can notice that, for now, no redistributions exists with the wall/FA bypasses. The latter choice is based on the mock-up setup. First, the fuel assembly is stood up straight in the test section so that no gap differences exist around the fuel assembly. Second, the main crack of symmetry comes from the injection of Q_{cp} within the central bundle, to that only a few imbalance in terms of axial flow might exist between the right and left bypasses. Thirdly, the sides of the assembly are confined so that the fluid tends toward remaining within the bundles according to Model 3. In other words, this test section only fosters forces applying on bundles, and events might unfold as if all the circulations were intra-assembly-based.

Another remark is that only one lateral element is given for each assembly span. It implicitly implies that the pressure is homogeneous along S_B. In fact, porous codes or CFD codes would lead to a thinner discretization axially, but as we want to keep a macroscopic 'network approach', we chose to only keep one element laterally. The results will tell if this assumption is acceptable or not: are our forces near to the experimental ones?

Under these conditions, the total lateral hydraulic force is given by $F_{Bu} = \sum_{i=0}^{3} F_{Bu_i}$ where

F_{Bu_i} stand for every bundle related-force from span 1 to 3. The results of both campaigns have been gathered in Figure 3-16.

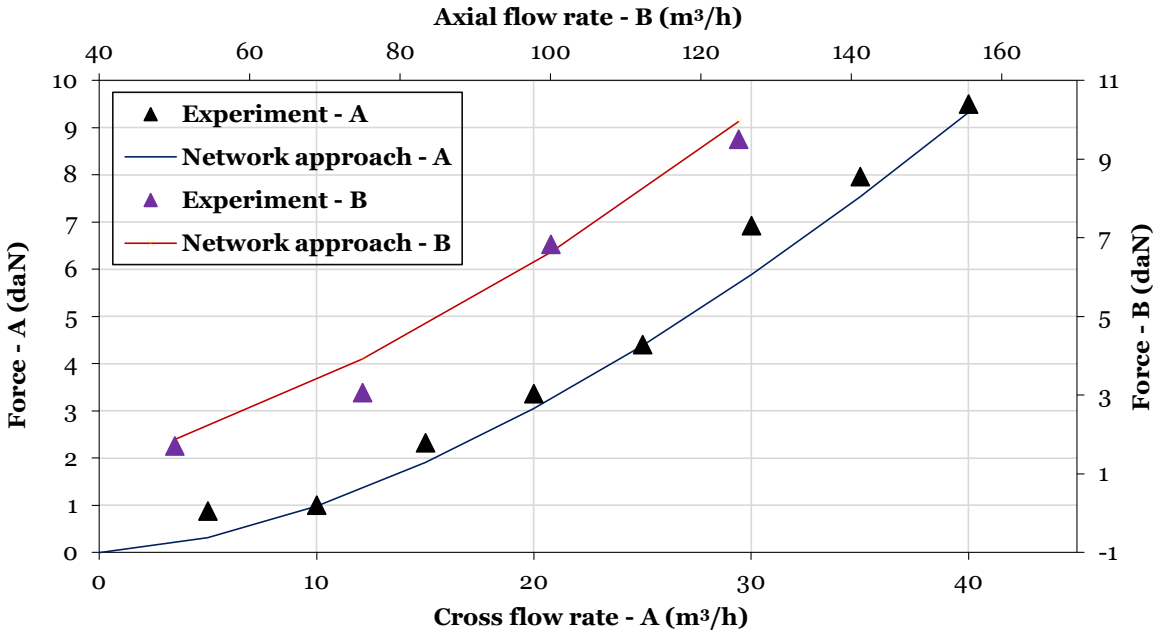

Figure 3-16 - MISTRAL's campaigns

One can observe that both campaigns results are in good agreement with the Phorcys' calculations. In the style of Wanninger [9] who validated this approach for a porous code, we can argue that the Eole correlation can be judged reliable for use in our network approach to estimate the lateral pressure drop in the PWR bundle and the associated force with one lateral element for each span.

3. Force model related to the flow being put in the upright position

The force F_{UP} introduced in chapter 1 stems from the behavior of the flow in the inner bundle cross-flow presented in the last section. It is indeed based on the inclined velocity inside the bundle being put in the upright position. As a result, the flow rates highlighted in the bundle approach (Figure 3-13) can give an estimation of this force.

As a reminder, the forces F_{UP} can be valued thanks to (Eq. 3-17):

$$F_{UP} = \frac{1}{2}\rho \sin(2\theta)\, S_g\, v_\infty^2 \qquad \text{(Eq. 3-17)}$$

In practice, the incident flow (of velocity v_∞) which goes into the grid is not trivial. Its lateral component v_x oscillates between V_X (outside the rods) and βV_X (between two fuel rods), so does the angle θ which directly depends on the lateral component (see for instance 7.1.3 for further details). As a consequence, the formula (Eq. 3-17) can reach two different

values defined by the two couples of variables giving the two extreme forces:

$$\begin{cases} (\theta_1, \theta_2) = \left(\tan^{-1}\left(\dfrac{S_g |Q_B|}{S_B \left|Q_g\right|} \right), \tan^{-1}\left(\beta \dfrac{S_g |Q_B|}{S_B \left|Q_g\right|} \right) \right) \\ \left(v_{\infty_1}, v_{\infty_2}\right) = \left(\sqrt{\left(\dfrac{Q_g}{S_g}\right)^2 + \left(\dfrac{Q_B}{S_B}\right)^2}, \sqrt{\left(\dfrac{Q_g}{S_g}\right)^2 + \beta^2 \left(\dfrac{Q_B}{S_B}\right)^2} \right) \end{cases} \quad \text{(Eq. A-1)}$$

With the notation introduced in Figure 3-13:

$$\begin{cases} Q_g = Q_{g1} & (Q_B > 0) \\ Q_g = Q_{g2} & (Q_B < 0) \end{cases} \quad \text{(Eq. A-2)}$$

Assuming that the mean lateral component of the cross-flow (defined by the average of the extreme values V_X and βV_X) can depict the force, we can show (7.1.3) that:

$$\overrightarrow{F_{UP}} = \frac{1}{2}\left(F_{UP}(\theta_1, v_{\infty_1}) + F_{UP}(\theta_2, v_{\infty_2})\right) \frac{Q_B}{|Q_B|} \overrightarrow{e_x} \quad \text{(Eq. A-3)}$$

In practice, the post-processing of every force is calculated through an object called 'elementary mesh' in Phorcys, defined at each FA span, for further details see Appendix F 7.1.3.

4. Combining local models to build up the FA

As the reader may have understood two distinct hydraulic networks were built to model major redistributions occurring in the FA. The first one is the network focusing on redistributions between bypasses and grids ('grid-focused') and the second one is a network which deals with cross flows going through FA bundle sections from one side to the other ('bundle-focused'). In Figure 3-17, we summed up the two different approaches which aimed at estimating the forces 'V' and 'Bu' on both the bundle and the grid. At first sight, those models are incompatible. With the first one, we focus on redistributions occurring at the grid scale, located between two nearby fuel assemblies. The other one rather focuses on cross flows occurring in the inner section of one FA, and the associated lateral hydraulic resistance based on the Eole correlation.

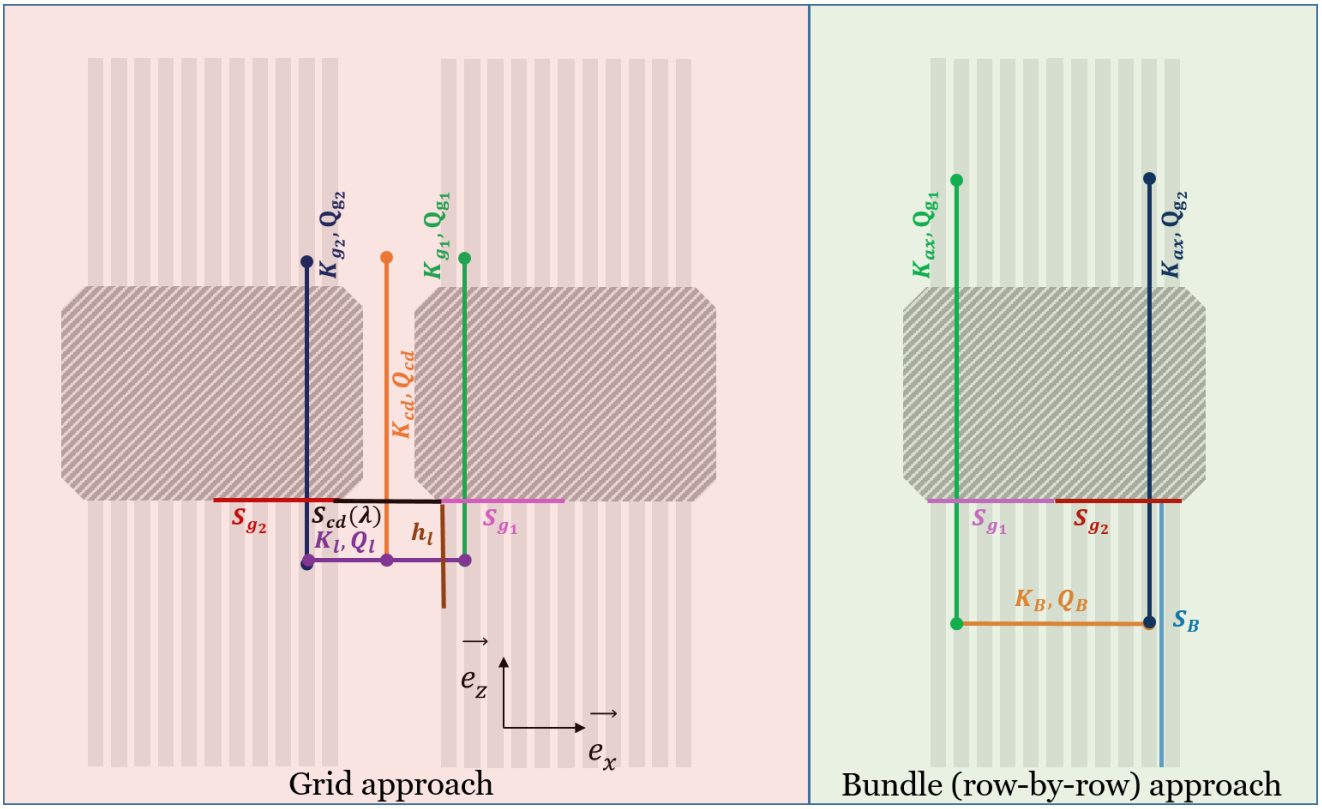

Figure 3-17 - Comparison of two approaches at local scales

In a network the nodes represent one pressure. The nodes of the grid approach must be nearby the grids, whereas they lie 'in the middle' of the bundle height in the bundle approach. The question is: how do we make the most of those two separated models to set up a network at a full FA scale?

This question is quite intricate. Firstly because theoretically those redistributions, at local scales, do not really occur at the same 'level'. One can argue that grid redistributions are even more local than inner bundle redistributions which occur along the full height of the bundle, so that we could almost consider grids' models as 'more local'. Secondly, they imply different resistances. In fact, axial resistances in the grid approach only contain 'grid loss coefficients' (made of local and frictional components [58, 59]), whereas K_{ax} is a combination of both grid losses and the bundle friction outside the inner grid (which can be estimated thanks to the Darcy-Weisbach' formula). In other words, an additional resistance is present in K_{ax} compared to K_g. The latter is due to the fact that inner bundle redistributions are assumed to happen within one full span (between 40 to 50 centimeters tall).

The differences exhibited above are highlighted in Figure 3-18. As a matter of fact, the redistribution between fuel assemblies at the grid scale are depicted with the red arrow, and the inner bundle redistributions are depicted with the blue arrow.

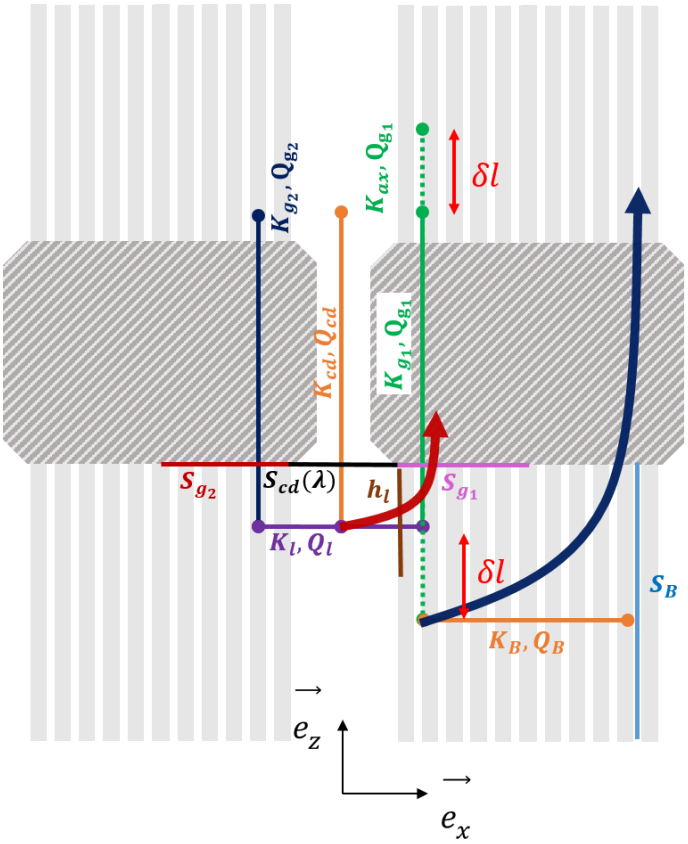

Figure 3-18 - Schematic view of height between the approaches

The term δl represents the difference of localization between the two approaches which we used to estimate the forces, the goal is to join the links. In order to join up the branches, different solutions can be suggested at this stage. The first one may be the most direct, yet quite raw, solution *(A)*. It would consist in discretizing the full span in slices whose height can reach a value up to the same order as h_l. Another try would be to neglect the friction part of K_{ax} so that $\delta l = 0$ to join the two parts *(B)*. It could be a reasonable hypothesis given that a majority of the loss in K_{ax} lies in the grid loss (K_g) (see for instance [22]). The last solution would be to conserve energy equations in each part (which were validated separately), along with a node joining ($\delta l = 0$) *(C)*. The solutions are summed up in Figure 3-19.

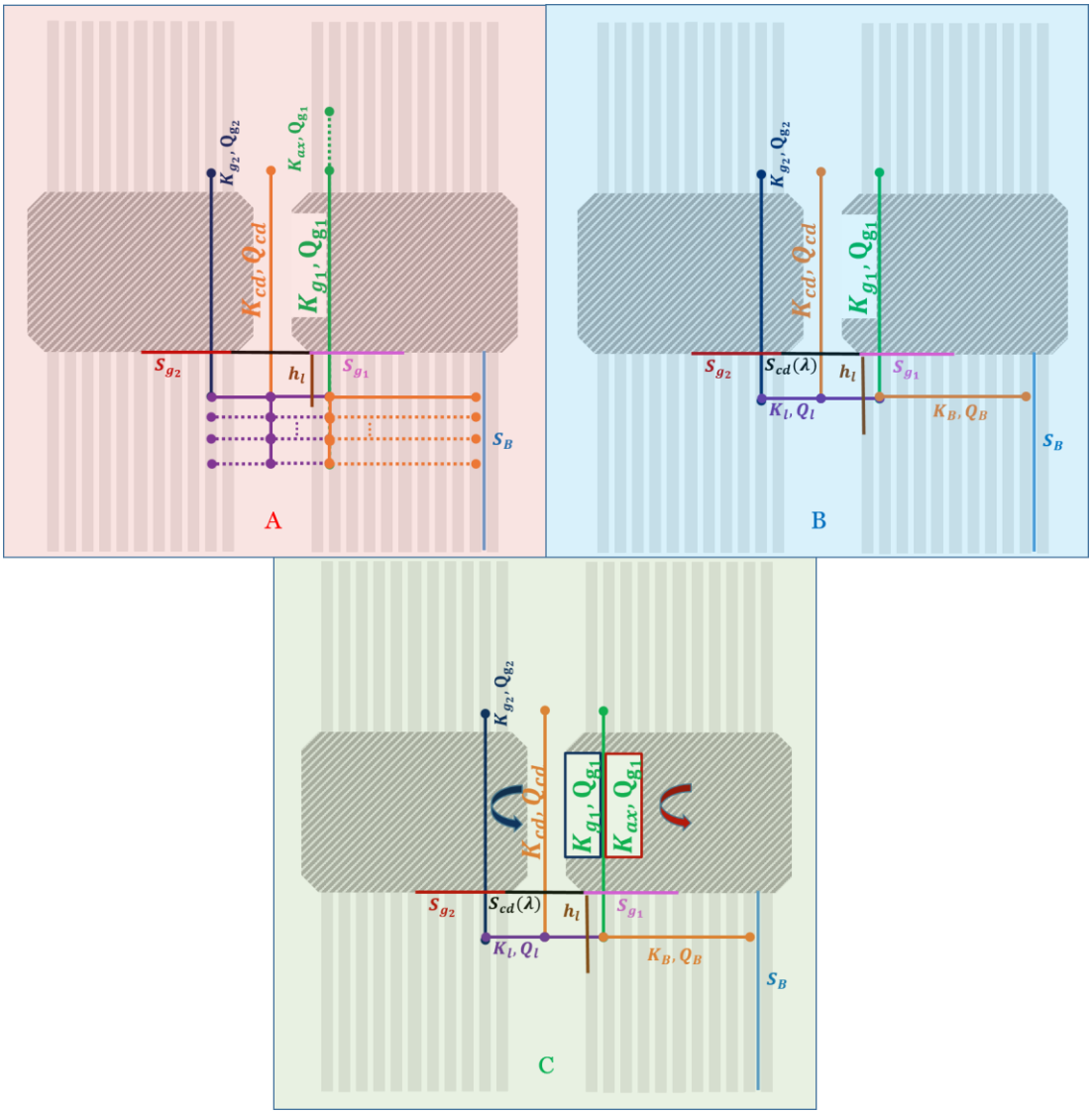

Figure 3-19 - Different solutions to join the two approaches, (B) and (C) differing from the expression of the axial resistance used for the FA in the inner bundle loop

Let us make some comments on those solutions.

- Solution *(A)* is the most direct one. On the other hand, it can add up to 40/50 elements per span to discretize homogeneously the height of the span. Additional purple elements between FAs are, in actual fact, almost useless as we saw that the redistribution in the bypasses occurred only nearby the grid level as the bypass seems to act as a barrier to cross flows [74]. Even neglecting the additional purple elements leads to 20/25 additional elements in total (in this case only the orange ones). Adding so many elements (more than 10^2 per FA) makes no sense in a network approach whose goal is specifically to estimate redistributions through macroscopic meshes so that otherwise a porous approach might be more appropriate. Of course one could argue that we could opt for 'simplified approach *(A')* splitting the bundle in two parts instead of 50 or more (one of h_l and one of $H_B - h_l$), but the whole interest of this method would fade away because the maximal cross flow would be located in the $H_B - h_l$ section and almost no flow would cross the h_l section, which is similar to the other approaches. What is more,

as every other methods, it would assume an 'homogenized' single pressure along S_B when calculating the lateral pressure drops piloting the cross-flows.

- Solution *(B)* is the easiest one, because neglecting axial friction compared to the grid local loss leads directly to $\delta l = 0$. The hypothesis would make sense as the friction loss in the bundles embodies less than 20% of the total axial loss. This method conserves the number of elements, but may lead to a little overvaluation of the axial flow rate due to the undervaluation of the loss.
- Solution *(C)* is an hybrid one. On the one hand it conserves the number of elements, and on the other side conserves the energy equations in every section which were validated in an independent manner. In other words, as seen in Figure 3-19, in terms of energy the grid branch is linked to a K_{g1} resistance in the grid approach, whereas it is linked to a K_{ax} resistance (K_{g1} plus a span of axial friction on the rods) in the bundle approach. Formally, in Figure 3-20, the latter leans on the hypothesis that the bundle axial flow rate variation on δl is small enough so that the pressure loss associated to K_{ax} can be estimated only through Q_g. In other words $Q_{ax1} \sim Q_{ax2} \sim Q_{g1}$.

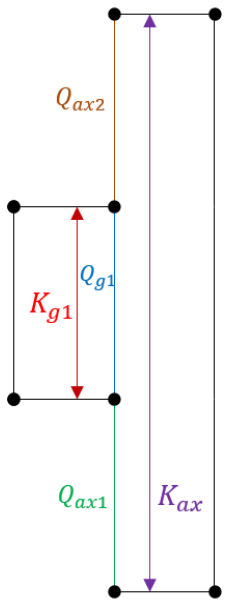

Figure 3-20 - Hypothesis of (C)

In every 'case – *i.e.* simplified *(A), (B), (C)* – the main assumption is the same, the pressure is 'homogenized' along the lateral cross-section of the bundle S_B with a value piloting the cross-flows intensity. It is indeed what infers the Bernoulli's principle within one pipe. Considering that in lateral elements the pressure is 'homogenized' could be inadequate for chaotic variations of the pressure axially. This assumption was also used for the calculations undertaken for the MISTRAL experiments and the proximity of our results encouraged us to keep this assumption for the rest of the works. In what follows we have chosen to look at *(C)*, with our code structure this solution is easy to cope with, so that we can refrain from the additional hypothesis in *(B)*. On the other hand, a version simplified of *(A)* (two lateral elements within the bundle) would tend toward useless complication of the network structure, leading to similar results.

Finally we can draw a diagram of our simplified FA, using bundles and CD. The latter FA is depicted in Figure 3-21.

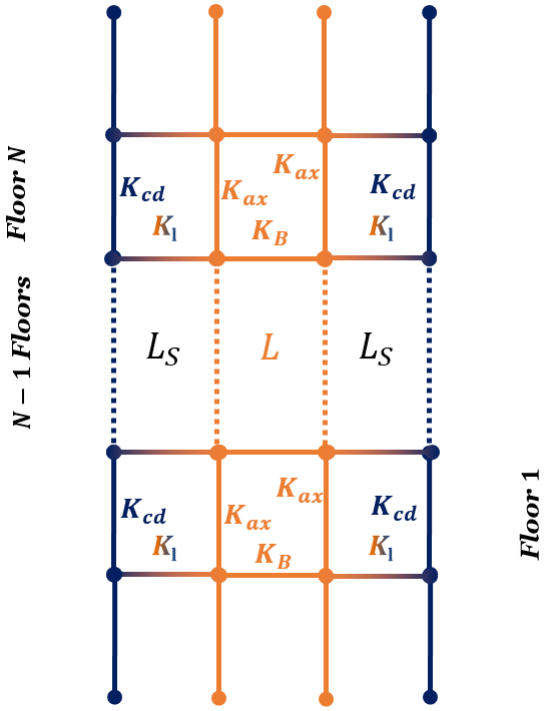

Figure 3-21 - FA scale model gathering local scale models

L_S stands for the stagnation point loop (correction of resistances with an equivalent one (Eq. 2-18)), this is due to Model 2 or 3. L is an 'inner-FA' loop. For more information about the loops management see Appendix F.

5. Validating the FA model behavior with a CEA experiment

5.1. *The apparatus*

We now need to test the assembly model. The single assembly model can be assessed through a dedicated experiment. The latter has been presented a couple of times in the literature, including for instance [43, 75, 76]. Those experiments were performed with a full fuel assembly. It is made of 264 fuel rods (+25 guide tubes) of height 4.5 meters and a linear density of about 200 kg/m. Both guide tubes are welded to a top and bottom nozzle. The latter is located on a lower core plate which ensures injection through 4 injection tubes. The flow withdrawal in ensured by a square hole located in the upper core plate. The test section is eight times larger in the bow direction than in the other direction. More precisely, 20 mm gaps surround the FA in the mock-up in its bow direction, and only 5 mm gaps surround the FA the other way around. The FA grids are around 20 cm wide.

The hydraulic loop containing the FA is the HERMES T loop. It puts single phase water into circulation and is designed to handle a full scale PWR 1300 MW fuel assembly (unlike in the MISTRAL or Eole tests for instance). The pump can supply up to 1200 $m^3.h^{-1}$ in terms of axial flow and 400 $m^3.h^{-1}$ in terms of cross-flow at 35 bar and 170°C. In other words, the

flow rate supplied can be the same as in real PWR conditions. The loop operates at a lower temperature than a real PWR (see the introduction), it enables better measurements. In the following operation, the temperature was set to 50°C only. Figure 3-22 and Figure 3-23 highlight the experimental mock-up.

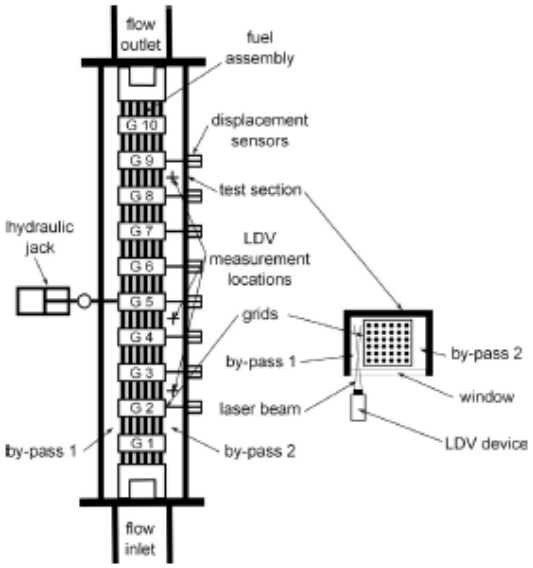

Figure 3-22 - Experimental apparatus from [75]

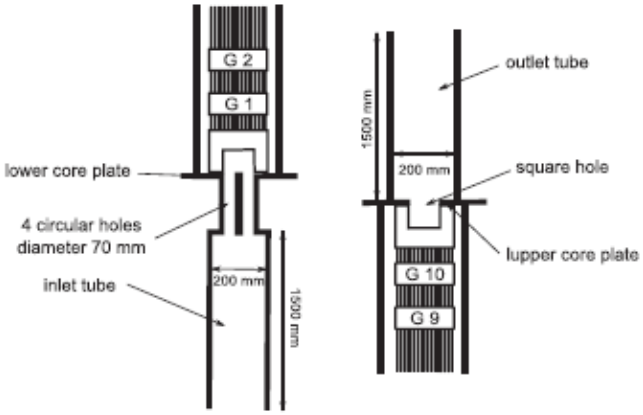

Figure 3-23 - Inlet (left) and outlet (right) flow boundary conditions from [75]

Both dynamic and static tests were run. During the static ones, axial velocities were measured in the FA and its bypasses with a Laser Doppler Velocimetry (LDV) device. The values were probed between grids 2/3, 4/5, and finally 8/9. Measurements were done every 2 mm in the spanwise direction in each bypass. The static tests, which interest us, are of two types. The first was performed with the FA at rest. The second, quasi-static, consisted in a slow displacement of grid 5 within a 1 cm range. We consider here the values standing for the maximum 1 cm displacement, right-oriented, imposed on the 5^{th} grid through a hydraulic jack. The related force is measured with a load cell. The displacements of grids 2 to 9 were measured thanks to Linear Variable Differential Transformer sensors. To find out further details about those experiments, we invite the reader to consider for instance [76] or [75].

Contrary to other apparatus which can be found in the literature, for instance GLASSTRAN within the Framatome's PETER loop in Erlangen [50, 16], this device is bounded by rigid walls. In other words, the bypass between the FA mock-up and its surrounding walls is FA-wall type, like external bypasses in a real PWR (next to the core shroud). One can then understand that the inter-grids areas in this case do not shape a convergent-diffuser, but rather a 'half convergent-diffuser'. On paper, it is not *exactly* what have been validated above, which concerns inter-assemblies gaps. Theoretically, it is still possible to use our CDs, conserving the cross-sections reduction rate ($\chi_{ext} = \Lambda/\lambda$) imposed by this kind of external geometry. To do so, it is possible to double λ, the derivation is quite direct:

$$\chi_{ext}(\lambda) = \frac{\lambda + h\tan(\alpha)}{\lambda} = \frac{2\lambda + 2htan(\alpha)}{2\lambda} = \chi_{cd}(2\lambda) \qquad \text{(Eq. 3-18)}$$

Yet, one must notice that using 2λ elements is unreliable in this case. First, the equivalence remains, hydraulically speaking, an approximation compared to a real 'half' convergent-diffuser which has not been studied in this project. Secondly this approximation would imply elements whose thickness could overtake 6 cm. The latter value is much higher than the ones validated, and this would physically call for a need of higher h_l (which depends on λ) which were not used for the validation neither. However, for such a range of very large gaps (more than 1 cm), the assumption $\chi_{ext}(\lambda) \sim \chi_{cd}(\lambda)$ is still acceptable, because it only leads to deviations around 10 % (whereas the error reaches 60% for a nominal gap, and the hypothesis $\chi_{ext}(\lambda) \sim \chi_{cd}(\lambda)$ would be raw). In other words, we will use in this part convergent-diffusers for the redistribution, whose width equals 20 mm.

The network used for the calculations are indicated in Figure 3-24.

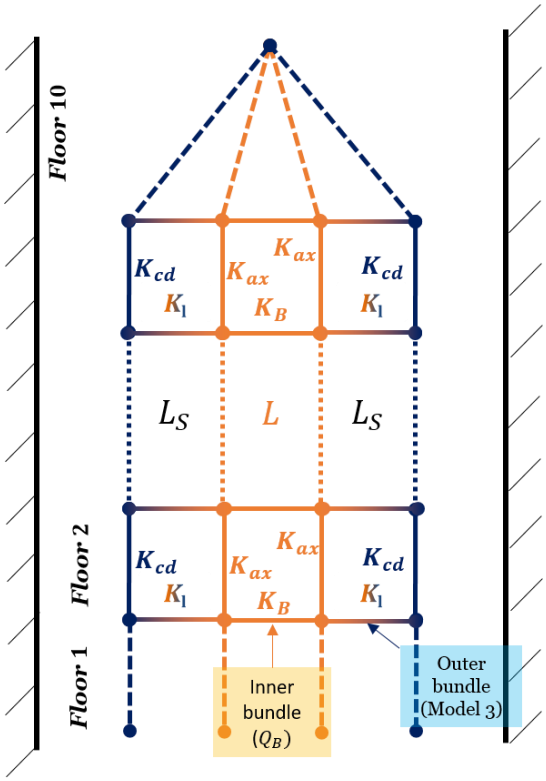

Figure 3-24 - Network implemented for the tests

At this stage, no specific model exists for the nozzles as we set up the FA directly from ours, thus we will directly inject the flow in the first assembly span (floor). It is not a strong hypothesis given the Fournier's results [14] showing that lower core plate high-speed jets spread to the first grid. By a matter of symmetry, top boundary conditions are imposed on the 10th floor. The latter consist in a free outlet (equal pressure) at the top. The entrance flow rate of the test is injected through the bottom of the assembly (*i.e.* the flow rate in each half axial element of the FA is 50% of the total entrance flow rate, and the bypasses are dry). In practice there is always a little flow in the bypass – not exactly 0% - and the distribution of flow rates at the system inlet remains uncertain. To make sure that the bottom conditions were not 'crucial' to give a good estimation of the redistribution we changed by 5% the inlet distribution (consequently the inlet conditions are nearer to a homogenous velocity inlet conditions) and observed that the flow behavior was not very sensitive to this reasonable change (maximal deviation of 7% in terms of axial flow rates).

Due to the system topology, the forces are calculated from the 2nd to the 9th floor. We know that the redistribution upstream from the first grid (and also the 10th) exerts a force, but their impact are rather small on the final assembly deformation because of their very small bending moments (they are close to the extremities) as observed by Wanninger when introducing the concept of 'equivalent forces' [22]. Thus, it justifies that one can reach a suitable bow without considering the first and last floors. This assumption is validated thereafter. Also, given the very important widths found in the system, there is no need to correct so much Model 2 hydraulically, to so that a h_f value of 5 cm (asymptotic value) is enough. Similar patterns of forces were found out for h_f values of 2 cm.

5.2. *Verification of hydraulic parameters through redistribution*

We can make sure that our choices are consistent comparing the velocities of both the tests and our FA model. In practice, LDV points in the tests were probed on a line, whereas our velocities are integrated on a cross-section, because they are bulk velocities. It is thus irrevocable that a deviation will exist between the tests raw results and our own results.

Results [76] highlighted that the fluid mostly redistributes on the first third of the FA height and stabilizes thereafter. More precisely, the authors observed that the fluid tends toward going into the gaps all along its journey in the mock-up. It is coherent with our results at the grid scale (beyond $\lambda = 7$ mm the coolant 'prefers' to flow into the CD rather than the grids). It is yet necessary to make sure that our FA scaled model is able to reproduce such a behavior on its full height. Figure 3-25 shows the evolution of the velocities with respect to a couple of different entrance velocities. In the tests two lines of probes exist in each surrounding bypasses, for this reason there are two velocities for each bypasses (BP1 and BP2).

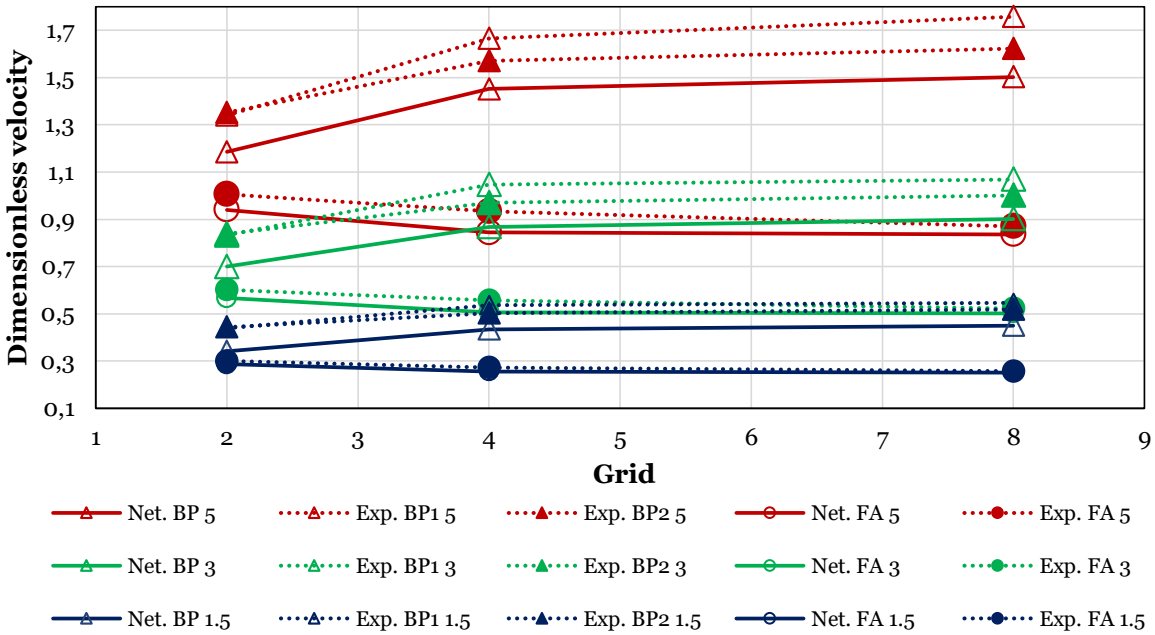

Figure 3-25 - Redistribution rates in the fuel assembly (FA) and its bypasses (BP)

For Phorcys' results, we consider the numerical flow rate at the outlet of the CD N divided by Λ (and not λ) when comparing to the experimental velocity measured in the bypasses between grid N/N+1, because in practice, a jet spreads from the outlet of the CDs for large gaps [67]. In other words, the closest velocity may be the one exiting the N^{th} CD. The experimental points are obtained averaging the line of velocities in each bypass. One can see that a slight difference appears between the two bypasses due to the asymmetry of a grid, this has already been noted in [76], and the difference seems to increase with the axial entrance velocity. Yet, such a difference is not directly observable in our network as the system is purely symmetric.

As remarked just above, an expected deviation between the model and the experiments is noticeable, above all in the bypasses. It is interesting to note that this deviation is almost constant for all velocities. This is certainly due to the difference between bulk velocity and local velocity on the line of measure, or maybe because inlet boundary conditions are not exactly the same. Results show that the network is able to reproduce well the behavior of the fluid: across its track over the top of the mock-up, the coolant tends toward gradually leaking into the gaps due to the important thickness of the bypasses (20 mm). This behavior has been observed at the grid scale, but yet is noticed again at the FA scale. Also, it shows that using an unmodified CD for large bypasses is justified.

5.3. *Coupled simulation of the assembly bow with the same hydraulic parameters*

The next step of this work is to see if the set of forces calculated on the full height of one FA through Phorcys is coherent. Unfortunately in this experiment, the forces are not probed as remarked by Joly [43]. In other words, we cannot ensure our forces reliability directly. Yet, the grid displacements were measured by LVDT sensors. Consequently we can validate our set of forces through the displacements brought about.

To calculate displacements, it is necessary to bow the FA structure. The latter is not directly the subject of the current project, but an in-house code at CEA has been built up in the past to specially account for the FA mechanics. It consists in a software overlay leaning on the CEA's code Cast3M [77]. The latter overlay is based on a framework (Figure 3-26) made of Timoshenko beams and contact elements including fuel rod-grid, guide tube-grid, or even inter-grid contact. For further details about simplified mechanical models of FA based on Timoshenko beams see [78] or [22].

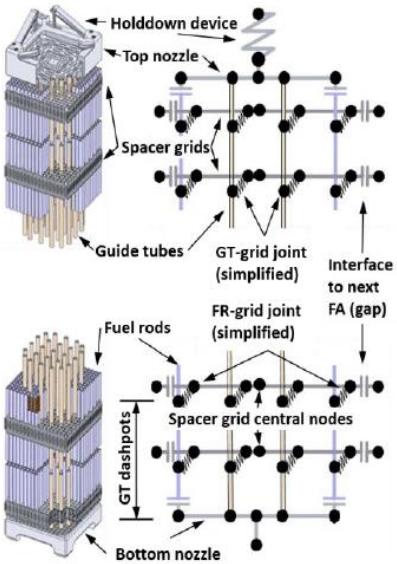

Figure 3-26 - Example of mechanical framework of a FA as seen in [78]

Then, we need to couple Phorcys and Cast3M in a partitioned manner as both solver are used separately. In practice, we will further see that at this scale, a convergence is reached quickly so that a one-way coupling would give a good estimation of the converged state as agreed with [79, 22]. Generally, the main disadvantage of a two-way coupling is the higher computational time [80], but the hydraulic solver speed allows to directly opt for this method. It also guarantees energy conservation at the fluid-structure interface – see again [80] -, one-way couplings do not.

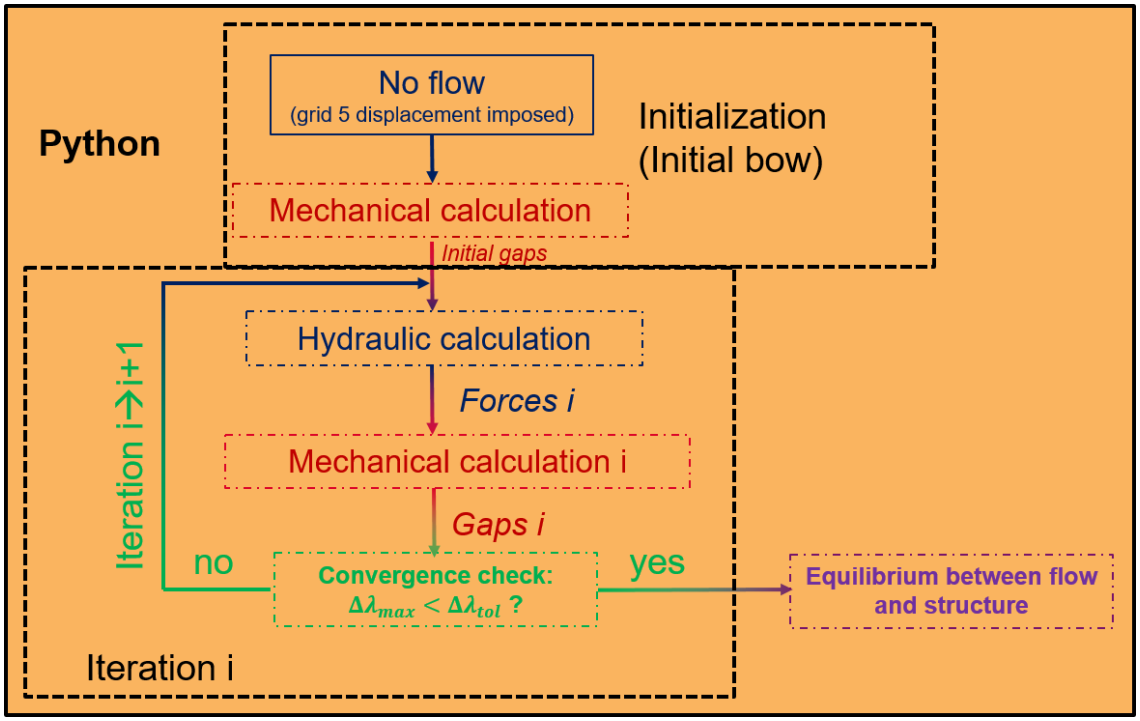

Figure 3-27 - Coupling between Phorcys and Cast3M

The coupling scheme is shown in Figure 3-27. The goal of the algorithm is to find out stationary equilibrium between the fluid and the structure. This fixed-point algorithm [81] is wholly adapted from Horvath's [16], except that the author used a CFD solver whereas we use our network solver. The fixed-point initialization starts considering the previous mechanical equilibrium, which in our case consists in the assembly being bowed by the jack in standing water (5^{th} grid shifted by 10 mm as said above). Then, hydraulic forces are pulled out from this initial state and are sent back to the mechanical solver. The other way around, the new set of gaps λ brought about by the deformation are updated in the hydraulic solver. Thus, a reciprocal process between the solvers is being instanced (two-way coupling). The iterations stop when the convergence criterion is reached, *i.e.* the maximal change in λ in the system is lower than the user-defined tolerance.

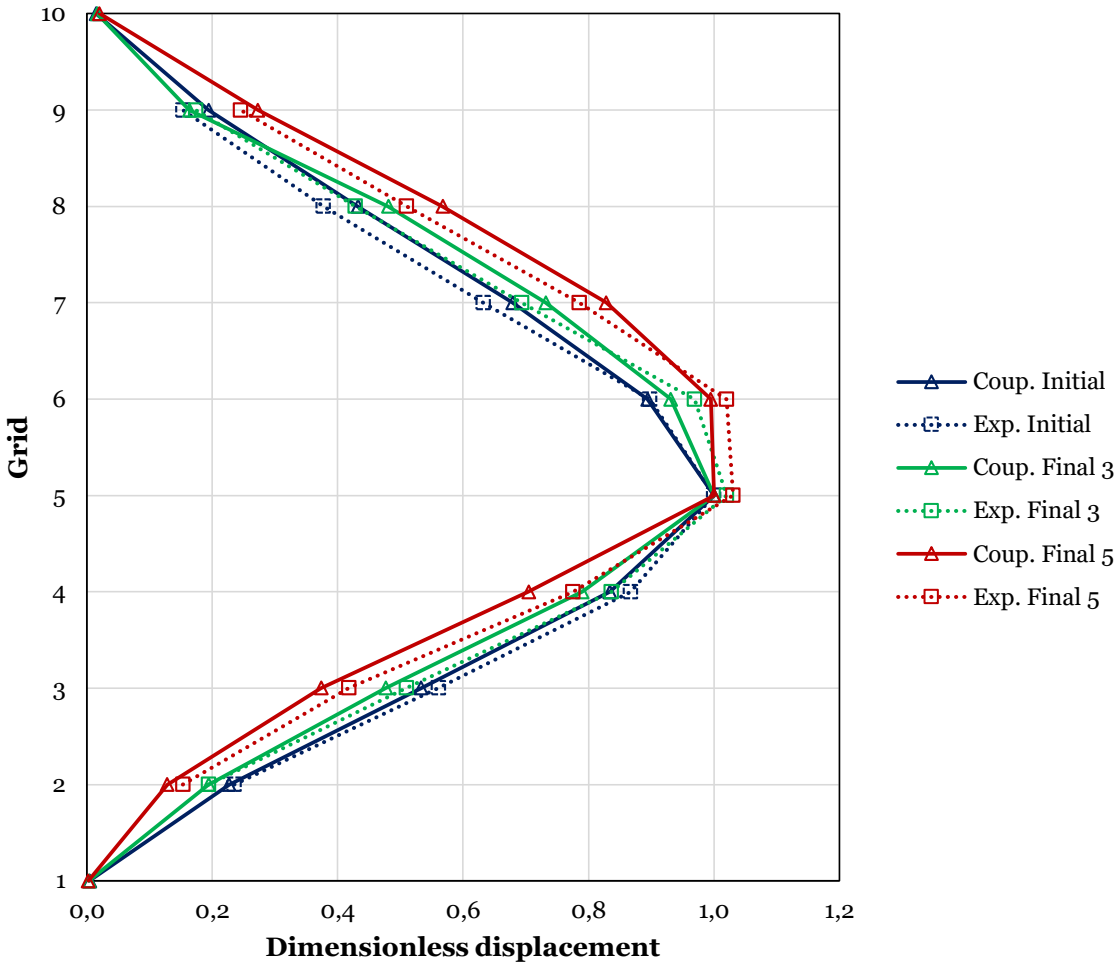

Figure 3-28 - Grids displacements (FA bow)

Figure 3-28 depicts dimensionless grids displacement. It represents the FA bow at the maximal path of the jack bounded to grid 5. The initial state (no flow) can be found through the blue curves. One can see that only few discrepancies exist between experimental points and the mechanical model: the bow is slightly underestimated before the 5th grid and overestimated afterward (reaching ~10% at grid 8). Nevertheless, the behavior when hydraulic loads are applied is coherent. In other words, those differences are conserved. One can also notice that experimental final states do not exactly match the same value as the initial state for grid 5. It can be explained by the fact that the device used for moving the jack was not the same as the device used for measuring the grids displacement.

In what follows, we focus on the 5 m/s case because on the one hand, it is the closest condition to real PWRs, and on the other hand, the final shape of the FA is similar whatever the inlet velocity is. In order to assess the differential deformation of the FA due to the fluid forces compared to the initial state with no flow, we need to pick up the grid displacement measures leaning on the same base: we will consider the experimental displacements when the 5th grid displacement exactly equals the same displacement as imposed in the mechanical simulation (we remind that, in practice, this test was *quasi-static*). This will prevent from obtaining a no-null differential deformation at grid 5. These differential deformations are highlighted in Figure 3-29.

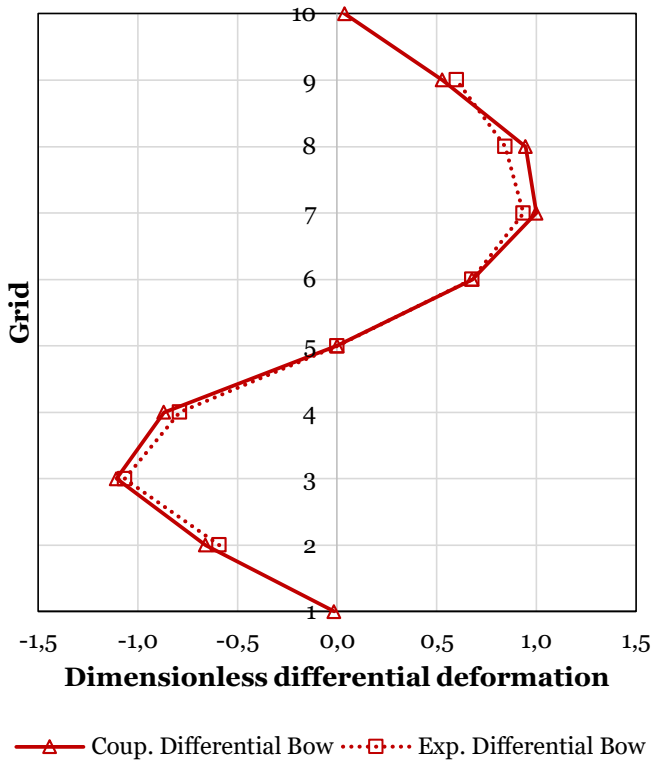

Figure 3-29 - Differential deformation

Numerical and experimental results are in very good agreement. The consequences of hydraulic loads are well depicted by the coupling involving the FA model set up previously. In other words, the set of forces calculated produces excellent results in term of mechanical deflection. Let us take an interest in the latter hydraulic loads.

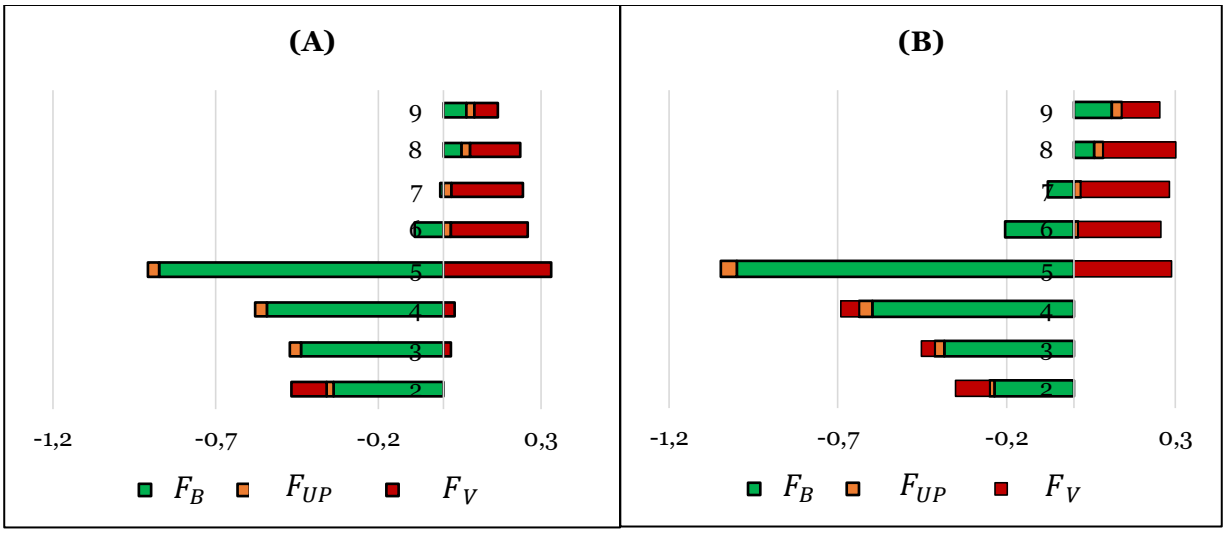

Figure 3-30 - Dimensionless hydraulic loads exerting on the fuel assembly (A) one-way (B) two-way

Figure 3-30 shows the hydraulic forces either (A) without iterating, (B) reaching a converged state (in only 6 iterations). In other words, in the first case, the mechanical deformation is obtained directly after a first application of loads, whereas in the second,

round-trips are performed between the solvers. The total sum reaches -1.23 in (A) and -1.44 in (B), in other word the total lateral force only vary by 15% between the two cases. Compared with the force value exerted on the jack, it turns out that (A) is 11% away from the measured value, whereas (B) is only 3% away. The converged solution is thus nearer in terms of total lateral forces to the experimental value noted in the test, even if the one-way approach gives a good approximated solution. Some F_V (at grid 3 and 4) changes sign between iteration 1 and 6, it is a trend already observed in [16]. The large value of forces at grid 5 is due to the metallic shims surrounding the grid 5 for the measure which strongly reduce the hydraulic diameter locally.

It is interesting to note that bundle forces are higher than grid forces before grid 5, and lower afterward. Also, while the F_{UP} direction is the same as the cross-flow in the inner bundle (oriented toward Q_B, see Figure 3-24), F_B is a combination of a couple of different sub-forces: inner bundle force (F_{Bu}), and outer bundle forces (again see Figure 3-24) due to redistribution through h_l (F_{M3_1} and F_{M3_2}), as indicated in Appendix F. Consequently they can have different signs (grids 6 and 7). The composition of F_B is detailed in Figure 3-31 (A) as well as the composition of F_V in Figure 3-31 (B). Both figures are plotted with the forces obtained at steady-state (Figure 3-30 (B)).

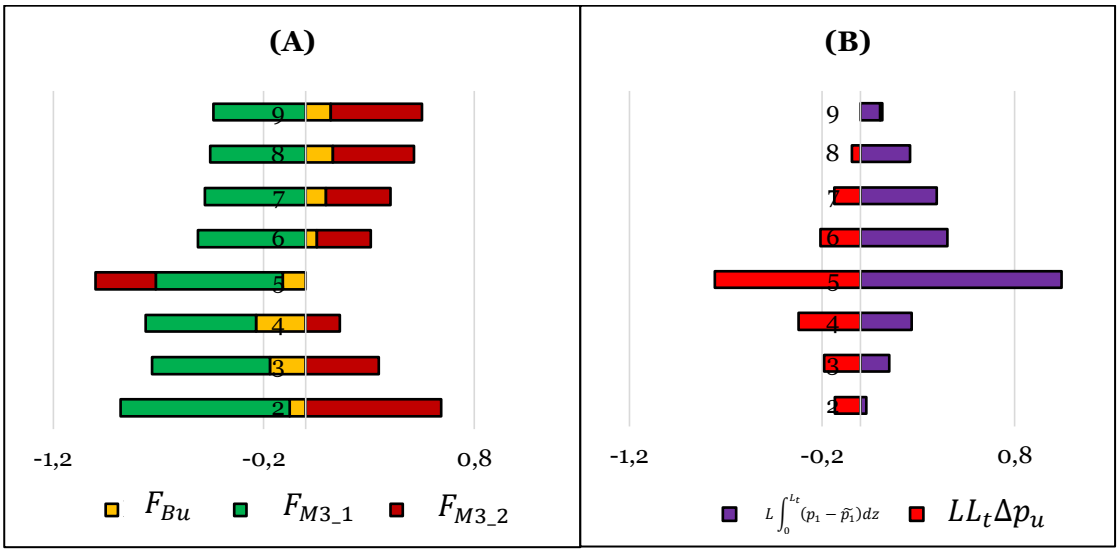

Figure 3-31- Dimensionless components of the forces F_B (A) and F_V (B)

One can notice that the inner bundle force F_{Bu} follows the same shape as F_{UP} (Figure 3-30). This shape is given by the inner lateral cross flow Q_B. The latter tends toward going to the larger gaps (to the left before grid 5, and to the right afterward). Local bundle forces induced by the redistribution upstream from the grid (F_{M3_1} and F_{M3_2}) do not compensate in the first third of the assembly ($F_{M3\_1} > F_{M3\_2}$) so that the total force F_B is oriented to the left hand side. In the top of the FA, $F_{M3\_1} \sim F_{M3\_2}$ so that the sign of F_B is mainly given by F_{Bu}.

Globally, F_{Bu} is quite lower than the other forces laterally. This is due to the test

configuration: only one FA is considered, there are no 'macroscopic' flows within assemblies as one could find in a row of FAs. In parallel, the flow tends toward leaking massively toward the gaps in the bottom of the FA (Figure 3-25), but unequally in function of the gaps width. This is the root of the imbalance between F_{M3_2} and F_{M3_1} before grid 5.

As for F_V, one can see that the term $L\int_0^{L_t}(p_1-\widetilde{p_1})dz$ balances with $LL_t\Delta p_u$ in the bottom of the FA. While $LL_t\Delta p_u$ follows the negative total pressure gradient tendency (the flow is globally 'attracted' to the left where a bigger gap lies), it gets smaller as the flow rides the FA up because the redistribution decreases axially. $L\int_0^{L_t}(p_1-\widetilde{p_1})dz$ is an unnerving force, with such large gaps it tends toward increasing the deflection. When $LL_t\Delta p_u$ gets smaller within the FA last third, $L\int_0^{L_t}(p_1-\widetilde{p_1})dz$ dominates F_V. In other words, as F_{Bu} plays a second order role in the top of the FA (grids 7 to 9), $L\int_0^{L_t}(p_1-\widetilde{p_1})dz$ is the main origin of the FA upper half being deformed to the right hand side (and thus the root of the 'S-shaped' differential deformation).

To further analyze the impact of F_V, let us imagine another test case. We consider the same configuration, but every gap width is reduced by ten. The gaps are now 2 mm wide, and the deformation imposed is 1 mm. As the gap dimensions are reduced to 'nominal' orders, we can set h_l back to 2 cm (median value), and we impose $\chi_{cd}(2\lambda)=\chi_{ext}(\lambda)$. The same value of velocity (5 m/s) was conserved to better highlight the only impact of the confinement.

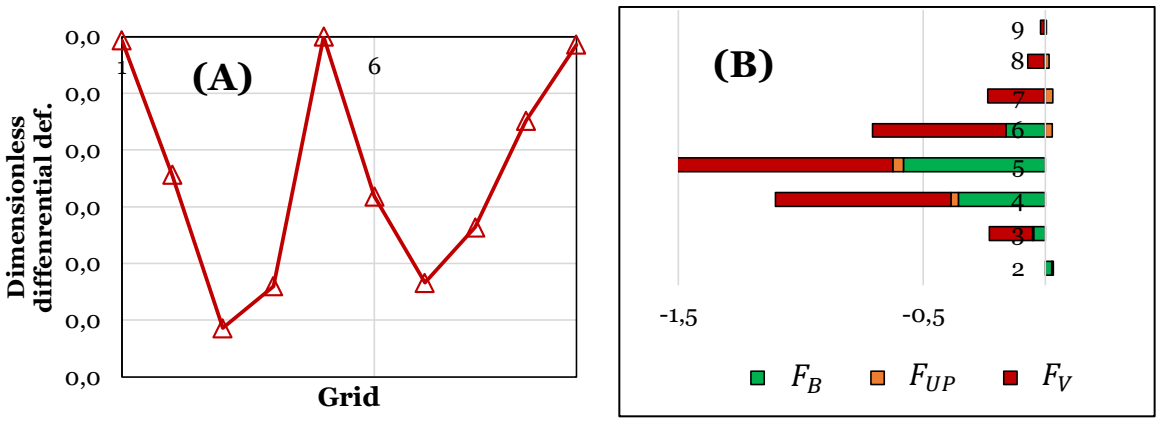

Figure 3-32 - Differential bow of the test case (A) associated forces (B)

It is interesting to note that with this imaginary – more confined – case, the whole deformation is carried by F_V. In this case, F_V does represent a stabilizing force in that it is purely oriented toward the larger gaps. In other words, without the need of detailing the components, one can say that once again F_V is a the root of the final shape of the deformation (one can notice that in the upper half the FA all forces are oriented positively except F_V). Of course, the case has no experimental reference because such a mock-up does not exist. We found out anyway the – gap equalizing - effect behavior of the FA subjected to nominal wall effects as found out in [16] for instance.

6. Partial conclusion

In this section, we introduced our forces models in each component of a FA: F_V and F_B, and F_{UP}. The first one is obtained through pressure profiles in the CD and their integration along the total height $L_t = 2h + H$, while the second one F_B (made of the forces in the inner bundle and upstream from the grid at the h_l scale, respectively named F_{Bu}, F_{Mod3_1} and F_{Mod3_2}) leans on existing works, above all [28] and [9]. It has been shown that it can give proper results when implemented in a network-based model through the MISTRAL experiments. F_{UP}, standing for the upright position force, resulted in forces whose values reached 10^0 to 10^1 N. It is much lower than the other grid force F_V.

Secondly, we looked after experiments performed in the HERMES loop at CEA Cadarache [75]. Not only, our model can produce very satisfying results in terms of deformation, but we also pointed out the impact of the convergent-diffuser related force (F_V) on the final equilibrium state. The change of behavior with a more confined, imagined, situation highlighted this impact. Practically, it was shown that the pressure force on grids (F_V) was not always gap-equalizing (counter-balancing the deformation), as often stated.

As we ensured that both models and forces could give good results at the FA scale, we can come along with a larger scale, *i.e.* the core scale (row of assemblies and full core).

Chapter 4: Using fuel assembly model to depict larger scales behaviors

Highlights of the chapter

- A row of fuel assemblies is set up through lining up single FA models.
- A coupling is proposed with a home-based mechanical code and several inlet/outlet velocity profiles are suggested.
- An accurate knowledge of the flow conditions is necessary to depict the associated pattern of deformations.
- Several methods to extend the simulations to the third dimension are suggested, from the simplest to the more complex.
- The simplest 'row-by-row' method presented in the literature seems appropriate in terms of forces to perform further two-way couplings, on the basis of test cases run with a mini-core.

1. Combining FA models to constitute a row of FAs

1.1. *From one FA to a row of FAs*

In the previous part, we gathered local models to depict fuel assemblies hydraulic and mechanical behaviors through a coupled approach between our own code, Phorcys, and an in-house code developed at CEA. The model highlighted proper results in terms of hydraulics and bow. We also pointed out the role played by the grid force on the resulting shape of the FA bow. In this part, we assemble several FA models into a full row of FAs. This is a next step forward within our commitment to being able to depict hydraulic redistributions at a full core scale. We can yet make a remark about such scales. We do not possess detailed, parametric tests, for such greater scales. It means that no further experimental measures are available at this stage of the project. We can therefore formulate analysis, and compare qualitatively with respect to numerical results.

A row of assemblies (M Floors, N FAs) is schematized in Figure 4-1.

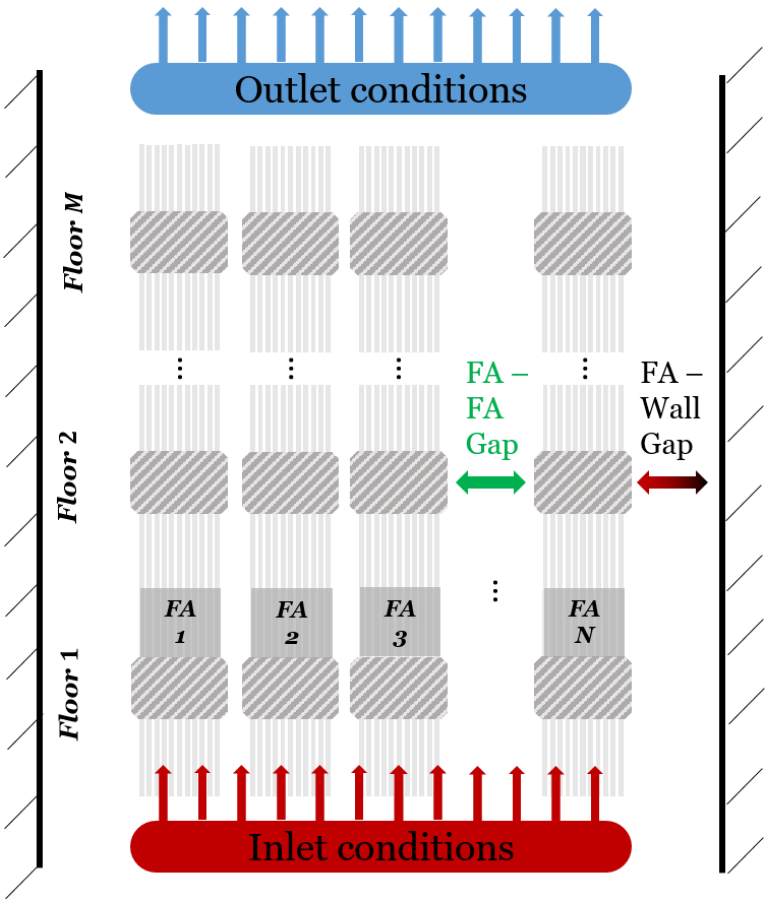

Figure 4-1 - Schematic of a row of FAs

The transition from one FA to a row of FAs is almost direct, because in these conditions, only 2D redistributions are considered and one can simply adjoin a couple of FA networks to build up a full row as done in [50] (Figure 4-2). However, one has to pay a certain attention to its construction.

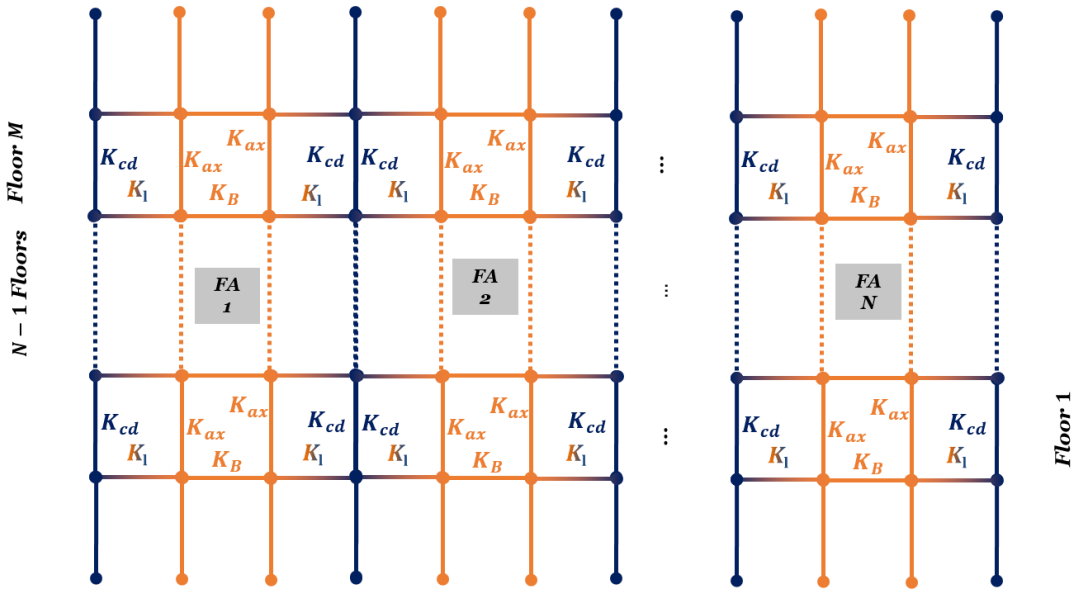

Figure 4-2 - Network for a row of FAs

- Contrary to the FA case, two distinct kinds of bypasses exist. The first one is the inter-grid area (FA-FA gap), it is exactly a convergent-diffuser that has been studied earlier in this manuscript. The second one is a FA-wall kind of bypass. In other words, two conditions on cross-sectional ratios must be considered. The first one stands for $\chi_{\mathrm{cd}}(\lambda)$, and the second one lies in $\chi_{\mathrm{cd}}(2\lambda) = \chi_{ext}(\lambda)$. All gaps are generally of the same order of magnitude (*i.e.* $\sim 2\ mm$). It is the reason why the condition $\chi_{\mathrm{cd}}(2\lambda) = \chi_{ext}(\lambda)$ is necessary, whereas the assumption $\chi_{\mathrm{cd}}(\lambda) \sim \chi_{ext}(\lambda)$ (considered for the experimental tests in chapter 3.5) is not acceptable for such dimensions of gaps. As explained in the previous chapter, it means for instance that if the external gap is 1 mm wide, then a 2 mm convergent-diffuser is solved instead (Figure 4-3).
- Inlet and outlet boundary conditions are necessary given on the full range of the row. Unlike to previous cases where only one FA was concerned, here the flow is injected at the bottom of N FAs, and extracted at the top. In other words, a couple of different adjustments have to be undertaken to fulfill the whole mass conservation within this system. The next section lays emphasis on this point.
- A system composed of N FAs is more unstable numerically than only one FA. It follows that the algorithm of fixed-point coupling must also be adapted. As stood by Horvath [16], it is necessary to correct the algorithm by introducing an under-relaxation term [81]. The latter is such that every single displacement is relaxed through the result of the previous iteration. In the following, we adopted the same method advised in [16]. When exporting the inter-grid widths after a mechanical calculation, the gap λ_i obtained is corrected such as $\lambda_i^{new} = \lambda_i^{old} + \omega(\lambda_i - \lambda_i^{old})$. Where λ_i^{new} is the width at location i which will be transmitted to hydraulics, λ_i^{old} is the width at location i obtained at the previous iteration, λ_i is the width obtained after the mechanical calculation, finally $\omega \in]0,1]$ is the under-relaxation factor (when $\omega = 1$, there is no relaxation).

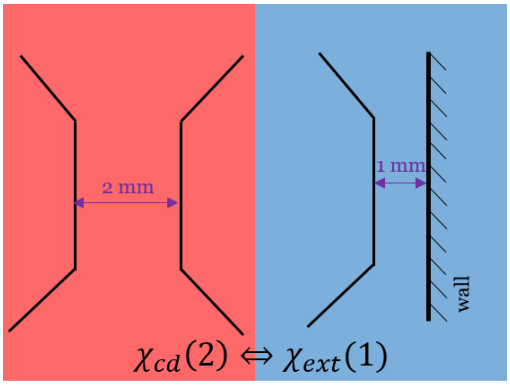

Figure 4-3 - Equivalence of cross-sectional ratio

1.2. *Coping with the boundary conditions*

Boundary conditions are imposed on the top and bottom of the rows. Fostered by the literature, we set about imposing at the same time inlet and outlet velocities. Ideally, we could obtain the latter conditions with coupled calculations between the core, upper and

lower plena as undertaken in [14, 82]. Not only, such calculations are not part of our work, but also they would result in important calculation times at this time. It is the reason why, along with different authors including [16, 22], ideal velocity profiles are chosen. Those profiles usually rest upon findings on the flow within the upper and lower plena. Studies including [13, 14, 15] highlight that the flow in the lower plenum tends toward depicting a revolution paraboloid (axis symmetry), whose maximum can be potentially shifted due to an asymmetry of the pumps [13]. In the upper plenum, studies [17, 16] pointed a symmetry of the flow towards the hot-leg nozzles (plane symmetry). It is why the flow is often assumed to be higher at the center of the lower core. In the upper core, the flow is thus higher on two sides of the core, depicting an axial symmetry.

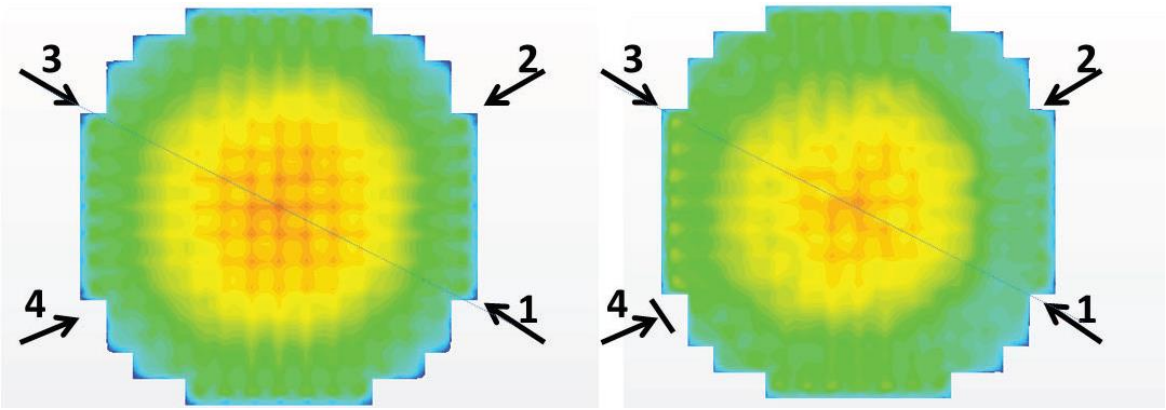

Figure 4-4 - Example of core inlet velocity (color map related to magnitude) for two different cases: unshifted (left), shifted with non-operating loop 4 (right) [13]

In terms of 2D rows, it turns out that the velocities are symmetrical with respect to the median plane of the core (Figure 4-5).

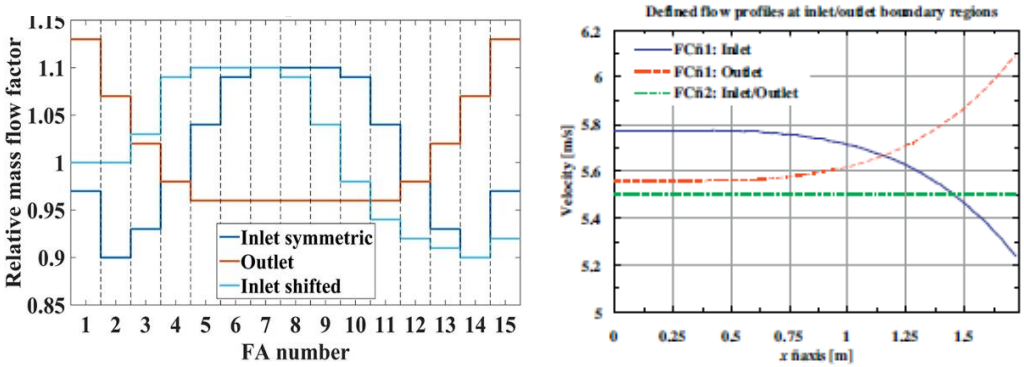

Figure 4-5 - Example of hydraulic top and bottom conditions of velocity in the literature from (left) [9] (right) [16]

In our case, it is also important to note that such conditions are not insignificant.

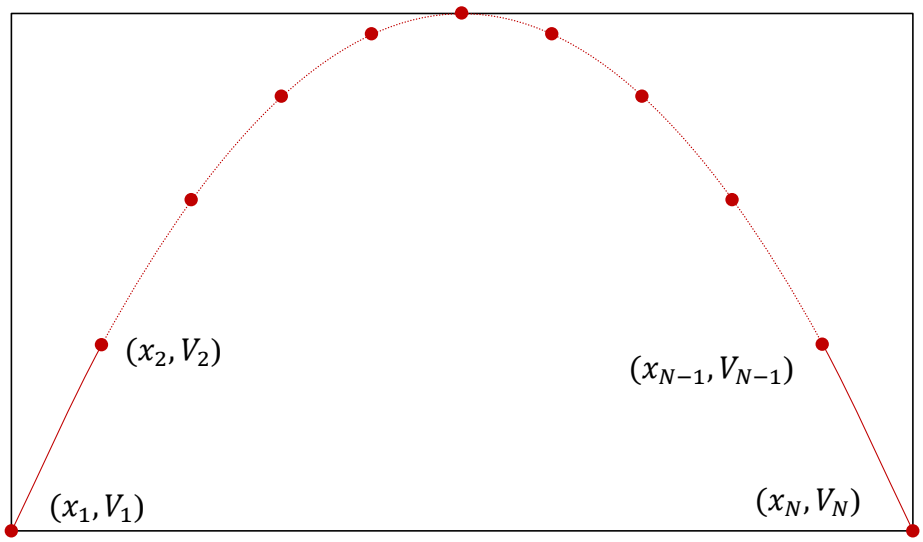

Figure 4-6 - Insight into an inlet profile of velocity and probed velocities (V_1, V_2, …)

We want to impose inlet bulk velocities V_i following a certain analytical curve v (Figure 4-6), which depends itself on a couple of user parameter (mean velocity, min to max ratio, central shift,…):

$$(V_1, V_2, \dots, V_N) = \big(v(x_1), v(x_2), \dots, v(x_N)\big) \qquad \text{(Eq. 4-1)}$$

Where the x_i represent the centers of bypasses and fuel assemblies. We also impose outlet bulk velocities W_i following an analytical curve w.

$$(W_1, W_2, \dots, W_N) = \big(w(x_1), w(x_2), \dots, w(x_N)\big) \qquad \text{(Eq. 4-2)}$$

Even if the bulk velocitiy is prescribed at the bottom and the top, mass flows at inlet and outlet are not guaranteed to be conserved once discretized, in other words:

$$\sum_{i \in inlet} V_i S_i = \sum_{j \in outlet} W_j S_j \qquad \text{(Eq. 4-3)}$$

Where S_i are the associated cross-sections of either bundles or water gaps. In other words it remains a constraint which must be enforced. In order to satisfy (Eq. 4-1) and (Eq. 4-2) with the constraint (Eq. 4-3) a Lagrange multipliers method has been implemented which is used at the beginning of the hydraulic calculation. It consists in setting up the Lagrange function $L = f - \lambda g$, where f is a function to minimize, g is the constraint and λ is a Lagrange multiplier. The solution $(V_1, V_2, .., V_N, W_1, W_2, \dots, W_N)$ is such as $\nabla_{V_1,..,W_N,\lambda} L = 0$. Outlet and inlet conditions are optimized at the same time.

In the following pages, we will intend to analyze patterns of bow with four kinds of boundary conditions, which all have in common to impose a mean velocity of 5.5 m/s:

- Homogeneous conditions ($V = Constant$) at the inlet and outlet.
- Conditions proposed by Horvath [16], following a quartic polynomial (Figure 4-4) – authors considered a half row -.
- Parabolic conditions (max to min ~15% as suggested in [13]).
- Parabolic conditions with shifted entrance.

Figure 4-7 sums up the conditions imposed and optimized beforehand with Phorcys. Although optimized points look like they fall upon the demanded curves, it is not strictly the case. The very small differences (valued at most 1%) allow to enforce mass conservations throughout the core.

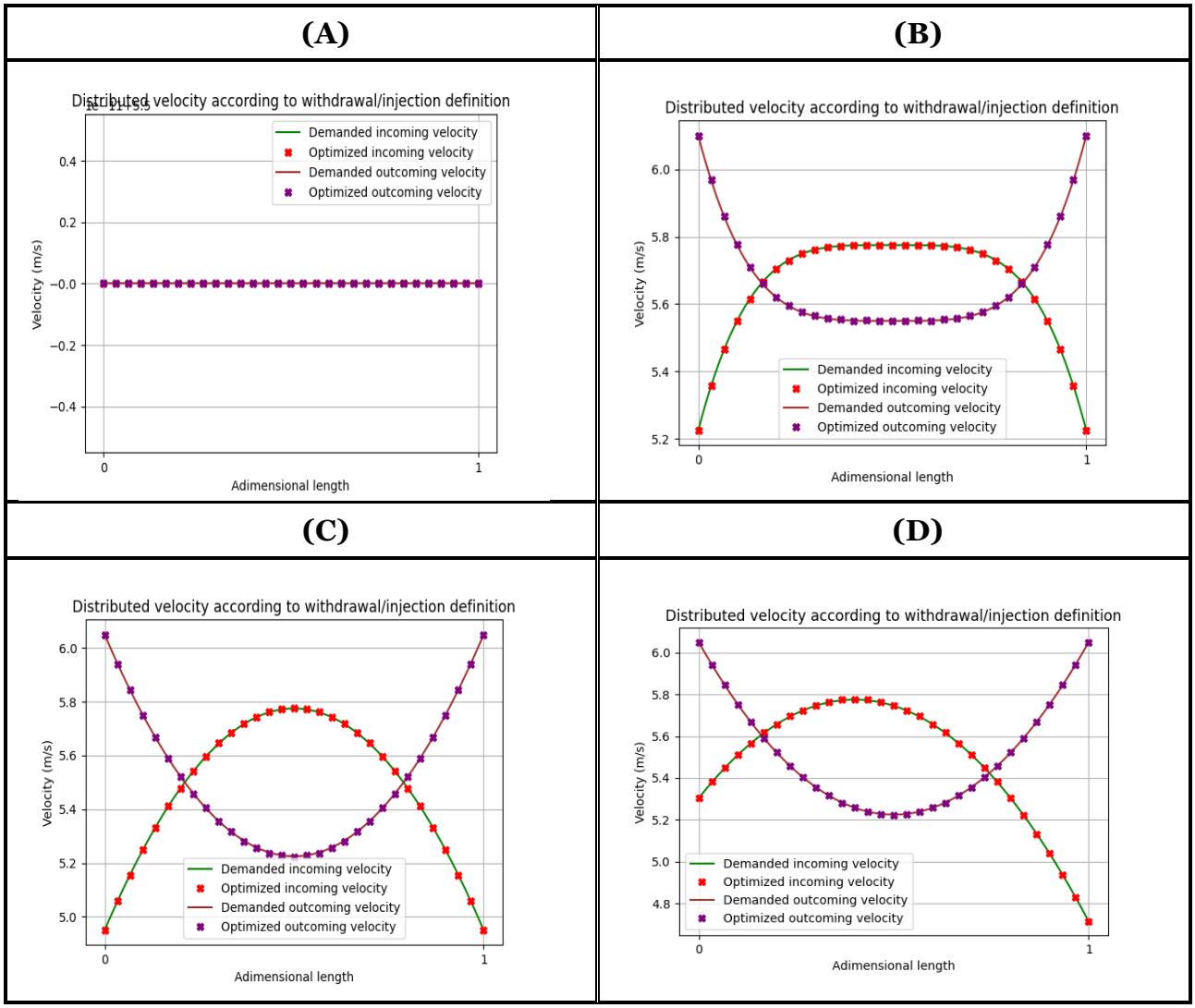

Figure 4-7 - (A) Homogenous conditions (B) Horvath's conditions (C) parabolic conditions (D) Shifted conditions

2. Analysis of a couple of different hydraulic conditions

2.1. *Homogenous conditions (A)*

The interest of homogeneous conditions is that no redistribution due to the shape of

the profile occurs. The only redistributions are due to the difference in terms of axial loss coefficients between the bypasses wall-FA and FA-FA.

The results are highlighted in Figure 4-8. The frames, given by Phorcys, are always organized as follows: at the top we find the forces at each floor (grid + bundle) (forces at iteration 1 in hatched lines and at equilibrium in plain colors) and at the bottom we find the associated deformations (dotted lines draw deformations at iteration 1 and full lines depict the deformation at equilibrium). Nominal gaps (2 mm) are defined between the FAs.

In Figure 4-8 we find out the forces and deformations for homogeneous velocity profiles.

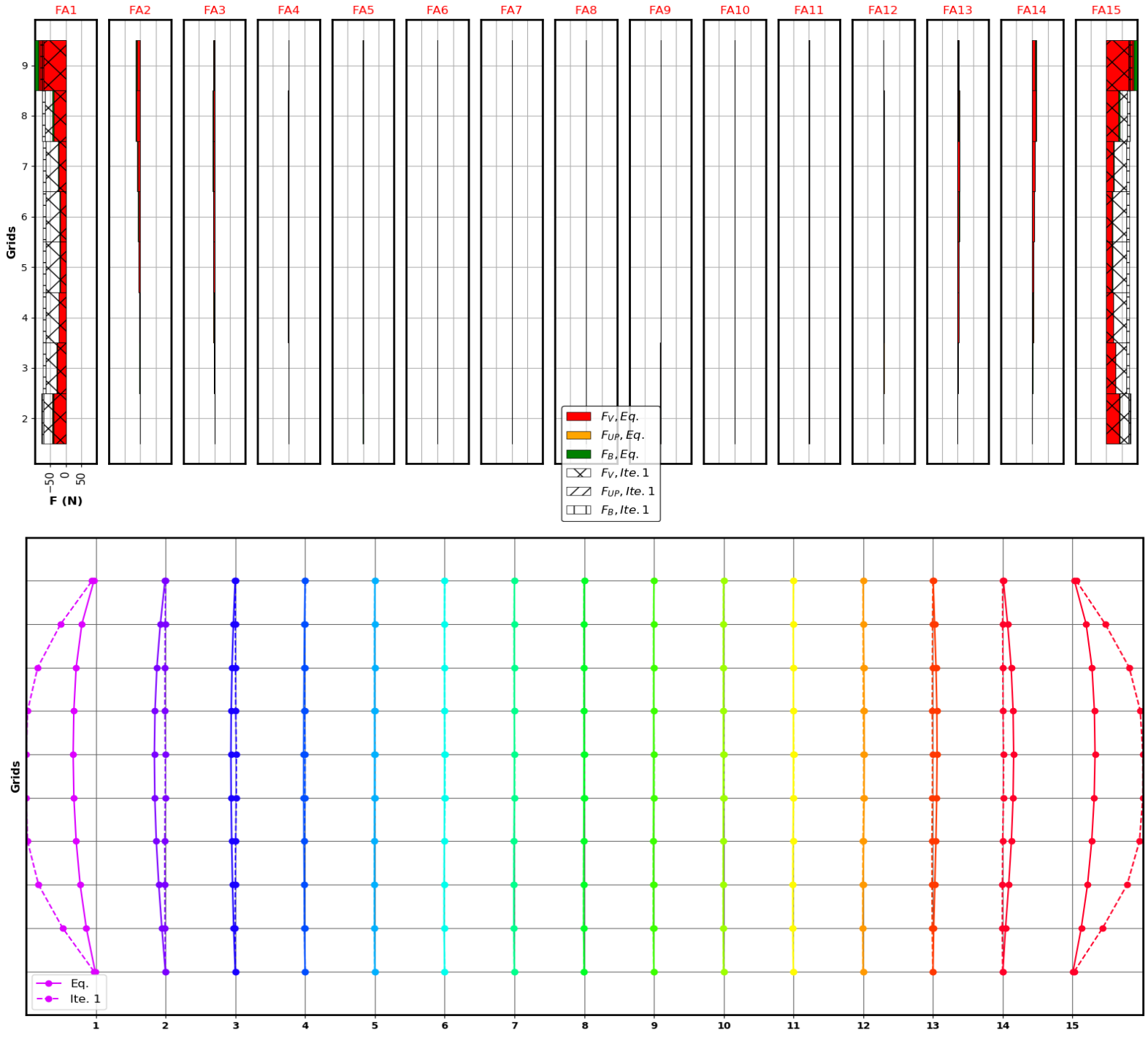

Figure 4-8 - (Top) forces (bottom) deformations – Condition A

The results are very similar to the one already highlighted by Horvath. This configuration explicitly points out an impact of one-way and two-way couplings. The one-way coupling overestimates importantly the deformations such as external FAs touches upon the walls. Also, only the external FA is being deformed – strongly -, while the others undergo very small forces. As the iterations go on, the assemblies 2 to 14 progressively undergo forces due to the initial deformations of assemblies 1 and 15. As a result, at equilibrium, every FA is being deformed (with the highest deformation at the walls and the lowest at the center). Two remarks can consequently be made. Considering two-way coupling is important as it depicts a much different pattern of deformation, and homogeneous conditions can bow the row on their own. It is important to note that only deviations of pressure loss between wall-FA and FA-FA tends toward bowing the core following a 'barrel' pattern. Once again, the same conclusions were formulated in [16].

In terms of forces, grids forces are much higher than bundle related forces. It is also a trend noticed in [16]. This tendency is explained by low macroscopic redistributions in the core, the only local redistributions being explained by the deviations of axial losses between the wall and external FAs. Thus, we find out similar patterns with a – much faster - network approach (Horvath used a CFD approach).

2.2. *Horvath's conditions (B)*

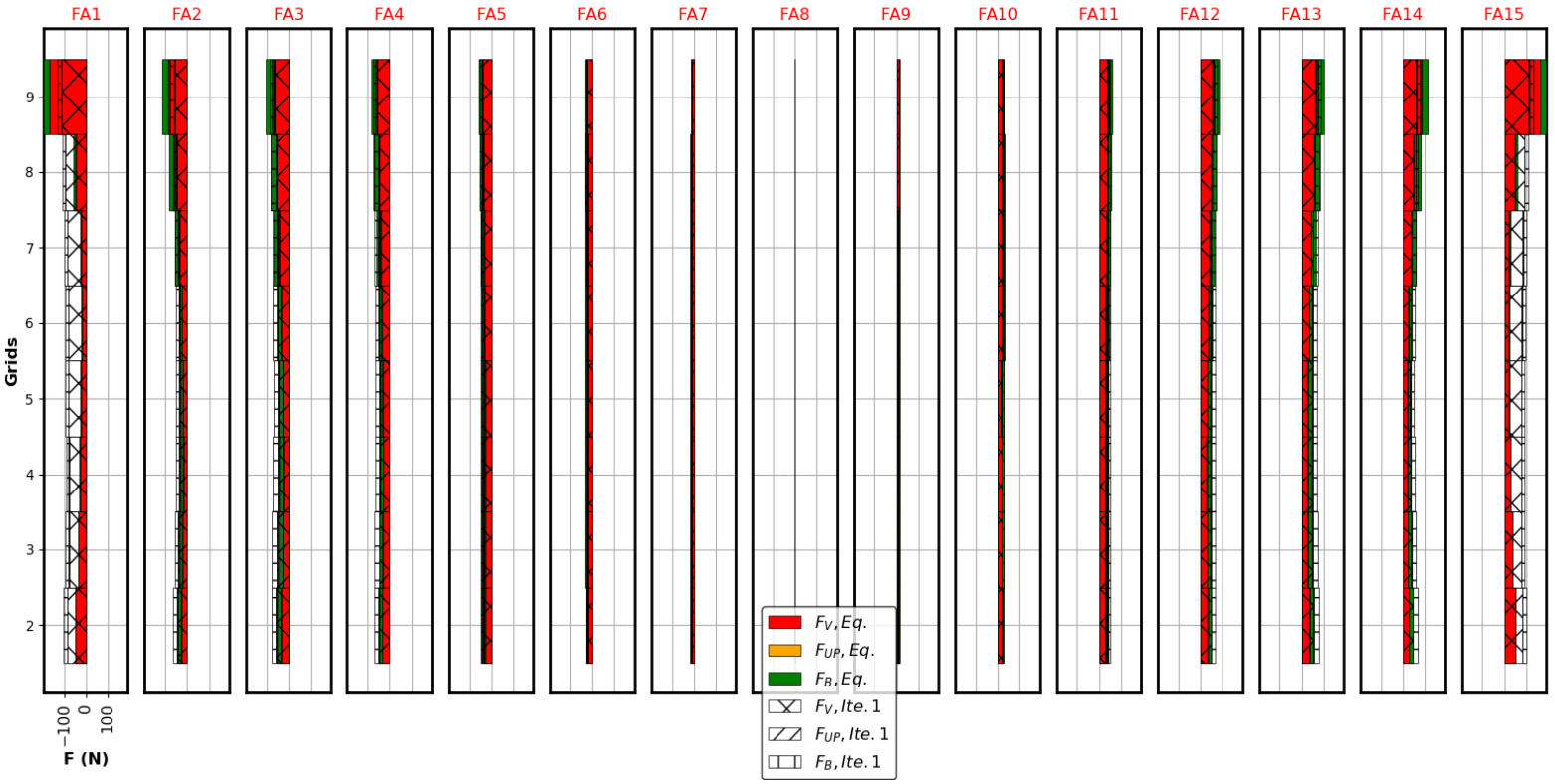

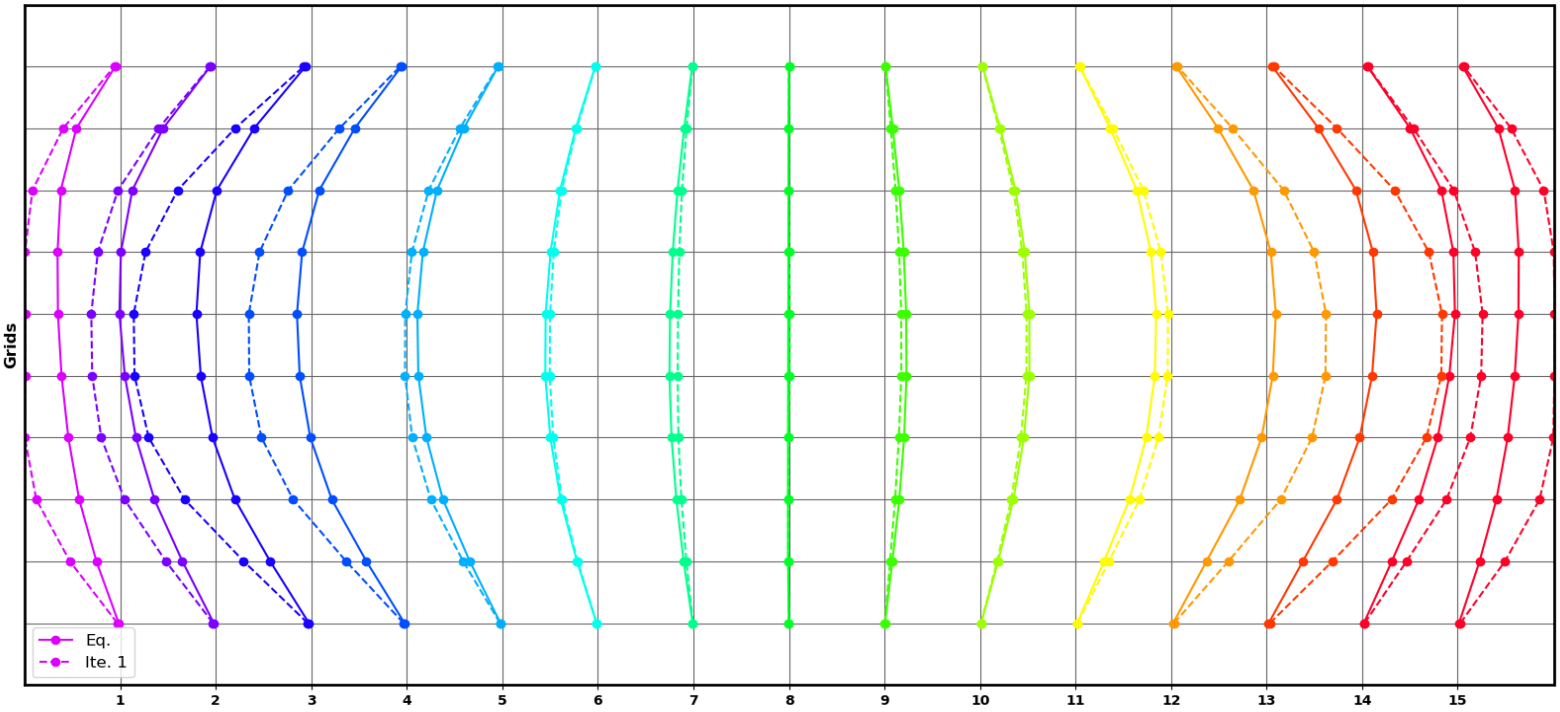

Figure 4-9 - (Top) forces (bottom) deformations – Condition B

In Figure 4-9, we considered boundary conditions as considered by Horvath, its model of profile being findable in [16]. Unlike previous homogeneous conditions, all assemblies are deformed at first iteration. FAs 1 to 4 and 12 to 15 are strongly bowed, whereas assemblies 5 to 11 are less impacted. This is due to the gradient of velocity being quite important at the core left and right borders. External fuel assemblies also close external gaps (FA-wall) at first iteration. At equilibrium, deflections are reduced compared to iteration 1 even though they remain higher than deflections at homogeneous conditions. The latter remark has also been pointed out in [16]. A maximum gap of 3 mm is found out between assemblies 5 and 6 at mid-height. The overall pattern of deformations is once again a 'barrel' pattern. In terms of forces, they are obviously higher than the ones relying on homogeneous velocity profiles. It is interesting to note that bundle forces are almost as important as grid forces for FAs 2 to 4 and 12 to 14 where the profiles gradient is the highest. Grid forces are very important compared to bundle forces regarding external FA, as noticed for homogeneous condition. This comes from the fact that these locations include the greater gradient in terms of λ distribution (1λ for FA-FA gaps, and 2λ for FA-wall gaps to take into account the half-CD). However, this grid 'superiority' at the core shroud was also highlighted in the author's results [16].

Once again, our semi-analytical models can depict very well the shapes noticed in the literature with a lower computational cost. As agreed with Horvath, a two-way coupling between mechanics and hydraulics seems necessary not to overestimate the bow pattern compared to one only path from hydraulics to mechanics.

2.3. *Parabolic conditions (C)*

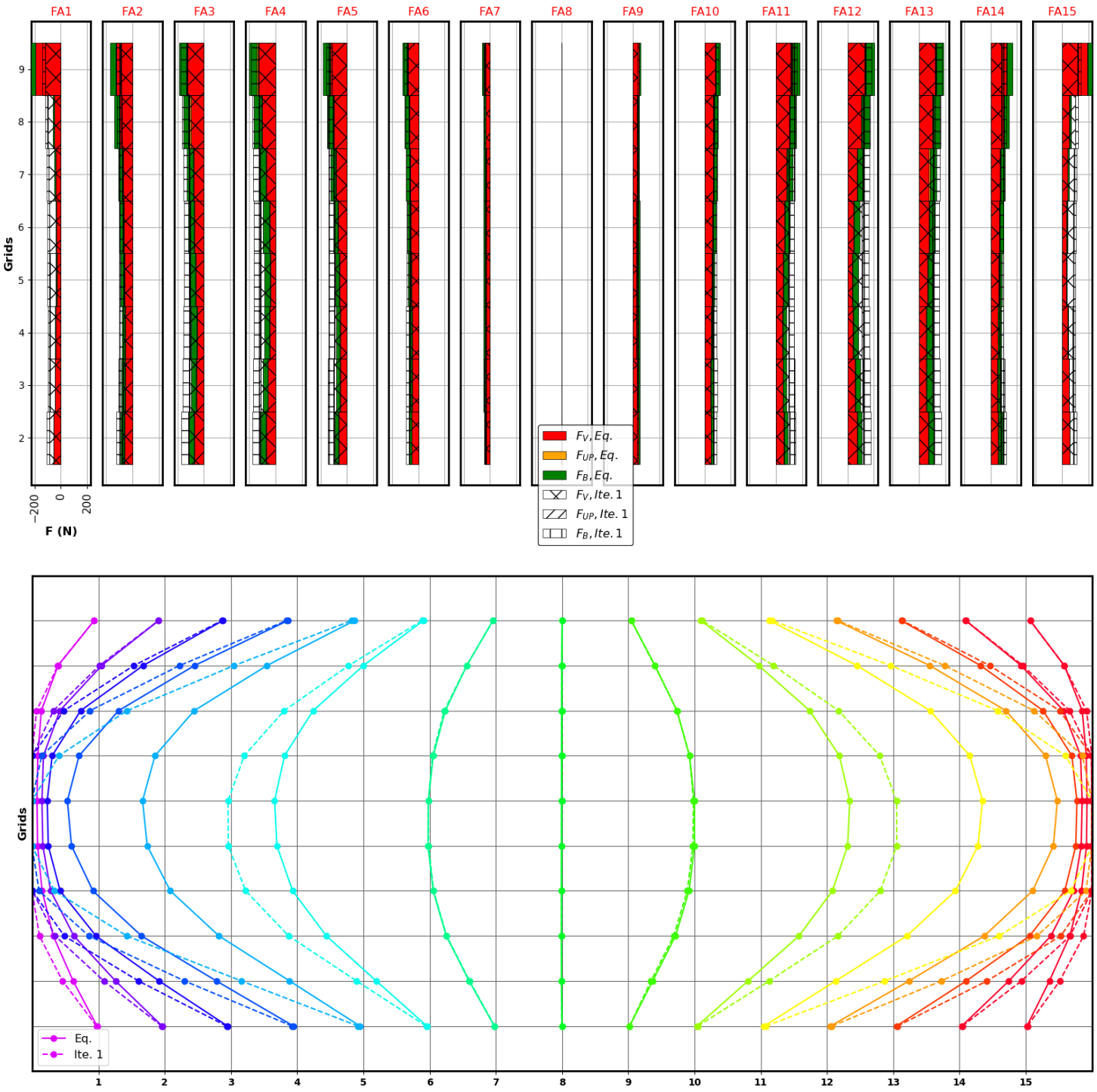

Figure 4-10 - (Top) forces (bottom) deformations – Condition C

In Figure 4-10 we find out the forces and deformations for an ideal parabolic velocity profiles. The results give very different results. Again, converged deflections are reduced compared to the first iteration. It is interesting to note that this time 5 gaps are closed, after

the 1st iteration, on each side of the row, and 4 gaps remain almost closed at equilibrium ($\lambda \sim 10^{-4}\ m$). The latter phenomenon is also linked to higher forces. A maximal gap of 5 mm is found out, located between FAs 9 and 10 (and 5/6), at mid-height. 28 gaps possess gaps overtaking 4 mm, principally situated around the first and last quarter of the row. In other words, a great number of gaps have more than doubled with these hydraulic conditions.

In terms of forces, the pattern is similar to the previous case. Higher forces are found on the top and bottom of the assembly, coherent with [22, 16]. As mentioned, the parabolic conditions involve higher forces, most likely because the velocity gradient is more widely distributed (from 4.9 m/s at the wall bypass to 5.8 m/s at the row center) than with the flattened profile of Horvath. Between the first and last quarter of the row, bundle and grid forces have the same order of magnitude. In addition, grid forces seem higher at the shroud vicinity.

Globally, deflections seem to be very dependent on the velocity profiles, and a concrete knowledge of the boundaries seems necessary to fully depict the whole pattern (number of closed gaps, maximal and minimal mechanical deflections …). Yet, parabolic profiles could be seen as a mean to study macroscopic, qualitative tendencies at the core scale.

2.4. *Shifted conditions (D)*

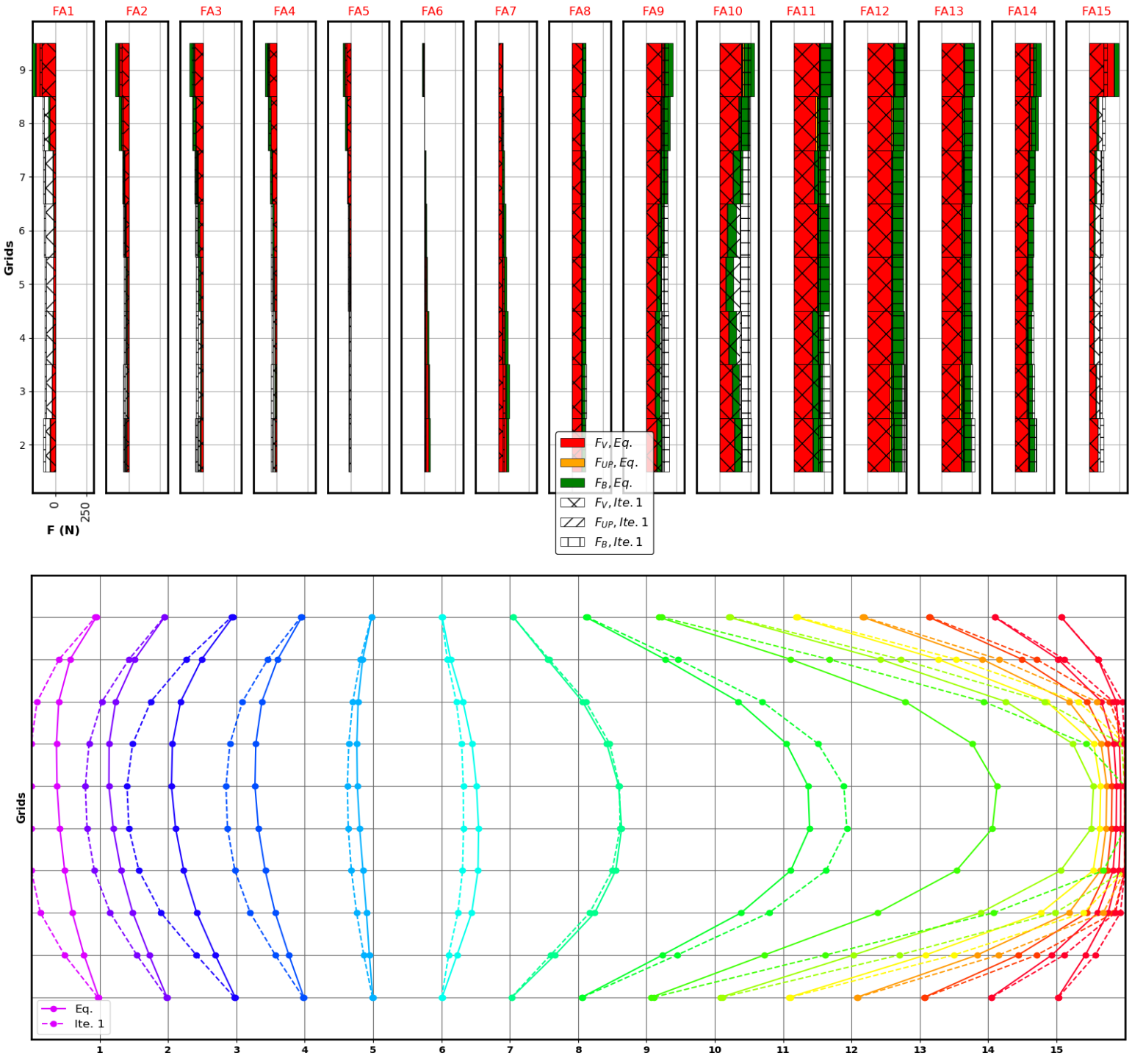

Figure 4-11 - (Top) forces (bottom) deformations – Condition D

In Figure 4-11, a shifted inlet profile of velocity is imposed compared to the previous condition (C). One can notice that the deformation tends to 'flee' the maximum of the entrance profile. In other words, maximal deflections are found at the right hand side of the row, whereas the maximum of the profile was shifted to the left. This effect is particularly important, given that 6 gaps are closed at the right hand side ($\lambda \sim 10^{-4}\ m$). At first iteration 7 gaps were closed. Once again, iterations reduce deflections. At the left hand side, the FAs

are much less impacted (no contact at all). This is due to the maximum velocity being shifted to the left: we noticed that less bow was noticed in the vicinity of the maxima. An interesting shape is the one on FA5. Its maximal deflection is clearly shifted to the top no longer at mid-plane. This FA is a witness of the boundary conditions: maximum of entrance at its foot, thus almost no forces all way down its first half, and 'normal reversed' conditions at its top, and thus forces exist only in the second half. 28 gaps are higher than 4 mm, exactly like with (C) conditions, but the highest value reaches almost 6 mm, it is 1 mm more than the highest value reached with (C) conditions. The pattern is very similar to the one obtain by Wanninger at beginning of cycle with a shifted inlet velocity.

In terms of forces, once again they are globally maximal at the top and bottom of the FAs (with the higher forces at the top), except FA4 to 7 whose forces are either higher at the top or at the bottom with respect to the boundary conditions. Forces at the right hand side are almost doubled with comparison to the left hand side ones. The latter remark is certainly due to the fact that the gradient of inlet velocity is higher at the right hand side given the shifted profile.

In conclusion, with a macroscopic network-related approach, we reach satisfactory patterns in a reduced amount of time – always limited by the mechanical solution time -. Thus, even if a precise knowledge of inlet and outlet conditions is necessary to reach a satisfactory state of equilibrium, 'ideal profiles' of velocity let us observe qualitative bow patterns. This approach could be judged reliable to give insights for sensitivity analyses, for instance in terms of hydraulic conditions, as we have done in this section. Its quantitative validation holds in the appreciation of real measures, which are inaccessible at this time. A future experiment which will be run at the CEA with 3 FAs (similar to the one explained in [83] in the PETER loop), could give measures to validate quantitatively the semi-analytical models developed at a row scale.

3. From the row to the full core

This section is a prospective work regarding possible methods to extend the 2D hydraulic description of the FAs to a full core. At this stage, no coupling has been performed between hydraulics and mechanics.

3.1. *Method 1 – state-of-the-art – the 'row-by-row' model*

The use of hydraulic network models for simulating FSI systems in nuclear reactor cores was grounded in the works of Stabel [50, 22]. The authors explained how to take the global hydraulic behavior of one fuel assembly into account through a preliminary calibration process with CFD simulations and experimental measures. Their models have then been extended to simulate planar rows of fuel assemblies.

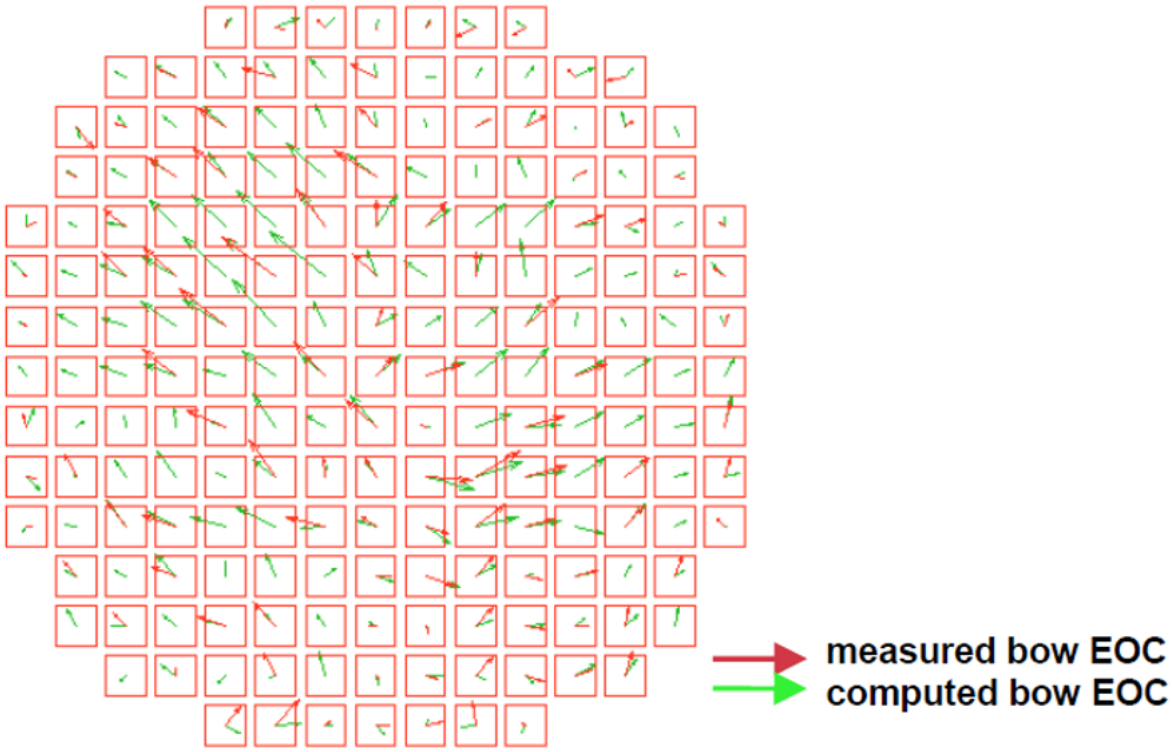

Figure 4-12 - Bow pattern at the end of the cycle measured and computed, from [50]

However, estimating the forces on a 3D basis is not that simple. The approach developed in [50] (further called the Row-By-Row approach or Method 1), is based on the sweeping of all rows in one core. It is explained as the following: 'a total core may be represented by a number of row models oriented parallel to the two orthogonal directions of the core'. In other words, by sweeping over all rows in one core, it is possible to find every behavior along the x- and y- axis. Stabel adds 'Hereby it is assumed that the two directions may be treated independently on each other. This is a strong assumption which must be justified a posteriori by comparison between simulation results and measurement results of bent FAs'.

The author tried the approach out on a 1300 MWe-like type of reactor (max of 15 assembly per row, i.e. 2x15=30 rows to compute), which led to good agreement with core measurements (see Figure 4-12). This model can be thus justified along with the hypothesis adopted (independence of the two orthogonal directions laterally in the core). According to Stabel, the model allowed to get the bow macroscopic characteristics back 'such as core bow patterns, amount and distribution of bow amplitudes, relationships of bow to FA types or fuel management schemes'. This approach is the most intuitive that can be found out to obtain the two components of lateral forces on each assembly's floor.

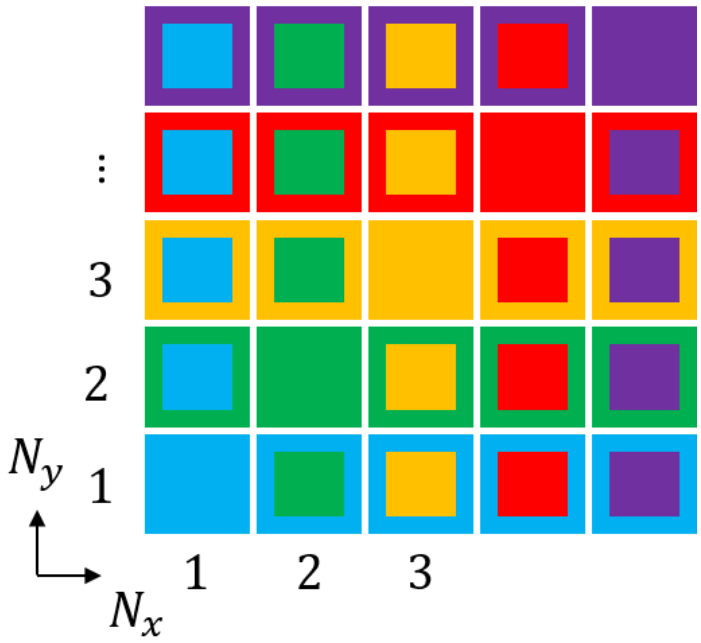

Figure 4-13 - Layout of the successive hydraulic calculations, rows N_x are indicated through the filling color, rows N_y are indicated through the line color

Figure 4-13 shows the outline of the method as implemented in our own code. The idea is to split the system in vertical and horizontal rows along the x- (N_y rows) and y- axis (N_x rows). For instance, all fuel assemblies depicted with green-filled cells belong to the row $N_x = 2$, as well as cells framed with yellow belong to the row $N_y = 3$. Therefore, single color cells belong to rows fulfilling the condition $N_y = N_x$.

Hydraulic calculations are performed on every row, in the two orthogonal directions, and the related forces are exported in separate files for each row. When all files are available, the reconstruction of the two components is initiated. Let F be a lateral force defined by $\vec{F} = \overrightarrow{F_x} + \overrightarrow{F_y}$, with $\overrightarrow{F_x}$ and $\overrightarrow{F_y}$ the two components along each axis.

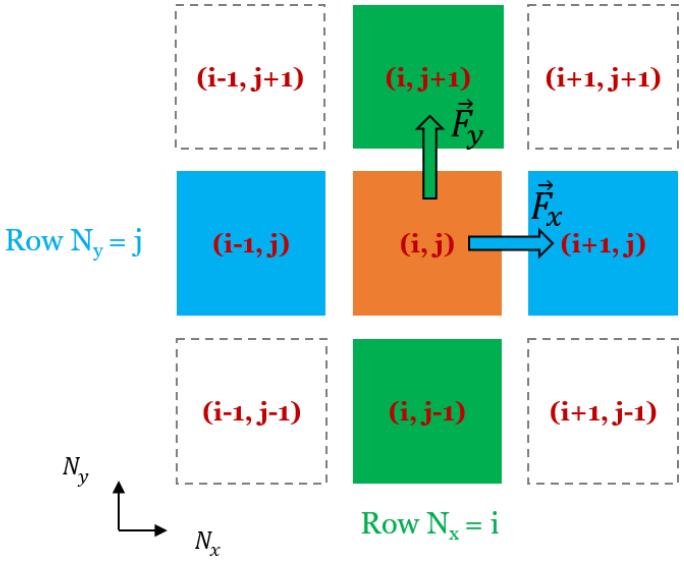

Figure 4-14 - Layout of the two components reconstruction (in orange, FA (i,j); in green, FAs in row $N_x = i$; in blue FAs in row $N_x = j$; in white, unused FAs for (i, j) force calculations)

If one considered the forces that apply on fuel assembly (i,j) (see the associated cell in Figure 4-14). Then, the component F_x is obtained through the results of cell (i,j) in row $N_y = j$ (in blue). This method resting upon the main assumption that the two orthogonal directions may be treated independently of each other, white cells (the ones on the diagonals) have no impact on the reconstructed force in cell (i,j) as they belong neither to row $N_x = i$ nor to row $N_y = j$.

3.2. *Method 2 – 3D redistribution – coolant flowing in straight lines*

The next method is similar to the row-by-row method, and more thorough at once. Its likeness lies in the assumption that the fluid flows along the two separate orthogonal directions, but these directions are coupled inside the FA (not in the water gaps).

The graph is equivalent to the 2D approach in the x- and y- directions (see Figure 4-15). Nevertheless, every cross-section parameter (*e.g.* S_g, S_l, ...) must be adapted as the network contains now four nodes in each FA. Consequently, from now on, every axial and lateral cross-sections are divided by two.

As the coolant is supposed to flow in straight lines, elements based on K_B and K_l (both based on the Eole correlation [28]) only depends on the associated axial elements to which they are bounded. In other words, resistances are only defined in the planes $(\overrightarrow{e_x}, \overrightarrow{e_z})$ and $(\overrightarrow{e_y}, \overrightarrow{e_z})$ and their expression does not change comparatively to the 2D case (chapter 3).

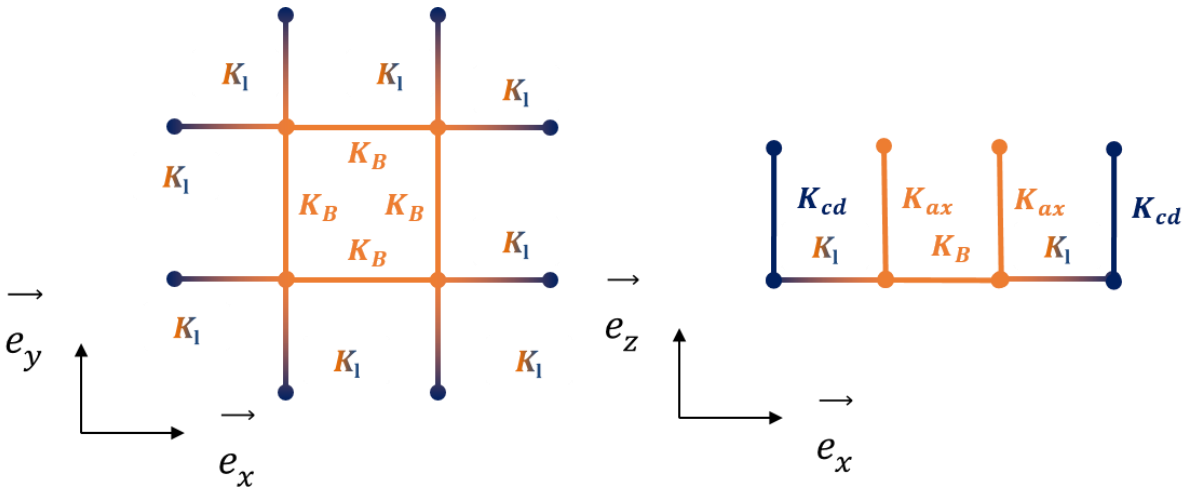

Figure 4-15 - Elementary fuel assembly for 3D redistribution

An example of a whole hydraulic network obtained for a 3x3 cluster of fuel assemblies is available in Figure 4-16.

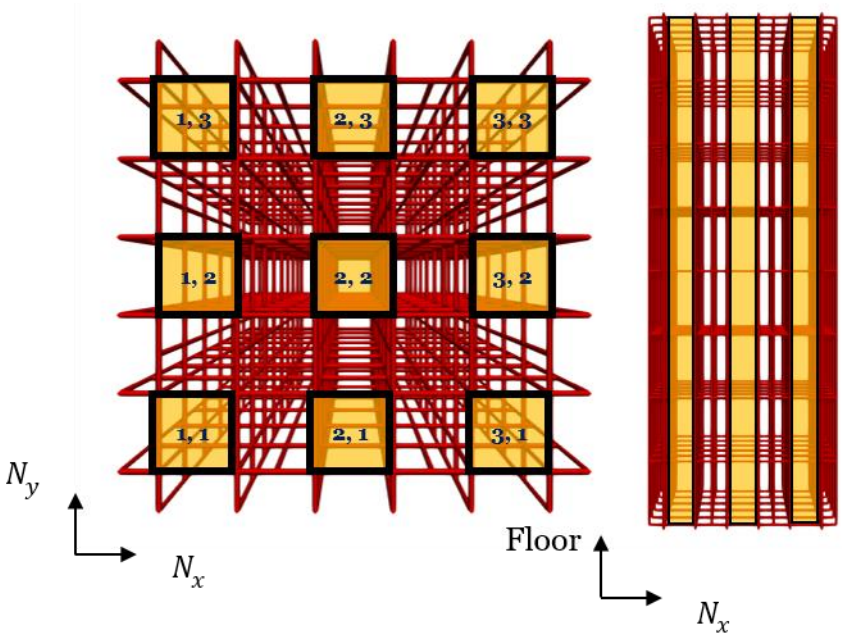

Figure 4-16 - 3D 3x3 cluster of fuel assemblies (view from Paraview)

Fuel assemblies depicted in Figure 4-15 are colored in orange. One can notice that this cluster is made up of nine elementary fuel assemblies gathered together end-to-end.

At this point a remark should be set up on how energetic equations should be implemented in those particular 3D systems. The problem's outline is illustrated in Figure 4-17 as a practical example.

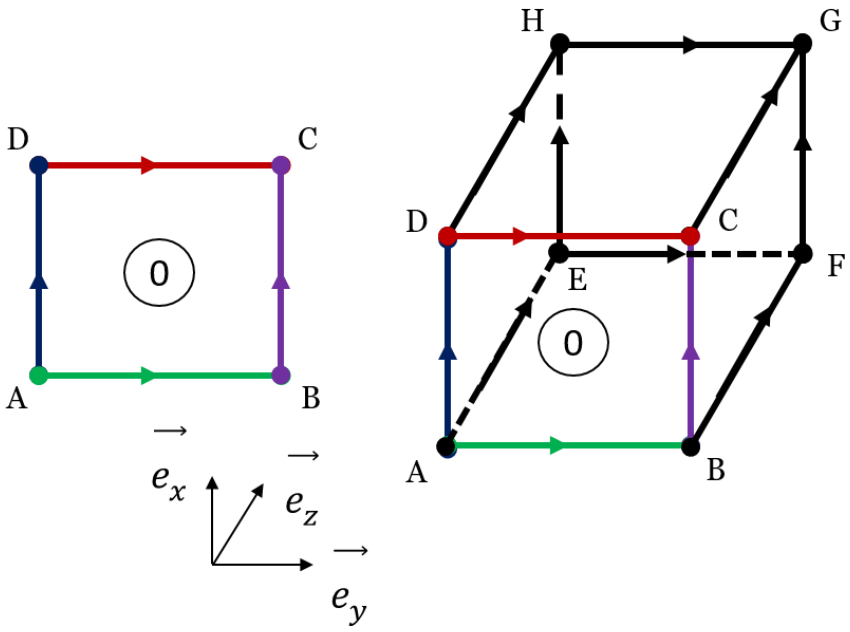

Figure 4-17 - Planar loops equation (left), 3D loop equations (right)

At the left hand side of the Figure 4-17 a simple 2D network's loop is highlighted, its energetic equation (0), is the following:

$$\Delta P_{AB} + \Delta P_{BC} - \Delta P_{CD} - \Delta P_{AD} = 0 \qquad \text{(Eq. 4-4)}$$

Where ΔP_i stands for the pressure drop in section i. Orientations are both indicated through arrows in the figure. Moreover, $N_N = 4$ nodes equations (mass conservation) can be drawn out of the system, for a total of 5 equations. One node is actually redundant, if N_N is the number of nodes, N_L the number of loops and N_E is the number of elements (branches), the Euler formula tells us that for a connected planar graph, $N_L + N_N = N_E + 1$ (see Appendix F). We can thus show that one node equation can be written as a linear combination of the others.

The right hand side of the Figure 4-17 is the same network but 3D – extruded along the z-axis. If one simply applied the Euler formula above, he would surely find a deviation of 1 between both sides of the equation. The problem is that this classic formula is not available for non-planar graphs.

However, diving into the loop equations can enlighten us about such a deviation. They are the following on every face except (0).

$$\begin{cases} \Delta P_{EF} + \Delta P_{FG} - \Delta P_{GH} - \Delta P_{EH} = 0 \\ \Delta P_{BF} + \Delta P_{FG} - \Delta P_{CG} - \Delta P_{BC} = 0 \\ \Delta P_{AB} + \Delta P_{BF} - \Delta P_{EF} - \Delta P_{AE} = 0 \\ \Delta P_{AD} + \Delta P_{DH} - \Delta P_{EH} - \Delta P_{AE} = 0 \\ \Delta P_{CD} + \Delta P_{CG} - \Delta P_{GH} - \Delta P_{DH} = 0 \end{cases} \qquad \text{(Eq. 4-5)}$$

Combining (1)-(2)+(3)-(4)-(5) we obtain:

$$\Delta P_{AB} - \Delta P_{BC} - \Delta P_{CD} - \Delta P_{AD} = 0 \qquad \text{(Eq. 4-6)}$$

Which is the equation of loop (0). In other words, extruding the network in 3D leads to one loop equation which is a linear combination of the other loop equations. Extruding again along the z-axis would lead to the EFGH loop being redundant, and so on so forth by recurrence.

Consequently, for a 3D network extruded along the z-axis, we will need all loops parallel to the planes $(\overrightarrow{e_x}, \overrightarrow{e_z})$ and $(\overrightarrow{e_y}, \overrightarrow{e_z})$, and only one layer of loops parallel to the plane $(\overrightarrow{e_x}, \overrightarrow{e_y})$, all the other layers being linear combinations of the other loops present in the system.

3.3. *Method 3 – 3D redistribution – no lateral flow in the bypasses*

The network is the same as presented in Figure 4-15. We take into account 3D effects inside the bundle by adapting the lateral resistances based on the Eole correlation [28]. The aim is to consider oblique flows across the bundle no longer within independent, orthogonal planes, but in all three directions at the same time.

As a reminder, a lateral pressure drop based on this correlation is based on the following equation:

$$\Delta P(\theta) = \frac{\rho N K_{\perp} \xi(\theta) \beta^2}{2 S_L^2 \sin(\theta)^2} Q_L^2 \qquad \text{(Eq. 4-7)}$$

With θ being defined as the following:

$$\theta = \begin{cases} \tan^{-1}\left(\dfrac{S_1 |Q_L|}{S_L |Q_1|}\right) & if\ Q_L > 0 \\ \tan^{-1}\left(\dfrac{S_2 |Q_L|}{S_L |Q_2|}\right) & if\ Q_L < 0 \end{cases} \qquad \text{(Eq. 4-8)}$$

With (Q_1, S_1) and (Q_2, S_2) being respectively the flow rates and axial cross-sections in the axial elements departing at the starting node and ending node (chosen by convention) of the bundle. (Q_L, S_L) is the cross flow and the related lateral cross-section (L = B for inner-bundle or l for outer-bundle).

Resting upon [84] and [85], a modification of the expression can be undertaken to consider 3D effects. Butterworth, based on porous media accounts, pointed out that the addition of a $\cos(\phi)$ factor seemed adequate to depict the pressure drop produced by an inclined flow rotated around the bundle of cylinders. In our example (see Figure 4-18), ϕ is the flow angle of incidence with respect to the bundle horizontal plane.

As a result, the general form of the bundle pressure drop seen by Q_L is the following:

$$\Delta P(\theta) = \frac{\rho N K_\perp \xi(\theta) \beta^2}{2 S_L^2 \sin(\theta)^2} \cos(\phi)\, Q_L^2 \qquad \text{(Eq. 4-9)}$$

Where $K_\perp$ also becomes a function of ϕ, as the norm of the velocity now includes the transverse velocity v_t.

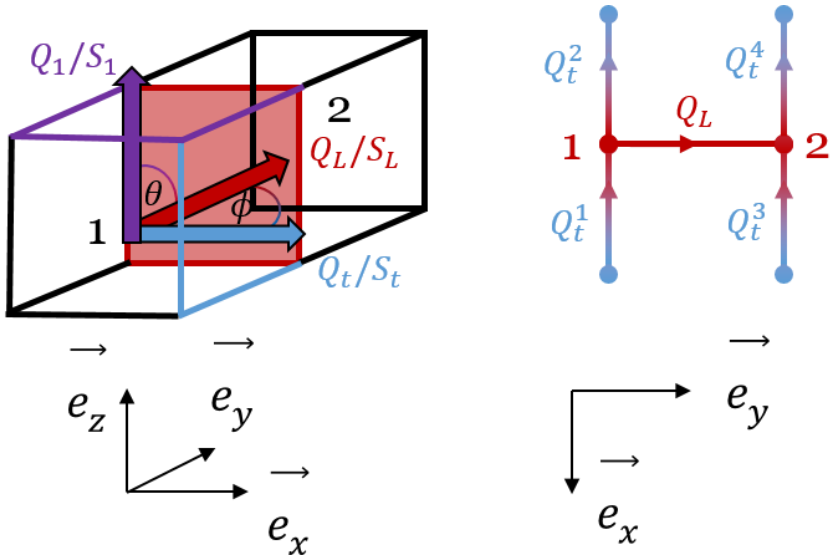

Figure 4-18 - Bundle crossing from volume 1 to volume 2 (left), associated network in the plane $(\overrightarrow{e_x}, \overrightarrow{e_y})$ (right)

To calculate v_t, which will be used to calculate ϕ and the norm of the velocity, let us consider the network depicting the bundle crossing in Figure 4-18. The conventions in terms of flow direction are indicated through arrows. First, we need to choose the right flow rates Q_t. To do so, we need to check the sign of Q_L. If Q_L is positive (node 1 to node 2 by convention), we will analyze the sign of the transverse flow rates linked to node 1 *i.e.* Q_t^1 and Q_t^2; otherwise if Q_L is negative (node 2 to node 1) we will analyze the sign of the transverse flow rates linked to node 2 *i.e.* Q_t^3 and Q_t^4. Once the right node is isolated, we need to consider the flow rates leaving the node. To explain this step, let us consider that Q_L is positive, so the flow crossing the bundle is going from 1 to 2. In this case, the two transverse flow rates related to the pressure loss are Q_t^1 and Q_t^2 as explained above. From here five cases are possible.

- If Q_t^1 and Q_t^2 are both positive, then it means that only Q_t^2 is leaving node 1 and stands as the only candidate for determining v_t.
- If Q_t^1 and Q_t^2 are both negative, it means that only Q_t^1 is leaving node 1 and stands as the only candidate for determining v_t.
- If Q_t^1 is negative and Q_t^2 is positive, it means that both Q_t^1 and Q_t^2 are leaving node 1 and stand both as candidates for determining v_t.
- If Q_t^1 is positive and Q_t^2 is negative, it means that no transverse flow rate is leaving

node 1 and consequently that v_t is null.

- If elements related to Q_t^1 and Q_t^2 do not exist at all (if node 1 is a bypass node for instance, where lateral flows are not allowed by this method), then v_t is consequently null.

Once candidates for v_t have been identified on the basis of the node 1 way out, the v_t calculation relies in Figure 4-19. Node 1 is indicated in black, and every flow rates candidate are shown along their cross-sections.

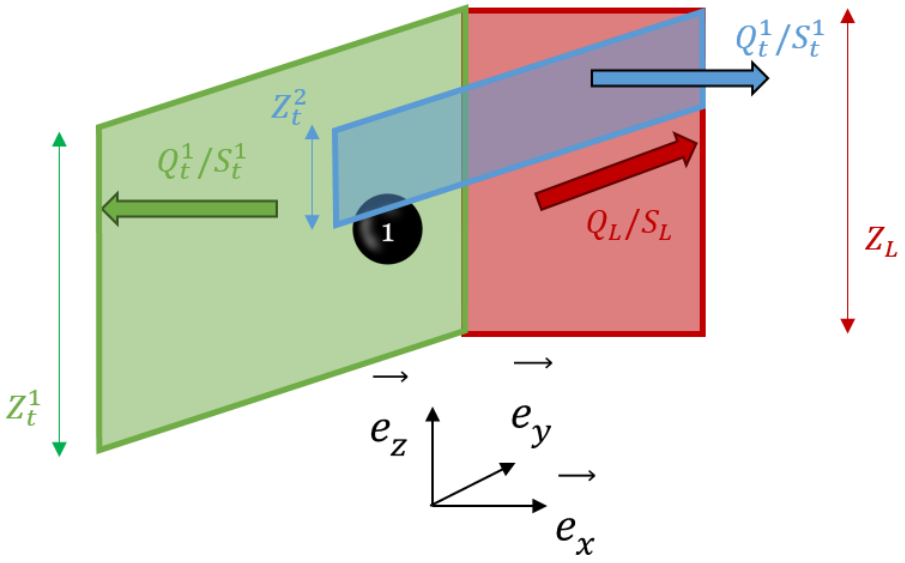

Figure 4-19 - v_t calculation layout

One can notice in Figure 4-19 that in some cases, v_t (*i.e.* the terms Q_t^i/S_t^i) does not apply on the S_L's full height. For instance, if S_t^1 consists in an internal bundle cross-section (in green), and S_t^2 in a Model 3's cross-section (in blue). Consequently, having Figure 4-19 as an example, the velocity inferred by the blue section must be balanced to depict the fact that it applies only on one reduced part of the red section.

Let Z_t be the height related to S_L along the z-axis. v_t is given by the following averaging formula:

$$v_t = \frac{1}{Z_L}\int_{Z_L}(v_t^2 - v_t^1)dz \qquad \text{(Eq. 4-10)}$$

In other words,

$$|v_t| = \frac{|v_t^1 Z_t^{1*} - v_t^2 Z_t^{2*}|}{Z_L} \qquad \text{(Eq. 4-11)}$$

With,

$$Z_t^{i*} = \begin{cases} Z_t^i \ \ if \ \ Z_t^i < Z_L \\ Z_L \ \ if \ Z_t^i > Z_L \end{cases} \qquad \text{(Eq. 4-12)}$$

Finally, ϕ is obtained through:

$$\phi = \tan^{-1}\left(\frac{|v_t|S_L}{|Q_L|}\right) \qquad \text{(Eq. 4-13)}$$

3.4. *Method 4 – 3D redistribution – flow in the bypasses and corners*

The last method completes Method 3, adding:

- Axially, coolant branches in the fuel assemblies corners (i.e. the bypasses shaped by the corners of the assemblies).
- Laterally, coolant branches in the bypass.

In broad strokes, the method authorizes the fluid to go in every possible direction. The added resistances are wholly based on common correlations that were used in this manuscript as no further studies were undertaken. In other words, the resistance located in the corner area of the FAs was chosen so that it is the local pressure loss associated with the reduction ratio of the cross-sections drawn out by each CD of the grids surrounding the FA. One has to notice that a null value in this area is forbidden: a null value would lead to all flow rates rushing through the corners axially. This reduction ratio is shown in Figure 4-20 through the blue and green squares. Consequently, if all FAs touch each other, the corner is closed and the resistance becomes infinite. The idea is the same for corners nearby walls.

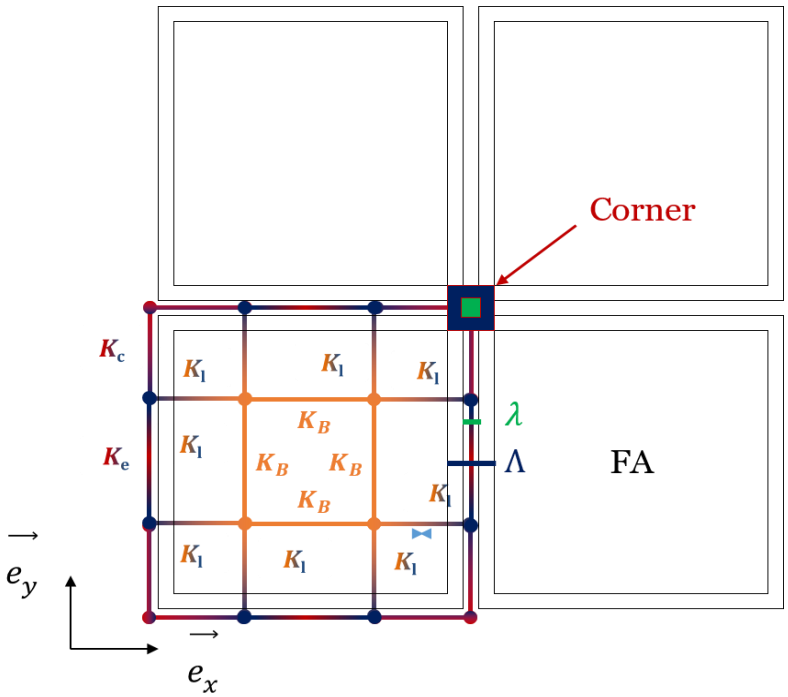

Figure 4-20 - Method 4's features (new branches in red)

Unlike to previous methods where the flow crossed the FA from side to side, now it can go through the bypass in the span wise direction. The correlation used is utterly based on (Eq. 4-9) with the assumption that FAs move only a little (a few mm) compared to the bundle pitch so that the pitch-to-diameter ratio β is conserved. Two elements are then introduced whose resistances are named respectively K_e and K_c. The first one, consisting in $N = 15$ rows of fuel rods, links intra-bypass points, whereas the second links the CD with the corner ($N = 1$). The latter choice is coherent with the adopted values of N in the CD's Model 3 ($N = 1$).

This method finally takes into account every cross-section of the core which would be concerned by deformations. It is possibly one of the most advanced method realizable with the tools that we have at our disposal. At the moment it is thus considered as a reference compared to the three other methods.

4. Comparison of the 3D methods

Eight test case have been set up to compare every method with each other. They consist in a mini-core cluster of 8x8 nuclear fuel assemblies. This choice has been legitimate through a compromise between having enough fuel assemblies to represent a full industrial nuclear core, and being sufficiently fast to compute to be repeated several times. The mean axial velocity is 5.5 m/s, the density is 700 kg/m^3 and the maximal deviation ratio (extremum-mean)/mean of velocity is imposed at 5.10^{-2}.

In order to account for every physical effects occurring in a core, 8 cases were performed for every method. They are summed up in the following table:

Test	*Shifted inlet*	*Hyperbolic para. outgoing*	*Deformation*
1	✗	✗	✗
2	✗	✓	✗
3	✗	✗	✓
4	✗	✓	✓
5	✓	✗	✗
6	✓	✓	✗
7	✓	✗	✓
8	✓	✓	✓

Table 4-1 - Test cases for 3D comparison

Where,

- Shifted inlet means that the maximum of the velocity parabolic profile coming in the core is shifted by 20% to cause an arbitrary substantial displacement (see Figure 4-21). This displacement of the maximum of flow profile is a classic way to represent asymmetric core inlet boundary conditions. This option allows to guarantee that the method correctly handles an incoming flow displacement.
- Hyperbolic parabolic outgoing means that the outgoing velocity profile is turned

from a revolution paraboloid (the same as the entrance) to an hyperbolic one (see Figure 4-21). The latter may be closer to a core's realistic outgoing flow profile. This option allows to guarantee that the method correctly handles different outgoing profiles. At this time, outgoing flows are indeed more unsung than incoming flows.

- Deformation means that several water gaps were changed from their nominal value of 2 mm. An arbitrary C-shape bowing is therefore imposed on the (N_x = 3, N_y = 3) fuel assembly, changing both east, west, north and south water gaps on every grid level. This option allows to guarantee that the method correctly handles singularities provoked by a change in λ.

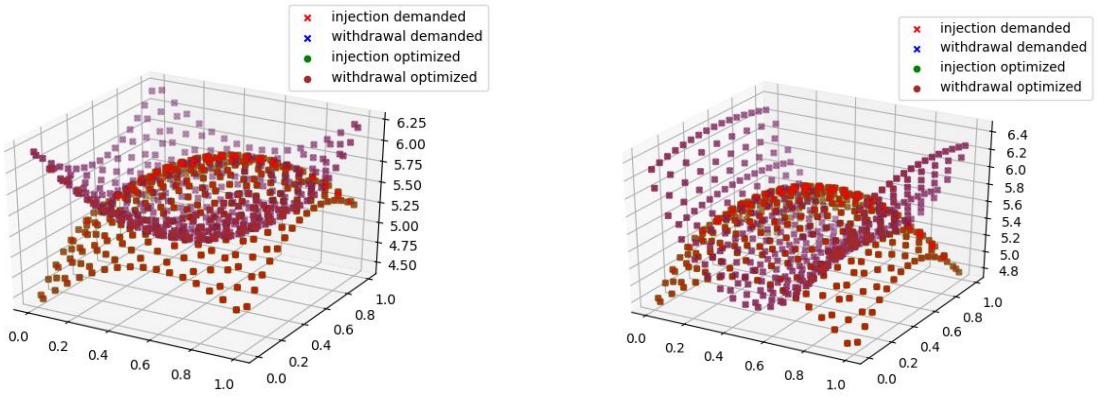

Figure 4-21 - (left) velocities (m/s) in test 5 (right) velocities (m/s) for test 2

The goal of those methods is to evaluate the two components of the lateral force. We want to ensure here that every method is consistent with each other regarding this particular goal. Therefore, the main physical value which is going to be compared is the lateral magnitude of the force defined by:

$$F_L = \sqrt{F_x^2 + F_y^2} \qquad \text{(Eq. 4-14)}$$

Where F_x and F_y are the two lateral components defined by:

$$\begin{cases} F_x = F_{UP}^x + F_V^x + F_B^x \\ F_y = F_{UP}^y + F_V^y + F_B^y \end{cases} \qquad \text{(Eq. 4-15)}$$

F_L is calculated on every floor of grid in the system, on every fuel assembly. Consequently, there are too many values of F_L in a 8x8 cluster simulation to be properly analyzed separately. That being said, one can understand that a statistical tool has to be used to compare two methods. The latter is the mean difference (further named MD) between methods i and j scaled by the maximum F_L^{max} found in all methods, defined as follows:

$$MD_{F_L}(i,j) = \frac{\sum_{k=1}^{N_{F_l}} |F_{L,k}^{i} - F_{L,k}^{j}|}{N_{F_L} F_L^{max}} \qquad \text{(Eq. 4-16)}$$

Where N_{F_L} is the total number of lateral forces. As F_L is a norm, its comparison is not able to tell about F_x and F_y directions. For this reason, N_{F_x} and N_{F_y} represent the respective numbers of F_x and F_y which do not have the same direction in all the system, between methods i and j.

Results of the comparison between method *i* and method *j*	**Number of the test**	
	Result of $MD_{F_L}(i,j)$ (%)	
	Result of N_{F_x}	Result of N_{F_y}

Table 4-2 gives the results for comparison between Methods 1, 2 and 3. A help to read the table is proposed just above.

Test / (i, j)	1		2		3		4		5		6		7		8	
(3,2)	0.77		0.41		0.76		0.40		0.84		0.53		0.81		0.51	
	0	0	0	0	1	1	0	3	1	1	5	3	1	1	5	1
(3,1)	2.42		2.57		2.46		2.60		2.49		2.65		2.52		2.66	
	0	0	0	0	0	0	1	6	9	9	16	10	8	8	15	8
(2,1)	2.59		2.96		2.63		2.98		2.87		3.16		2.84		3.13	
	0	0	0	0	1	1	1	3	8	8	15	9	7	7	14	7

Table 4-2 - Comparison of methods 1, 2 and 3

First of all, one can say that the difference between Method 2 and 3 leads to very similar results in terms of MD_{F_L} with very little scattering. Maximal errors (~0.8 %) are obtained for outgoing conditions which might be the farthest from reality (tests 1, 3, 5 and 7). For test 8, which is a priori the most consistent according to reality, the MD_{F_L} is only 0.51 %. As a reminder, the only difference between the two Methods is the 3D resistance in the bundle. Those results tend to show that adding v_t and the angle Φ does not seem to affect Method 2 that much in terms of lateral forces. Compared to Method 2, Method 1 seems to be more detrimental with MD_{F_L} around 3% for each test. Test 6 gives the maximum mean error with $MD_{F_L} = 3.16$ %. In both cases, the flow is still going in straight lines. The major difference is that Method 2 leads to 3D redistribution to fulfill the boundary conditions, whereas Method 1 has to fulfill boundary conditions on every row. Figure 4-22 depicts the distribution of $MD_{F_l}(2,1)$ in the 8x8 cluster, and the associated histogram.

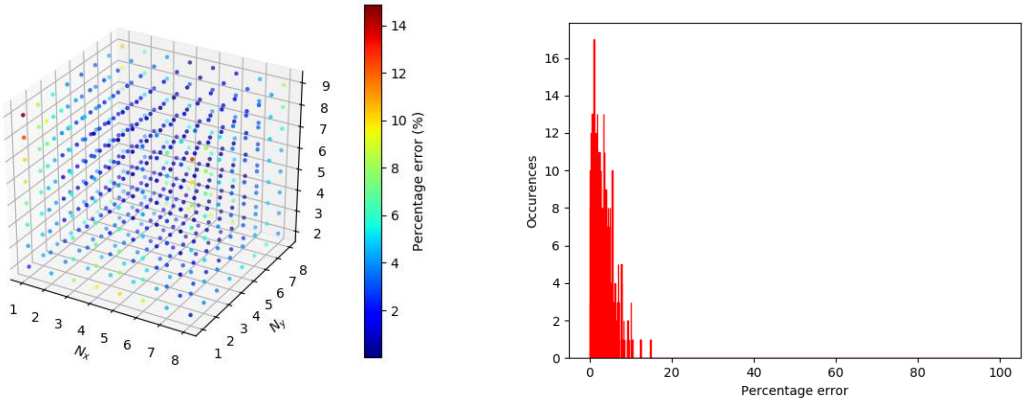

Figure 4-22 - (left) scattet plot of MD_{F_L} (right) histogram of $MD_{F_L}(2,1)$

We can see that upper bounds are obtained near the top corner ($N_X = 1, N_y = 1$) of the core, i.e. in the direction of the shifted inlet velocity. Relatively, it represents a 14 % deviation which is more than acceptable.

Method 1 seems nearer to Method 3 than to Method 2 for every single test, with a maximum MD_{F_L} of 2.66 % regarding tests 6 and 8. The only reason of this observation is that the boundary conditions processing in Method 1 leads to results closer to Method 3 with 3D effects in bundle. One explanation is that Method 3 tends to foster diagonal redistributions due to the factor introduced in the bundles, the fluid sees less resistance and consequently forces along diagonals and thus seem reduced compared to Method 2. At the same time, Method 1 boundary conditions on extreme rows can be relaxed to fulfill mass conservation locally, leading to less redistribution and thus reduced forces on the same locations than Method 2. Finally, it is not surprising that Method 1 is nearer to Method 3 than Method 2, because in vicinity of the cluster corners (where main deviations appear), both those two methods tend toward reducing forces compared to Method 2.

One must have observed that some comparisons led to different directions of F_x and F_y (N_{F_x}>0 and N_{F_y}>0). A deeper analysis shows that each time those cases occur for very low values of the two components (i.e. F_x << 1 and F_y << 1). Thus, it can be inferred that for substantial values of F_L every forces have the same direction and that core bowing patterns would be very much the same.

Table 4-3 gives the results for comparisons regarding the method 4 with the 3 others.

Test / (i, j)	1		2		3		4		5		6		7		8	
(4,3)	3.98		6.28		3.88		6.15		5.40		7.26		5.13		7.00	
	96	96	32	96	89	89	36	95	33	33	44	80	35	35	49	75
(4,2)	4.75		6.68		4.64		6.55		6.24		7.78		5.94		7.50	
	96	96	32	96	90	90	36	92	32	32	49	77	36	36	54	74
(4,1)	4.22		5.50		4.13		5.38		5.21		6.25		4.96		6.02	
	96	96	32	96	89	89	35	89	24	24	40	70	29	29	46	67

Table 4-3 - Comparisons with method 4

Method 3 and Method 1 are the closest compared to Method 4 for every cases. Regarding Method 3, it is not surprising as the Method 4 is fully based on Method 3 with slight improvements to take into account lateral flows in the water gaps. However it is interesting to note that Method 1 (the simplest) performs better than Method 3 in terms of mean difference for tests 2, 4, 5, 6, 7, 8 i.e. every tests except 1 and 3. In other words, as soon as there is hyperbolic outgoing conditions or a shifted inlet, the row-by-row method is the closest to Method 4. Certainly, this is because those two methods reduce the redistribution in the FA: Method 4 authorizes the fluid to flow in other branches – lateral bypasses and assemblies corners – while Method 1 relaxes inlet and outlet boundaries constraints where mass conservation cannot be conserved. As a result, when every additional option is added (C-shaped assembly, hyperbolic outlet and shifted inlet) the row-by-row method gives best results compared to the last method.

Regarding the numbers N_{F_x} and N_{F_y}, differences appear between Method 4 and the 3 others (Method 1, 2 and 3). The widest differences match the cases where no option is selected (test 1) with $N_{F_x} = N_{F_y} = 96$. At first sight, 96 represents an important amount of deviations between the components of lateral forces (i.e. ~15 % of every components). However a deeper analysis of this test shows that Method 4 almost cancels all forces in the central core ($F_L \sim 0$), these forces being either positive or negative. More precisely, they reach very low value at floors 5 and 6. Whereas the other methods do not 'cancel' the forces for the same regions ($F_L \neq 0$), they can reach values of a few Newton (4 N). By neglecting forces lower than 5 N, both N_{F_x} and N_{F_y} become zero (in other words all methods give the same directions of forces in test 1). However, some other tests still conserve non-zero values of N_{F_x} and N_{F_y} with this '5 N filter' even though it only affects 3 % of the components. A deeper analysis shows that it mainly concerns hyperbolic outgoing tests (i.e. 2, 4, 6, 8) and especially the x component (parallel to the outgoing flow) for forces still located at mid-height (floors 5 to 6), and near to the core borders. In those areas, Method 4 also gives forces whose values are almost zero, whereas the other methods gives forces whose values are non-zero, comprised between 5 and 10 N (not affected by the filter). However, one has to keep in mind that it only concerns 3% of the total forces and those areas concern the lowest forces in terms of norm. In every case, it is reassuring to note that the introduction of the C-shape deformed FA (and thus the introduction of singularities in terms of λ) does not seem to impact the components (test 3 gives $N_{F_x} = N_{F_y} = 0$ with the 5 N filter).

Let us analyze the computational time of each method. Table 4-4 gives the ratio between times elapsed during the redistribution calculation.

Compared to / Test	1	2	3	4
1	1			
2	6	1		
3	6	1	1	
4	11	2	2	1

Table 4-4 - Comparisons of methods (redistribution time)

As one can see, a clear difference appears between Method 1 and Method 2. Redistribution calculations in all the 16 rows (2x8 rows) of Method 1 is on average 6 times faster than the redistribution calculation in Method 2. Method 2 and Method 3, which differ from the additional $\cos(\phi)$ term added in the bundles resistance, are obviously running within a similar amount of time. Method 4 is much slower than the others (about 11 times slower than Method 1 for instance), because of the successive additions of every methods plus all additional elements peculiar to this method. Consequently, for the same numerical method (Wood's LTM), for this size of core, Method 1 is distinguishable from the others through its time efficiency.

The choice between the 4 proposed methods lies in a concession of having enough accuracy in terms of forces (so that the set of forces sent to mechanics is coherent), and considering time-saving calculations to be able to perform two-way coupling calculations which seem necessary to highlight proper bowing patterns. Even though Method 4's calculation times could be certainly optimized at this stage, results show that the row-by-row method (so called Method 1) initially proposed by Stabel in [50] seem adequate to be implemented in a further 3D coupling scheme, being both time-saving and close to Method 4 in terms of forces.

5. Partial conclusion

In this section, we transposed FA network models to a row of 15 fuel assemblies. A coupling was realized between the structure and the fluid. Four types of velocity inlet and outlet profiles were considered to analyze the sensibility of the structure pattern. Having in mind a lack of experimental measures for this kind of scale, we compared, qualitatively, bow behaviors with respect to the literature. In particular, a couple of macroscopic tendencies of the row were depicted. Parabolic and Horvath's profiles lead to the classical 'barrel' pattern as usually seen in the literature, with a difference lying in the number of FA affecting each other. Homogeneous profiles lead to forces exclusively located on external FAs at first iteration, and then lead to gap equalizing at equilibrium (similar to a barrel pattern). This

effect is well reproduced by the model. Finally, the FAs tendency to 'flee' the inlet profile maximum (the FAs move toward the right when the profile is shifted to the left) is again reproduced with the hydraulic model. Generally, one can put forward that the proposed coupling approach seems operational to uncover intricate bowing patterns.

Moreover, we tried out to extend our models to the third dimension. We analyzed the set of lateral forces calculated by four 3D methods with increasing details, on the basis of a mini-core made of 8x8 fuel assemblies. It turned out that the 1st method (stemming from the literature [50]), leaning on a sweeping of 2D rows of FAs in two orthogonal directions, gives correct results besides being time-saving. In fact, its results are in good agreement with the more complex network set up (Method 4). At this stage, we consequently recommend this method for further coupling applications. Those results were consolidated only from a hydraulic point of view (no coupling in 3D at the moment), and through a couple of different conditions (boundary conditions, presence of 4 deformed bypasses through the introduction of a C-shaped FA). This comparison should be also reviewed by means of a full-coupled approach (final state with a real pattern of bowed FAs as undertaken with the row). Finally, experimental measures as well as results drawn from finer simulations (at least porous simulations with similar conditions) would help to assess the validity of the row-by-row method. Even though our first sets of forces are coherent with patterns found out at the core scale, the fact remains that every single method has been compared to Method 4 as the reference, which remains a rather coarse simulation with large elements.

Chapter 5: From mechanics to neutronics: reproducing large deflections at the FA scale to access neutronic consequences *(interaction 1)*

Highlights of the chapter

- A strategy to depict FA shapes with neutronics is studied.
- Semi-discrete 3D models for Monte Carlo neutronics proposed to handle fuel rod bow.
- The 3D models accuracy is assessed through a comparison with a continuous toroidal model at the fuel rod scale.
- The stacking model is easy to implement but yielding spurious effects for large bowing.
- A new 'segments' model is proposed with fully mastered implementation framework.

A part of this manuscript chapter has been recently published in [86]. It comes from the works in the previous multi-physics Master's thesis [6], which were reassessed and improved.

Once the hydro-mechanical coupling is operational, the issue is to send the different hydro-mechanical parameters to a neutronic solver (both the set of gaps λ and the grid displacements) to be able to run multi-physical analyses. Actually, the most direct and convenient manner to reproduce at best large fuel assembly bows is going through a Monte Carlo approach. The latter indeed features, through the associated codes, a certain amount of different native 3D geometries to depict spatial curves induced by the grid displacements. At the FA scale, a Monte-Carlo calculation is fully realizable and comparable. It could also be a tool for validating further deterministic 3D approaches.

1. Depicting fuel assembly bow with neutronics

1.1. *Interest for taking fuel assembly bow into account within neutronic analyses*

Since assembly bow has been observed in a nuclear core following RCCA (Rod Cluster Control Assembly) insertion issues [3] in the early 1990's (we remind in this section the profile of a bowed assembly in Figure 5-1 and pieces of available public knowledge information in Figure 5-2). Neutronic modeling of bowing has then received much attention, because of several significant consequences. Those include fuel cycle management [19, 20], ex-core instrumentation [31], safety regarding departure from nucleate boiling [87, 32], rod design evolution [88] (since neutronic effect also has in return an actual impact on mechanics, see for instance [7, 89]), and more generally core management policies [5]. The range of deformation can lead to 20 mm - wide water gaps within the core [90, 3, 88], representing a

reference value used further to validate the proposed models. In [31], the author considers a maximal deflection of 1 cm, leading to water gap openings of the same order of magnitude. Fuel assembly bowing patterns are also known to be classically C-shaped, or S-shaped [3, 91, 21] - named respectively first order and second order deformation patterns later -, and in certain cases, calculations have shown that assemblies could undergo W-shaped deformations [9]. Obviously, actual in-core assembly bowings are not ideal, in the sense that they are not literally C-shaped, S-shaped or even W-shaped. The first two patterns are nonetheless representative enough to provide the necessary evaluation of the proposed modeling strategy, built to handle thereafter any kind of deformations.

Figure 5-1 - View of a PWR bowed fuel assembly [12]

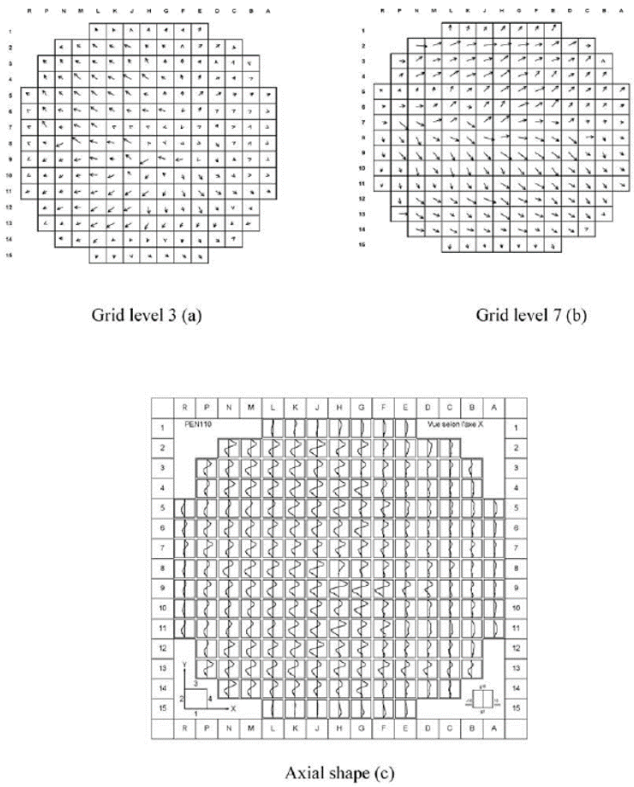

Figure 5-2 - Public domain information about fuel assembly bowing and axial deformation [3]

1.2. *Monte-Carlo modeling of rod/assembly bowing*

Monte-Carlo method is a stochastic way of simulating neutronics. It does not require meshing since equations of geometric surfaces are directly taken into account. Almost any geometry can be very accurately handled, yielding generally rather computationally demanding simulations, standing as reference solutions for complex situations. Monte-Carlo results are also classically used to validate deterministic meshed methods to be used for engineering purposes. This method has recently shown its reliability to model a PWR fuel assembly for parametric studies [92].

Recent developments in 2D Monte-Carlo simulation (core midplane) to consider bowing consists in shifting one entire rod horizontally from its initial pin cell position. For instance, in [19], authors consider a 3x3 pin cell lattice with SERPENT-2 [93], and shift the central rod to simulate a deformation, in [32] they consider a 7x7 pin cell lattice (also with SERPENT) and also shift the central rod. This action implicitly changes the moderating volume. The method remains similar at the scale of an assembly, considering a 3x3 lattice of assemblies, and shifting the central one [90, 20].

A recently presented 3D model divides the rod bowing in several cylindrical layers [19], and then shifts the layers independently to simulate a C-shaped deformation, demonstrating the feasibility of simulating 3D deformations with SERPENT-2 [93]. This model is then further used in a 3x3 assembly lattice (the assembly in the middle is made of 3D C-shaped rods), in a second article from the same author [20]. Even though this is not directly the topic of the section, a deterministic approach of assembly bowing is also presented in [20]. The next chapter of the manuscript deals with deterministic approaches.

To contribute on this topic, this next chapter thus describes two Monte-Carlo 3D-models of one single fuel rod implementing approximate discrete representation of the rod. The first model (called stacking, see below) is very similar to the one used in [19], to connect with the identified state-of-the-art, while the second model is a new approach specific to the current chapter. The obtained results for both models are compared and discussed using a comparison with a reference solution based on an exact geometric representation of the deformed rod available only for pure analytical C-or S-shape bowing. Upscaling from the rod to the fuel assembly is also considered, provided well-chosen hypotheses.

Finally, all the simulations in this chapter are performed using TRIPOLI-4® software [94], developed at CEA. The cross sections library used is JEFF3.1.1 [95]. All simulations are normalized to a unit source, so that k_{eff} equals the production rate.

2. Efficient and accurate model of fuel assembly bowing for a Monte-Carlo neutronic solver

2.1. *Modeling framework for rods and assemblies*

In terms of modeling of structures, TRIPOLI-4® software, and more generally classical Monte-Carlo simulation programs for neutronics, allows modeling a large number of 3D geometries through analytical shapes. A combination of toroidal shapes can be used to represent typical first order and second order bowing shapes of the rods, as illustrated in Figure 5-3, but this comes with a significant computational cost of the associated simulations (see Figure 5-16 later on) due the numerical overhead of geometrical operations involving toroid structures compared to classical shapes, especially when dealing with partial or complete assembly(ies) composed of numerous rods.

Moreover, this strategy reaches a limit when considering the generic deformation of an assembly with no analytical expression usually available in MC codes. This justifies the need for alternative semi-discrete approaches able to handle any kind of transverse displacement along the rod, as stated in the Paragraph 2.3. The idealized first order and second order bowing shapes in Figure 5-3 are yet of primary interest since they are compatible with TRIPOLI-4® modeler, and thus provide valuable reference solutions to evaluate the capabilities of the proposed extended modeling approaches.

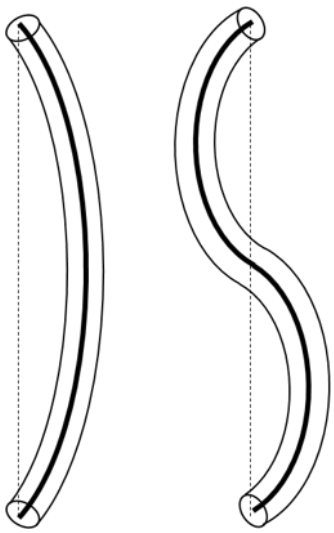

Figure 5-3 - Typical first order (left) and second order (right) deformed shape of a fuel rod (represented as an equivalent beam for the sake of simplicity, with neutral fiber displayed in thick black line)

The characteristics of a deformed rod are deduced from the reference properties of a straight rod using the following set of basic hypotheses, derived from the Small Perturbation hypothesis, fully applicable with maximal deflection of 1 cm along ~4 m long rods (see [96] for some general elements about PWR fuel assembly design):

1. The section of the deformed rod remains circular with a constant radius along the

rod equal to the radius of the straight rod and orthogonal to the neutral fiber.

2. Under Hypothesis 1, the conservation of the total mass of the rod and of the density of the material yields the conservation of the volume between straight and deformed rod, and thus the conservation of the length of the neutral axis of the rod (as illustrated in Figure 5-4).

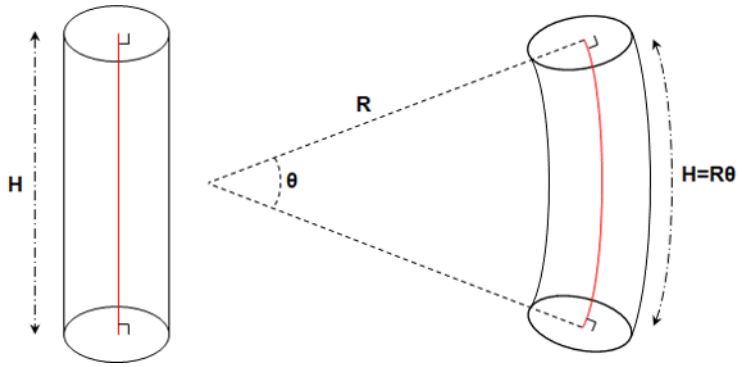

Figure 5-4 - Conservation of the length of the neutral fiber of the rod (in red) between the straight rod on the left and the deformed rod of the right

Practically, given a classical parametrization of the neutral fiber as a function $\boldsymbol{f}$ (scalar function for plane strains or vector function with 2 components for generic 3D strains) of the vertical coordinate z, Hypothesis 2 writes:

$$\int_{z_0}^{z_1} \sqrt{1 + \|\nabla \boldsymbol{f}\|^2}\, dz = H \qquad \text{(Eq. 5-1)}$$

Where z_0 and z_1 are the altitudes of the lower and upper ends of the rod respectively, H is the height of the straight rod.

Finally, for further work involving a partial or complete fuel assembly built from a series of rods, it would be additionally assumed that all the rods have the same deformed shapes, corresponding to the global shape of the assembly, so that the results in the present chapter directly apply. This rather classical hypothesis is supported by the presence of several grids along the assembly, acting as spacers and keeping the pitch of the rod lattice constant (see again [96]).

2.2. *Representation of deformed rods*

Toroidal reference model

It corresponds to a simple arc shape, whose maximal deflection is given at mid-height. It is represented by a full torus (in black in Figure 5-5) cut by two planes (in green), so that the length of the resulting torus section is equal to the length of the straight rod.

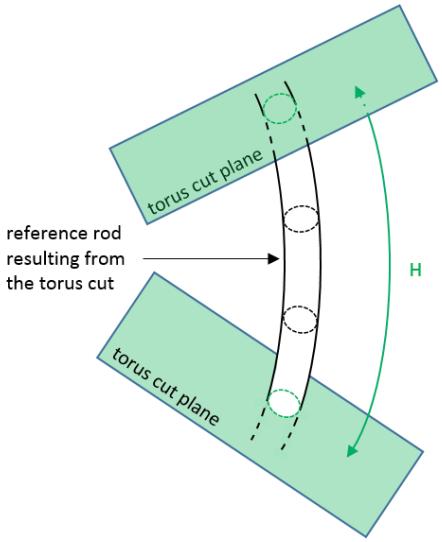

Figure 5-5 - Illustration of the toroidal reference model

First alternative modeling derived from the work of Li at al.: stacking modeling

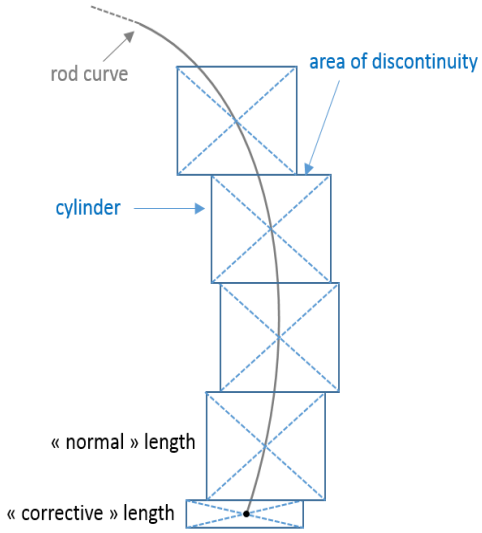

Figure 5-6 - Stacking modeling with corrective length to ensure total length conservation

Stacking modeling, illustrated in Figure 5-6 is geometrically rather simple. It consists in "stacking" small vertical cylinders with their centroids located on the neutral fiber of the deformed rod.

The advantage of such a method comes from the set of non-overlapping cylinders, all vertically oriented: the quantity of fuel in the straight rod is thus natively preserved. In return, the association of vertically oriented cylinders exhibits the following drawbacks:

1. some severe discontinuities in the description of the rod can occur if too few cylinders are used in the area of maximal slope of the deformed rod introducing some important gaps in its modeling ; this can result in side effects regarding the global influence of the rod onto neutronics,

2. the total height of the cylinders and the actual length H of the rod are not equal (once the rod is deformed), as the sum of the axial lengths of the cylinders is equal to the distance z_1-z_2 between both ends of the deformed rod, without taking its curvature into account, i.e., starting from (Eq. 5-2):

$$\sum_{i=0}^{Number\ of\ cylinders} h_i = z_1 - z_2 \neq H \qquad \text{(Eq. 5-2)}$$

One potential way to circumvent this last issue, especially for significantly bowed rods where it could alter the physical solution, is to introduce two "corrective" cylinders of very low height at the top and bottom of the stack to retrieve the right length of the rod (as shown in Figure 5-6).

New alternative modeling for generic deformed shape: segments modeling

This method models any deformation by discretizing the rod into small inclined cylindrical segments oriented according to the local curvature of the deformed rod, as illustrated in Figure 5-7.

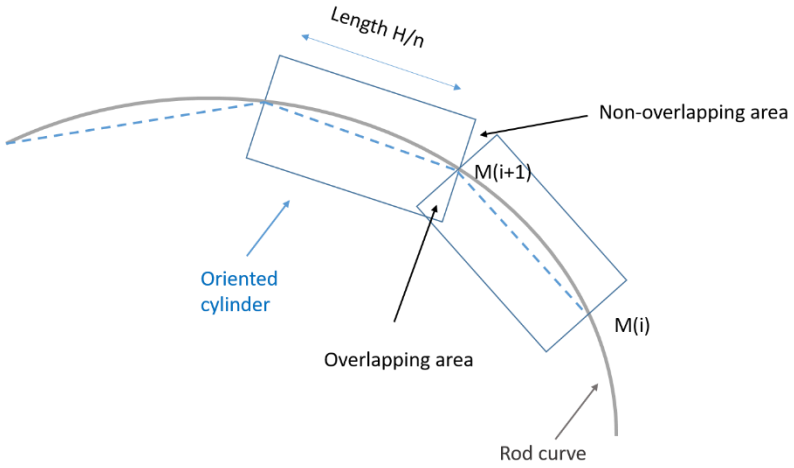

Figure 5-7 - Illustration of segments modeling accounting for actual rod curvature

The discretization in segments consists in cutting the curve of the deformed rod into small inclined cylinders called "segments", of axial length H/n, where H is the total length of the rod and n the number of segments of the discretization.

This representation defines implicitly a set of points $M(i)$ corresponding to the intersection of cylinder axis with the neutral fiber of the rod, so that a segment can be identified from the couple $[M(i), M(i+1)]$. The orientation of Segment $[M(i), M(i+1)]$ is then obtained from the string between points $M(i)$ and $M(i+1)$ and the length is much more accurately conserved, with a linear convergence towards the exact conservation with respect to the number of segments.

The proposed method yet exhibits some specific issues to be handled carefully to

perform robust and accurate Monte-Carlo simulations:

1. segment cylinders are overlapping each other (see overlapping areas in Figure 9) in the general case due to inclination, which requires to give priority to one segment over another,

2. the corollary of these overlapping zones is the existence of gaps (called "non-overlapping" areas in Figure 5-7) which causes a violation of the conservation of the amount of fuel in the rod provided the segment cylinder radius equals the rod radius.

These issues are solved by the following modeling guidelines:

1. always use an odd number of segments,

2. adjust the length of the segments with even identification numbers (id) to fill the spurious gaps as illustrated in Figure 5-8,

3. within the Monte-Carlo solver, give priority to the segments with odd id over the segments with even id to cancel the potential overlapping conflicts.

The length correction, denoted ε, for each segment can be deduced from a visualization of the default segment model built using the string lengths measured along the rod neutral fiber (for instance using T4G viewer of TRIPOLI-4®). It can also be computed in a preprocessing step from the initial length of the segment and the local curvature of the rod (however not implemented in this preliminary research). In the following paragraphs, the value of the correction is estimated for a maximal deflection of 20 mm and a number of 51 segments, and kept constant for all configurations, with no visible side effects thanks to the priority established within the segments.

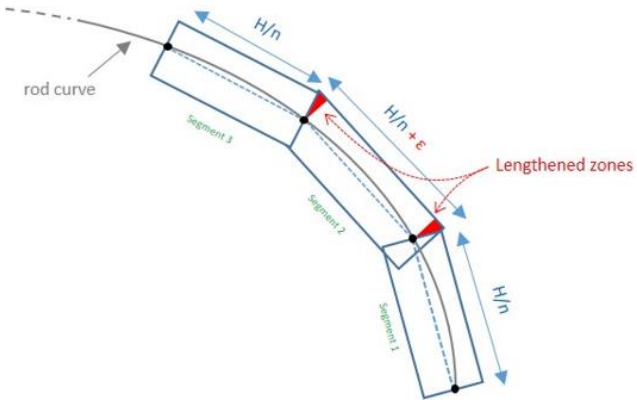

Figure 5-8 - Length correction to keep mass quantity, with segment 2 lengthened to close non overlapping areas

Building computational models from actual assembly bowing data

This last paragraph aims at concluding the current section dedicated to modeling strategies by giving some insights for processing industrial bowing data and building of relevant and accurate models taking them into account. Three engineering steps have thus to be considered.

First, bowing measures, obtained on-site in an actual plant after core unloading for instance, provide the deflection of the full assembly at a discrete number of locations along its main axis. If this number is in accordance with the targeted number of discrete items used to describe one modeled rod, they can be used directly to position the centroids of the stacked cylinders or the approximating segments accordingly. Otherwise, a reconstruction of the shape of the assembly from the discrete data is necessary.

This second step can be seen either from a purely mathematic point of view or from a mechanical one. Mathematically, it consists in choosing an interpolation function for the neutral fiber (the same for the assembly or the rods). When using polynomial functions, the order of the function is logically adjusted to the dominant shape observed in the original data, if any, resorting for instance to the basic classification provided in Paragraph 2.1. An alternative strategy is to deduce the shape of the assembly from a direct mechanical computation using a beam model for the assembly and introducing the measures as imposed displacements. In this case, a Timoshenko beam model is the most relevant choice, since the assembly can undergo large levels of shearing, and some constraints can be added to increase the fidelity to the industrial device. For instance, the curvature of the beam can be forced to zero at the grid levels to account for their effect as spacers in the assembly.

The final step consists in automatically generating the datasets for Monte-Carlo simulation from the geometrical data reconstructed above.

The complete automated process implemented in the current chapter is illustrated below for the significant case of a central symmetric second order analytical shape of the rod (see Figure 5-9).

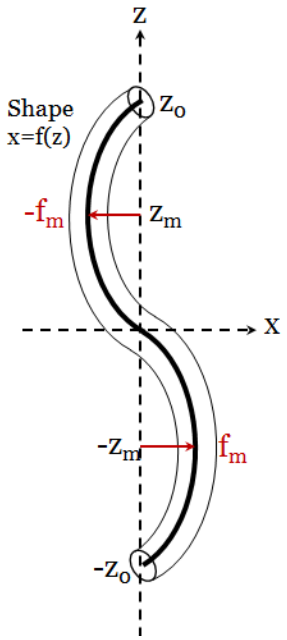

Figure 5-9 - Typical central symmetric second order shape of the neutral fiber with two maximal deflection points at respective coordinates (f_m, $-z_m$) and (z_m, $-f_m$)

The global deflection x is approximated along the vertical direction z through the polynomial expression:

$$f(z) = az + cz^3 \qquad \text{(Eq. 5-3)}$$

With the set of coefficients given by:

$$\begin{cases} \dfrac{\mathrm{d}f}{\mathrm{d}z}(z_m) = 0 \\ f(z_m) = -f_m \end{cases}, \qquad yielding\ a = -\frac{3f_m}{2z_m}, c = \frac{f_m}{2z_m^3} \qquad \text{(Eq. 5-4)}$$

Given the global shape of the neutral fiber of the rod, Hypothesis 2 provides the value for extremum vertical coordinates z_0 through the solution of the non-linear equation:

$$\int_{-z_0}^{z_0} \sqrt{1 + \left(-\frac{3f_m}{2z_m} + \frac{3f_m z^2}{2z_m^3}\right)^2}\, dz = H \qquad \text{(Eq. 5-5)}$$

(Eq. 5-5) can be solved analytically using Formal Calculus software or in closed form. Once the reference shape of the rod is completely defined, segments are automatically generated taking into account the guidelines expressed in the previous paragraph. The model built from the conditions above is shown in Figure 5-10, with significant shrinkage along the vertical axis for illustration purposes (as stated in Paragraph 3.1, H is classically close to 4 m, for maximum deflection around 10 mm).

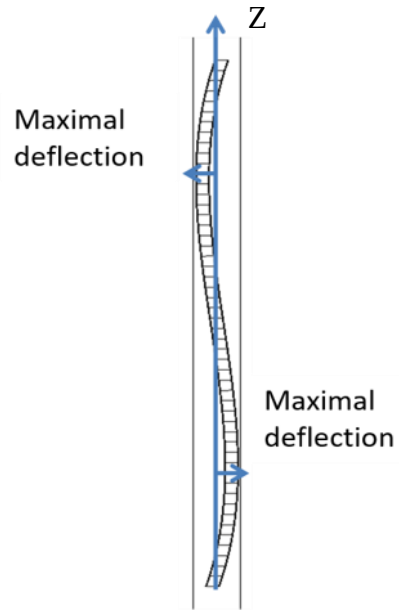

Figure 5-10 - Illustration of TRIPOLI-4® modeling through segments for planar symmetric second order rod deformation (vertically shrunk view stemmed from T4G viewer)

3. Compared results for first order rod deformation

The comparison is carried out in the case of French PWR 900 MW geometry. The length of the rods is thus H=3.658 m, with a lattice pitch of p=1.26 cm, and a fuel rod diameter of d=9.5 mm. The considered physical situation is given in Figure 5-11 and views of the computational models are given in Figure 5-12, with maximal deflections of λ = 10 mm, 20 mm and 25 mm. We define α = p-d. This situation illustrates an external bowed fuel rod with an increased water gap on the left and a fuel rod row on the right (following the same deflection). The neutron sources are distributed in the fuel volume inside the rod and neutrons are generated following a Watt fission spectrum. A maximum of 100 000 batches (20 discarded) of 10 000 particles has been set up for all simulations.

The toroidal analytical model provides the reference solution against which the semi-discrete approaches (stacking and segments) are confronted. For the stacking or segment approaches, various numbers of discrete entities are considered, from 20 to 550 stacked cylinders and from 21 to 101 segments respectively, to better highlight the impact of discretization on both models. For the latter modeling, the length correction is computed once for the case with 51 segments and applied to all other configurations with commented results whenever necessary.

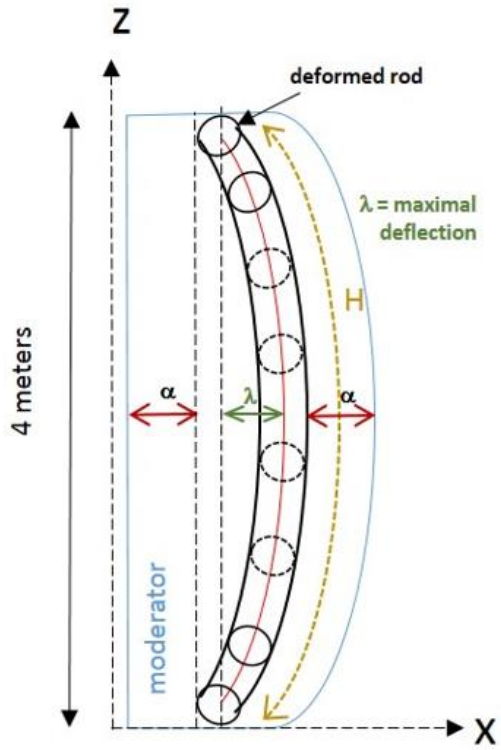

Figure 5-11 - Considered geometry and boundary conditions for the first order comparison case (lateral, top and bottom boundaries are set to reflection, Y-axis boundaries are set to translation)

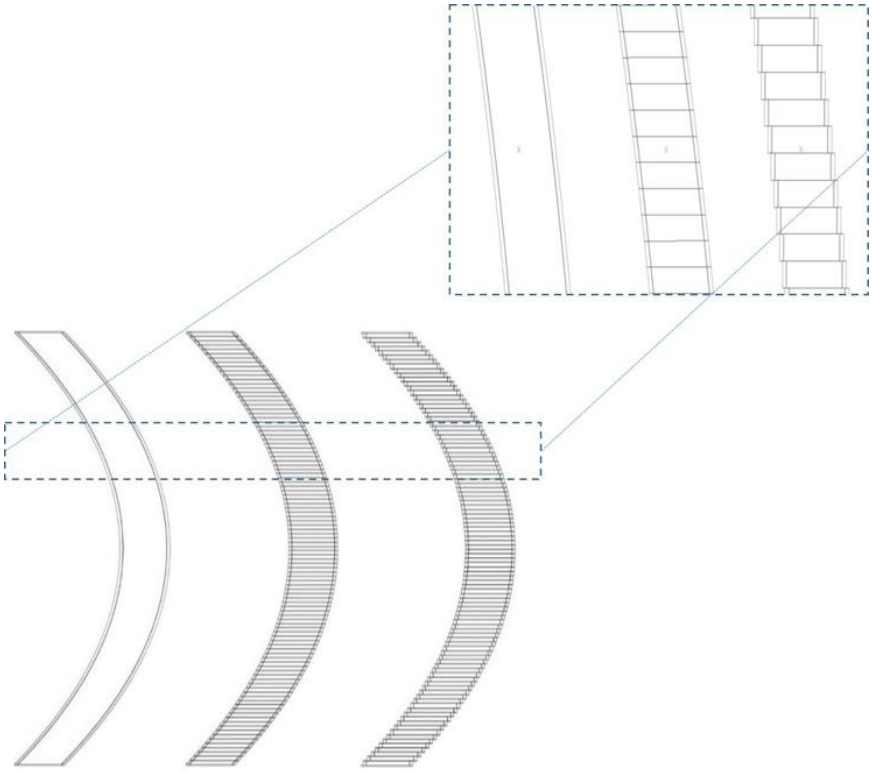

Figure 5-12 - Illustration of computational models for first order deformation, with distinction between the inner part of the rod with fuel properties and the lateral part with cladding properties (from left to right: cut torus (reference), segments, and stacking, scales not conserved for the sake of clarity). The fuel-clad gap is too small to be observed on the figure.

Selected quantities of interest for the assessment of the various models are neutron production rate in Uranium 235 (U5), neutron absorption rate in Uranium 238 (U8) and global k_{eff} coefficient for the chosen configuration. Conditions are close to the ones of a French 900MW start: no previous irradiation, fuel in new condition, boric acid concentration of 1 440 ppm, a 5% U5 enrichment (see [5, 10] for general statements about French PWRs). 3σ-error bars are associated in following graphics to all quantities resulting from Monte-Carlo statistics. It is noticeable that all performed simulations involved the same number of emitted neutrons. Deviations from the reference obtained with the toroidal model therefore derive only from differences in reaction rates.

Detailed results are given in the next two paragraphs for the 20 mm-deflection situation, whereas results for all deflections are compiled in section 3.3.

Remark 1:

Adjusting vertical and horizontal scales in Figure 5-12 (and identically in Figure 5-19) logically results in some distortions of the elementary shapes implemented in the reference model and in the segment model. The torus does not appear as such due to the apparent modification of the angle between the extremum sections and the neutral fiber, and 2D-projections of segments are transformed from rectangles into parallelograms. These visual artifacts do not affect the purpose of the proposed view, which is to highlight the major differences between the semi-discrete approaches and the reference, especially close to the interfaces between discrete entities.

Remark 2:

There would be no relevance in comparing the results presented below to results from a close configuration implementing a straight rod. The proposed test case is designed to compare the modeling approaches. The solution is greatly influenced by the arbitrarily chosen boundary conditions, with a fuel/moderator ratio given by the global geometry of the computational domain, so that the actual value of the multiplication factor is physically meaningless. The foreseen comparisons shall be performed in further research through the proper modeling of a partial or complete nuclear core configuration implementing potential bowing of some fuel assemblies.

3.1. *Neutrons production and absorption rates*

Results for neutron production in U5 are provided in Figure 5-13, whereas results for neutron absorption in U8 are provided in Figure 5-14.

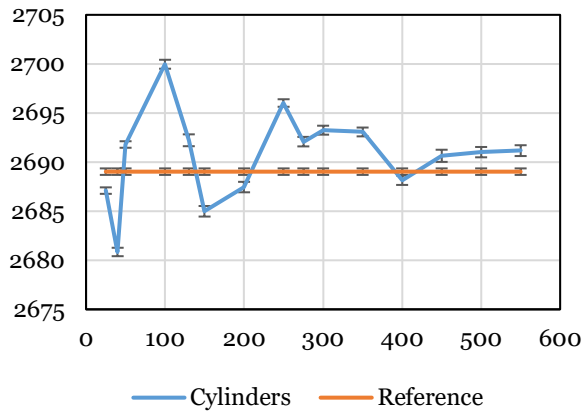

(a) Production rate (s^{-1}) obtained with stacking modeling implementing 20 to 550 cylinders

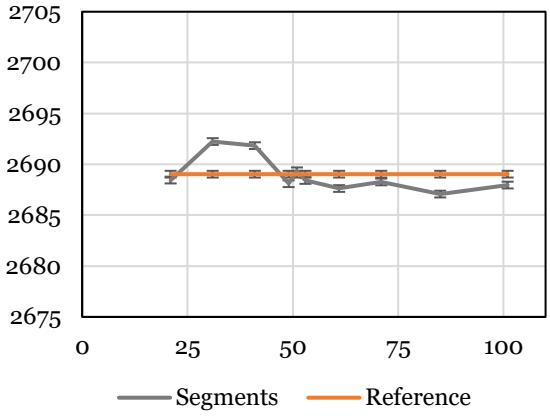

(b) Production rate (s^{-1}) obtained with segment modeling implementing 21 to 101 segments

Figure 5-13 - Neutron production rate in U5 for stacking and segment modeling compared to reference

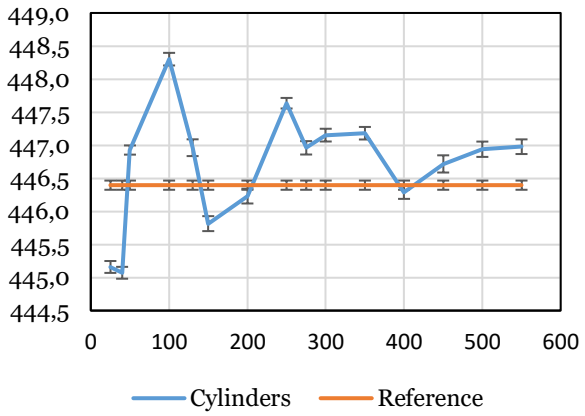

(a) Absorption rate (s^{-1}) obtained with stacking modeling implementing 20 to 550 cylinders

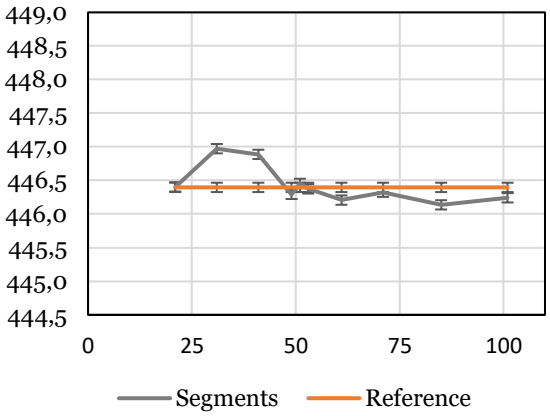

(b) Absorption rate (s^{-1}) obtained with segment modeling implementing 21 to 101 segments

Figure 5-14 - Neutron absorption rate in U8 for stacking and segment modeling compared to reference

The segment modeling generally yields results much closer to the reference than the stacking modeling. The simulation with 51 segments (for which the actual correction is computed) is here the most accurate compared to the reference.

As far as stacking modeling is concerned, the configuration with 400 cylinders provides the most accurate results compared to the reference, but the accuracy seems to decrease for higher numbers of cylinders, with no obvious explanation (see Paragraph 4.3 for further analysis).

3.2. *Global k_{eff} coefficient*

If previous results provided insights about the proximity of behavior of the semi-discrete models compared to the reference, results in terms of k_{eff} coefficient have priority to actually evaluate their accuracy. They are given in Figure 5-15.

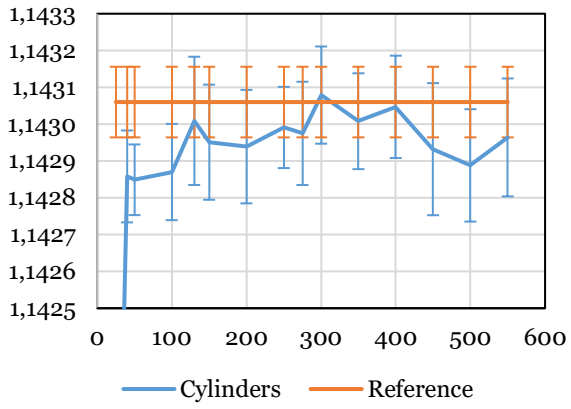

(a) k_{eff} obtained with stacking modeling implementing 20 to 550 cylinders

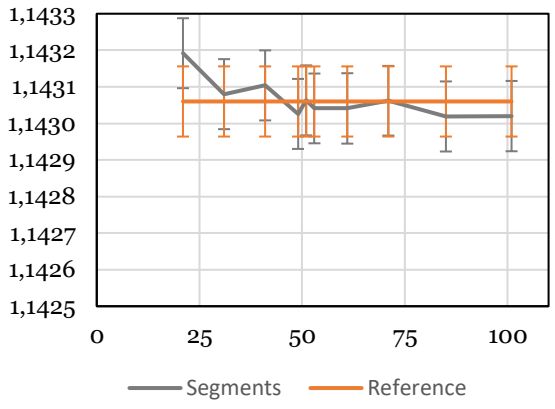

(b) k_{eff} obtained with segment modeling implementing 21 to 101 segments

Figure 5-15 - k_{eff} coefficient for stacking and segment modeling compared to reference

Results obtained with segment modeling are again closer to the reference than those obtained with stacking modeling. It is noticeable that the latter seems to systematically underestimate the rod reactivity which could prove to be an issue when dealing with safety evaluations. Some fairly accurate results are yet observed for some high number of stacked cylinders (around 300) but they are difficult to predict and lack robustness since higher numbers can still produce large deviations. Taking into account that the computational cost of stacked cylinders is close to that of segments for the same number of elements (see Figure 18), it demonstrates that segment modeling with the guidelines proposed in Paragraph 3.2.3 should definitely be preferred to represent the bowed fuel rod in the present configuration (more accurate, with less elements).

Looking deeper into segment modeling, the range of segment numbers producing accurate results is quite wide (from 51 to 71). Smaller numbers should be avoided, with a significant increase of the deviation from the reference when going down towards 21 segments. Higher numbers around 100 segments do not show the expected accuracy, which can be imputed to the length correction which should be specifically computed for these configurations. Anyway, trying to retrieve some accuracy with high numbers of segments appears easily feasible but worthless since they come with higher computation cost than the accurate range identified above. Figure 5-16 shows simulation times (in terms of number of realizations, or batches, per second, with the higher the number, the better the computational performance). It can be observed the semi-discrete approach is more efficient than the reference for less than 71 segments, since rotated cylinders require less geometric operations than the toroidal shape to compute their interaction with neutrons.

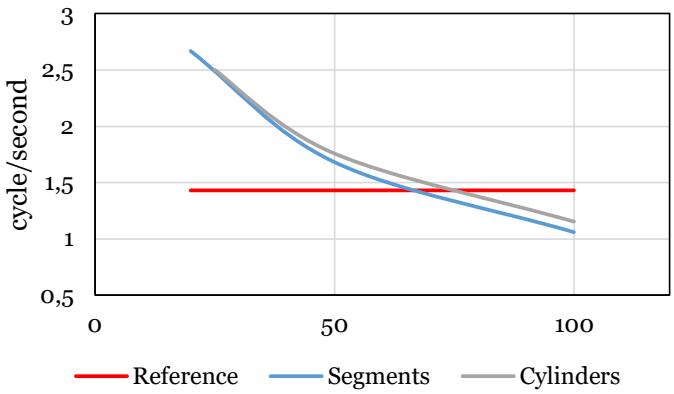

Figure 5-16 - Computational performance in terms of batches per second, for segment and stacking modeling and reference toroidal modeling

3.3. *Partial conclusion for first order rod deformation*

Results in terms of deviation for production rate (in %), absorption rate (in %) and k_{eff} coefficient (in pcm) with respect to the reference for both semi-discrete approaches and the three considered deflections are gathered in Table 5-1. For comparison purposes, the same 'lower' range of number of discrete entities is chosen for stacking and segment modeling, i.e. 30 to 101.

		SEGMENT			**STACKING**		
	Deflection	Deviation			Deviation		
		Min	Mean	Max	Min	Mean	Max
U5 (%)	10	0.02	**0.05**	**0.10**	**0.01**	0.07	0.21
	20	**0.01**	**0.05**	**0.12**	0.08	0.21	0.41
	25	0.01	**0.03**	**0.07**	0.01	0.11	0.27
U8 (%)	10	0.00	**0.03**	**0.08**	0.00	0.07	0.21
	20	**0.01**	**0.05**	**0.13**	0.03	0.22	0.43
	25	**0.01**	**0.04**	**0.08**	0.02	0.13	0.24
KEFF (PCM)	10	6.90	10.57	16.40	**0.70**	**5.38**	**13.10**
	20	**0.20**	**2.47**	**4.40**	14.00	20.73	35.60
	25	**0.40**	**3.80**	**6.20**	0.80	17.40	37.90

Table 5-1 - Compiled results for both semi-discrete approaches and three values of deflections (10, 20 and 25 mm): deviation for production rate (in %), absorption rate (in %) and k_{eff} coefficient (in pcm). For rates: $\sigma < 0.1$ %, and for keff: $\sigma < 15$ pcm.

These global results confirm the observations made for the specific case of the 20-mm deflection: for similar numbers of discrete entities, segment modeling is more accurate in almost all cases.

Stacking approach shows low accuracy when the deflection increases, which can be easily understood with the schematics in Figure 5-17. Large deflections yields high slopes for the neutral fiber, especially when it crosses the initial axis of the straight rod. This tends to

increase the exchange surface between the fuel and the moderator while volume of fuel and moderator are still the same using stacking modeling. This could have an impact on reactions rates.

The segment modeling should then be preferred in most cases involving dominant C-shape rod deformation and if chosen for its easier implementation, the stacking approach should be restricted to small deflections.

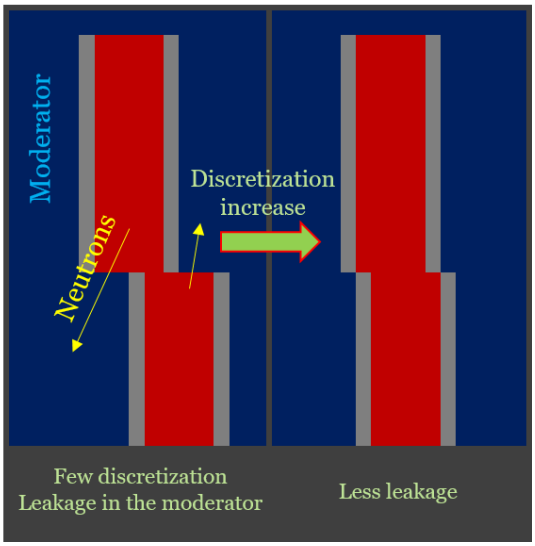

Figure 5-17 - Representation of high-slope sections with stacked cylinders; leaking surfaces between fuel core (in red) and moderator (in blue) ignoring the cladding (in grey)

4. Compared results for second order rod deformation

Clear conclusions could be drawn after considering first order deformation in previous section. The present section aims at confronting them with the significant case for which a reference solution is fully available, in the hope of being able to design solid guidelines for generic bowing patterns of rods and assemblies.

A second order pattern is thus considered, especially introducing sections of higher slopes along the rod for the same level of deflection compared to first order deformation. The physical setup for TRIPOLI-4® is illustrated in Figure 5-18 (notations are the same as before) and views of the computational models are given in Figure 5-19.

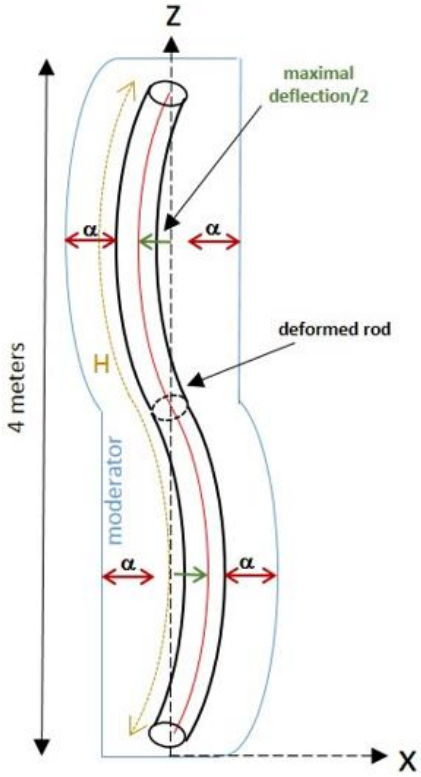

Figure 5-18 - Considered geometry and boundary conditions for the second order comparison case (lateral, top and bottom boundaries are set to reflection, Y-axis boundaries are set to translation)

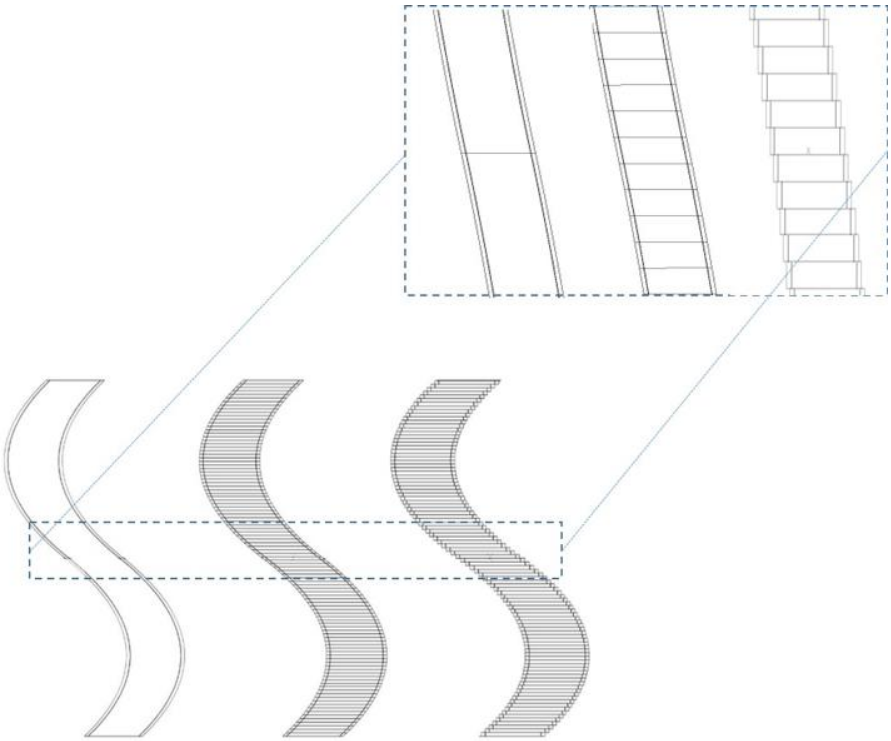

Figure 5-19 - Illustration of computational models second order deformation, with distinction between the inner part of the rod with fuel properties and the lateral part with cladding properties (from left to right: cut torus (reference), segments, and stacking, scales not conserved for the sake of clarity). The fuel-clad gap is too small to be observed in the figure.

The quantities of interest are the same as those in the previous section. Detailed results are given for a deflection of 10 mm for each half of the second order bowing pattern, which yields a cumulative deflection of 20 mm along the rod, like for the first order bowing pattern above. Deflections of 20 mm and 25 mm are also considered, with results gathered in Paragraph 5.3. The geometric correction for the segment modeling is kept from the previous section in the case of 51 segments along the rod.

4.1. *Neutrons production and absorption rates*

Results for neutron production in U5 are provided in Figure 5-20, whereas results for neutron absorption in U8 are provided in Figure 5-21.

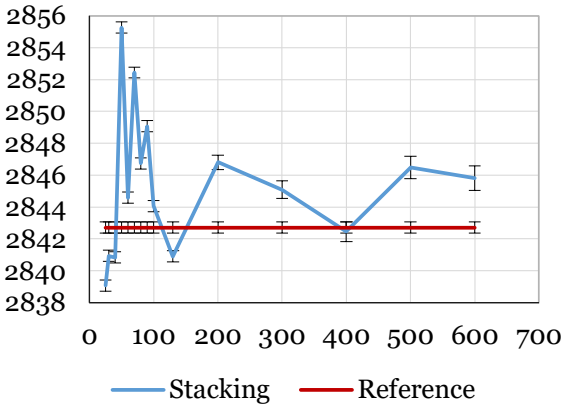

(a) Production rate (s^{-1}) obtained with stacking modeling implementing 20 to 600 cylinders

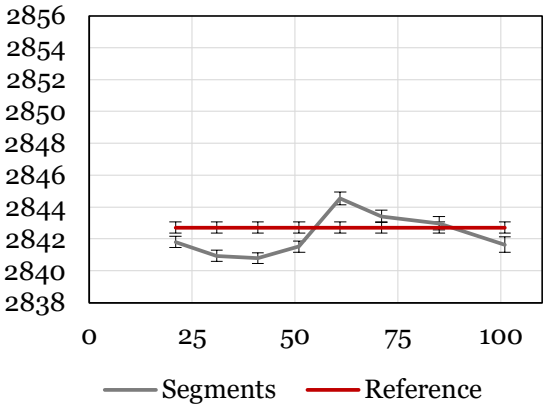

(b) Production rate (s^{-1}) obtained with segment modeling implementing 21 to 101 segments

Figure 5-20 - Neutron production rate in U5 for stacking and segment modeling compared to reference

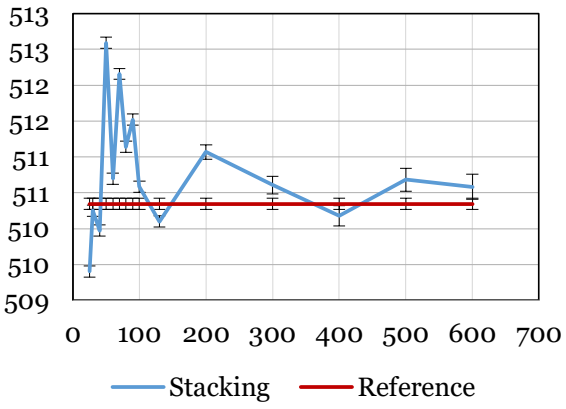

(a) Absorption rate (s^{-1}) obtained with stacking modeling implementing 20 to 600 cylinders

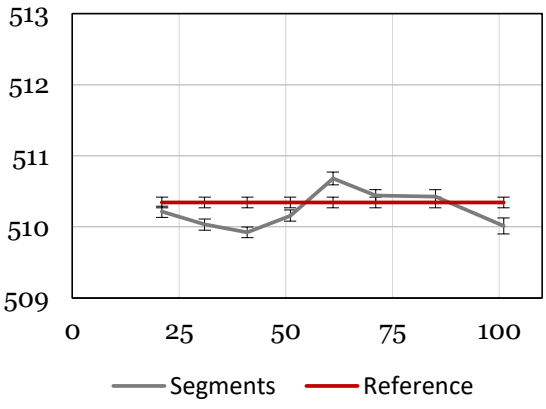

(b) Absorption rate (s^{-1}) obtained with segment modeling implementing 21 to 101 segments

Figure 5-21 - Neutron absorption rate in U8 for stacking and segment modeling compared to reference

The observations made in section 3.1 still hold in the present situation, with amplified drawbacks for the stacking approach. The segment modeling again yields results close to

the reference and the length correction computed for 51 segments with the first order bowing pattern accurately apply in this case with the second order pattern.

4.2. *Global k_{eff} coefficient*

Results for both modeling are given in Figure 5-22.

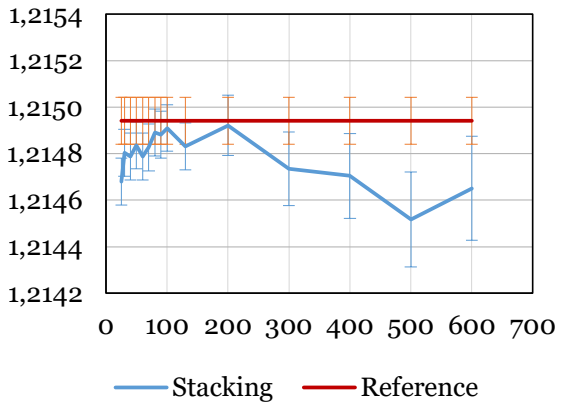

(a) k_{eff} obtained with stacking modeling implementing 20 to 600 cylinders

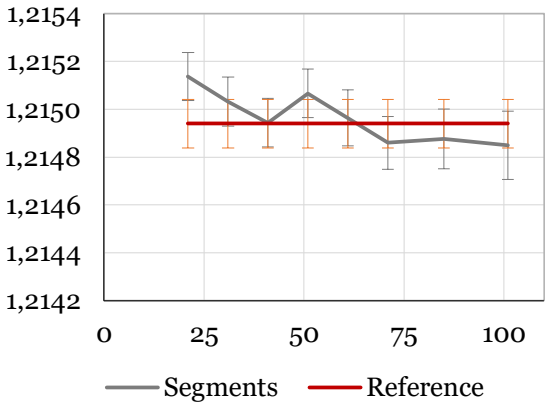

(b) k_{eff} obtained with segment modeling implementing 21 to 101 segments

Figure 5-22 - k_{eff} coefficient for stacking and segment modeling compared to reference

Observations from section 3.2 apply again. A significant discrepancy is observed when increasing the number of stacked cylinders over 200, which can be seen as an aggravated consequence of the complex neutron leakage process through singular interfaces between cylinders already mentioned above, since increasing the number of cylinders also increases the number of such interfaces.

4.3. *Partial conclusion for second order rod deformation*

Like in section 3.3 for the first order deformation, results in terms of deviation for production rate (in %), absorption rate (in %) and k_{eff} coefficient (in pcm) with respect to the reference for both semi-discrete approaches and the three considered deflections are gathered in Table 5-2. The same range of numbers of discrete entities is chosen for stacking and segment modeling, i.e. 30 to 101.

		SEGMENT			STACKING		
	Deflection	Deviation			Deviation		
		Min	Mean	Max	Min	Mean	Max
U5 (%)	10	**0.00**	**0.02**	**0.02**	0.05	0.12	0.20
	20	**0.01**	**0.04**	**0.07**	0.05	0.17	0.44
	25	0.04	**0.13**	**0.33**	**0.01**	0.14	0.35
U8 (%)	10	**0.01**	**0.03**	**0.05**	0.03	0.10	0.19
	20	0.02	**0.05**	**0.08**	0.02	0.17	0.44
	25	0.05	**0.13**	**0.32**	**0.01**	0.15	0.34
K_{EFF} (PCM)	10	**0.90**	**2.73**	**7.00**	2.30	6.26	10.70
	20	**0.40**	**6.87**	**12.70**	3.00	9.99	15.30
	25	**0.10**	**6.25**	**13.20**	10.30	18.70	33.70

Table 5-2 - Compiled results for both semi-discrete approaches and three values of deflections (10, 20 and 25 mm): deviation for production rate (in %), absorption rate (in %) and k_{eff} coefficient (in pcm). For rates: $\sigma < 0.1$ %, and for keff: $\sigma < 15$ pcm.

These results, in terms of keff and rates, confirm that segment modeling should be preferred over stacking modeling, which must be restricted to very small deflections with second order deformation (a few mm).

Concerning segment modeling specifically, the accuracy of the results obtained in both configurations suggests that this approach exhibits enough regularity and robustness to be extended as expected to mixed-type generic bowing patterns.

5. Partial conclusions

The present study proposed two semi-discrete approaches to represent the effect of fuel rod/assembly bowing onto neutronics, the first based on stacked vertical cylinders to approximate the curved geometry and the second implementing rotated cylinders, named segments, instead.

Fully tested on C-shaped and S-shaped deformation patterns, both modeling can be used with a satisfactory accuracy for small deflections. However, despite specific constraints to build accurate datasets out of segments, especially related to the length correction requested to avoid gaps between consecutive segments, this latter approach produces more robust results when dealing with deflections of any shape and amplitude (see Table 5-3 for a full summary of the proposed evaluation).

Reference modeling built out of analytical shapes (torus and planes)	Semi-discrete approaches	
	Stacking modeling	Segment modeling
Easy to implement but restricted to basic bowing patterns	Easy to implement for any kind of geometry	Implementation possible for any kind of geometry with practical constraints to handle with care: length correction, priorities between entities to manage overlapping areas
Exact representation of the geometry for the suitable bowing patterns	Singular surfaces between stacked cylinders with spurious effects increasing with the bowing deflection (systematic k_{eff} underestimation observed in particular)	Fairly accurate representation of any curved geometry, assuming a relevant value for the length correction factor
Non-applicable to actual in-core deformation patterns	Accuracy and robustness for neutronics ensured only for small deflections in the case of complex bowing patterns	Recommended approach for representing actual in-core rod/assembly bowing patterns and their effect onto core neutronics

Table 5-3 - Main conclusions of the evaluation of stacking and segment approches to represent first and second order bowing patterns

However, because of the associated computation time, these 3D Monte Carlo models can only be used for studies in limited scales (a few FAs). For a full core scale, the approach requires too many volumes (each fuel rod is split into tens of volumes), and a different strategy must be undertaken: it is necessary to adopt a 3D deterministic strategy. The models developed in this chapter could then be used as a reference for validation regarding a couple of FAs.

In the next chapter, we lay the foundations of this further 3D deterministic modeling through the setting up of necessary elements within a 2D geometry.

Chapter 6: Basis of a deterministic approach to depict deformations with large water gaps

Highlights of the chapter

- For bigger 3D core calculations including large fuel assembly deformations and water gaps (up to 20 mm), a first 2D deterministic model is studied.
- We assume the hypothesis that each pin-homogenized cross-section in one FA quarter only depends on the adjacent water gap width. The latter assumption will be assessed *a fortiori* to ensure the modeling trustworthiness.
- Cross-sections were generated through lattice calculations for the east quarter of the central fuel assembly in a mini-core cluster of 5x5 assemblies, for different values of gap width. The lattice calculations are evaluated with the related stochastic calculations.
- Through a core solver, the homogenized cross-sections are reinjected in all FA quarters of the mini-core, each characterized by the adjacent gap width.
- Results highlight that the independency hypothesis of cross-sections in one quarter is valid for every test case run, and the strategy can be considered ready for further use.

1. From the stochastic to the deterministic approach

1.1. *About the deterministic features*

In the previous section we set up and validated models for the deformation of fuel rods. Each fuel rod can be gathered together to constitute a bundle of fuel assembly. Even though those models served for instance to highlight the weight of the deformation against the weight of related thermal hydraulics effects in a previous study [6], it is *a priori* not designed to depict power effects at a full core scale. The reason why such models cannot be used for larger scales is that the Monte-Carlo method is time-consuming: in such situations, it remains a reference method for validation. The segment methods could be contemplated as a mean for validation or for modeling rather limited scales (a couple of FAs). As a result, the other usual approach is the deterministic one. The latter is used to solve core-scaled systems through dedicated schemes [97]. Whereas the Monte-Carlo method solves the Boltzmann transport equation following a probabilistic approach, the deterministic approach lies in solving the same equation but through the discretization of space and energy. The integro-differential equation (from [98]) is available in (Eq. 6-1):

$$\frac{1}{V_n}\frac{\partial\psi(\mathrm{r},\mathrm{E},\Omega,\mathrm{t})}{\partial\mathrm{t}} + \Omega\nabla\psi(\mathrm{r},\mathrm{E},\Omega,\mathrm{t}) + \Sigma(\mathrm{r},\mathrm{E},\Omega)\psi(\mathrm{r},\mathrm{E},\Omega,\mathrm{t}) = Q(\mathrm{r},\mathrm{E},\Omega,\mathrm{t}) \qquad \text{(Eq. 6-1)}$$

This equation represents a neutron balance equation. The first term stands for the

neutron variation density per time unit (zero at steady-state), the second one is the streaming of neutron outside the considered volume, the third is the total reaction rate, made of scattering to another energy, and every kind of absorption. The different variables are: ψ, the angular flux, V_n the neutron velocity module, the phase-space is defined by $(\mathrm{r}, \mathrm{E}, \Omega, \mathrm{t})$, with r being the location point, E the kinetic energy, Ω the unitary vector depicting the neutron direction and t the time. Finally, Σ is the total macroscopic cross-section (the sum of the isotopes density in the volume multiplied by their microscopic cross-section), and Q is the neutron source term, made of every positive contribution to the neutron balance: the fission rate, the scattering to E, and possibly an external source.

One can estimate the number of degrees of freedom of the problem considering the three variables of interest.

First, the cross-sections of any heavy isotopes highly depends on the energy. Uranium 238, for instance, is the most abundant isotope in PWRs fuel. In order to assess its resonances in the epithermal domain (Figure 6-1), a few hundreds of energy groups are needed.

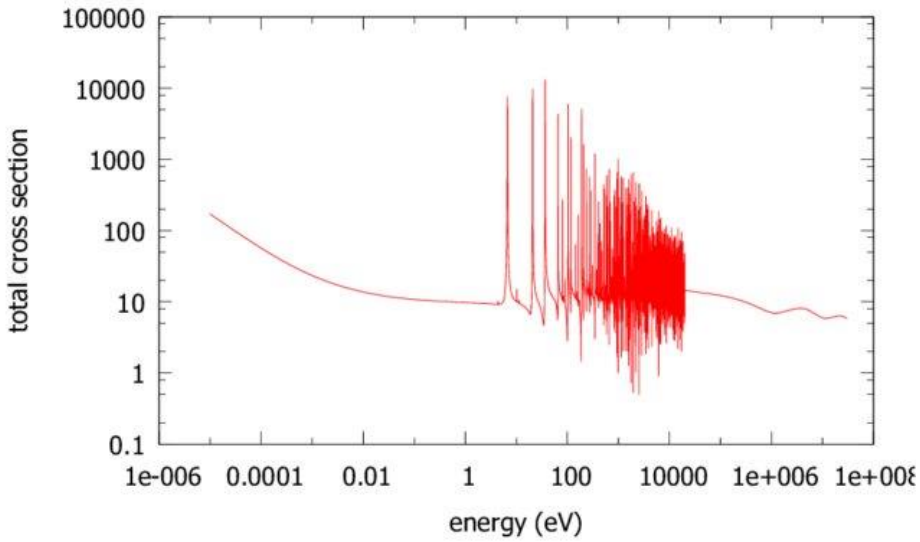

Figure 6-1 - Total cross-section of U238 from [99]

Second, in practice, an important amount of spatial cells in needed. As the typical size of the mesh size to capture flux gradients in a PWR fuel is about a couple of millimeters (dimension of a rod cladding), and a core is in the order of a few meters, one needs about 10^9 spatial cells to draw the full core [98]. Another reason for such a mesh refinement is the self-shielding. In some regions, the flux variation is sudden. For instance, when neutrons, not entirely thermalized (epithermal energy), get back through the fuel pellet, they face U238 whose absorption cross-section present resonances (see again Figure 6-1). As a result, in the outer ring of the fuel cell (tens of micrometers), the flux highly decreases for this energy range.

Third, about 10^2 directions may be treated.

The problem dimension is thus 10^{13} (again see again [98]). Given the amount of degrees of freedom, two strategies can be considered:

1. Direct calculations, i.e. without any simplification, through dedicated acceleration and massive parallelism (High Performance Computing) [100].
2. The reduction of the system dimension. In this one, more classical, the flux is solved for homogenized macro-regions and a limited number of energy groups (condensation). The latter approach is possible through a two-steps neutronic calculation scheme. In the first step, 2D fine calculations are performed (lattice calculations) taking into account every fuel heterogeneity. Then, defining macro-regions (homogenization) and a reduced energy mesh (condensation), it is possible to set up homogenized cross-sections preserving the reaction rates calculated with the previous fine energy and spatial meshes. For instance, when cross-sections are homogenized at a fuel cell dimension, the thinnest cell (which was about a couple of millimeters wide), is now of the order of a centimeter. It is a preparation step for larger simulation. The next – second – step is thus the core calculation. It consists in simulating the whole – larger scaled – domain (a full core for instance), defined by the same macro-regions and configured with the homogenized cross-sections obtained at step one. An example of two-steps calculations is in [101].

1.2. *An insight into the tool*

The code used in this part is mainly APOLLO3® [102]. Developed at the CEA, APOLLO3® is a multi-purpose deterministic code, split into two parts specialized in both core and lattice calculations:

- Lattice calculations can process both self-shielding and flux calculations taking into account heterogeneities. In the end they can generate homogenized, condensed, cross-sections which can be used for full core calculations. They are mainly based on Collision Probabilities and the Method Of Characteristics (MOC) through the TDT solver for instance [103]. An equivalence module is also available for the SuPer-Homogenization (SPH) method [104]. In a nutshell, the latter is used for guaranteeing that core calculations using homogenized cross-sections – generated through lattice calculations - can reproduce the reference results found with lattice calculations.

- Core calculations deal with higher scale systems, made of macro-regions defined previously along with the associated pre-generated cross-sections. Two solvers are available in APOLLO3® for computations: MINOS [105] and MINARET [106]. MINARET, used for core calculations in this section, can handle both SP_N (Simplified-P_N) and S_N (Discrete Ordinated) methods, with unstructured meshes.

The code is mainly written in C++ and FORTRAN90, and a computer overlay in Python facilitates the user's data files writing [98].

1.3. *Strategy of the water gaps enlargement modeling*

Whereas Monte Carlo codes have dedicated capabilities to directly model FA bow through 3D native elements [107, 108] (SERPENT-2, MNCP-5, TRIPOLI-4® see chapter 5), doing so in deterministic codes is a harder task: use of cross-sections libraries, extruded-3D geometries, codes optimized for straight FAs, are so many features driving deterministic modeling of bow more complex. In fact, some codes, like SIMULATE3, includes pre-defined functions to facilitate instantiation of FA bow, rather limited (unidimensional and constant) [11, 109]. The user could also define manually a 'gap card' in x- and –y directions to describe FA bow [108].

An example of gap map as used by Berger is shown in Figure 6-2. However, the bowing itself is not simulated by the code; the bowed geometry is described only through the variation of pre-generated cross-sections [108]. At this stage we do not have further details on these cross-sections generation step.

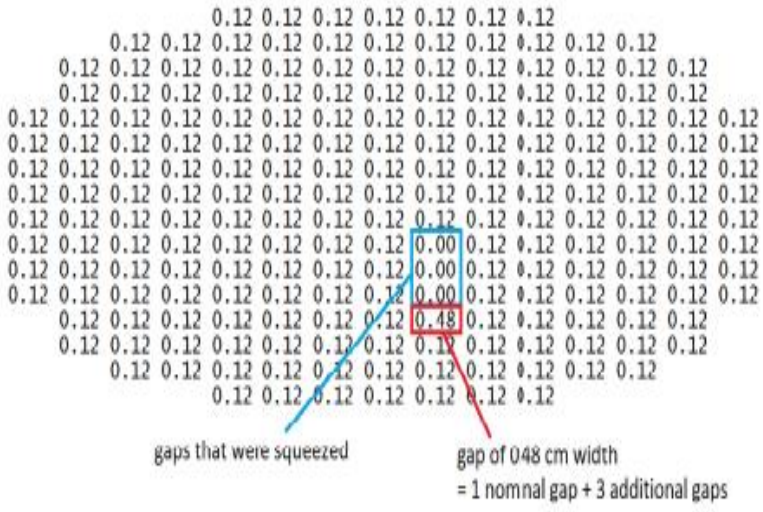

Figure 6-2 - Example of gap card used by Berger [108]

A 'delta gap model' (DGA) was latter implemented in CASMO5 to generate cross-sections of fuel assemblies with varying gaps [110]. The connection with the code SIMULATE5 (allowing 'cosine and 3D shape' bow models [11]) was performed thanks to the linkage code CMSLINK5. CASMO5 can also be used on its own to perform multi-assembly calculations without generating data for further application (in SIMULATE5 for instance). Contrary to neutron noise effects related to rod vibrations whose amplitude is rather small (~1 mm) (see [111] or [112, 113] with DYN3D), fuel bow can pass a couple of centimeters. In other words, in deterministic codes it means that the fuel assembly steps out of its initial cell: as soon as the FA displacement is higher than a half nominal gap (~1 mm) outermost rods of one FA overtake the FA dedicated space [114]. The latter remark leads to a couple of concrete and practical issues:

- First, generating cross-sections with only one assembly leads to overemphasize the

gaps surrounding it. It does not represent in theory the flux seen by an isolated and deformed FA in a core set up.

- Second, in order to provoke such gaps in a real configuration, one has to consider an important number of FA. It could be complicated to model such configurations in a lattice code, with a limited number of FA without isolating one displaced FA.

For these reasons, Li in [107, 20], had to restrict the displacement of fuel pins and FAs in the calculations. In other words, as said by Li 'For the channel bowing, the displacements are prohibited from crossing the mid-planes of the inter-assembly gaps in the case of no insertion of control blades'. The author thus used maximal displacements of 1.5 mm rightwards for the assembly model, and maximal diagonal displacements of 1.5 mm at the full core scale. Rochman [115] also restricted his FA displacement to 1.5 mm with the same code CASMO5 (Figure 6-3). However such displacements are too low to depict actual in-core ones which can reach 20 mm. A couple of different other methods exist, with the assumption that all FAs stay straight (not bowed) but modifying instead densities or cross-sections according to the gap increase [114, 116, 117]. The use of limited displacements is often associated with a need of modifying deeply the geometry otherwise, because fuel rods indeed crop adjacent cells. In the present chapter we thus propose a strategy to depict strong displacements, up to 20 mm.

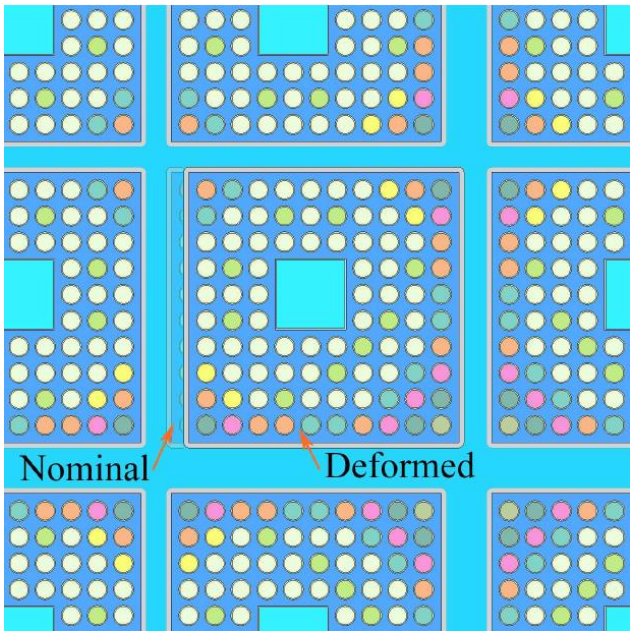

Figure 6-3 - Displaced central FA in a a cluster of 3x3 BWR FAs, from [115]

1.4. *The proposed deterministic strategy to take FA bow into account*

In order to perform deterministic calculations, we have chosen a classical two-steps scheme, in 2D. The latter is mandatory as a future 3D modelling would be based on the same 2D cross-sections. In other words, the current work is a prospective one toward a 3D deterministic modeling strategy. The first step consists in generating a library of cross-

sections over a well-chosen geometry. We homogenize the cross-sections at the pin scale. Our assumption is that the fuel assembly quarter facing up to the adjacent water gap can be characterized by its thickness. The latter will have to be checked to ensure the modeling reliability. As a result, the four areas of the FA (let us say east, south, west and north) – see Figure 6-4 - contain cross-sections at the pin scale which *only* depend on the corresponding water gap (let us say λ_e, λ_s, λ_w, λ_n).

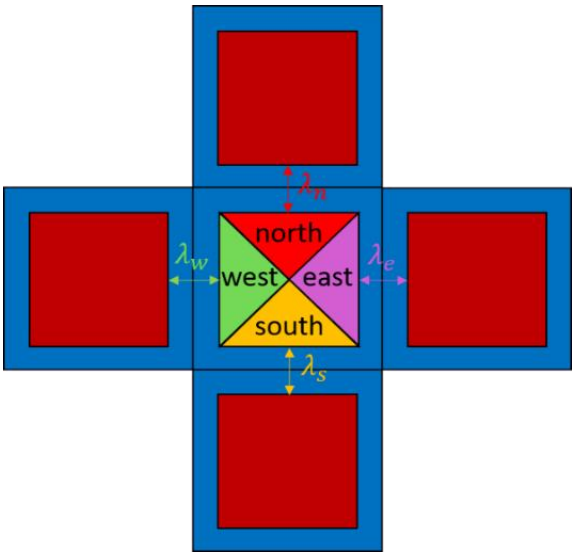

Figure 6-4 - FA and surrounding gaps

This assumption, which could be justified through the small mean free path in a PWR, is however rather strong given that it requires every FA quarter not being influenced by its adjacent neighbors at first order. Formally it assumes that every cross-section can be written $\Sigma_i = f(\lambda_i)$ (i being e, s, w or n). The latter is motivated by the number of calculation needed for further dependencies. In fact, dependency on two variables makes no sense as automatically, for instance if Σ_w depends on λ_n, it necessarily also depends on λ_s. Consequently, without the one-variable dependency, one would have to directly deal with three variables. Even more, the extreme case is dependency on every variable, *i.e.* $\Sigma_i = f(\lambda_e, \lambda_s, \lambda_w, \lambda_n)$. However both three variables and four variables cases lead to a great sampling (for instance with 10 values of λ, 1540 different combinations are necessary with 4 gaps and 1000 with 3 gaps) to correctly describe cross-sections. Thus, we need a simplification to generate in a library, and this assumption is consequently $\Sigma_i = f(\lambda_i)$ as expressed above.

After this assumption is investigated over a couple of physical values of interest, the next step will thus consist in running upper scale calculations while upgrading the field of λ_i according to the two FA quarters surrounding it.

2. Generating a library of cross-sections in a mini-core context

We have chosen to run flux calculations at a core scale based on a classical two-steps scheme with APOLLO3®.

2.1. *The geometry*

In this context, we have decided to generate a cross-sections library leaning on a dedicated geometry taking on board gaps which can be up to 20 mm wide. The geometry of reference is the same as underlined in [114, 118], i.e. a cluster of 5x5 fuel assemblies. The latter choice is a compromise between having enough fuel assemblies to depict a full core behavior (given that flux effects of high deformations can spread over 4 fuel assemblies [6]), and the geometry is small enough so that the calculation can be run in affordable time (~10 hours) with the code APOLLO3® while respecting memory limits. The corresponding nominal geometry is sketched in Figure 6-5. All geometries have been set up with the ALAMOS module of SALOME [119].

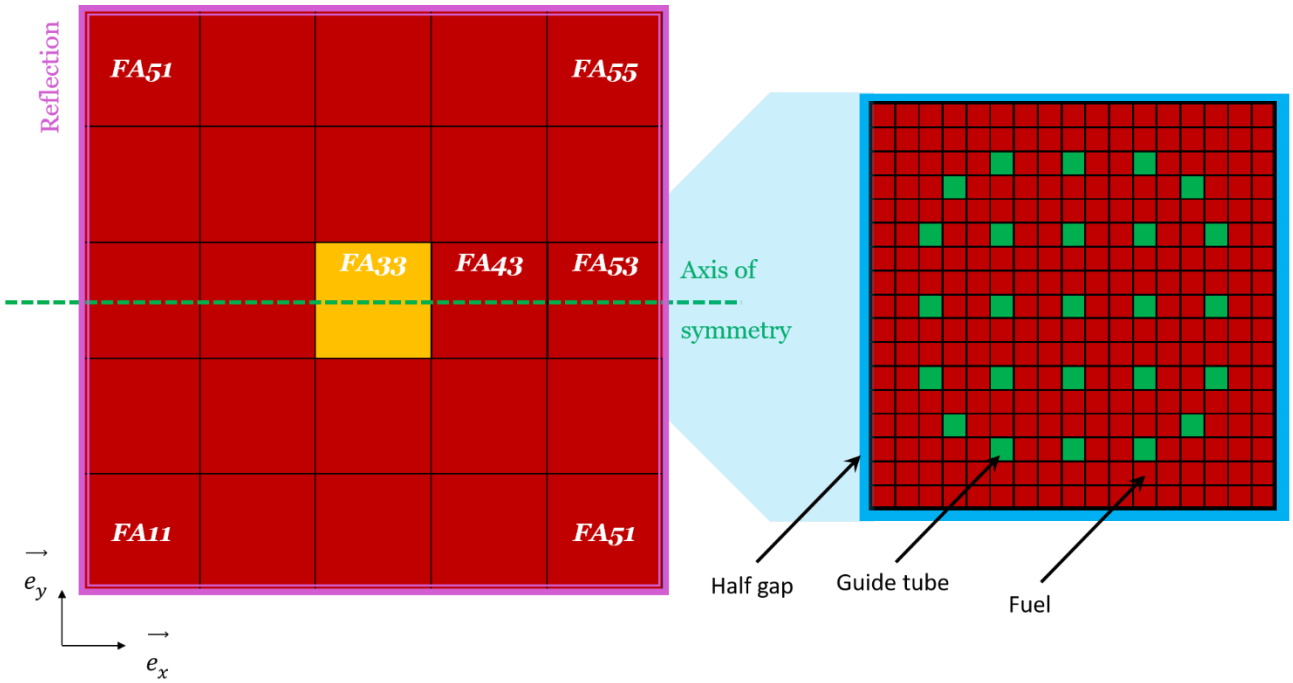

Figure 6-5 - Nominal geometry

In the figure FAXY represents the FA on column X and row Y. By symmetry, FA11 and FA51 are respectively the same than FA51 and FA55. In the zoom in the fuel assembly at the right hand side, guide tubes (control rods not slotted) are present in cells filled with green plain color, whereas the gaps and fuel are present in cells filled with blue and dark red plain colors. At this stage the cluster is surrounded by reflective boundary conditions. A further use of cross-sections for full core calculations would lead to the introduction of leakage models.

Considering that nominal gaps are 2 mm wide, the geometry with fixed boundaries can depict, in theory, gaps up to $1 + 1 + 4 * 2 = 10\ mm$ pushing all FAs within one row to the core shroud (one millimeter on the shrouds – because of reflective boundary conditions -, and 2 between the FAs). With reflective boundaries it would lead to a 20 mm gap. On the other hand, the gap at the other end would be completely closed.

A less drastic solution would consist in pushing for instance 2 FAs to one way and the 3 others at the other end (for instance in [114]), resulting in a 10 mm wide water gap. On the other hand, two gaps would be closed at each side of the row. The issue is summed up in Figure 6-6.

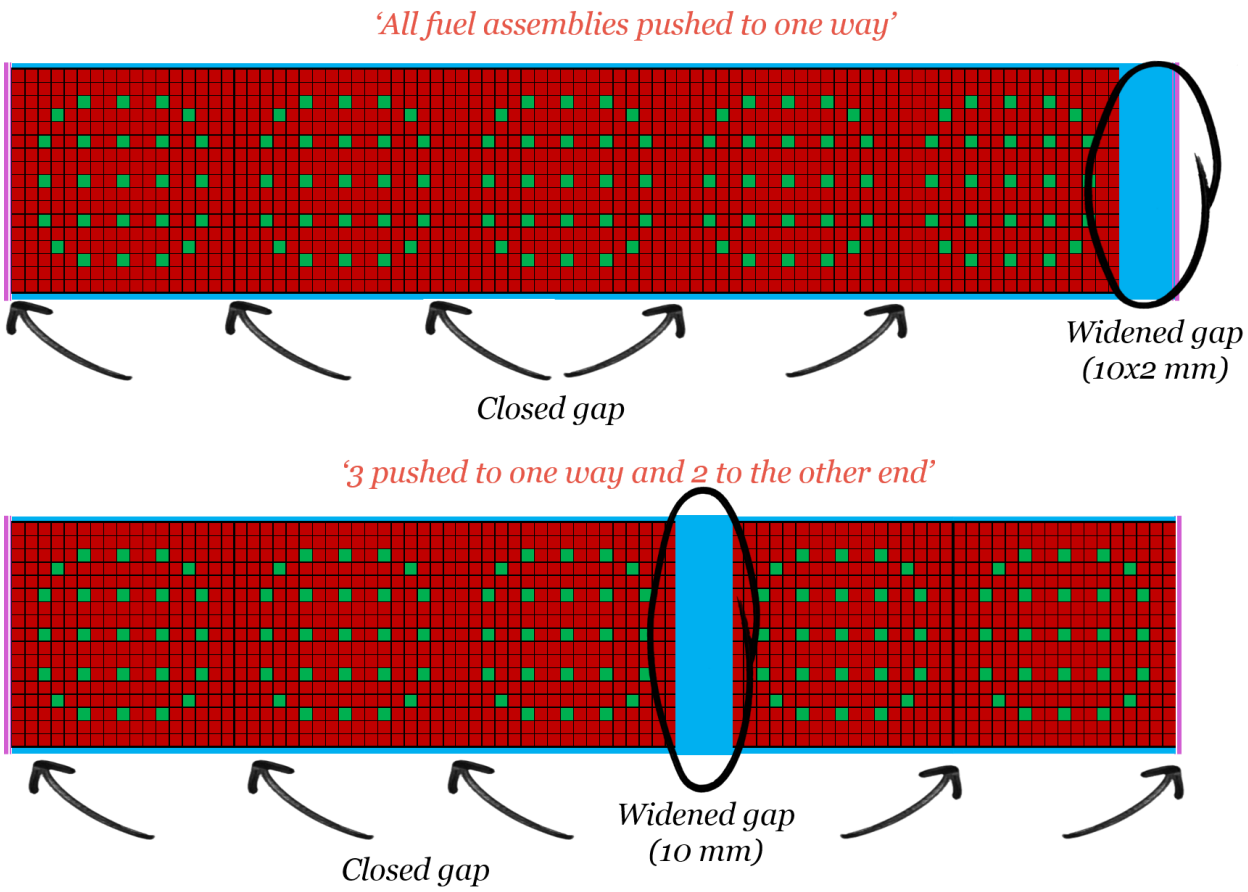

Figure 6-6 - Different solutions to enlarge a gap with fixed boundaries

With every solution leading to large gaps enlargement, every FA is displaced with closed gaps. The only way not to disrupt other FA is to limit its displacement in its dedicated space (i.e. a displacement limited to 1 mm [107]). However, an alternative solution can be proposed to isolate one FA without disrupting the others. The method is suggested hereafter.

In order to generate localized gaps whose value can reach 20 mm, we will process as follows:

- The gap located to the east of FA33 is changed.
- To conserve nominal gaps values between assemblies FA43 and FA45, they are both shifted to the right hand side.
- The water gap located at the east of FA53 is preserved.

Under these assumptions, all happens as if only FA33 was disrupted in an infinite medium. The resulting geometry (at the mini-core scale) is shown in Figure 6-7. The values of gaps considered are 0, 0.4, 2, 3, 5, 8, 12, 16, 20 and 25mm.

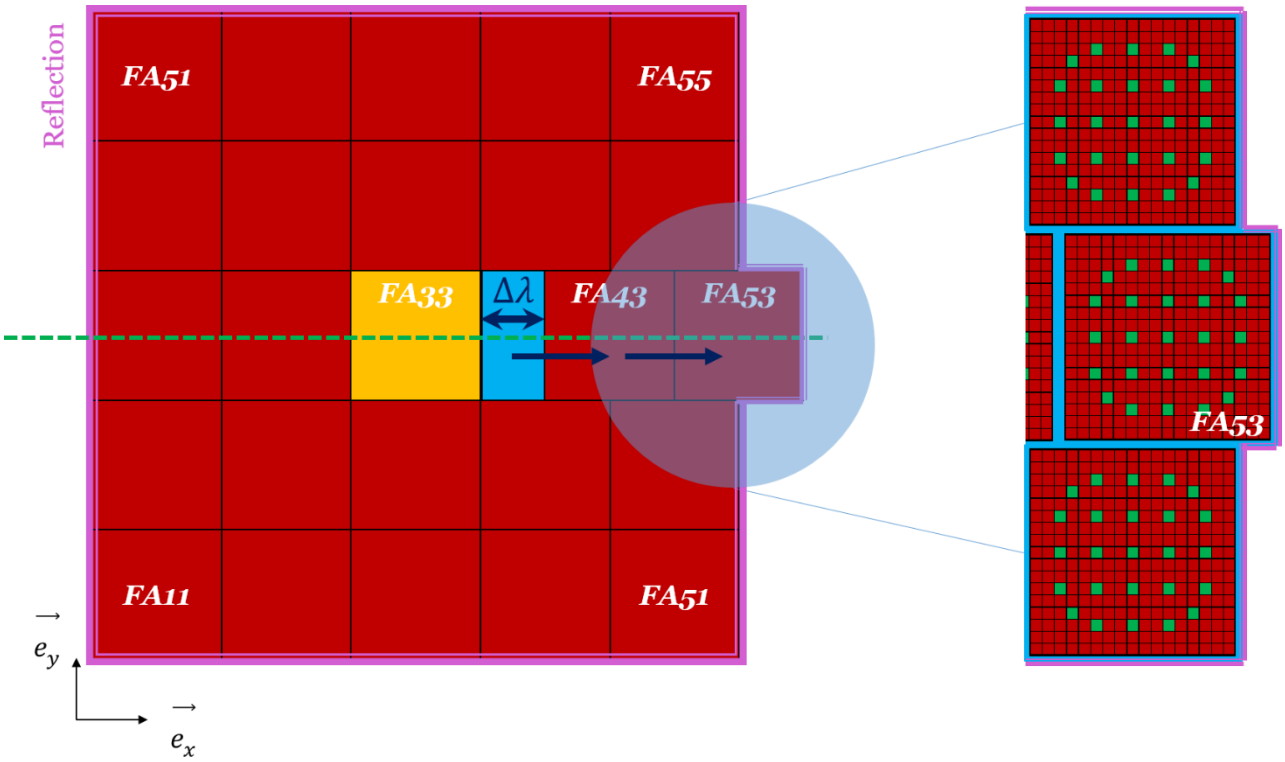

Figure 6-7 - Introduction of a Δλ water gap at the east of FA33

We can see that when fuel assemblies FA53 and FA43 are shifted to the right hand side, the nominal gap located between FA33 and FA43 widens so that its width becomes $\lambda = \lambda_{nominal} + \Delta\lambda\ (mm)$. For a set of λ up to 20 mm, those calculation can reproduce a gap enlargement isolated at the east of FA33. Every other FA - except FA43 obviously – preserves its nominal gaps at the east, south, west and north.

In practice, such a geometry is possible with a Monte Carlo code, for instance TRIPOLI-4®. However, for a lattice code, which needs to proceed an infinite medium based on axes of symmetry, the protrusion shaped by FA53 at the right is not possible. In order to preserve this logic, the same geometry is modelled, but regions are added on the top and bottom of the protrusion to turn the shape into a classical rectangle.

To fill up the new areas, we have chosen an inert material. In our case it is made of helium traces. The impact of this choice will be further assessed. The layout is in Figure 6-8.

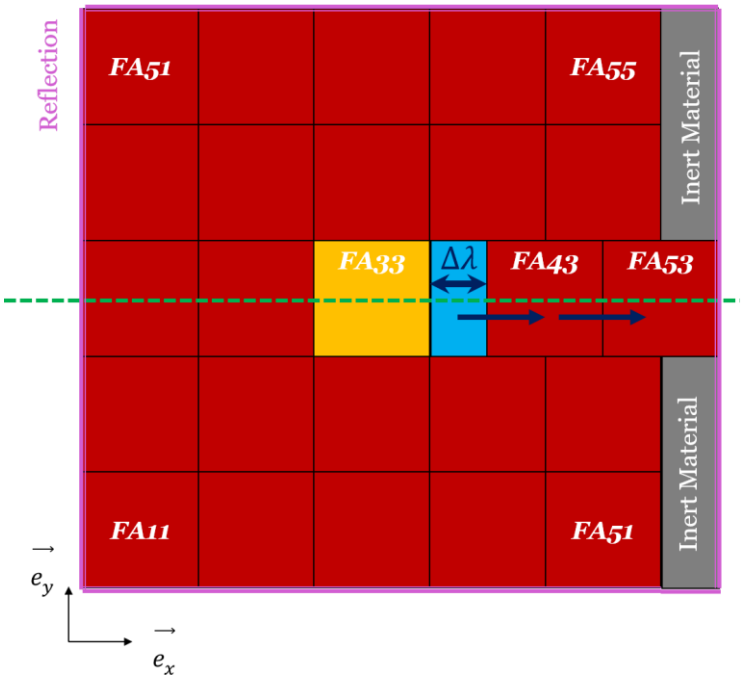

Figure 6-8 - Δλ water gap and inert material

The change introduced in this geometry for the APOLLO3® calculation does change the boundary conditions at the right. Even though no interaction happens in the inert material, the reflection is postponed further in the geometry. As a result, this geometry will need a validation afterwards with respect to a TRIPOLI-4® calculation (which can handle the protrusion) in order to ensure that its impact over the FAs is negligible.

2.2. *From self-shielding to homogenization*

The flux calculation in lattice calculations generally go through three different inner steps along with three different geometries (Figure 6-9): self-shielding (STEP 1), flux calculation on a thinner mesh (STEP 2), and finally homogenization (and condensation) on a coarser mesh (STEP3).

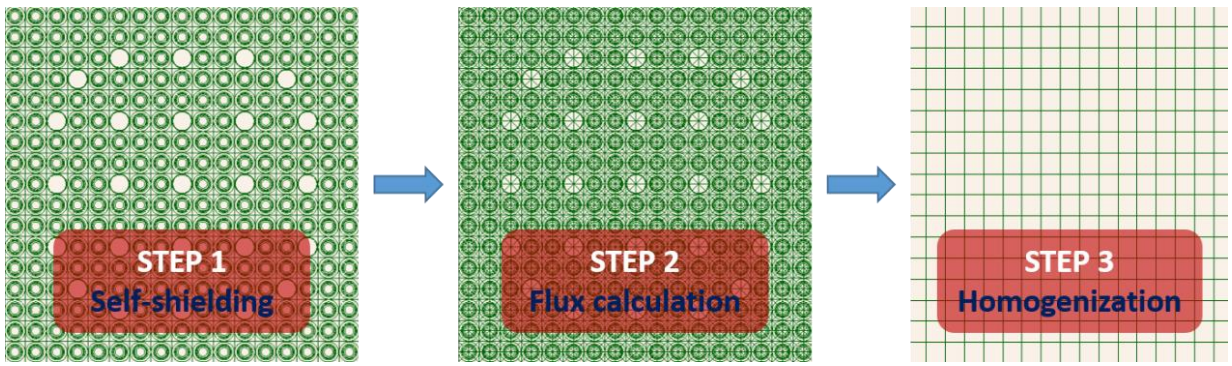

Figure 6-9 - Geometries of one FA, from left to right: self-shielding, flux, homogenization

The configuration of interested is characterized as follows:

- ❖ The fuel assemblies' composition is homogenous geometry-wide without previous irradiation. Every FA is composed of the same densities of isotopes.
- ❖ The FA composition is only made of new fuel characterized by a 5% enrichment of uranium 235 (U5). No plutonium exists.
- ❖ The boric acid concentration is 1800 ppm.
- ❖ The conditions are thus close to a beginning of cycle (BOC) of a starting core (see [5, 10]) for general statements about French PWRs).

Such a simplified composition is yet justified by the fact that tilt phenomena – which may result from FA bow - (increase of the Quadrant Power Tilt Ratio [120, 5]) may occur even at the start of the reactor [4].

STEP 1 – Self-shielding

Regarding the self-shielding, the calculation is performed:
:

- ❖ Through the Livolant-Jeanpierre model based on the slowing-down equation of the neutrons in a context of infinite and homogenous mixture.
- ❖ The angular dependency is removed and thus self-shielding calculations are realized with P_0 scattering cross-sections (i.e. isotropic scattering), see for instance [121].
- ❖ The latter model factorizes the flux as a product between a slowly varying function (asymptotic flux) which is the solution of the slowing-down equation within the moderator, and another one being the fine-structure flux whose value is one outside of resonances while capturing the local behavior of the flux in the vicinity of cross-sections peaks.
- ❖ This factorization leads to the fine-structure equation which is often solved through the Collision Probability method. A space and energy equivalence is processed to obtain self-shielded cross-sections.

Further details are available for instance in [97, 98, 122, 123].

In our case, the self-shielding is done on one single FA to preserve time and memory for calculations. Self-shielded isotopes are the ones presenting with resonances i.e. uranium isotopes (U8, U5), and natural zirconium and iron.

A zoom in the geometry used for the calculations is available in Figure 6-10.

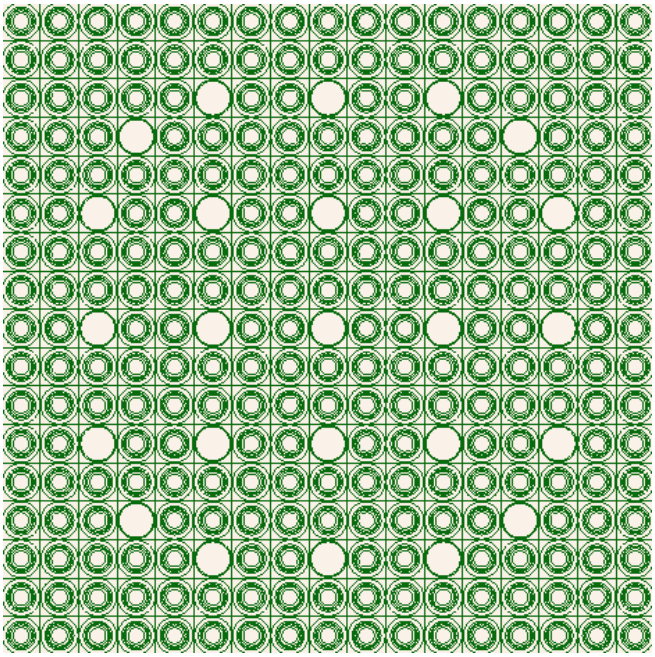

Figure 6-10 - Geometry used for the self-shielding (~2 10^3 regions, 264 fuel rods and 25 guide tubes per assembly)

STEP 2 – Flux calculation

After having introduced self-shielded cross-sections, it becomes possible to run a flux calculation with 281 groups of energy. In this part we make use of the MOC (Method Of Characteristics) available in the TDT solver of APOLLO3® lattice. P_3 scattering cross-sections are used at this step (anisotropy degree of 3) as advised for instance in [124]. Consequently, unlike the previous step, the cells have to be refined and are thus split into eight sectors.

A zoom in the geometry used is available in Figure 6-11.

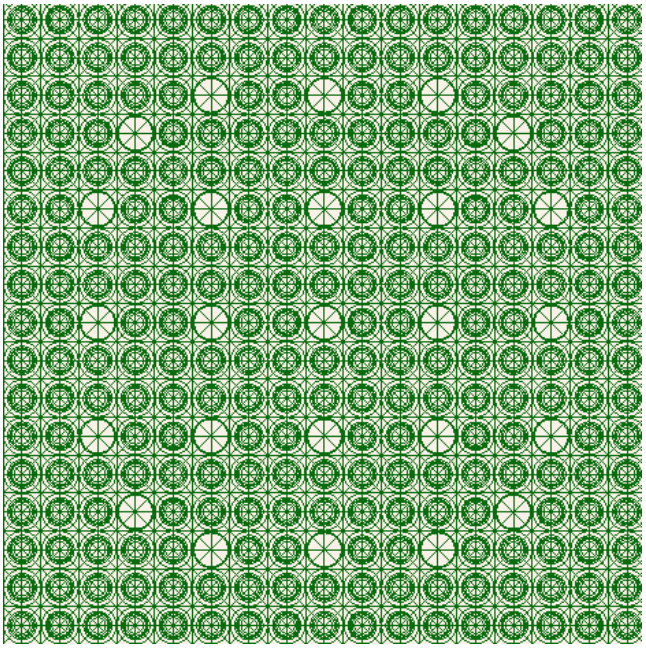

Figure 6-11 - Geometry used for the flux calculation (~1.6 10^4 regions per assembly)

STEP 3 - Homogenization

Once the flux has been calculated in the refined mesh, the next and final step in the preparation of cross-sections is to condense and homogenize the cross-sections. Condensation consists in reducing the number of energy groups, while homogenization leads to considering macro-regions containing a 'homogeneous dough'. The choice of macro-regions is up to the user through the geometry of homogenization, yet it is an important choice given that it will directly affect the elementary mesh of core calculations. Homogenization have long been performed at a full FA scale (all the FA cross-section is homogenized) [125], however improvements in technical specs have made homogenization at the pin cell become the norm.

The geometry that we used for homogenization is shown in Figure 6-12.

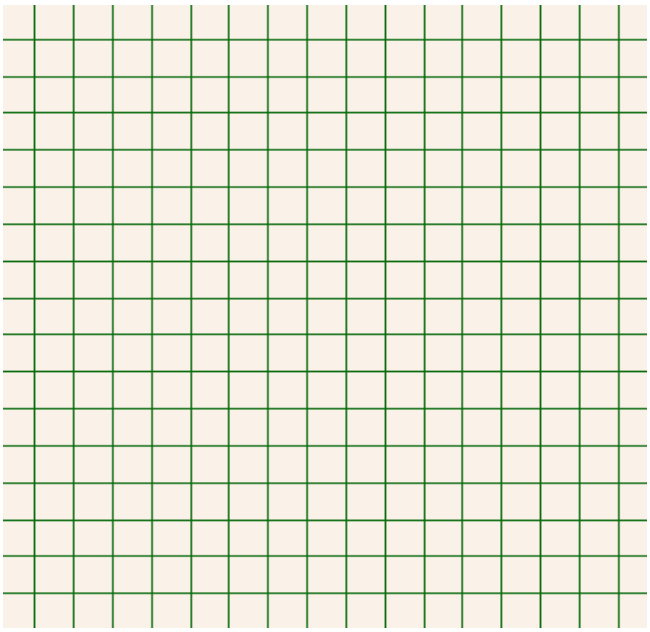

Figure 6-12 - Geometry used for the homogenization (one macro-region per fuel rod)

2.3. *About step 2 – flux calculation – and comparison with reference simulations*

In fact, before pulling homogenized cross-sections from the calculation, we want to make sure that the flux calculation performed gives the same results as given in a reference code, TRIPOLI-4®, through the use of simple 3D-extruded straight rods. The Monte Carlo geometry is the same as shown in Figure 6-7. In other words, no inert material complete the deformed cluster as the code can handle so.

In TRIPOLI-4® simulations the parameters are the following:

- 10^4 neutrons are simulated per cycle (batch size).
- A maximum 10^5 cycles is demanded.

- ❖ 80 cycles are discarded.
- ❖ For the gap between FA33 and FA43 we chose values of 0.4, 2, 5, 12 and 20 mm.

In practice, such a mini-core simulation is long with the Monte Carlo method, and no calculation ended up reaching the maximum of 10^5 cycles (because of the time allocated on the calculation server), but rather $\sim 10^4$ cycles. The layout is shown in Figure 6-13, the gaps surrounding FA33 were highlighted in light blue. One can see the coolant in dark blue, the fuel pellet in red and the cladding in green. In order to compare reaction rates, all APOLLO3® (AP3) calculations were normalized to the total production rate in the TRIPOLI-4® (T4) calculations. Error bars stand for $3\sigma_{T4}$ intervals.

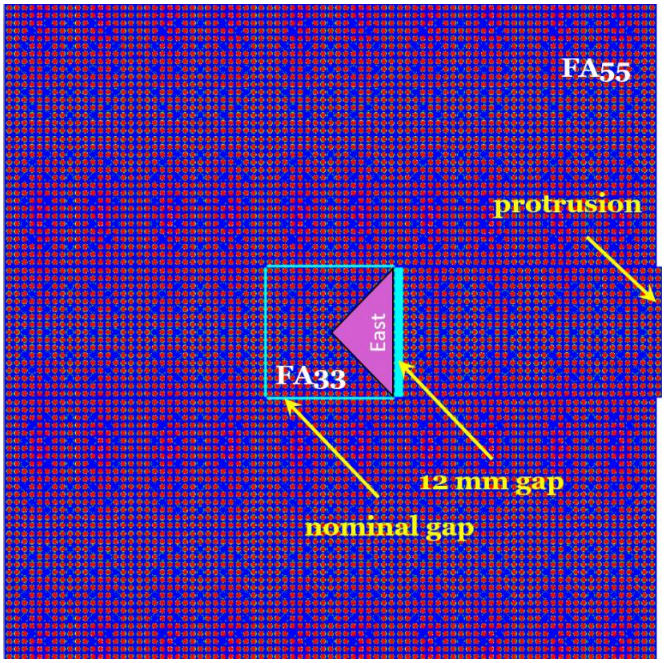

Figure 6-13 - Monte Carlo geometry as seen by the T4G viewer

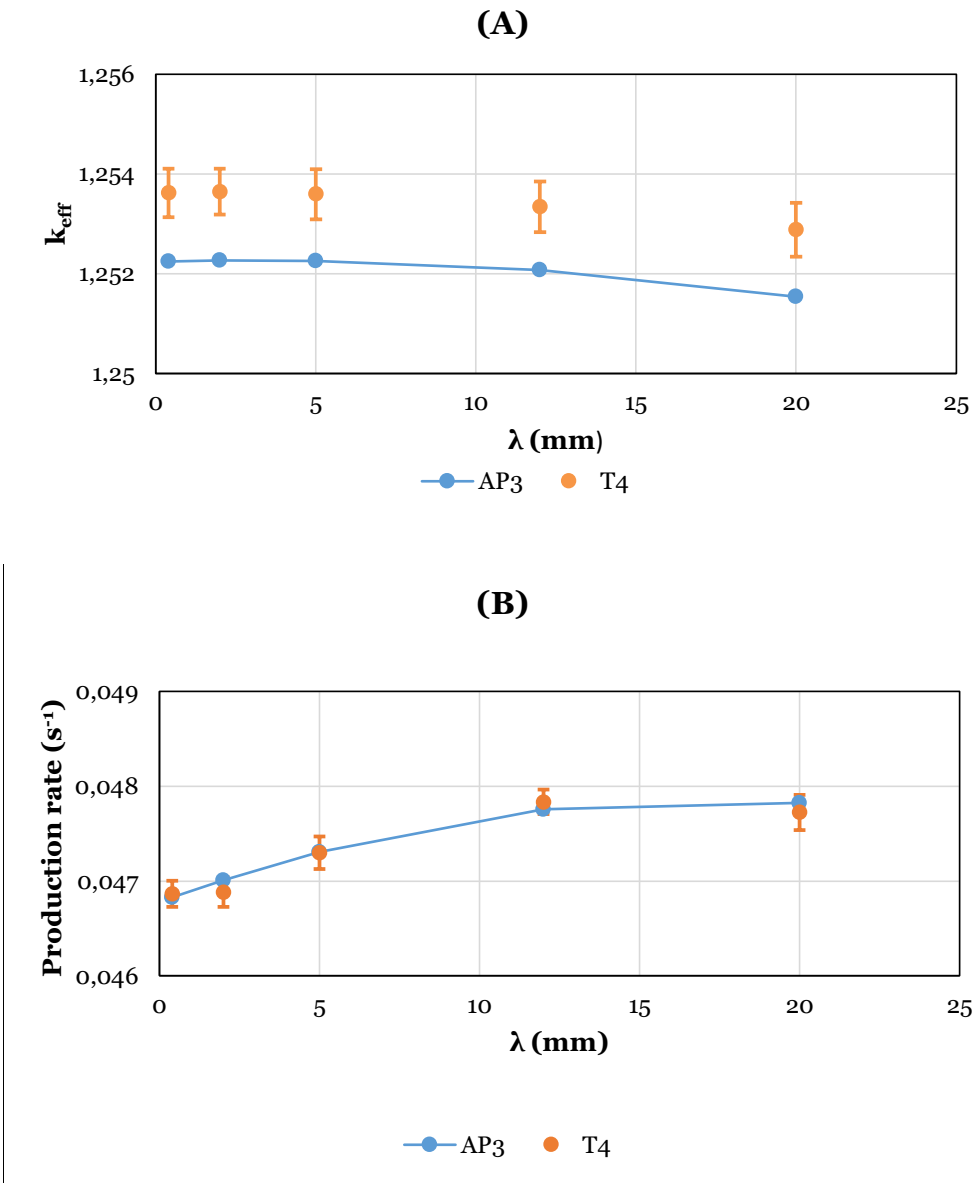

Figure 6-14 - (A) Multiplication factor k_{eff} evolution (B) production rate induced by U5 (FA33) (σ_{T4}<1% for rates, σ_{T4}<30pcm for k_{eff})

In Figure 6-14, we plot the comparison in terms of multiplication factor and integrated production rates in the disrupted central assembly FA33. The values are given with respect to the width λ of the gap at its west.

As one can see, in terms of multiplication factor k_{eff}:

- No calculation matches the ones given by the Monte Carlo method even including the error bar.
- The difference between two points is quite constant whatever the value of the gap is. In other words, considering the uncertainty of about 20 pcm with the Monte Carlo method, the difference between both two approaches is constant for every considered gap (0.4, 2, 5, 12 and 20 mm).
- The difference is around 130±10 pcm which is a result more than satisfactory for our case and our requirements when comparing deterministic results to stochastic ones

(best practice typically expects deviations lower than 200 pcm).

This constant deviation between both methods can be due to a couple of simplifications or numerical schemes from the self-shielding step to the flux calculation one (for instance, meshing, self-shielding parameters, …).

It means that in terms of k_{eff} the deviations are due to the deterministic model itself, and not the gap widening introduced.

One can see in Figure 6-14(A) that 4 other points were added (respectively for 3, 8, 16, and 25 mm), these states serve as additional points to supply our future cross-sections library.

In terms of local FA production rates, every point obtained with the deterministic approach is in the 3σ range obtained with TRIPOLI-4®. In order to further address the differences between both simulations, we compiled in Table 6-1 compiled results obtained for production rate in U5 (Figure 6-14 (B)) and absorption rate in U8 (as advised in [114]).

λ (mm)	Prod. U5 (%)	Abs. U8 (%)
FA33		
0.4	0.07	0.16
2	0.27	0.58
5	0.03	0.50
12	0.16	0.21
20	0.21	0.64
FA55		
0.4	0.44	0.09
2	0.30	0.21
5	0.79	0.29
12	0.53	0.69
20	0.67	**1.18**

Table 6-1 - Comparison of reaction rates |T4-AP3|/T4 for different gaps and FAs (σ_{T4} < 1%)

This table reads as the relative deviation between both codes with TRIPOLI-4® as the reference, for reaction rates, in two different FAs: 33 and 55. U5 production rate in FA33 has already been highlighted in Figure 6-14. The choice of FA33 and FA55 has been justified through their location: FA33 is the central assembly facing the gap widening, whereas FA55 comes up to the inert material and is the direct witness of the change of boundary conditions at the right hand side of the geometry (Figure 6-8).

First of all, one can notice that deviations are rather small, compared to our deterministic modeling expectations. The maximal one (1.18% in bold) is obtained for the U8 absorption in FA55 when the gap is 20 mm wide. In this extreme case the U8 rate given by AP3 is only '20 pcm' far from the error bar. The deviation, in this assembly, increases as the gap widens. The latter is related to the inert material widening (the inert part is as wide as the gap). In terms of production rate, it is included in a [0.3, 0.8] range with a minimum reached for the nominal case (undisturbed geometry). It shows that postponing the reflection conditions by a gap

distance away has quite an impact on absorption for the wider widths, yet it remains fully acceptable. In other words, adding inert material still locally depicts the behavior of the original cluster as simulated by T4, even though a small deviation appears at the right hand side for both production and absorption rates.

Regarding FA33, which is close to the gap, in terms of U5 the gap impact is invisible as highlighted above. Slight deviations appear for U8 regarding 2, 5 and 20 mm gaps. However, they remain widely acceptable (less than 5 pcm in terms of absolute deviation).

λ (mm)	Prod. U5 (%)	Abs. U8 (%)
East Qu.		
0.4	0.41	0.07
2	0.31	0.62
5	0.06	0.77
12	0.39	0.33
20	0.50	0.12

Table 6-2 - Comparison of reaction rates in FA33 east quarter |T4-AP3|/T4 for different gaps and FAs (σ_{T4}<1%)

Table 6-2 is a zoom in the east section of the FA33 (see Figure 6-13). It represents the quarter of the FA directly in contact with the gap enlargement. As one can see, the deviations are really small (the absolute deviation is about a few pcm).

The results given by the flux calculation are satisfying with respect to the reference obtained with Monte Carlo. In other words, we can consider that these calculations can be the starting point to generate the library cross-sections. For a 20 mm gap a power increase in FA33 of 2% is observed, whereas it is about little less than 1% for 5 mm.

2.4. *About step 3 – homogenization –*

From now on, the next inner step consists in homogenization and condensation. In our case, we will consider 20 groups of energy. To do so, we need a geometry of homogenization (Figure 6-12). The goal of this step is to generate the cross-sections associated with FA33, which will be used to depict the behavior of a core calculation in any configuration of interest.

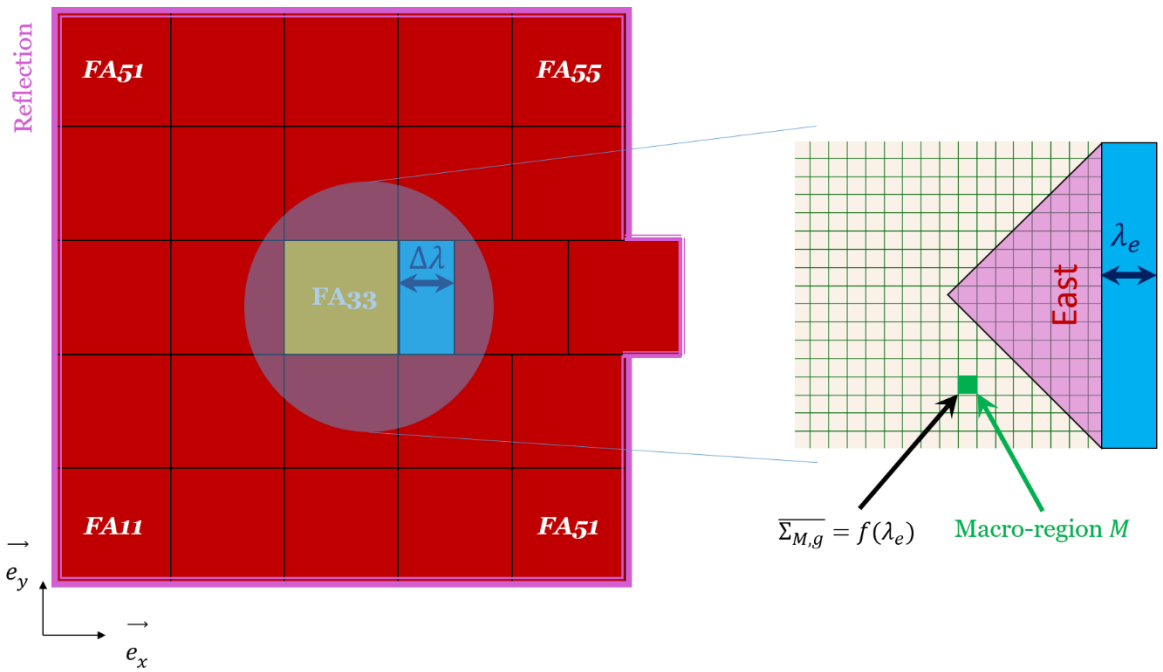

Figure 6-15 - Cross-sections' homogenization from APOLLO3® lattice

Once the flux is obtained in all the geometry, we homogenize at the pin scale (Figure 6-15). The goal of this step is to preserve the reaction rates, so that [125]:

$$\overline{\Sigma_{M,g}} = \frac{\sum_{m\in M} V_m \Phi_{m,g}\Sigma_{m,g}}{\sum_{m\in M} V_m \Phi_{m,g}} = \frac{\sum_{m\in M} V_m \Phi_{m,g}\Sigma_{m,g}}{V_M \overline{\Phi_{M,g}}} \qquad \text{(Eq. 6-2)}$$

V_M is the volume of region M, $\overline{\Sigma_{M,g}}$ is the cross-section in group g in M (see Figure 6-15), $\overline{\Phi_{M,g}}$ is the associated averaged flux. V_m is the volume of micro-regions making up M (cladding, pellet, …), $\Sigma_{m,g}$ is the cross-section in group g in m, and $\Phi_{m,g}$ is the associated flux.

In APOLLO3®, The homogenized cross-sections $\overline{\Sigma_{M,g}}$ are stored in a MPO (MultiParamOutput) in the form of a HDF file (a format to store large amounts of data).

Each cross-sections obviously depends on the width λ as all $\Phi_{m,g}$ depend themselves on the water gap at the east of FA33 (Figure 6-15). Consequently, every $\overline{\Sigma_{M,g}}$ is stored along with a 'UserParameter', in this case λ (state point). The code is then able to interpolate every $\overline{\Sigma_{M,g}}$ according to the state points (as a reminder, we run calculations for λ=0, 0.4, 2, 3, 5, 8, 12, 16, 20 and 25 mm).

2.5. *Toward the validation of the cross-sections' independency assumption*

As mentioned above, nothing guarantees that the cross-sections *only* depends on one gap (in this case that $\overline{\Sigma_{M,g}} = f(\lambda_e)$), especially for large gaps. This assumption has to be checked *a fortiori* reusing the cross-sections when two gaps are changing together.

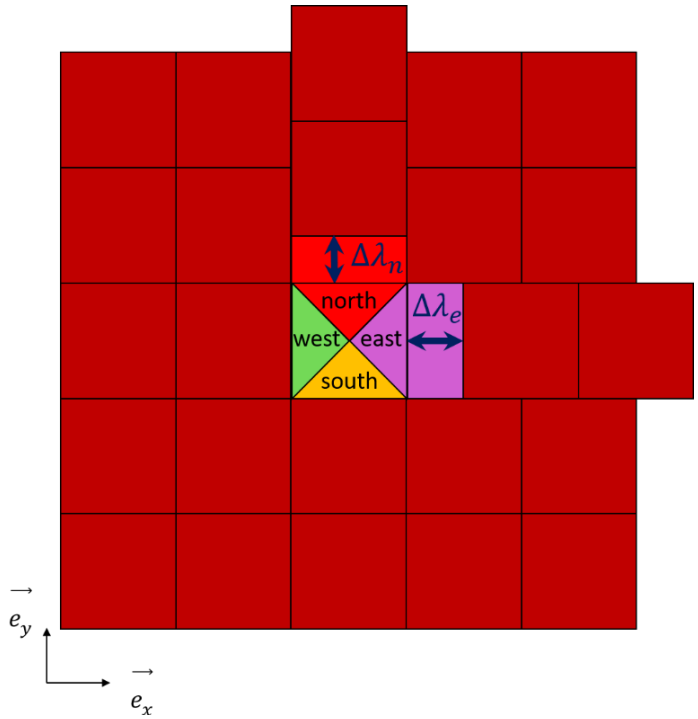

Figure 6-16 - Mini-core with two enlargements

For instance, in Figure 6-16 this means that the purple section of the FA only depends on the purple gap, and that the red section only depends the red gap.

We also need to export cross-sections related to water regions, but the difference with fuel regions is that in theory they do not depend on the gaps width at all. Indeed, in those regions there is only one volume filled with water, so that (Eq. 6-2) simply gives $\overline{\Sigma_{M,g}} = \Sigma_{m,g}$.

3. Using one-variable dependent cross-sections within a 2D geometry in a core solver

3.1. *Equivalence within a core calculation*

Once the library is generated, an intermediate step is necessary to ensure its reliability when used in a core context. In fact, when using the homogenized cross-sections in a core calculation, we do not find back the same reaction rates as obtained in the lattice calculation, because the averaged flux obtained in the lattice solver is not the same in the core solver. In other words, we need to modify the cross-sections so that the simulation run with macro-regions gives the same reaction rates.

A set of so-called SPH (SuPer-Homogenization) factors [104] are thus associated with homogenized cross-sections to preserve the reactions rates obtained in the lattice calculation macro-regions. Equations of SPH factors $\mu_{M,g}$ are (from [125]):

$$\Sigma_{M,g} = \overline{\Sigma_{M,g}}\,\mu_{M,g} \qquad \text{(Eq. 6-3)}$$

Where $\Sigma_{M,g}$ is the total cross-section in the macro-region M, used for the core calculation and g is the group. $\overline{\Sigma_{M,g}}$ is the lattice total cross-section obtained with a lattice calculation. In practice, only one reaction is essential as every reaction cross-section are proportional to the associated reaction rate. In APOLLO3® this is the total cross-section. The goal is thus to satisfy the following reaction rates equation (Eq. 6-4):

$$\Phi_{\mathrm{M,g}}\Sigma_{M,g} = \Phi_{\mathrm{M,g}}\overline{\Sigma_{M,g}}\,\mu_{M,g} = \overline{\Sigma_{M,g}}\,\overline{\Phi_{\mathrm{M,g}}} \qquad \text{(Eq. 6-4)}$$

Where $\Phi_{\mathrm{M,g}}$ and $\overline{\Phi_{\mathrm{M,g}}}$ are the core and lattice scalar fluxes (angular flux integrated in angle), $\mu_{M,g}$ is obtained through [98]:

$$\mu_{M,g} = \frac{\overline{\Phi_{\mathrm{M,g}}}}{\Phi_{\mathrm{M,g}}(\,\mu_{M,g})} \qquad \text{(Eq. 6-5)}$$

In practice, this equation (non-linear) is solved using a fixed-point algorithm included in APOLLO3®, for every groups and regions. We used the MINARET solver along with the S_N method. Once the set of $\mu_{M,g}$ preserving the reaction rates with respect to the reference calculation are found out, they are exported in the library to be taken into account in core calculations.

This operation has been undertaken beforehand for our 10 state points (we run calculations for λ=0, 0.4, 2, 3, 5, 8, 12, 16, 20 and 25 mm as said in 2.4).

3.2. *Configurations of interest*

Four configurations were undertaken to judge for gaps independency two at time. They are summed up below.

- (A). Two water gaps (east and north) have the same value ($\lambda_e = \lambda_n$).
- (B). The same water gaps vary but this time $\lambda_e \neq \lambda_n$.
- (C). Is a test with 4 very different gaps in FA33 so that $\lambda_e \neq \lambda_n \neq \lambda_s$
- (D). Similar to A., but the gap corner at the top right of FA33 is changed. To do so, FA45, FA54, FA44 and FA55 are also shifted by both right and top displacement value.

Configuration (A) allows to notify if two quarters, characterized by the same cross-sections can reproduce the reference calculation. In other words we, check the respective independency of the north and east gaps against each other. Configuration (B) allows to see if the change in λ is well reproduced by the library, and differs from configuration (A) in that

three different values of gap exist around the assembly. Configuration (C) includes 4 different gaps in the geometry (2, 5, 12 and 20 mm), including almost all studied gaps. Finally, configuration (D) has been set up to study the impact of a corner widening in the assembly with large gaps. In fact, in PWRs, the corners in the vicinity of the core center can widen due to FAs being deformed radially (the 'barrel' pattern). Other gaps were imposed to the nominal value (2 mm). Every configuration is represented in Figure 6-17.

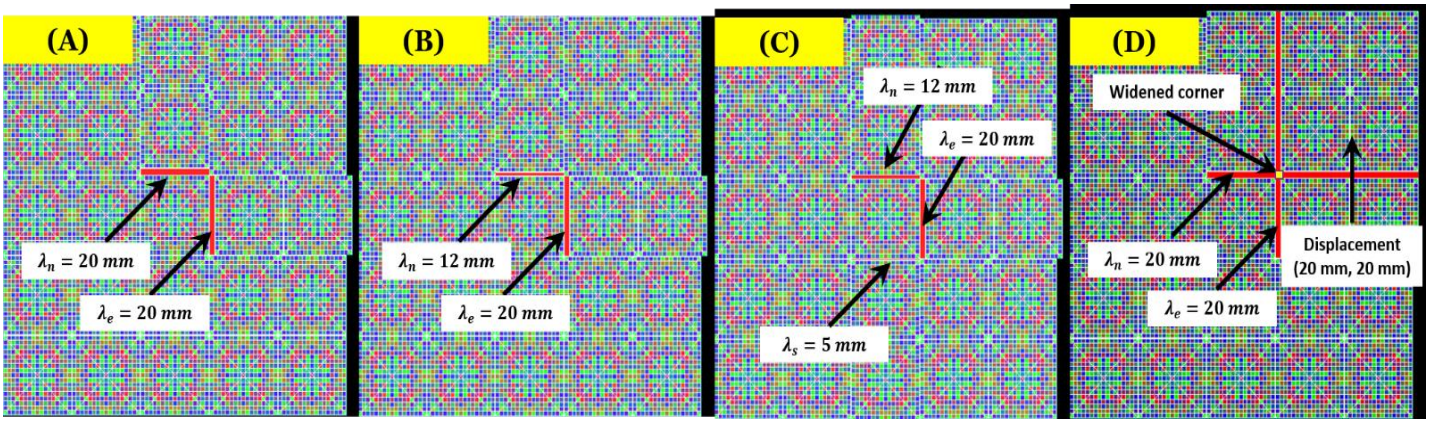

Figure 6-17 - Configurations of interest for the core solver (different colors are used to distinguish the regions, i.e. repeated in each FA half-quarters but including different gap settings)

In fact, in the figure, we can see the domain with every related macro-regions as displayed by the APOLLO3® viewer. Every color stands for the material used in the region. One can see that each quarter of the FAs (east, north, west, and south) is repeated.

However, each quarter's materials are characterized by the user parameter λ. The upgrade of these parameters are performed through a python class 'assembly' imported in an APOLLO3® dataset and used as a subroutine to manage fields and quarters related to each FA.

The values for the numerical tests are summarized in Table 6-3.

Configuration	λ_e (mm)	λ_n (mm)	λ_s (mm)
(A)			
(A-1)	0.4	0.4	
(A-2)	2	2	
(A-3)	5	5	
(A-4)	20	20	
(B)			
(B-1)	20	5	
(B-2)	20	12	
(C)			
(C-1)	20	12	5
(D)			
(D-1)	5	5	
(D-2)	20	20	

Table 6-3 - Numerical tests for each configuration

Corresponding TRIPOLI-4® simulations were also performed for the same configurations, to serve as a reference. Every relative deviations of deterministic calculations will be given with comparison with the latter T4 calculations.

3.3. *Results of configuration (A)*

Config.	Prod. U5 (%)	Abs. U8 (%)		k_{eff} (pcm)
FA33			Cluster	
A-1	0.11	0.38	A-1	138
A-2	0.22	0.51	A-2	139
A-3	0.16	0.04	A-3	123
A-4	0.18	0.06	A-4	129

Table 6-4 - Comparison of reaction rates in FA33 \|T4-AP3\|/T4 and k_{eff} in the cluster - config. (A) (σ_{T4}<1% for rates, σ_{T4}<30pcm for k_{eff})

Table 6-4 sums up the relative deviations between deterministic calculations and the stochastic reference, obtained for reaction rates in FA33 and multiplication factor in the cluster.

In terms of multiplication factor, every deviation is included in the range [123, 139]. Given that the uncertainty about the TRIPOLI-4®calculations are about 20 pcm, one can argue that the deviation is the same for every calculation run. The latter matches the deviation of ~130 pcm that was already observed for the lattice stage, it is thus conserved with APOLLO3® core and the model used for cross-sections (each quarter of assembly characterized by the adjacent gap).

In terms of reaction rates in FA33, both codes are in good agreement. The maximal deviation is 0.51% obtained for absorption at nominal conditions. We could add that in this case the APOLLO3® value is 2 pcm far from the TRIPOLI-4®'s uncertainty interval. In other words, all values are almost mixed up. Thus at the assembly scale, one can say that our model reproduces quite well the effect for two varying gaps with a library set up for one independent gap.

Let us zoom in on the east quarter of FA33 to analyze the same deviations (Table 6-5). The east quarter faces the gap enlargement, so does the north quarter. Yet, in this case $\lambda_e = \lambda_n$, thus one quarter is enough.

Config.	Prod. U5 (%)	Abs. U8 (%)
East Qu.		
A-1	0.08	0.56
A-2	0.28	0.57
A-3	0.46	0.21
A-4	0.59	0.28

Table 6-5 - Comparison of reaction rates in FA33 east quarter \|T4-AP3\|/T4 - config. (A) (σ_{T4}<1%)

In the east quarter, locally, the simulations are in good agreement. The impact of the water gap must be limited enough so that the characterization per quarter seems correct to depict the impact on reaction rates.

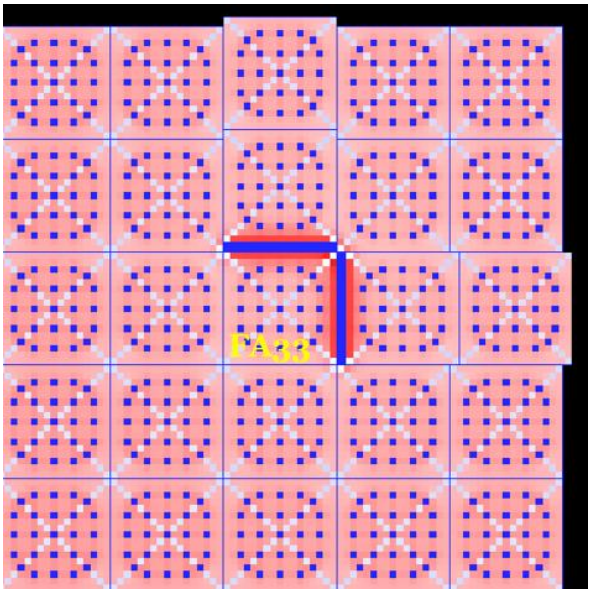

Figure 6-18 - Volume-integrated fission rates in the geometry (A-4)

We see in Figure 6-18 the fission rates in the geometry. The impact of the maximal gap enlargement ($\Delta\lambda = 18\,mm$ with $\lambda_e = \lambda_n = 20\,mm$), is globally strong within the first external rows of FA33 (about 3, in accordance with [6]). The rise in fission rate does not seem to spread over adjacent quarters (west and south). Now, let us take in interest in configuration (B).

3.4. *Results of configuration (B)*

Config.	Prod. U5 (%)	Abs. U8 (%)		K_{eff} (pcm)
FA33			**Cluster**	
B-1	0.13	0.30	**B-1**	142
B-2	0.33	0.01	**B-2**	144

Table 6-6 - Comparison of reaction rates in FA33 \|T4-AP3\|/T4 and k_{eff} in the cluster - config. (B) (σ_{T4}<1% for rates, σ_{T4}<30pcm for k_{eff})

Table 6-6 sums up the results obtained for reaction rates in FA33 and multiplication factor in the cluster in configuration (B). Two different cases were assessed: in every case the east gap is held constant (20 mm), whereas two values were imposed at the north, 5 and 20 mm. Thereby, three very different values of parameters coexist at the same time in FA33, including the nominal value at the west and south gaps (*a priori* the most common value in a PWR).

In terms of multiplication factor, the deviation is a bit higher than in Config. (A) and

almost constant for B-1 and B-2. However, seeing the uncertainty of tens of pcm, one can argue that the deviation is still constant compared with every previous cases. One cannot tell if this higher deviation is due to the presence of 3 different gaps.

In terms reaction rate, every value pulled from the APOLLO3®calculation are included in the T4 uncertainty range. Thus, all value are mixed-up. Configuration (B) is thus well reproduced by our cross-sections library. A zoom in the north and east quarter is given in Table 6-7.

Config.	Prod. U5 (%)	Abs. U8 (%)	Config.	Prod. U5 (%)	Abs. U8 (%)
East Qu.			North Qu.		
B-1	0.71	0.16	**B-1**	0.2%	0.58
B-2	0.66	0.12	**B-2**	0.25	0.30

Table 6-7 - Comparison of reaction rates in FA33 east and north quarter |T4-AP3|/T4 - config. (B)
(σ_{T4}<1%)

The maximal deviations observed are obtained for the production rate in the east quarter (where lies the maximal enlargement). For the production rate in B-1, in the east quarter of FA33 (going with the 0.71% deviation), the APOLLO3® value is only 5 pcm far from the TRIPOLI-4®'s uncertain interval. Globally, higher deviations are obtained for production compared to Table 6-5. This change could be attributed to the use of 3 different gaps from the library whereas FA33 only used 2 values of user parameter for configuration (A).

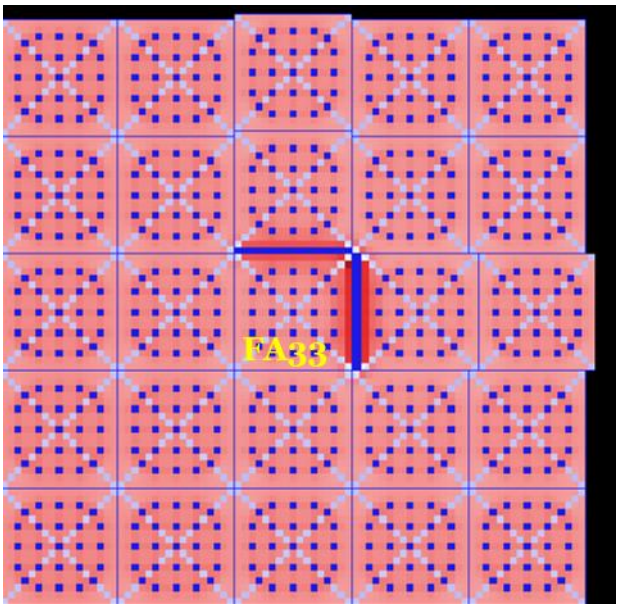

Figure 6-19 - Volume-integrated fission rates in the geometry (B-2)

In Figure 6-19, we can see that the impact on fission rates involved by two gaps enlargement is also held in the rows which are flushing the east and north gaps. This is coherent with the observation in configuration (A) where two large gaps were imposed.

To conclude, the configurations studied in (B) are well depicted by the quarter cutting proposed in the model, even with three different gaps.

3.1. *Results of configuration (C)*

Even if the results seem to highlight an independency for every corner, in (C) every single gap have a different value. At the east we find a 20 mm gap, a 12 mm one at the north and finally a 5 mm one at the south. Obviously, the west gap equals the nominal value.

Config.	Prod. U5 (%)	Abs. U8 (%)		k_{eff} (pcm)
FA33			Cluster	
C-1	0.31	0.61	C-1	140

Table 6-8 - Comparison of reaction rates in FA33 \|T4-AP3\|/T4 and k_{eff} in the cluster - config. (C) (σ_{T4}<1% for rates, σ_{T4}<30pcm for k_{eff})

Table 6-8 sums up the results obtained for reaction rates in FA33 and multiplication factor in the cluster in configuration (C). In terms of multiplication factor, the result is in a similar range compared to (A) and (B). In terms of reaction rates, both TRIPOLI-4® and APOLLO3® are very close to each other regarding this configuration. The rate for U8 obtained with APOLLO3® is included in the error bar of TRIPOLI-4®, so does the rate obtained for U235 In other words the values are the same.

In Table 6-9 we gathered the results regarding both north, south and east quarters.

Config.	Prod. U5 (%)	Abs. U8 (%)	Config.	Prod. U5 (%)	Abs. U8 (%)	Config.	Prod. U5 (%)	Abs. U8 (%)
East Qu.			North Qu.			South Qu.		
C-1	0.45	0.22	C-1	0.02	0.24	C-1	0.77	0.94

Table 6-9 - Comparison of reaction rates in FA33 east, north and south quarter \|T4-AP3\|/T4 - config. (C) (σ_{T4}<1%)

One can see that the east quarter induces higher rate deviations than the north one. It comes with a higher gap width at the east of 20 mm. However, one can notice that the south quarter implies even higher deviations. The latter could be explained by the independency hypothesis: in this case every quarter sees a different gap value. The south quarter, characterized with 5 mm, is surrounded by two large gaps at both north and east (of 12 and 20 mm). Such values might involve overtaking flux effects over the south quarter, which is itself little disrupted compared to a nominal gap (delta of 3 mm). However one has to remind that such a configuration may be exaggerated, as such gaps are unlikely to arise in a core. Secondly, the related effect is less than 1%, which is limited compared to the assumption of independency. In Figure 6-20 we showed a map of fission rate in the configuration of interest. We can for instance notice the difference of gap enlargement impact between the east and the south.

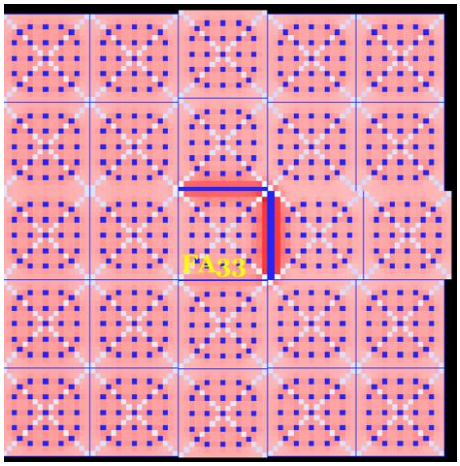

Figure 6-20 - Volume-integrated fission rates in the geometry (C-1)

3.2. *Results of configuration (D)*

In (D) the corner at the top right of FA33 is disrupted so that every FA from 45 to 55 undergo a displacement along the x- and y- axis.

Config.	Prod. U5 (%)	Abs. U8 (%)		k_{eff} (pcm)
FA33			Cluster	
D-1	0.05	0.58	D-1	132
D-2	0.06	0.22	D-2	152

Table 6-10 - Comparison of reaction rates in FA33 |T4-AP3|/T4 and k_{eff} in the cluster - config. (D)
(σ_{T4}<1% for rates, σ_{T4}<30pcm for k_{eff})

In terms of multiplication factor, the deviation in D-2 is a bit higher than before. However, given the uncertainty interval, one can say that the deviation is still conserved compared to (A), (B) and (C).

In terms of production rate in FA33, the deviation is almost nonexistent. In terms of absorption rates, the maximal deviation is 0.58% in D-1. It matches an APOLLO3® value 1 pcm away from the TRIPOLI-4®uncertainty interval. In other words, at the FA33 scale the effect of the corner widening is quite limited. The latter must be explained by the rather limited impact in terms of rates in the FA (rows surrounding the corner), where the quarter are already characterized with large gaps. Let us go deeper in the west quarter of FA33 (Table 6-11).

Config.	Prod. U5 (%)	Abs. U8 (%)
East Qu.		
D-1	0.41	0.69
D-2	0.52	0.04

Table 6-11 - Comparison of reaction rates in FA33 east quarter |T4-AP3|/T4 - config. (D)
(σ_{T4}<1%)

In terms of local reaction rates, the maximal deviation is again obtained for D-1 regarding absorption (0.69%). Yet, the corresponding value of APOLLO3® is included in the uncertainty range of TRIPOLI-4®. Thereby, even locally in the east quarter FA33 the reaction rates are well depicted in the presence of a corner widening.

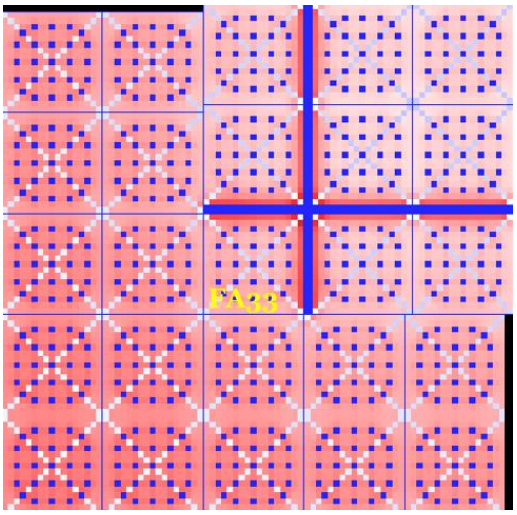

Figure 6-21 - Volume-integrated fission rates in the geometry (D-2)

In Figure 6-21 we can see that the effect of the corner widening in local and limited to a restricted number of rows surrounding the corner. This is the reason why our model is still valid for such corner changes.

The configurations D-1 and D-2 are thus globally well reproduced in terms of reaction rates and multiplication factor by the quarter discretization and the associated homogenized cross-sections.

4. Partial conclusion

In this section we have studied a two steps neutronic scheme to depict the influence of fuel assembly bow. The first step consisted in generating a library of neutronic cross-sections homogenized at the pin cell scale, which is able to include any change of gap (from a closed gap to a 20 mm wide gap). To do so we set up a mini-core of 5X5 fuel assemblies and disrupted the gap at the east of the central assembly. In fact, to prevent us from generating a library taking into account the effects of the 4 surrounding gaps at the same time – which would lead in an important number of long calculations -, we made the assumption that one single gap was enough. The latter assumption implicitly guesses that each quarter of the FA (cut along its diagonals) is independent from each other. Consequently, we ran calculations for different sizes of gap (increases and decreases) in a lattice code and checked their results with respect to a reference (Monte Carlo simulations). Then we could homogenize the pin cells located in the east quarter of the FA. Doing so for several values of width, we obtain a consolidated library of cross-sections for all cells contained in one quarter depending on the adjacent gap width.

The second step is to use those cross-sections in core calculations. Every FA can then be cut in four quarters and each of them has cross-sections depending on the adjacent gap. To check the validity of gap independency, we considered a couple of different cases and compared them to Monte Carlo simulations.

Deviations observed between APOLLO3® and TRIPOLI-4® in terms of reactions rates and k_{eff} are acceptable given the accuracy we look for our modeling. These results, highlighted the expected independency of each FA quarter, and also the lack of influence brought by a corner enlargement. This allows to use only one gap parameter for our homogenized cross-sections library.

All results obtained in this section make it possible to engage in a 3D full core modeling, including large water gaps up to 20 mm, using the MINARET Tetra solver (S_N) in APOLLO3®.

Preliminary 2D calculations, in this chapter, highlight a maximal power increase provoked by a double 20 mm gap enlargement (compared to a nominal configuration) of 10% in the fuel assembly quarter facing the 20 mm gap, and about 4% in the whole fuel assembly.

Conclusion and open prospects

1. A look back at the problematic

In this manuscript we took an interest in an industrial well-known phenomenon in PWR nuclear cores: fuel assembly - static - bow. The latter addresses an important amount of operating issues among which we can cite the delayed action of the rod cluster control assembly, difficulties for the fuel assembly handling.

Fuel assembly bow gives rise to a couple of different interactions between core physics. Consequently the subject is classified among multi-physical studies. Within all interactions whipped up by thermal hydraulics, mechanics and neutronics, we took on the so-called fluid-structure interaction or FSI (interaction between thermal hydraulics and mechanics), and the linking of mechanics towards neutronics.

The first interaction aims at depicting fuel assemblies' deflection, based on a round-trip (two-way) coupling between forces induced by hydraulics, and in return the displacements of the fuel assembly. Those coupled interactions must be compared to deformation patterns observed ex-core. The second one aims at building up a link between the equilibrium resulting from the coupling itself and its impact onto core neutronics. The reason of studying such an interaction is twofold. In fact, aside from all operational related issues, fuel assembly bow might be at the root of azimuthal tilt phenomena in the core (asymmetry of the power with respect to the core quadrants) accelerating the burn-up locally. Moreover, even though it does not seem to be as important as others parameters over deformation at the moment, in order to further study the return from neutronics to mechanics along full cycles of operation, it is necessary as a first step to be able to deform geometrically the FAs in the neutronics calculation.

The multi-physical environment of our work was summed up as follows (Figure 7-1), where λ stands for the set of gap widths in the core, and F for the set of hydraulic forces.

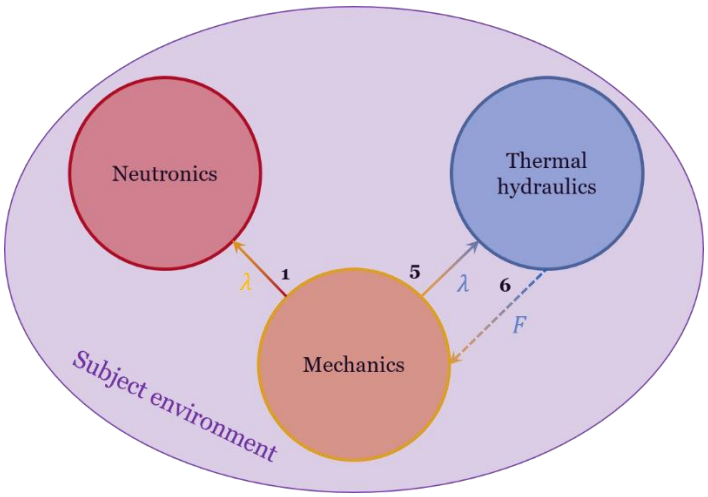

Figure 7-1 - Subject environment

We gathered our proposal in terms of models for each interaction in Table 7-1.

Interaction / Details	Fuel assembly or lower scales			Core scale (row/full-core)		
	Interaction 1	Interaction 5	Interaction 6	Interaction 1	Interaction 5	Interaction 6
Modelling	Stacking, Segments	Framework of Timoshenko beams	Hydraulic networks	Cross-sections with respect to adjacent gap	Framework of Timoshenko beams	Hydraulic networks
Codes	TRIPOLI-4®	Cast3M	Phorcys	Apollo3®	Cast3M	Phorcys

Table 7-1 - Scales, and related models

2. About fluid and structure interactions (5 and 6)

2.1. *Conclusion*

These interactions are obviously representing the main coupling, as hydraulic forces stemming from flow redistribution have a major impact on the final deformation of the fuel assembly. Our project mainly deals with interaction 6 and considered interaction 5 through the use of an in-house existing model. However both are necessary to strictly account for equilibrium states within the core cycles.

Regarding the linking from hydraulics to mechanics, it consists in evaluating hydraulic forces exerting on different sections of a FA span. We sorted them out into three main categories.

The first one is based on internal forces acting on one mixing grid and was called F_{UP} (for upright position). It is estimated through the fluid being put in the upright position inside the grid as suggested for instance in [30] through CFD simulations regarding non-axial flows in an assembly span, and latter taken over by Wanninger when considering lateral volumetric source terms in a grid for porous modelling of a FA row [22]. From our results, we can argue that this force, which can be valued up to 10^1 N depending on the configuration of interest, seems to be of secondary order compared to the two others below.

The second one leans on cross-flows in a FA bundle F_B. The latter force is split further into two parts. The first one is the force due to lateral pressure losses in the inner bundle F_{Bu} and the second one leans on leaking cross-flows stemming from local redistributions from the FA to its surrounding bypasses (or 'gaps'). We pointed out that orders of magnitude of F_B could reach up to 10^2 N and are of great importance on the final bow.

Finally, the third type of force (so-called F_V) regards the redistribution between bypasses and FAs and is due to the difference in pressure around one grid. It depends on the grid

displacement. For this reason is has often been attributed as an added stiffness of the FA. The role played by the grids on the FA shapes has been suspected in the literature [43] and has been at the center of attention of recent works, in terms of upstream redistributions [73, 27] and related forces [46], but it has never been studied in such an extent as in our work.

In our work, we especially focused on the bypass-FA redistribution. From a 1D model of the convergent-diffuser – Model 0 - (space area between grids) we built up a very simple model (Model 1) of the redistribution based on two 1D channels (branches or elements) one for the grid and one for the gap itself. Successive tries and comparisons led to two improvements for this initial model. The first one consisted in taking into account stagnation points effects when the gap closes up, through the addition of corrective terms in hydraulic resistances initiated from dynamic pressure deviations between the two branches (Model 2). Finally we added the lateral resistance of cross-flow in a few rows of fuel rods, based on the so-called Eole correlation [28], when going from one way to another (Model 3). The latter model also introduces the cross-section of leakage and a number of crossed rods. Models 2 and 3 were validated with comparison with a CFD model, with a remarkable advantage for Model 3 regarding the lowest thicknesses of gap. Model 2 (which does not depend on anything but geometrical parameters) was validated on its own through a brand-new experimental mock-up made of two 3D printed grids in a middle of which lies a variable gap. From the flow rate and pressure drops we set up pressure profiles from the Bernoulli's principle and compared them to CFD results. We highlighted that the force F_V is thus the combination of a profile term and an upstream pressure drop term, and its value can be up to hundreds of Newton (the same order as F_B).

Gathering both bypass-FA and inner FA-FA redistributions (with a lateral inner bundle also depicted by the Eole correlation) through hypotheses – including homogeneous lateral pressure – it is possible to obtain a full wireframe of one FA as undertaken in [50]. We made the most of this effort to program a hydraulic python package named Phorcys, solving our own hydraulic networks. This code is then two-way coupled with a validated in-house structural code of FA relying on a framework of Timoshenko beams and contact joints. The result of the coupling has been brought face to face with CEA's experimental results and highlighted good agreement, hydraulically and mechanically, what strengthened our faith regarding the set of forces exported from Phorcys. We also pointed out the very important role of F_V on the final shape of the FA, and emphasized that it could behave in ways previously undescribed in the literature (non gap-equalizing).

Later on, we have studied qualitatively a coupling regarding a row of FAs (Figure 7-2) for a different set of incoming flows. A precise knowledge of boundary conditions seems of first importance to better highlight deformation patterns. At a core scale (mini core of 64 FAs), we demonstrated that lateral forces given by a simple 'row-by-row' method (so called Method 1), leaning on a vertical and horizontal sweeping of the rows in the core and already industrially-used [50] seems relevant to consider further IFS couplings. As no comparison with more detailed approaches has been done in the literature, we compared this method to more intricate ones and realized that the pattern of lateral forces was quite equivalent. In

practice, it is also clearly possible to simulate a full rounded-type industrial core (Figure 7-3).

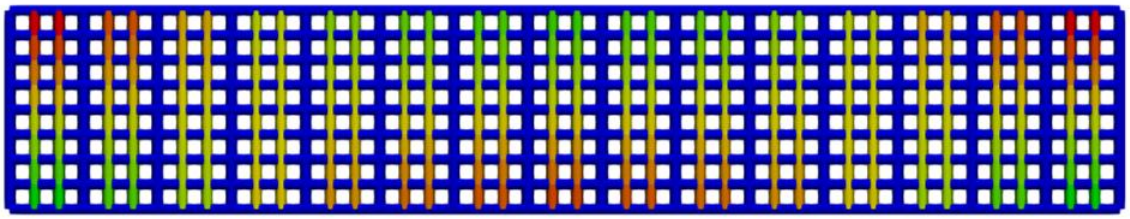

Figure 7-2 - Flow rates visualization with Paraview (15-FAs row calculation with Phorcys), a scale threshold has been chosen to highlight axial flow rates in FAs (in green-red gradation)

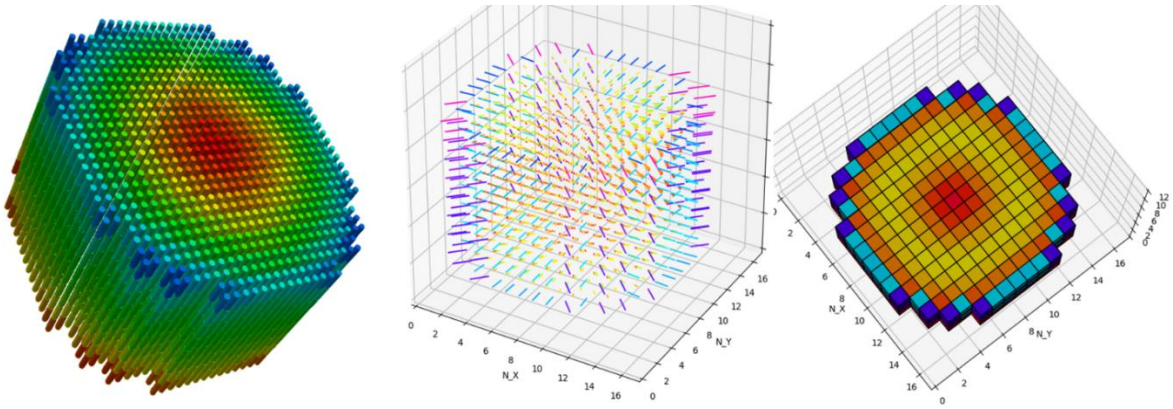

Figure 7-3 - Example of a 1300 MW core calculation with Method 1 in Phorcys, from left to right: axial flow rates in FAs (Paraview), directions of total lateral forces, norm of total lateral forces at floor 3

2.2. *Prospects*

An important amount of prospects could be proposed for all scales.

At the grid scale, Model 3 uses parameters of leakage cross-section S_l and number of crossed rods N. Even though we could have highlighted minor impact of N on the redistribution, h_l plays an important role on the pressure drops (no role on flow rates) and results depend on its value. An asymptotic hydraulic behavior of Model 3 is also demonstrated for h_l from 30 to 50 mm, as results converge towards Model 2's. As we observed a dependency of h_l and the gap width λ, we always adopted 'best-practice' values of h_l (from 20 to 50 mm) according the system studied. A future work on constructing a direct law $h_l = f(\lambda)$ in an industrial context could be necessary.

In terms of external gap (FA-gap), we used modified or unmodified aspect ratios of cross-sections of a convergent-diffuser, depending on the value of λ, to account for 'half-convergent-diffusers'. A different study could be undertaken to dive deep into a dedicated hydraulic resistance and its validation.

At the fuel assembly scale, we assembled bypass-FA redistributions and inner FA-FA models together with an assumption of homogenized lateral pressure. We could have chosen a refined axial discretization, what could be judged out of scope in a simplified –

coarser – network approach. It could be interesting to compare Phorcys results with porous – refined – approaches using our convergent-diffuser correlation. An existing model of Darcy-Forchheimer in Cast3M-Fluid could be reliable to do so.

Also, we did not model the nozzles in this work. We considered that the fluid was injected or withdrawn through the first and last floors of the FA. Consequently, scanning different solutions for nozzle-related redistributions could be of interest in the future.

At the core scale, our results on a row of 15 FAs are still qualitative given the lack of suitable experimental data. A mock-up of 3x1 fuel assemblies at the CEA could help out validating a model in such a configuration in the future.

Regarding a full 3D core, a coupling with roundtrips between structure and hydraulics is still to be pursued. We only analyzed hydraulic forces and no whole coupling has been undertaken at this stage. Given the complexity of such a system, an important under-relaxation factor might be necessary to make the fixed-point algorithm converge (or use another algorithm). In terms of computational time, the structural code may be the 'limiting reactant' currently and may lead to much longer simulations for two-way couplings. A more recent, un-optimized, version of Phorcys indeed succeeded in simulating a feasibility configuration consisting in a ten thousands FAs-core (100 x 100 FAs) with Method 1 (Figure 7-4) within a limited amount of time (a few hours) and 1300 MWe core in only a few minutes; provided that the matrix is stored in memory with a CSC sparse formulation. From the mechanical side, the same framework of beams is used at the core scale (see Table 7-1). However, the use of reduced mechanical FA models studied under-way by Leturcq [126, 127, 128] might tremendously improve mechanical computation times and authorize fast coupling in the near future. The latter would let us catch a glimpse on intricate sensibility analysis, relying for instance on the uncertainty platform URANIE.

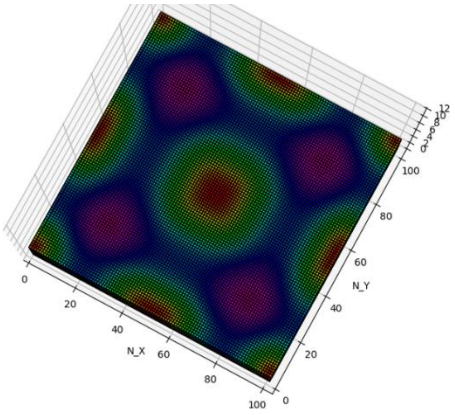

Figure 7-4 - Feasibility test case of ten thousands FAs (norm of total lateral forces)

Aside from FSI, the EOLE correlation is used in 3D at the moment at the core scale. Such a core usage has been called into question for several configurations [30] due to the difference in terms of confinement between an experimental vein and a core environment. A proper attention could be paid to study a dedicated core correlation.

Finally, the more precisely we know the boundary conditions in terms of incoming flow, the more accurate the deformation patterns are. In our analysis of 3D forces in a core, we simply adjusted incoming planar profiles of velocity found out in the literature to the 3D core. In theory, a two-way coupling between a core model and a vessel (including plena) model is necessary to account for accurate boundary conditions. The latter coupling has been already realized in the literature [14, 82]. One could consider doing so with a simplified vessel simulated by a CFD code like TrioCFD, and a core simulated by Phorcys or any porous code. This would highly improve the 3D surface of velocity at the core inlet and outlet.

3. About mechanics to neutronics (interaction 1)

3.1. *Conclusion*

In this section, we give insights on the outcomes of deformation onto core neutronics. The latter could include at the same time static bow along with radio protection or core-related issues like power tilts as well as vibration-induced noise. Neutronics deals most of the time with straight and undeformed geometries. With a growing interest in optimizing industrial systems considering fuel deformation over the past few years, the number of broadcast publications focused on deformed geometries has increased importantly, including Gen II/III reactors as well as and Gen IV ones [129].

While a Monte Carlo approach often let the user unfold every kind of classical 3D volumes, the deterministic one is by design more complex geometrically-speaking. The different steps required by a classical deterministic scheme (self-shielding, generation of cross-sections, equivalence …) generally imply structured grids made of pin cells, and the third dimension at the core scale is often treated with axial extrusion.

As a first attempt we highlighted that classical C and S-shapes can be depicted at the by the so-called segment method with a Monte Carlo code. While a stacking method, standing for a vertical stacking of axially-extruded cylinders, is often used in published material [19, 108], we showed through parametric simulations that inclined segments are closer to a continuous – toroidal - reference whatever are the level of discretization and the assembly deflection. The latter segment method can serve as a mean for modelling spatially-limited scales as fuel rods or even a couple of FAs. It can also be seen as a reference for 3D simulations undertaken with deformed FA in a further deterministic modelling. Indeed, even though the stochastic approach is known as a validation mean for deterministic calculations, the Monte Carlo approach would probably be too time-consuming to reach suitable dispersion [130] (up to several weeks) for depicting a 3D full core with segments (except if one has access to important computing resources, i.e. time and processors). For this reason a deterministic approach is preferred for full core calculations.

The latter approach often relies on two different steps. First, a lattice calculation which can be fast and accurate enough to generate a cross-section library. Second, a core calculation which puts the latter library to good use. The core calculation is undertaken on a

homogenized geometry with a reduced number of energy groups (condensation), which authorizes reasonable simulation times.

In order to take into account deformations, we proposed a way to generate cross-sections at the pin scale. The latter approach is based on an assumption that each quarter of assembly could be independent from each other. In theory, when homogenizing, all fuel-related cross-sections must depend on the different gaps surrounding one FA, i.e. four gaps respectively at the east, west, north and south. However, the number of calculations needed for taking into account all gaps increases importantly. In other words, if one considers a library leaning on 10 different widths of bypass to fill up a range of consistent values, it stands for about 10^3 combinations sampling. At a rate of a couple of hours for each calculation the generation could be intricate. As a matter of fact, this is the reason why we decided to prove that each quarter of assembly can be considered independent from each other with respect to several physical values.

To do so, we set up homogenized cross-sections along with only one variable gap. We further reused this library on different test cases and highlighted that every core calculation depicted the reference given by the equivalent Monte Carlo calculation. This primary step is thus of importance to generate a library regarding any kind of deformation at the core scale and the associated neutronics core calculation.

3.2. *Prospects*

At this stage, it becomes possible to perform a full core calculation in two dimensions with every possible deflection as soon as it conserves the set of λ values in the suitable range of generation. Through a subroutine, one can transfer hydro-mechanical results of a FSI coupling (displacements and bypasses' widths) to a software dedicated to neutronics data setting like the ALAMOS module of SALOME [119]. A coupling on a row of 15 FAs with a shifted inlet velocity profile can be used as an example, as it is the only configuration available at the moment (Figure 7-5). The data of the equilibrium was exported to ALAMOS which can generate the appropriate mesh for APOLLO3® thanks to the structure displacements. Within an APOLLO3® dataset, a python subroutine can then map the set of λ to every quarter of FA (see again Figure 7-5) to parameter the cross-sections. An example of flux map obtained in group 4 is also shown in Figure 7-5. In this example a maximal increase of power was observed at the west of FA8 of about 3%, and 1% in the whole assembly. An example of core data linking with arbitrary values of λ (once again, no fluid-structure coupling is operational at this scale yet), is shown in Figure 7-6.

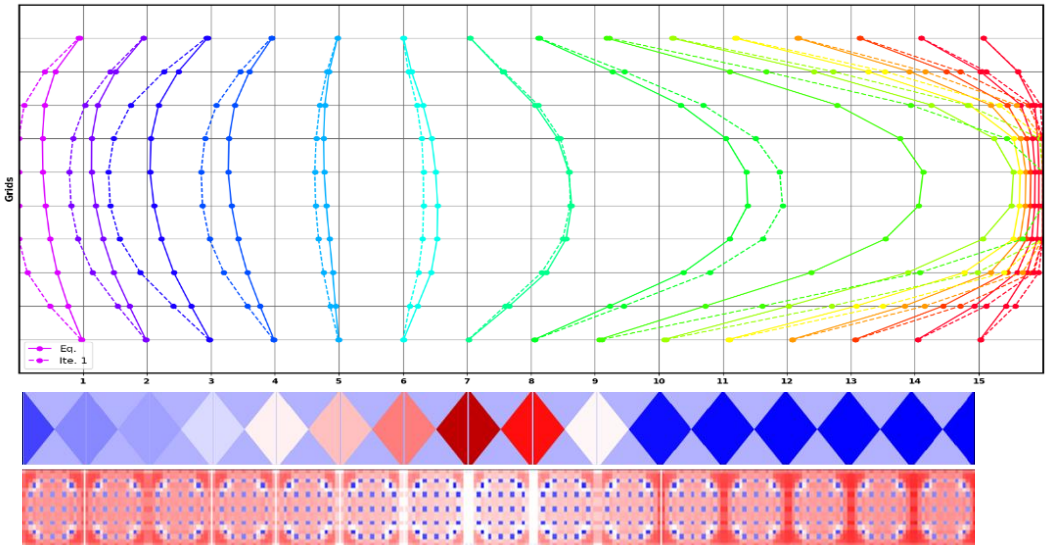

Figure 7-5 - (top) deformations stemming from a FSI coupling with shifted inlet conditions, (bottom) field of gaps parameters λ sent to APOLLO3® to preset the cross-sections and the associated flux in group 4

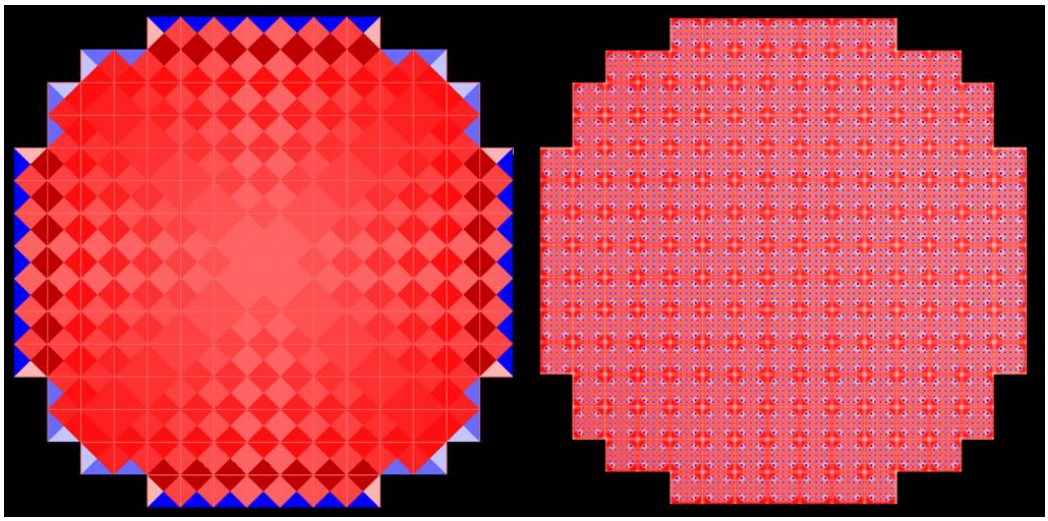

Figure 7-6 - (left) field of gaps parameters λ used to preset the cross-sections (right) associated resulting fission rates

Attention must be paid in order to account for core-scaled phenomena. It would be necessary to generate the same library in the lattice code with leakage conditions [131]. In fact, at the core scale, an amount of neutrons leaks from the core whereas we considered reflective conditions without leakage. The latter ones are necessary to be compared to Monte Carlo calculations in which leakage models remain a research area (see for instance [132]).

What is more this scheme is at this stage available in 2D. A work is yet necessary to extend this approach for an additional dimension. At the moment, a research effort is set about using 3D unstructured geometries in the MINARET [106] solver of APOLLO3®. If possible, a simplified 3D geometry of fuel assemblies could be designed through a CAD software like SALOME [66]. The latter would consist in a partition of axial volumetric groups

to make out any macro-region and filled up with tetrahedrons elements (Figure 7-7). One could characterize each axial elements with respect to the averaged axial width of the adjacent water gap. In this case, the segment method along with a Monte Carlo code could be used as the validation mean, for instance regarding one fuel assembly.

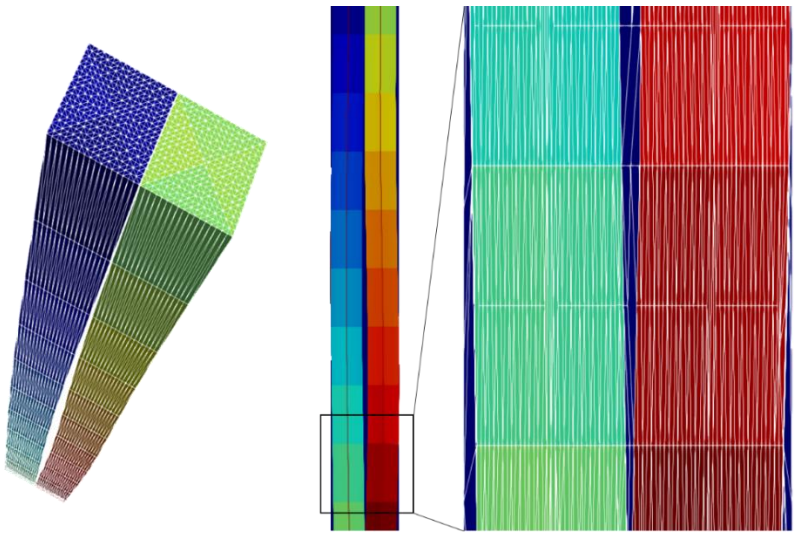

Figure 7-7 - 3D fuel assemblies (SALOME), from left to right: 3D overall view, axial cross section, zoom in the 2D axial cross section

Appendix A: Derivation of the UP force

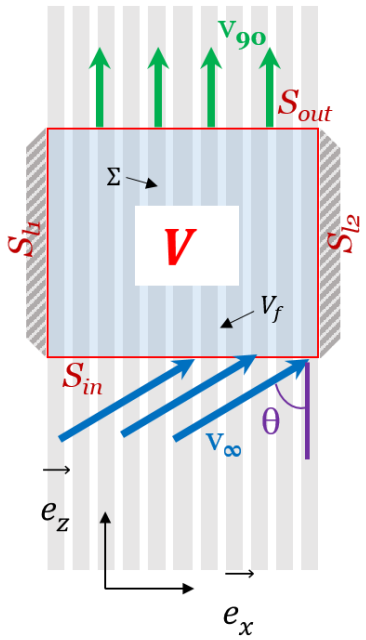

Figure A-1 - Lateral force caused by the flow across a grid

Let V be the grid volume and $\partial_V = S_{int} + S_{out} + S_{l1} + S_{l2}$ its frontier. This volume contains the grid structure (bundle and straps) Σ of frontier ∂_Σ , and the fluid volume V_f of frontier ∂_{V_f}. Inside the fluid volume, the velocity at a point M is $\vec{v}(M) = v_x(M)\,\overrightarrow{e_x} + v_z(M)\,\overrightarrow{e_z}$.

The momentum conservation principle gives:

$$\rho(\vec{v}.\nabla\vec{v}) = div(\bar{\bar{\sigma}}) \qquad \text{(Eq. A-1)}$$

Where $\bar{\bar{\sigma}} = -\bar{\bar{p}}\bar{\bar{I}} + 2\mu\bar{\bar{D}} = -\bar{\bar{I}}p + \mu(\nabla\vec{v} + {}^t\nabla\vec{v})$, μ being the dynamic viscosity and p the static pressure.

If one integrates the latter formula over V_f:

$$\iiint_{V_f} \rho(\vec{v}.\nabla\vec{v})\,d\tau = \iiint_{V_f} div(\bar{\bar{\sigma}})d\tau \qquad \text{(Eq. A-2)}$$

Using the Green-Ostrograski theorem, and the continuity equation $\nabla.\vec{v} = 0$:

$$\oiint_{\partial_{V_f}} \rho(\vec{v}.\vec{n})\vec{v}\,dS = \oiint_{\partial V_f} \bar{\bar{\sigma}}.\vec{n}dS \qquad \text{(Eq. A-3)}$$

Where $\vec{n}$ is a ∂V normal vector. It follows:

$$\oiint_{\partial_V} \rho(\vec{v}.\vec{n})\vec{v}\,dS + \oiint_{\partial_\Sigma} \rho(\vec{v}.\vec{n})\vec{v}\,dS = \oiint_{\partial_V} \bar{\bar{\sigma}}.\vec{n}dS + \oiint_{\partial_\Sigma} \bar{\bar{\sigma}}.\vec{n}dS \qquad \text{(Eq. A-4)}$$

With $\oiint_{\partial_\Sigma} \bar{\bar{\sigma}}.\vec{n}dS$ known as $\overrightarrow{F_{s\to f}}$. Giving that $\vec{v}|\partial_\Sigma = \vec{0}$,

$$\oiint_{\partial_V} \rho(\vec{v}.\vec{n})\vec{v}\,dS = \oiint_{\partial_V} \bar{\bar{\sigma}}.\vec{n}dS + \overrightarrow{F_{s\to f}} \qquad \text{(Eq. A-5)}$$

Developing both terms:

$$\begin{aligned}\iint_{S_{in}} \rho(\vec{v}.\vec{n})\vec{v}\,dS + \iint_{S_{out}} \rho(\vec{v}.\vec{n})\vec{v}\,dS + \iint_{S_{l1}} \rho(\vec{v}.\vec{n})\vec{v}\,dS + \iint_{S_{l2}} \rho(\vec{v}.\vec{n})\vec{v}\,dS \\ = \iint_{S_{in}} \bar{\bar{\sigma}}.\vec{n}dS + \iint_{S_{out}} \bar{\bar{\sigma}}.\vec{n}dS + \iint_{S_{l1}} \bar{\bar{\sigma}}.\vec{n}dS + \iint_{S_{l2}} \bar{\bar{\sigma}}.\vec{n}dS + \overrightarrow{F_{s\to f}}\end{aligned} \qquad \text{(Eq. A-6)}$$

We know that $\vec{v}_{S_{l1}} = \vec{v}_{S_{l2}} = \vec{0}$,

$$\begin{aligned}\iint_{S_{in}} \rho(\vec{v}.\vec{n})\vec{v}\,dS + \iint_{S_{out}} \rho(\vec{v}.\vec{n})\vec{v}\,dS \\ = \iint_{S_{in}} \bar{\bar{\sigma}}.\vec{n}dS + \iint_{S_{out}} \bar{\bar{\sigma}}.\vec{n}dS + \iint_{S_{l1}} \bar{\bar{\sigma}}.\vec{n}dS + \iint_{S_{l2}} \bar{\bar{\sigma}}.\vec{n}dS + \overrightarrow{F_{s\to f}}\end{aligned} \qquad \text{(Eq. A-7)}$$

Along the x-axis,

$$\begin{aligned}\overrightarrow{F_{s\to f}}.\overrightarrow{e_x} = -F_{UP} \\ = \iint_{S_{out}} \rho v_x v_z dS - \iint_{S_{in}} \rho v_x v_z dS - \iint_{S_{l1}} (p - 2\mu\partial_x v_x)dS \\ - \iint_{S_{in}} \mu(-\partial_x v_z - \partial_z v_x)dS \\ - \iint_{S_{l2}} (-p + 2\mu\partial_x v_x)dS - \iint_{S_{out}} \mu(\partial_x v_z + \partial_z v_x)dS\end{aligned} \qquad \text{(Eq. A-8)}$$

To make the reading easier, we can note the mean of ϕ over the surface A:

$$\langle\phi\rangle_A = \frac{1}{A}\iint_A \phi \text{ dS} \qquad \text{(Eq. A-9)}$$

We know that $\vec{v}_{S_{l1}} = \vec{v}_{S_{l2}} = \vec{0}$ and $v_{x_{S_{out}}} = 0$. Additionally, we assume that we can neglect the contribution of the pressure over S_{l1} and S_{l2}, given the small lateral pressure loss in the grid compared to the dynamic pressure and that the cross-sections (S_{l1} and S_{l2}) are at least one order of magnitude smaller than S_{in} and S_{out}. Finally, (Eq. A-8) becomes:

$$\begin{aligned}\overrightarrow{F_{s\to f}}.\overrightarrow{e_x} = -F_{UP} = -\rho S_{in}\langle v_x v_z\rangle_{S_{in}} + \mu S_{in}\langle\partial_x v_z\rangle_{S_{in}} \\ +\mu S_{in}\langle\partial_z v_x\rangle_{S_{in}} - \mu S_{out}\langle\partial_x v_z\rangle_{S_{out}}\end{aligned} \qquad \text{(Eq. A-10)}$$

Let U be the typical axial velocity, and $Utan(\theta)$ (θ inclination angle of the fluid) the associated lateral velocity. Let e be the length scale in both directions - in the bundle we could have distinguished each directions, but here the grid height is of the same order than the grid pitch -.

Consequently,

$$\begin{cases} \rho\langle v_x v_z\rangle_{S_{in}} \sim \rho U^2 \tan(\theta) \\ \mu\langle \partial_x v_z\rangle_{S_{in}} \sim \mu\langle \partial_x v_z\rangle_{S_{out}} \sim \dfrac{\mu U}{e} \\ \mu\langle \partial_z v_x\rangle_{S_{in}} \sim \dfrac{\mu U}{e}\tan(\theta) \end{cases} \qquad \text{(Eq. A-11)}$$

In other words, we can neglect the viscous terms if the following conditions are fulfilled:

$$\begin{cases} \rho U^2 \tan(\theta) \gg \dfrac{\mu U}{e} \\ \dfrac{\mu U}{e} \gg \dfrac{\mu U}{e}\tan(\theta) \end{cases} \qquad \text{(Eq. A-12)}$$

Thus,

$$\begin{cases} Re_\perp = \dfrac{\rho e U}{\mu}\tan(\theta) \gg 1 \\ \tan(\theta) \sim 1 \end{cases} \qquad \text{(Eq. A-13)}$$

The first condition is fulfilled, because the lateral Reynolds in the core is much higher than 1 (around 10^3), the second condition is also fulfilled as in practice $\tan(\theta) \ll 1$.

Consequently,

$$F_{UP} \simeq \rho S_{in}\langle v_x v_z\rangle_{S_{in}} \qquad \text{(Eq. A-14)}$$

Meaning that the force is mainly carried by the fluid inertia. The formula would give the well-known result (Eq. 1-5) if one applies uniform velocities to look after an order of magnitude. Another derivation would be to say that $\langle \partial_x v_z\rangle_{S_{out}} \sim 0$ by stating that the velocity can be split into a mean and a fluctuation in the grid which represents a periodic media.

Appendix B: Estimation of the lateral force applying on the FA bundle through the pressure drop

The goal of this appendix is to explain how we deduced the bundle force expression thanks to the Peybernès' correlation [28].

1. Preliminaries – forces exerted by a fluid phase within a solid phase

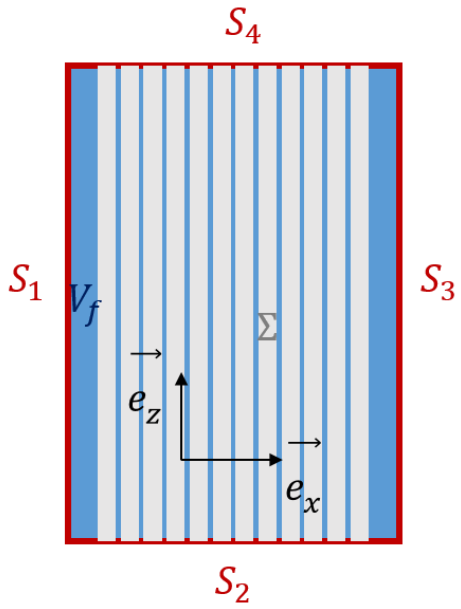

Figure B-1 - Problem treated (V)

The control volume V, whose frontier is $\partial_V = S_1 \cup S_2 \cup S_3 \cup S_4$, holds a solid phase Σ (frontier ∂_Σ), and a liquid phase V_f (frontier $\partial_{V_f} = \partial_\Sigma \cup \partial_V$). The velocity $\vec{v}$ is defined by $\forall M \in V_f$, $\vec{v} = v_x(M)\overrightarrow{e_x} + v_z(M)\overrightarrow{e_z}$. Through a similar development – projection of the N-S equation -, and the same notations as found in Appendix A, the lateral force applying on Σ by V_f is:

$$\begin{aligned}\overrightarrow{F_{V_f\to\Sigma}}.\overrightarrow{e_x} = {} & \rho S_1\langle v_x^2\rangle_{S_1} + \rho S_2\langle v_x v_z\rangle_{S_2} - \rho S_3\langle v_x^2\rangle_{S_3} - \rho S_4\langle v_x v_z\rangle_{S_4} \\ & + S_1\langle p\rangle_{S_1} - 2\mu S_1\langle \partial_x v_x\rangle_{S_1} - \mu S_2\langle \partial_x v_z\rangle_{S_2} - \mu S_2\langle \partial_z v_x\rangle_{S_2} \\ & - S_3\langle p\rangle_{S_3} + 2\mu S_3\langle \partial_x v_x\rangle_{S_3} + \mu S_4\langle \partial_x v_z\rangle_{S_4} + \mu S_4\langle \partial_z v_x\rangle_{S_4}\end{aligned} \qquad \text{(Eq. B-1)}$$

Where:

- For $i = 2,4$; $v_{x_{S_i}} = v_x(x, z = z_{S_i}) = v_{x_{S_i}}(x)$, et $v_{z_{S_i}} = v_z(x, z = z_{S_i}) = v_{z_{S_i}}(x)$
- For $i = 1,3$; $v_{x_{S_i}} = v_x(x = x_{S_i}, z) = v_{x_{S_i}}(z)$, et $v_{z_{S_i}} = v_z(x = x_{S_i}, z) = v_{z_{S_i}}(z)$

2. Analysis of the terms order

The cross sections are of the same order *i.e.* $S_1 \sim S_2 \sim S_3 \sim S_4 = S$. Let e be the horizontal scale of variation (the rod scale), and L the vertical scale of variation (the bundle height), we

assume that $e/L \ll 1$. Like in Appendix A, U is the typical axial velocity, and $\tan(\theta)\,U$ (with $\tan(\theta) \ll 1$) the associated lateral velocity.

1.3. Analysis of the viscous forces

$$\begin{cases} \mu\langle\, \partial_z v_x \rangle_{S_i} \sim \dfrac{\mu \tan(\theta)\, U}{L} \\ 2\mu\langle \partial_x v_x \rangle_{S_i} \sim \dfrac{2\mu \tan(\theta) U}{e} \\ \mu\langle\, \partial_x v_z \rangle_{S_i} \sim \dfrac{\mu U}{e} \end{cases} \qquad \text{(Eq. B-2)}$$

As $e/L \ll 1$, and $\tan(\theta) \ll 1$, thus $\frac{e\tan(\theta)}{L} \ll 1$ and the brown terms are neglected against the orange ones.

In the same way, $2\tan(\theta) \ll 1$, and the green terms are neglected.

It follows:

$$\begin{aligned} \overrightarrow{F_{V_f \to \Sigma}}.\overrightarrow{e_x} \simeq\ & \rho S_1 \langle v_x^2 \rangle_{S_1} + \rho S_2 \langle\, v_x v_z \rangle_{S_2} - \rho S_3 \langle v_x^2 \rangle_{S_3} - \rho S_4 \langle v_x v_z \rangle_{S_4} \\ & + S_1 \langle\, p\, \rangle_{S_1} - \mu S_2 \langle\, \partial_x v_z \rangle_{S_2} - S_3 \langle\, p\, \rangle_{S_3} + + \mu S_4 \langle\, \partial_x v_z \rangle_{S_4} \end{aligned} \qquad \text{(Eq. B-3)}$$

In other words, the friction terms related to the variations of the axial velocity along the x-axis dominates the other terms of friction. This is not a surprising result given that in the PWRs, the flow is quasi-axial, and that the pitch of the bundle is lower than the span pitch of a FA.

2.3. Analysis of the inertial forces

$$\begin{cases} \rho\langle v_x^2 \rangle_{S_i} \sim \rho \tan(\theta)^2\, U^2 \\ \rho\langle v_x v_z \rangle_{S_i} \sim \rho \tan(\theta)\, U^2 \end{cases} \qquad \text{(Eq. B-4)}$$

As $\tan(\theta) \ll 1$, we can neglect the red terms against the blues ones.
Thus:

$$\begin{aligned} \overrightarrow{F_{V_f \to \Sigma}}.\overrightarrow{e_x} \simeq\ & \rho S_2 \langle\, v_x v_z \rangle_{S_2} - \rho S_4 \langle v_x v_z \rangle_{S_4} + S_1 \langle\, p\, \rangle_{S_1} - \mu S_2 \langle\, \partial_x v_z \rangle_{S_2} \\ & - S_3 \langle\, p\, \rangle_{S_3} + \mu S_4 \langle\, \partial_x v_z \rangle_{S_4} \end{aligned} \qquad \text{(Eq. B-5)}$$

3.3. Comparison between the viscous and inertial forces

$$\begin{cases} \mu\langle\, \partial_x v_z \rangle_{S_i} \sim \dfrac{\mu U}{e} \\ \rho\langle v_x v_z \rangle_{S_i} \sim \rho \tan(\theta)\, U^2 \end{cases} \qquad \text{(Eq. B-6)}$$

The division between the viscous and inertial forces leads to the crosswise Reynolds number $Re_{\perp} = \rho \tan(\theta)\, Ue/\mu$. A substitution into the latter formula for operational values (we chose an angle of 1 degree, which might be a bit higher or lower depending on the position in the core) still leads to an order of magnitude of 10^3. In other words, the viscous forces due to the lateral variation of axial velocity are generally much lower than inertia in the crosswise direction, even for small angles.

It follows:

$$\overrightarrow{F_{V_f \to \Sigma}}.\overrightarrow{e_x} \simeq \rho S_2 \langle v_x v_z \rangle_{S_2} - \rho S_4 \langle v_x v_z \rangle_{S_4} + S_1 \langle p \rangle_{S_1} - S_3 \langle p \rangle_{S_3} \qquad \text{(Eq. B-7)}$$

Finally, the remaining forces are the pressure and inertial ones.

4.3. Pressure forces and inertial forces

$$\begin{cases} \langle p \rangle_{S_i} \sim p \\ \rho \langle v_x v_z \rangle_{S_i} \sim \rho \tan(\theta)\, U^2 \end{cases} \qquad \text{(Eq. B-8)}$$

(Eq. B-8) relates to a crosswise Euler number $Eu_{\perp} = p/\rho \tan(\theta)\, U^2$. Its value in a PWR core equals 10^4. In other words, it mainly remains the pressure forces, higher than the inertial terms, which themselves are higher than the viscous terms.

$$\overrightarrow{F_{V_f \to \Sigma}}.\overrightarrow{e_x} \simeq S_1 \langle p \rangle_{S_1} - S_3 \langle p \rangle_{S_3} \qquad \text{(Eq. B-9)}$$

Given that generally $S_1 = S_3$:

$$\overrightarrow{F_{V_f \to \Sigma}}.\overrightarrow{e_x} \simeq S_1 \left(\langle p \rangle_{S_1} - \langle p \rangle_{S_3} \right) \qquad \text{(Eq. B-10)}$$

In other words, most of the bundle lateral force, in PWR conditions, may stem from the pressure drop related term, which itself can be estimated through the Eole correlation.

Appendix C: Derivation of the extended Bernoulli's principle

1. The system

A part of the following content is based on courses dealing with real – viscous – fluids [133, 134, 135].

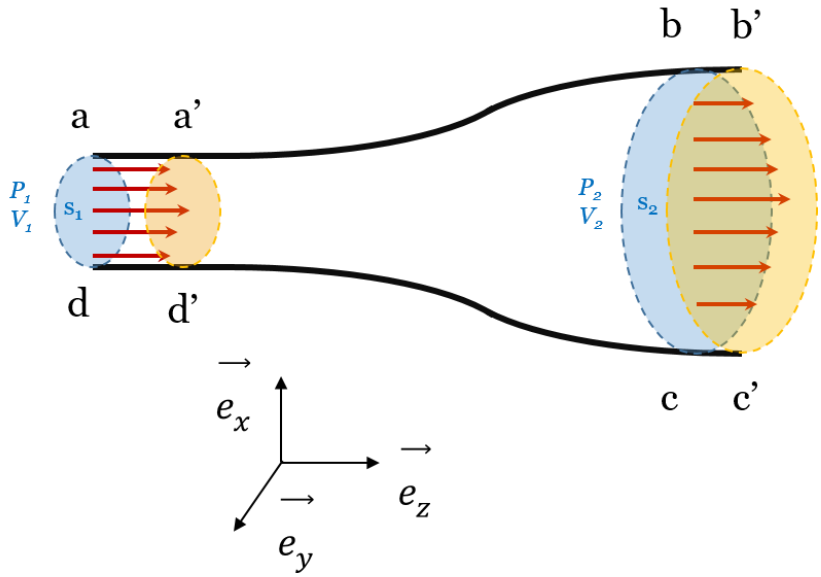

Figure C-1 - System

The system is shown in Figure C-1, let us consider $abcd$ (located between cross sections s_1 and s_2) as our control volume. After a time $\mathrm{d}t$ the fluid has gone to $a'b'c'd'$.

2. Mass conservation

Through mass conservation, within $\mathrm{d}t$, the elementary mass dm_1 (contained in $aa'd'd$) which entered the system during $\mathrm{d}t$, and the elementary mass dm_2 (contained in $bb'c'c$) which exited during the same $\mathrm{d}t$, must be equal. We will note this mass dm. This writes:

$$\rho Q_1 \mathrm{d}t = \rho Q_2 \mathrm{d}t \qquad \text{(Eq. C-1)}$$

Where ρ stands for the density, and Q for the volumetric flow rate.
In other words:

$$\rho \iint_{s_1} v(x,y) ds \mathrm{d}t = \rho \iint_{s_2} v(x,y) ds \mathrm{d}t \qquad \text{(Eq. C-2)}$$

Introducing the bulk velocity (or mean velocity) V:

$$\rho s_1 V_1 \mathrm{d}t = \rho s_2 V_2 \mathrm{d}t \quad \text{(Eq. C-3)}$$

We know that:

$$V\mathrm{d}t = \frac{1}{s}\iint_s v(x,y)\mathrm{d}t ds = \frac{1}{s}\iint_s \mathrm{d}l(s) ds = l_m \quad \text{(Eq. C-4)}$$

This is the mean distance travelled by the fluid on cross section s during $\mathrm{d}t$. With this notation we can deduce:

$$\rho l_{m_1} s_1 = \rho l_{m_2} s_2 \quad \text{(Eq. C-5)}$$

3. Energy conservation

We write the mechanical energy conservation as follows:

$$\Delta E_c = W_p + W_d \quad \text{(Eq. C-6)}$$

Where W_p is the pressure-volume work, and W_d is the dissipative forces work. The potential energy is not taken into account here.

1.3. Kinetic energy

Kinetic energy contained in $aa'd'd$ and $bb'c'c$:

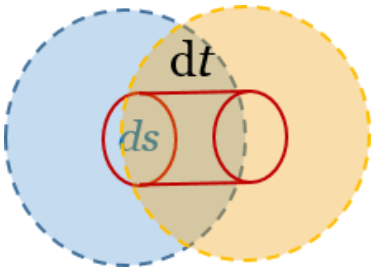

Figure C-2 - Elementary surface ds

E_c contained in infinitesimal volume is:

$$\mathrm{d}E_c = \frac{1}{2}v^2(x,y)(\rho v(x,y)\mathrm{d}t ds) \quad \text{(Eq. C-7)}$$

Thus energy in aa'd'd or bb'c'c is:

$$E_c = \iint_s \mathrm{d}E_c(ds) = \iint_s \frac{1}{2}v^3(x,y)\rho \mathrm{d}t ds \quad \text{(Eq. C-8)}$$

Introducing α as the kinetic energy coefficient defined by:

$$\alpha = \frac{1}{s}\iint_s \left(\frac{v}{V}\right)^3 ds \qquad \text{(Eq. C-9)}$$

It comes:

$$E_c = \frac{1}{2}\rho\alpha V^3 s\mathrm{d}t \qquad \text{(Eq. C-10)}$$

We know that:

$$sV = \frac{\mathrm{d}\tau}{\mathrm{d}t} \qquad \text{(Eq. C-11)}$$

Where $\mathrm{d}\tau$ is the volume aa'd'd or bb'c'c. We can write:

$$E_c = \frac{1}{2}\rho\alpha V^2 \mathrm{d}\tau \qquad \text{(Eq. C-12)}$$

In other words:

$$E_c = \frac{1}{2}\alpha \mathrm{d}m V^2 \qquad \text{(Eq. C-13)}$$

Kinetic energy variation during $\mathrm{d}t$:

Thanks to the latter result:

$$\Delta E_c = \frac{1}{2}\alpha_2 \mathrm{d}m V_2^2 - \frac{1}{2}\alpha_1 \mathrm{d}m V_1^2 \qquad \text{(Eq. C-14)}$$

2.3. Pressure-volume work

Considering a volume $\mathrm{d}l$, the pressure work is given as follows:

$$\delta \mathrm{W_p} = -p\mathrm{d}l \qquad \text{(Eq. C-15)}$$

In other words:

$$\mathrm{W_p} = \int_{aa'd'd} p_1 v_1(x,y)\mathrm{d}t ds - \int_{bb'c'c} p_2 v_2(x,y)\mathrm{d}t ds \qquad \text{(Eq. C-16)}$$

Noting <> the mean operator:

$$\mathrm{W_p} = s_1\langle p_1 v_1\rangle_{s_1}\ \mathrm{d}t - s_2\langle p_2 v_2\rangle_{s_2}\,\mathrm{d}t \qquad \text{(Eq. C-17)}$$

If p_1 is homogenous on the cross section, such as $p_1(x,y) = P_1$

$$\mathrm{W_p} = s_1 P_1\langle v_1\rangle_{s_1}\mathrm{d}t - s_2 P_2\langle v_2\rangle_{s_2}\,\mathrm{d}t \qquad \text{(Eq. C-18)}$$

In other words:

$$\mathrm{W_p} = s_1 P_1 lm_1 - s_2 P_2 lm_2 \qquad \text{(Eq. C-19)}$$

Thus:

$$\mathrm{W_p} = \mathrm{d}\tau(P_1 - P_2) \qquad \text{(Eq. C-20)}$$

3.3. Work of dissipative forces

Combining (Eq. C-6), (Eq. C-14) and (Eq. C-20):

$$\frac{1}{2}\rho\alpha_1 V_1^2 + P_1 = \frac{1}{2}\rho\alpha_2 V_2^2 + P_2 - \frac{W_d}{\mathrm{d}\tau} \qquad \text{(Eq. C-21)}$$

The term $W_d/\mathrm{d}\tau$ can originate from viscous friction, in this case it is a frictional loss. With ΔP_{12} the related total pressure loss:

$$\frac{W_d}{\mathrm{d}\tau} = -\Delta P_{12} = -\frac{1}{2D_h} f\rho V^2 L \qquad \text{(Eq. C-22)}$$

The latter formula is the Darcy-Weisbach equation, which can be found back through dimensional analysis. D_h is the hydraulic diameter, L the duct length, and f is the Darcy friction factor, whose value is often calculated thanks to correlations. For laminar flows, an analytical expression directly gives $f = 64/Re$.

This term can also originate from abrupt change of geometry (sudden change of cross sections, bends …), we talk about local losses:

$$\Delta P_{12} = \frac{1}{2} K\rho V^2 \qquad \text{(Eq. C-23)}$$

Where K is the local loss coefficient, which often only depends on the geometry for high Reynolds numbers. More generally, the extended Bernoulli's principle is:

$$\frac{1}{2}\rho\alpha_1 V_1^2 + P_1 = \frac{1}{2}\rho\alpha_2 V_2^2 + P_2 + \sum_i \frac{1}{2D_{h_i}} f_i \rho V_i^2 L_i + \sum_k \frac{1}{2} K_j \rho V_j^2 \qquad \text{(Eq. C-24)}$$

Where j and i are respectively every local and frictional losses the fluid has to come across between 1 and 2.

For turbulent flows, profiles are rather flat so that $\alpha \simeq 1$. In practice, α is always considered equal to 1.

Appendix D: Validation of the channel model

The goal of this appendix is to demonstrate the relevance of the 1D channel construction (Model 0, see chapter 2) built upon the three parts C_1, C_2 and C_3.

1. Notations

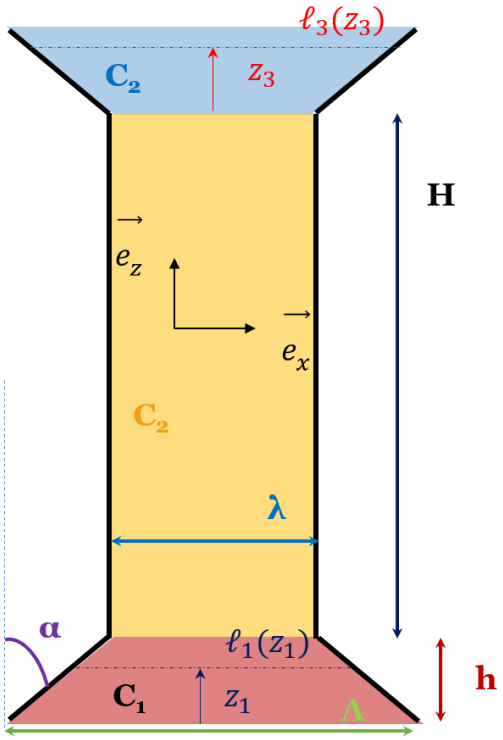

Figure D-1 - geometry considered for the area between two grids

Figure D-1 gives the 2D layout of the problem.

Let us define the linear maps $\ell_1 \equiv \ell_1(z_1)$ and $\ell_3 \equiv \ell_3(z_3)$ which are defined respectively by the points $\ell_1(0) = \Lambda$, $\ell_1(h) = \lambda$; $\ell_3(0) = \lambda$ and $\ell_3(h) = \Lambda$. z_1, z_2, and z_3 are the axial local variables which belong respectively to $[0, h]$, $[0, H]$ and $[0, h]$.

Thanks to the notations introduced before in the thesis, we can then define local bulk velocities based on continuity:

$$V_1(z_1) = V_e \frac{\Lambda}{\ell_1(z_1)}, V_2(z_2) = V_2 = V_1(h), V_3(z_3) = V_2(H) \frac{\lambda}{\ell_3(z_3)} \qquad \text{(Eq. D-1)}$$

Where V_e is the inlet bulk velocity.

2. Laminar flow

Considering a laminar flow with the assumption of parabolic (Poiseuille) velocity profiles in sections C_1, C_2 and C_3 can lead to an analytic 2D solution. It is an hypothesis for C_3 where a separation may occur even for low Reynolds. With those conditions, it becomes possible to integrate the Navier-Stokes equations to get a pressure loss.

Our model in laminar flow is adjusted with the right pressure losses. In fact, the Haaland correlation is not relevant for low-Reynolds flows.

As mentioned above in the thesis, integrating the Darcy-Weisbach equation [57], with, this time, a use of a Darcy friction factor such as $f = 64/Re$ [136], gives a laminar friction loss for Reynolds up to 2000.

We are going to show in this section that the pressure evolution for a laminar flow can be directly pulled out from the – incompressible, permanent- Navier-Stokes equations if the fluid velocity is considered as parabolic in C_1 and C_3 (fluid perfectly attached).

$$\begin{cases} \rho(\vec{v}.\nabla)\vec{v} = -\vec{\nabla}p + \mu\Delta\vec{v} \\ div(\vec{v}) = 0 \end{cases} \qquad \text{(Eq. D-2)}$$

Introducing $\vec{v}(x,z) = v_x(x,z)\overrightarrow{e_x} + v_z(x,z)\overrightarrow{e_z}$, the momentum conservation equation can be projected onto the x and z-axis:

$$\begin{cases} \rho\left(v_x\dfrac{\partial v_x}{\partial x} + v_z\dfrac{\partial v_x}{\partial z}\right) = -\dfrac{\partial p}{\partial x} + \mu\left(\dfrac{\partial^2 v_x}{\partial x^2} + \dfrac{\partial^2 v_x}{\partial z^2}\right) \\ \rho\left(v_x\dfrac{\partial v_z}{\partial x} + v_z\dfrac{\partial v_z}{\partial z}\right) = -\dfrac{\partial p}{\partial z} + \mu\left(\dfrac{\partial^2 v_z}{\partial x^2} + \dfrac{\partial^2 v_z}{\partial z^2}\right) \end{cases} \qquad \text{(Eq. D-3)}$$

Straight plane channel – C_2

Let us start with the central part C_2. We consider a Poiseuille flow between two vertical plates whose normal vectors are oriented toward the x-axis and located at $x_{min} = -\frac{\lambda}{2}$ and $x_{max} = \frac{\lambda}{2}$.

We assume the pressure gradient oriented toward the z-axis, and a velocity of the form $\vec{v} = v_z(x)\,\overrightarrow{e_z}$ (i.e. $v_x = 0$ in the plane channel).

The momentum conservation equations (Eq. D-3) thus turns into:

$$\frac{\partial p}{\partial z} = \mu\frac{\partial^2 v_z}{\partial x^2} \qquad \text{(Eq. D-4)}$$

After integrating along the x-axis, and taking into account the wall condition, the Poiseuille profile writes:

$$v(z_2) = v_m\left(1 - \frac{4x^2}{\lambda^2}\right) \quad \text{(Eq. D-5)}$$

Where v_m is the profile maximum:

$$v_m = -\frac{\lambda^2}{8\mu}\frac{\mathrm{d}p}{\mathrm{d}z} \quad \text{(Eq. D-6)}$$

Thus:

$$\mathrm{d}p = -\frac{8\mu v_m}{\lambda^2}\,\mathrm{d}z \quad \text{(Eq. D-7)}$$

In other words, between h and z_2 we find the Poiseuille equation between two plates. Finally:

$$\Delta p(\mathrm{z}_2) = p(z_2) - p(h) = -\int_0^{z_0}\frac{8\mu v_m}{\lambda^2}\mathrm{d}z = -\frac{8\mu v_m}{\lambda^2}z_2 \quad \text{(Eq. D-8)}$$

Convergent – C_1

Given the shape of the cross section evolution, dealing with a uniaxial velocity would be a coarse assumption. Consequently, in this part $\vec{v}(x, z_1) = v_x(x, z_1)\overrightarrow{e_x} + v_z(x, z_1)\overrightarrow{e_z}$.

We still consider a laminar flow, and a parabolic profile within the convergent. It comes that $v_x(x, z_1) = \phi(\mathrm{z}_1)\left(1 - \frac{4\mathrm{x}^2}{\ell_1^2}\right)$ where ℓ_1^2 depends on the altitude and ϕ must be determined.

Using the Green-Ostrograski theorem, the continuity equation (Eq. D-2) on a stream tube located between 0 and z_1 writes:

$$\iint_{\mathrm{z}=\mathrm{z}_1} v_z(x, z_1)dS - \iint_{z=0} v_z(x, 0)dS = 0 \quad \text{(Eq. D-9)}$$

Thus,

$$\int_{-\ell_1/2}^{\ell_1/2} v_z(x, z_1)dx - \int_{-\Lambda/2}^{\Lambda/2} v_z(x, 0)dx = 0 \quad \text{(Eq. D-10)}$$

With v_e the maximum of the entrance profile:

$$\int_{-\ell_1/2}^{\ell_1/2} \phi(z_1)\left(1-\frac{4x^2}{\ell_1^2(z_1)}\right)dx - \int_{-\Lambda/2}^{\Lambda/2} v_e\left(1-\frac{4x^2}{\Lambda^2}\right)dx = 0 \qquad \text{(Eq. D-11)}$$

ℓ_1 does not depend on x, we finally find:

$$\phi: z_1 \to \frac{v_e \Lambda}{\ell_1(z_1)} \qquad \text{(Eq. D-12)}$$

We can find the velocity along the z-axis:

$$v_z(x, z_1) = v_e \frac{\Lambda}{\ell_1(z_1)}\left(1-\frac{4x^2}{\ell_1^2(z_1)}\right) \qquad \text{(Eq. D-13)}$$

With two velocity components, the continuity equation (Eq. D-2) gives:

$$\frac{\partial v_x}{\partial x} = -\frac{\partial v_z}{\partial z} = \frac{v_e \Lambda \ell_1'(z_1)}{\ell_1^2(z_1)}\left(1-\frac{12x^2}{\ell_1^2(z_1)}\right) \qquad \text{(Eq. D-14)}$$

Then, we obtain v_x as a primitive of x, combining with (Eq. D-12):

$$v_x(x,z) = -\int_x \frac{\partial v_z}{\partial z} = \frac{v_e \Lambda \ell_1'(z_1)}{\ell_1^2(z_1)}x - \frac{4 v_e \Lambda \ell_1'(z_1)}{\ell_1^4(z_1)}x^3 + \psi(z_1) \qquad \text{(Eq. D-15)}$$

$\psi: z_1 \to \psi(z_1)$ is a map function of z_1 through integration with x. We have the boundary conditions $v_x\left(-\frac{\ell_1}{2}, z\right) = v_x\left(\frac{\ell_1}{2}, z\right) = 0$ because of the no-slip condition. Using the previous equation we find that for all z_1, $\psi(z_1) = 0$. Remarking that $\ell_1'(z_1) = -2\tan(\alpha)$ it comes:

$$v_x(x, z_1) = \frac{2\tan(\alpha)\, v_e \Lambda x}{\ell_1^2(z_1)}\left(\frac{4x^2}{\ell_1^2(z_1)} - 1\right) \qquad \text{(Eq. D-16)}$$

Combining (Eq. D-15) and (Eq. D-12) we finally have:

$$\vec{v}(x, z_1) = \frac{2\tan(\alpha)\, v_e \Lambda x}{\ell_1^2(z_1)}\left(\frac{4x^2}{\ell_1^2(z_1)} - 1\right)\overrightarrow{e_x} + v_e \frac{\Lambda}{\ell_1(z_1)}\left(1-\frac{4x^2}{\ell_1^2(z_1)}\right)\overrightarrow{e_z} \qquad \text{(Eq. D-17)}$$

Diffuser – C_3:

The fluid velocity in this part is similar to the one obtained in C_1.

Once the velocity field is wholly solved, integrating (Eq. D-3) gives the pressure field.

3. Turbulent flow

For turbulent flows, no analytical expression exists for the friction loss, it is then necessary to use the Darcy-Weisbach equation as well as a correlation for the friction coefficient f. We will consider the Haaland correlation (1983) [56] set up for turbulent flows so that $Re > 2800$ as mentioned before. The local losses are adapted from [55].

The turbulent model is the following:

- C_1 contains both local and friction losses
- C_2 only contains a friction loss
- C_3 contains both local and friction losses

The detail of the losses are depicted in chapter 2, consequently we will not explain them hereafter.

4. Validation of the 1D model

1.3. Laminar flow

CFD Model:

The CFD simulation has been run with the code *Cast3M* [77], the geometry represents the 1D channel that we set up in the thesis, but in 2 dimensions. The simulation has been run so that $Re = 50$ with a nominal (2 mm) gap. The mesh is given in Figure D-2.

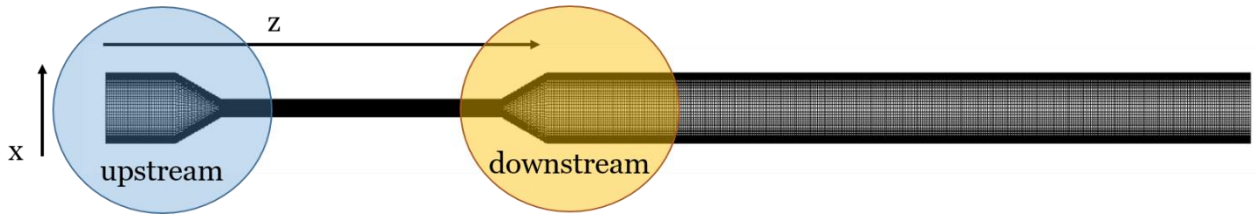

Figure D-2 - Mesh built with CAST3M

Results:

We compare the 2D analytical solution developed in section 2 (further called INS) against Cast3M results in terms of two different pressure losses: the pressure loss taken on the median line of the problem ($x = 0$), and the mean pressure loss (mean pressure on the inlet and outlet of the CD).

Model	CAST3M (x=0)	CAST3M (P_{mean})
INS (x=0)	2.26%	
INS (P_{mean})		0.50%

Table D-1 - Relative deviation INS compared to Cast3M

Table D-1 highlights relative deviations between our direct integrations of the Navier-Stokes equations (called INS), and the CAST3M calculation. The difference is globally very small, meaning two things: firstly, the hypothesis of the C_1 and C_3 profiles being parabolic seems relevant, and secondly, we can lean upon CAST3M to compare the 1D models within this layout. One can also notice that mean pressure and the pressure on $x = 0$ are close.

In Table D-2, we compare Model 0 of CD (see chapter 2) associated with adequate pressure losses against both CAST3M and INS. We also add a local loss, to observe the difference with a model only considering friction loss at low Reynolds.

Model	INS (x=0)	CAST3M (x=0)	INS (P_{mean})	CAST3M (P_{mean})
1D – friction and local loss	0.60%	0.10%	2.40%	0.08%
1D – friction loss	3.12%	2.64%	0.20%	2.46%

Table D-2 - Relative deviation INS compared to Cast3M

One can notice that deviations are all lower than 3%. The deviation is also reduced adding a local loss, except for INS (P_{mean}). The laminar flow interest lies in the possible comparison with a simple analytical model (INS). Those comparisons are fruitful, and encourage us to use CAST3M for the following state of the study. Also, one can note a decrease of deviations when adding the local loss, except for one case. All those decreases are a matter of a few percentages: almost all the loss can be assigned to the friction one, which is not really surprising considering a low-Reynolds flows.

2.3. Turbulent flow

CFD model:

Now, CFD simulations are mandatory in the sense that no analytical models are conceivable for higher Reynolds flows.

The calculations are again run with Cast3M, already used for the laminar calculation. Three simulations are performed for Reynolds of 5.10^3, 1.10^4 and 2.10^4. The turbulence is processed through an internal Spalart-Allmaras model.

Results:

Model	CAST3M (x=0)	CAST3M (P_{mean})
$Re = 5\,000$		
1D – friction and local loss	19.30%	20.99%
1D – friction loss	74.35%	74.89%
$Re = 10\,000$		
1D – friction and local loss	13.75%	19.25%
1D – friction loss	75.47%	77.03%
$Re = 20\,000$		
1D – friction and local loss	11.27%	17.12%
1D – friction loss	76.87%	78.40%

Table D-3 - Relative deviation between 1D and Cast3M

In Table D-3 we observe that:

- Without the local loss, deviations are strong. It shows that the loss is mainly based on its local part and that without considering it, the results are not relevant.
- The deviations are globally lower than 20% with local and friction losses. It means that the pressure loss with local losses give good results.
- As previously, one can note that only a few dispersion exists between the mean and the axial pressure loss.
- The deviations decrease along with the Reynolds number. It could stem either from the Darcy's loss coefficient in the Haaland correlation whose area of validity is set above $Re = 2300$, or the local loss coefficients whose validity is $Re > 10^4$. Also, the Spalart-Allmaras model might be more efficient for higher Reynolds.

According to the previous results, the 1D channel is thus considered pertinent for a wider use in laminar and in turbulent regimes.

Appendix E: Model 0 and the associated force

The goal of this appendix is to highlight the problem of Model 0, i.e. the 1D model of CD, without a parallel branch for the grid.

1. The redistribution without grids

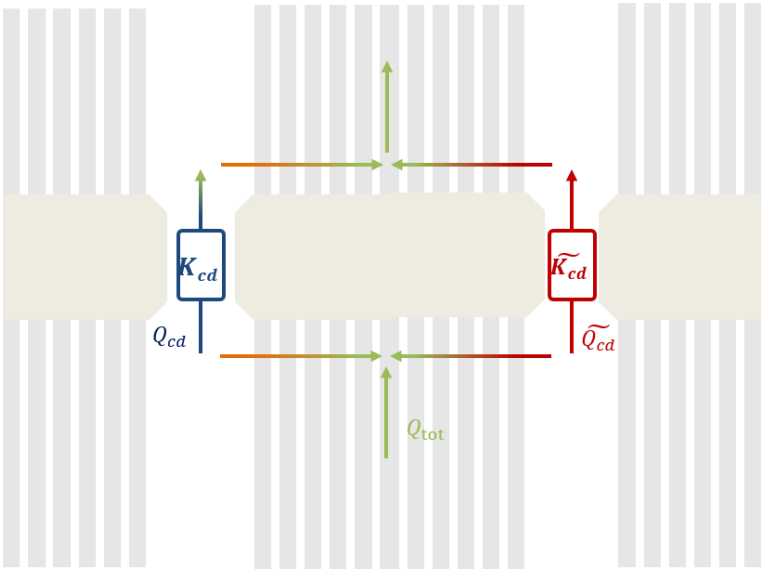

Figure E-1 - Additional lateral resistance due to cross-flows through the rod bundle (model 3)

In a first attempt, a first redistribution was based on Model 0. Working the assumption that forces could be estimated without taking into account the flow going through the grids. Thus, the set of equations is:

$$\begin{cases} \Delta P_{\mathrm{cd}}(Q_{\mathrm{cd}}) - \Delta\widetilde{P_{cd}}(\widetilde{Q_{cd}}) = 0 \\ Q_{cd} + \widetilde{Q_{cd}} = Q_{\mathrm{tot}} \end{cases} \qquad \text{(Eq. E-1)}$$

2. The associated force

Under this hypothesis, the force F_V is obtained directly through the geometrical component of the force. In fact, as no pressure difference exists between both branches, the term $LL_t\Delta p_u$ is null. Having in mind the notations of chapter 3:

$$F_V = L\int_0^{L_t}(p_1 - \widetilde{p_1})dz \qquad \text{(Eq. E-2)}$$

The calculation is run with the following conditions:

- We are interested in an isolated grid displacement. Consequently, we consider two bypasses such as the sum of their width i.e. λ and $\tilde{\lambda}$ is constant. In other words, $\lambda + \tilde{\lambda} = 4.10^{-2}\ m$.
- Several values of λ are chosen between 1.10^{-4} and $3.9\ 10^{-3}\ m$.
- Q_{tot} is calculated such as the entrance velocity equals $6\ m.s^{-1}$.

- $\rho = 700\ kg.m^{-1}$.
- The force (Eq. E-2) is calculated through the flow rates calculated in (Eq. E-1).

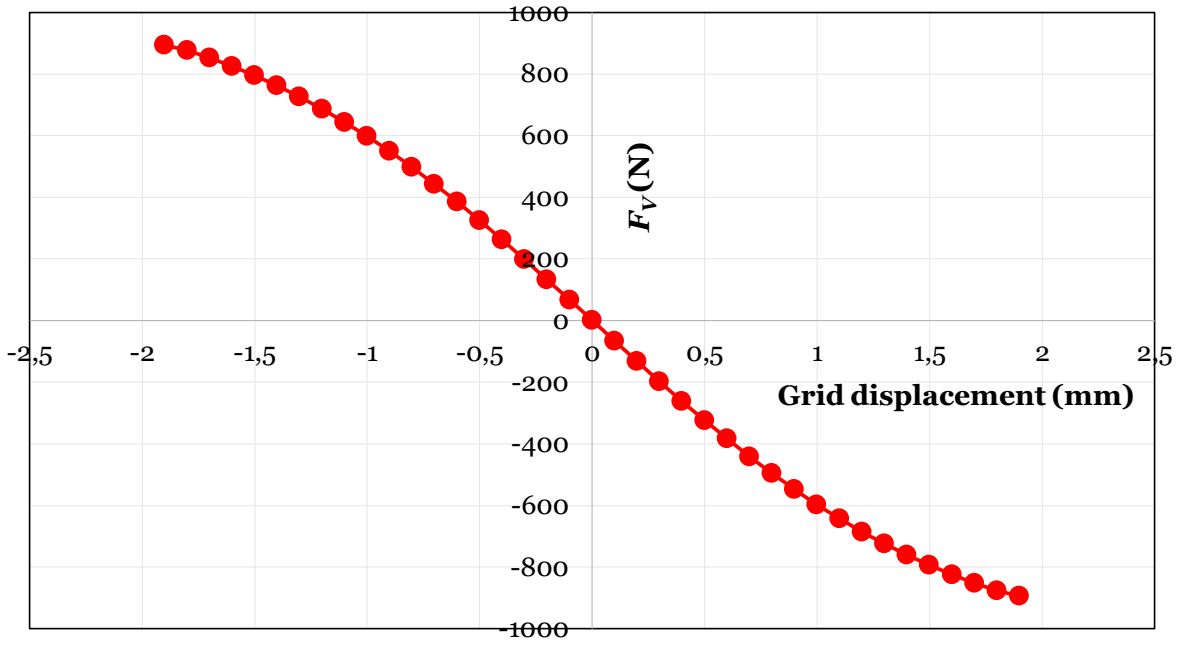

Figure E-2 - Force value with respect to the grid displacement

Figure E-2 gives the evolution of the force value with respect to the displacement. As one can notice, the latter can reach $8\,.\,10^2 N$ on its own. This value is much higher than the few orders of magnitude of total lateral force we could find out in the literature (see the introduction). Consequently, considering a global inflow into the inter-grid areas is misleading. In fact, the fluid bulk velocity could be overestimated in that when the water gaps tend toward shutting, a great amount of total flow rate at the inlet of the system might redistribute toward the spacer grids. The force direction is explained in the next section.

3. Importance of the convergent pressure loss

Model 0 includes three different parts. Their contribution depend on two parameters: the inlet velocity v and the width of the channel λ.

In order to give insights on the force direction under reasonable hypothesis, we are going to show that the total pressure variation is dominated by C_1. First we neglect the frictional loss in the system (see for instance Appendix D, for turbulent flows the local part is much higher). In this case, the total pressure variation given by C_2 is null, and the system is reduced to the pressure variations – dynamic pressure and local loss - of C_1 and C_3 (see for instance (Eq. 3-1) and (Eq. 3-3)). We saw that the difference between those terms can be arranged as follows:

$$\eta = \frac{1}{\rho v^2}\left(\Delta P_{C_1} - \Delta P_{C_3}\right) = \Phi\left(\frac{\lambda + C}{\lambda}\right)^2 + \Psi\left(\frac{\lambda + C}{\lambda}\right) - \omega \qquad \text{(Eq. E-3)}$$

Where C, is a geometrical positive constant, and Φ, Ψ and ω are positive constant depending on ρ.

We easily show that:

$$\forall \lambda > 0, \qquad \frac{\partial \eta}{\partial \lambda} = -\frac{1}{\lambda^3}(2\Phi C(\lambda + C) + C\Psi\lambda + \omega\lambda^3) < 0 \qquad \text{(Eq. E-4)}$$

Knowing that,

$$\begin{cases} \lim\limits_{\lambda \to 0} \eta = +\infty \\ \lim\limits_{\lambda \to +\infty} \eta = \Phi + \Psi - \omega \in \mathbb{R}^+ \end{cases} \qquad \text{(Eq. E-5)}$$

We can deduce that the function η is always positive, and that the pressure variation induced by C_1 is always larger to the one induced by C_3.

A Taylor expansion when λ tends toward 0 shows that:

$$\Delta P_{C_3} \simeq 0.14\ \Delta P_{C_1} \qquad \text{(Eq. E-6)}$$

In other words, for small λ, C_1 dominates the total pressure variation.

4. Sensitivity of the pressure variation in the convergent

As we know that C_1 overlooks the total pressure variation, let us analyze now the influence of both λ and v within ΔP_{C_1}.(pressure difference between 0 and h in (Eq. 3-1)).

We need to know when:

$$d\Delta P_{C_1}(\lambda, v) \geq 0 \qquad \text{(Eq. E-7)}$$

The logarithmic derivative writes:

$$\frac{dln\left(\Delta P_{C_1}(\lambda, v)\right)}{\Delta P_{C_1}(\lambda, v)} = \frac{2dv}{v} + f(\lambda)\frac{d\lambda}{\lambda} \qquad \text{(Eq. E-8)}$$

With f a function of λ. We want to ensure in the end that:

$$\frac{dv}{v} \geq -f(\lambda)\frac{d\lambda}{2\lambda} \qquad \text{(Eq. E-9)}$$

Integrating, we obtain that a positive variation of $\Delta P_{C_1}(\lambda, v)$ is given by:

$$d\Delta P_{C_1}(\lambda, v) \geq 0 \Longrightarrow (\lambda, v) \in \left\{(\lambda, v) \;/\; v \geq v_0\left(\frac{\lambda}{\lambda_0}\sqrt{(K_1 + K_2\lambda_0)/(K_1 + K_2\lambda)}\right), K_1, K_2 \in \mathbb{R}, (\lambda_0, v_0) \in \mathbb{R}^2\right\} \qquad \text{(Eq. E-10)}$$

In other words, from a point (λ_0, v_0), we can split the plane width/velocity in two zones: one where $d\Delta P_{C_1}(\lambda, v) \geq 0$, and thus the pressure loss increases, and one where the variation decreases. The frontier is defined by (Eq. E-10).

Figure E-3 we plot the velocity in the inter-grid area with respect to its width. We also plot the frontier defined in (Eq. E-10) with $(\lambda_0, v_0) = (2.10^{-3}, 6)$ (nominal case where both flow rates in the bypasses are equal).

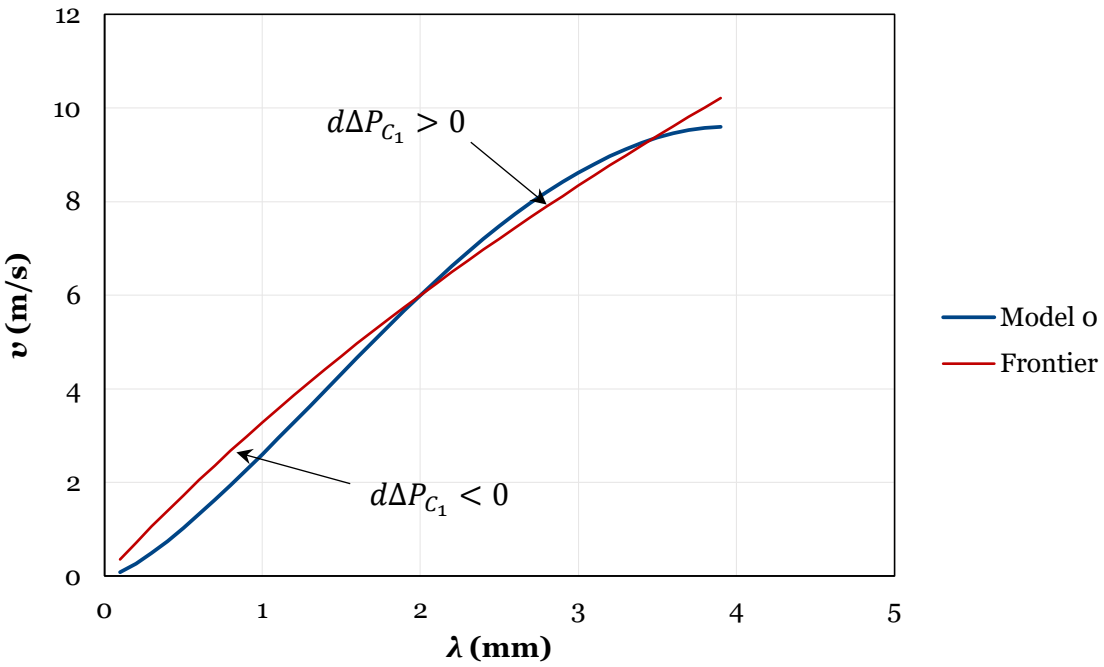

Figure E-3 - Sensitivity of ΔP_{C_1}

The competition between λ and v is not trivial, it is difficult to predict ΔP_{C_1} *a priori*. Let

us take Figure E-2 as an example. If the width to the right hand side decreases (i.e. the grid displacement is positive), the bypass to the right is located in the zone $d\Delta P_{C_1} < 0$, and the one to the left is located in the zone $d\Delta P_{C_1} > 0$. Therefore, the pressure at the right side of the grid is higher than the pressure at the left side. The force is thus negative. It is the other way around if the displacement is negative. We find back the result in Figure . In this case, the grid is thus attracted to the center like a mass bounded by springs (so called "gap equalizing" effect described in the literature).

Appendix F: *Phorcys*, a network-based tool designed for fluid redistributions

Every single hydraulic simulation run in this manuscript has been computed with a tool programmed during this project, named *Phorcys* (Figure F-1), we found necessary to broadly explain how it works.

Figure F-1 - Phorcys' logotype (ASCII art) displayed when the package is imported

As no code aims specifically at solving those kind of systems at the CEA, we undertook to program it from scratch. *Phorcys* has been designed through a commitment of being easily configurable given a set of water gaps width.

1. A reminder about steady-state grid networks

The most famous examples of hydraulic networks lie in water distribution systems – also called pipeline networks - which represent a particular field of civil and environmental engineering. Other fields have used networks to pursue researches, like hemodynamics [137], or nuclear core physics [50]. Two main types of hydraulic network patterns exist. The first one are branching patterns, starting from a source, and branches are split into several sub-branches at each node, then finally finish with dead-ends (it is similar to a tree). The second one are grid patterns, where loops are defined. In other words, while there is only one possible way for the fluid in branching patterns (from the trunk to the branches like a tree), the fluid contained in branches – or elements – in a grid network is free to flow in more than one direction. Their solution requires iterative methods. Grid networks contain three types of different components: nodes, elements, and loops. All these components are related to each other through two types of equations: the node equations also called 'mass conservation equations' or 'continuity equations', and the loop equations also known as 'energy conservation equations'. In other words, a network is a hydraulic analogy to electrical circuits, except that, as we will see, it is nonlinear. In our context, we look after steady state solutions, but it is also possible to study unsteady solutions (see for instance [138] dealing with water hammer issues).

1.3. Node equations

The equation at node j is [139] (Eq. F-1):

$$\sum_{\substack{i=0 \\ i \neq j}}^{N_j} Q_{ij} + q_j = 0 \qquad \text{(Eq. F-1)}$$

Where q_j is called the demand at node j (sign + for a node inflow and – for a node outflow), Q_{ij} is the flow rate through element ij (sign + for a node inflow and – for a node outflow), N_j is the number of elements related to node j. Those are called 'junction nodes', in that it makes a junction between different hydraulic elements through continuity, in contrast with the fixed grade nodes (see below).

2.3. Loop equations

In practice, two kinds of loops exist in the literature, respectively called 'primary loops' (or 'closed-loop') and 'open loops' (also known as 'pseudo-loops'), they are illustrated in Figure F-2. As explained by Wood [62], primary loops, are closed pipe circuits within the network which have no additional closed pipe circuits within them. According to Sarbu [139], open loops make the connection between two nodes whose head is known (also known 'fixed grade node' by Wood [62]).

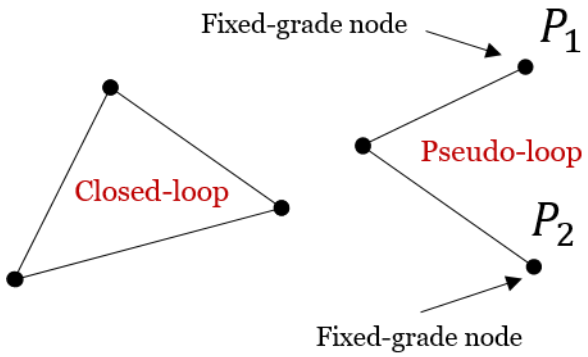

Figure F-2 - Illustration of the loops

Energy conservation equations in one loop m can be summed up by [139]:

$$\sum_{ij \in m} \epsilon_{ij} \Delta P_{ij} - f_m = 0 \qquad \text{(Eq. F-2)}$$

Where $\epsilon_{ij} \in \{-1,1\}$ stands for the orientation of the element ij within the loop. If the element has the same direction as the convention adopted, $\epsilon_{ij} = 1$, otherwise its value is -1. ΔP_{ij} is total pressure loss across element ij, often written has a head h_{ij} - as a reminder, head and total pressure are related to each other through $h_{ij}\rho g = \Delta P_{ij}$, they both are interpreted as the same physical and are often mixed up in the literature -. The f_m expression depends on the type of loop considered (whether closed or open). If one considers a closed-loop where an energy is added (*i.e.* a pump):

$$f_m = \sum_{ij \in m} \epsilon_{ij} H_{p,ij} \qquad \text{(Eq. F-3)}$$

With $H_{p,ij} = AQ_{ij}^2 + B|Q_{ij}| + C$ being a typical pump curve.
Otherwise, a simple closed-loop without any pump writes:

$$f_m = 0 \qquad \text{(Eq. F-4)}$$

For an energy conservation in an open-loop:

$$f_m = \Delta E \qquad \text{(Eq. F-5)}$$

Where ΔE is the energy difference between the loop entrance and exit.

As mentioned several times in this project, ΔP_{ij} is a nonlinear term with respect to flow rate Q_{ij}, it marks the difference with a common electrical circuit where generally the current intensity is proportional to the potential difference through a ratio read as the electrical resistance. In hydraulic network, it only happens when we take an interest in laminar flows. In fact, for a laminar flow, one can show that the Darcy loss coefficient becomes $64/R_e$ (known as the 'Hagen-Poiseuille law'), and ΔP_{ij} becomes linear with respect to the discharge Q_{ij}. Aside from this very special case ΔP_{ij} writes:

$$\Delta P_{ij} = K_{ij} Q_{ij}^{\alpha} \qquad \text{(Eq. F-6)}$$

Where K_{ij} is the hydraulic resistance and α the discharge exponent whose value depends on the formula adopted for the pressure drop. K_{ij} is an intricate map which contains every single parameter of the fluid physics crossing the element and its geometry (viscosity and element roughness through the Darcy or Fanning coefficient, cross section, hydraulic diameter, density, etc.).

3.3. Relation between loops, nodes and elements

The fundamental relation [61, 140] linking the number of nodes with the number of elements and loops is:

$$N_E = N_L + N_N - 1 \qquad \text{(Eq. F-7)}$$

Where N_E is the total number of elements – or pipes – in the system (we will see that in our case N_E also equals the number of equations), and N_L the number of closed-loop. N_N is the total number of nodes (junction of fixed grade), one is redundant. (Eq. F-7) can be derived from the Euler's polyhedron formula [141].

2. Methods

Many methods have been set up to solve pipeline networks, depending on the unknowns and the type of equations. The most famous ones are the loop-oriented, the node-oriented, the node-loop-oriented, and the pipes oriented methods.

1.3. Loop oriented methods

The loop-oriented formulation is most likely the most ancient one. It is often attributed to Hardy Cross (1885-1959), an American structural engineer author of the *moment distribution method* for structural analysis of statically indeterminate structures. The latter was then adapted as an iterative method to solve pipeline networks related systems [54]. It is historically the first method to calculate flow redistributions in large-scale water supply systems, it is also known as the single path adjustment method [62]. The Hardy Cross method aims at successively correcting the loop equations from an initial guess satisfying the continuity equations. The 'single path adjustment' method thus introduces a ΔQ_m term in each loop m independently whose expression is based on a Taylor expansion for small ΔQ_m compared to Q_{ij} in (Eq. F-2):

$$\sum_{ij\in m} \epsilon_{ij} K_{ij} \left(Q_{ij} + \Delta Q_m\right)^{\alpha} - f_m \sim \sum_{ij\in m} \epsilon_{ij} K_{ij} \left(Q_{ij}^{\alpha} + \alpha Q_{ij}^{\alpha-1} \Delta Q_m\right) - f_m = 0 \qquad \text{(Eq. F-8)}$$

So that:

$$\Delta Q_m = \frac{f_m - \sum_{ij\in m} \epsilon_{ij} K_{ij} Q_{ij}^{\alpha}}{\sum_{ij\in m} \alpha \epsilon_{ij} K_{ij} Q_{ij}^{\alpha-1}} \qquad \text{(Eq. F-9)}$$

The method stops when the change in flows is satisfactory. An improvement of this method has been proposed latter in [142] to solve simultaneously the whole system through a matrix system. This formulation is based on the unknowns ΔQ_m in each loop.

2.3. Node oriented methods

Those methods are based on the pressures and their adjustments. Cross was also the first to figure out this formulation through the single node adjustment which is similar to the single path adjustment method, but focuses on the pressures. An initial set of pressures is assumed, but does not have to fulfill any conditions [62]. The second step is to compute an adjustment factor which satisfies continuity of the flow. This adjustment factor is obtained through a gradient approximation. In other words, this method is the exact equivalent of the Hardy Cross method (the single path adjustment) but where the continuity equations are balanced, and the unknowns rely on the pressure adjustments. Many improvements have been undertaken since, like the simultaneous node adjustment method, the introduction of linearization within the node equations [143] or the variational formulation approach [139].

Wood and Rayes, back in 1981, [62] advised against using the node-related approaches, for the sake of issues including convergence difficulties. Nielsen [63] later agreed with Wood, and discouraged the use of pressures as primary unknowns.

3.3. Loop-node oriented methods

Contrary to the previous formulations where we put the emphasis on one equation or the other, this class of methods consists in solving directly both node and loop equations without any adjustment. The unknowns here are the flow rates in each element. This approach has been widely backed and spread by D.J. Wood at the time of the Fortran programming language expansion [61]. The resulting system contains exactly N_E equations (sum of the node and loop equations), which can be solved through a dedicated numerical method (mainly Newton-Raphson or linear theory [63]). This formulation is explained in details thereafter.

4.3. Pipe oriented methods

The previous methods focus either on the flow rates, or the node pressures. Todini and Pilati [144] introduced a method to solve simultaneously for the pressure and the flow rates. Writing the node equations (Eq. F-1) with respect to the flow rates (Eq. F-6), one obtains $N_N + N_E$ equations which creates a larger system than the previous methods. One advantage of this method is to prevent from defining loops which might be a time consuming task [145].

5.3. Other methods

A couple of different approaches use more unfamiliar techniques to solve hydraulic networks. Among them, we can quote for example the extended linear graph theory (ELGT) [146, 147, 148] which leans on graph theory (introduction of an equivalent linear graph), or probabilistic methods based on a maximal entropy approach (see for instance [149]).

3. Solving the node and loop equations in Phorcys

In Phorcys we chose to solve simultaneously the node and loop equations. In other words, we adopted a node-loop oriented method. The reason why such a formulation has been adopted is double. First, they are based on only one kind of unknowns (flow rates), which is a good manner to access both flow rates – used for validation for instance - and related pressure drops – for forces and validation - through a very simple post-processing: a pressure drop in one element is obtained multiplying the flow rate and the resistance (Eq. F-6). In fact, reconstructing the pressure field at nodes afterward is not that useful for our applications. Second, the reliability of these formulations combined with a quite easy implementation (see the 'Q-system' of [150] or [151]) gives them enough credit without the need of searching for intricate approaches. For this reason, some authors still use them

nowadays. Actually, the system is solved directly as a whole without building up any 'path'. Blended with the 'linear method theory' (LTM), the convergence is quickly reached, and is not really sensitive to the initial guess of flow rates in the whole system. Wood and Charles tested their method combined with 'LTM' on a large-scale network back in the days [61] and already pointed out its effectiveness compared to Newton-Raphson, or Hardy-Cross. This is the algorithm that we chose – even though others were tried out - . The only disadvantage of these methods leans on the fact that loops must be declared beforehand as stood previously in contrast with pipe oriented methods. Thereafter, we depict the different equations when no fixed-grade node exists in the system.

1.3. Continuity equations for LTM

Continuity equations, depending on nodes, only rely on (Eq. F-1) which can be seen as follows:

$$\begin{cases} \sum_{\substack{i=0 \\ i\neq j}}^{N_1} Q_{i1} = -q_1 \\ \dots \\ \sum_{\substack{i=0 \\ i\neq j}}^{N_{N_N-1}} Q_{i(N_N-1)} = -q_{(N_N-1)} \end{cases} \qquad \text{(Eq. F-10)}$$

The terms used in this equation were already explained earlier in this section. As a reminder, there are $N_N - 1$ unredundant equations with respect to a total of N_N nodes in the hydraulic system. q_j deals with the demand related to node j (positive for an entrance, negative for an exit, or zero is the node is just a 'junction' without demand).

In other words, the system can be summed up as follows:

$$\overline{\overline{A_t}} \begin{pmatrix} Q_1 \\ \dots \\ Q_{N_E} \end{pmatrix} = \begin{pmatrix} -q_1 \\ \dots \\ -q_{(N_N-1)} \end{pmatrix} = \bar{\bar{q}} \qquad \text{(Eq. F-11)}$$

Where $\overline{\overline{A_t}}$ - dimension $(N_N - 1,\ N_E)$ - is the continuity matrix (also known as the system topology matrix). It contains every interaction between nodes, and thus is responsible for the geometry of the network. $\bar{\bar{q}}$ - dimension $(N_N - 1,\ 1)$ - is the vector of demand. A very simple network is proposed in Figure F-3 to illustrate the equations.

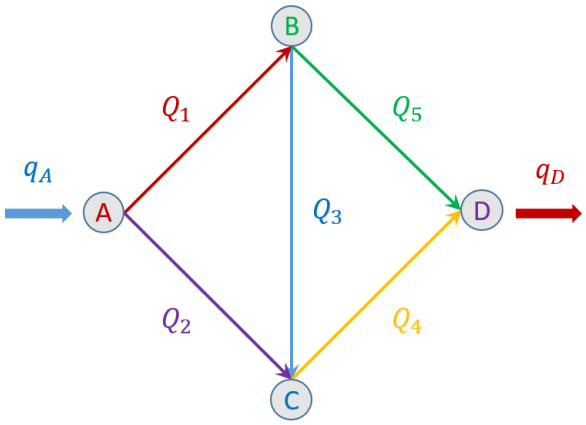

Figure F-3 - Illustrative network - continuity

On this example, (Eq. F-10) turns:

$$\begin{cases} -Q_1 - Q_2 = -q_A \\ Q_1 - Q_3 - Q_5 = 0 \\ Q_2 + Q_3 - Q_4 = 0 \end{cases} \quad \text{(Eq. F-12)}$$

By the way, one can check that equation at node D is a linear combination of the three others (knowing that necessarily $q_A = -q_D$ it can be obtained through equations 'green minus red minus blue'). (Eq. F-11) thus turns:

$$\overline{\overline{A_t}} \begin{pmatrix} Q_1 \\ Q_2 \\ Q_3 \\ Q_4 \\ Q_5 \end{pmatrix} = \begin{pmatrix} -q_A \\ 0 \\ 0 \end{pmatrix} \quad \text{(Eq. F-13)}$$

Where:

$$\overline{\overline{A_t}} = \begin{pmatrix} -1 & -1 & 0 & 0 & 0 \\ 1 & 0 & -1 & 0 & -1 \\ 0 & 1 & 1 & -1 & 0 \end{pmatrix} \quad \text{(Eq. F-14)}$$

2.3. Energy equations for LTM

Energy equations rely on (Eq. F-2) and (Eq. F-6):

$$\begin{cases} \sum_{ij \in m_1} \epsilon_{ij} K_{ij} Q_{ij}^{\alpha} - f_{m_1} = 0 \\ \dots \\ \sum_{ij \in m_{N_L}} \epsilon_{ij} K_{ij} Q_{ij}^{\alpha} - f_{m_{N_L}} = 0 \end{cases} \quad \text{(Eq. F-15)}$$

Where $(m_1, \dots, m_{N_L})$ are the different loops in the system. This system is nonlinear, due

to the α index. The main idea behind the so called 'linear theory' as presented historically by Wood [61], is to write the pressure drop as (Eq. F-16):

$$\Delta P_{ij} = K_{ij} Q_{ij}^{\alpha} = K_{ij} Q_{ij}^{\alpha-1} Q_{ij} \qquad \text{(Eq. F-16)}$$

From this consideration, given a certain iteration $k \in \mathbb{N}$ of the algorithm, Wood writes:

$$\Delta P_{ij}^{k} = K_{ij}^{k} Q_{ij}^{k} \qquad \text{(Eq. F-17)}$$

Where the resistance K_{ij}^{k} at iteration k is linearized as follows:

$$K_{ij}^{k} = K_{ij}\left(Q_{ij}^{k-1}\right)^{\alpha-1} \qquad \text{(Eq. F-18)}$$

Consequently, (Eq. F-15) becomes at iteration k:

$$\begin{cases} \sum_{ij \in m_1} \epsilon_{ij} K_{ij}^{k} Q_{ij}^{k} - f_{m_1} = 0 \\ \cdots \\ \sum_{ij \in m_{N_L}} \epsilon_{ij} K_{ij}^{k} Q_{ij}^{k} - f_{m_{N_L}} = 0 \end{cases} \qquad \text{(Eq. F-19)}$$

In other words, Wood turned the energetic system into a linear system at iteration k:

$$\bar{\bar{K}}^{k} \begin{pmatrix} Q_1^k \\ \cdots \\ Q_{N_E}^k \end{pmatrix} = \begin{pmatrix} f_{m_1} \\ \cdots \\ f_{m_{N_L}} \end{pmatrix} = \bar{\bar{f}} \qquad \text{(Eq. F-20)}$$

Where $\bar{\bar{K}}^{k}$ - dimension $(N_L,\ N_E)$ - is the matrix of hydraulic resistances at iteration k. The right hand side term obviously equals a null vector when all loops are closed ones. $\bar{\bar{f}}$ - dimension $(N_L,\ 1)$ -, is the vector giving the energy conditions. By analogy with the continuity equations, let us illustrate the latter system on the same example (Figure F-4).

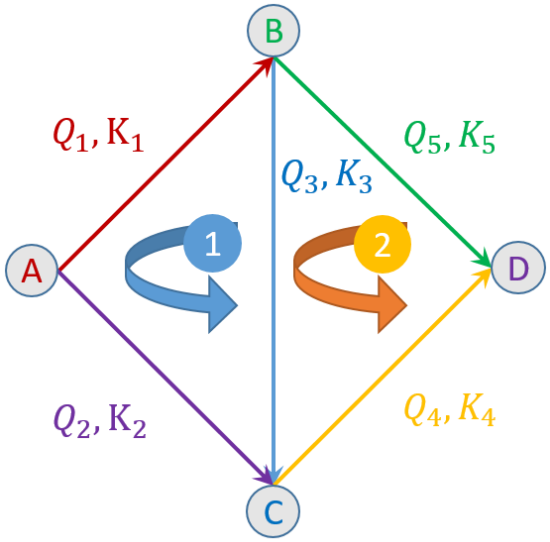

Figure F-4 - Illustrative network – energy

On this example, there are two closed loops, and thus two energy equations:

$$\begin{cases} -K_1 Q_1^{\alpha} + K_2 Q_2^{\alpha} - K_3 Q_3^{\alpha} = 0 \\ K_3 Q_3^{\alpha} + K_4 Q_4^{\alpha} - K_5 Q_5^{\alpha} = 0 \end{cases} \qquad \text{(Eq. F-21)}$$

The sign of the terms (ϵ_{ij}) depends on the convention chosen for tracking the oriented loops.

At iteration k:

$$\bar{\bar{K}}^k \begin{pmatrix} Q_1^k \\ Q_2^k \\ Q_3^k \\ Q_4^k \\ Q_5^k \end{pmatrix} = \begin{pmatrix} 0 \\ 0 \end{pmatrix} \qquad \text{(Eq. F-22)}$$

Where:

$$\bar{\bar{K}}^k = \begin{pmatrix} -K_1^{k-1} & K_2^{k-1} & -K_3^{k-1} & 0 & 0 \\ 0 & 0 & K_3^{k-1} & K_4^{k-1} & -K_5^{k-1} \end{pmatrix} \qquad \text{(Eq. F-23)}$$

3.3. Using the LTM algorithm

In practice, the whole system of equations is obtained combining (Eq. F-11) and (Eq. F-20), *i.e.* gathering both node and loops equations. The whole system at iteration k can be put into the following form:

$$\bar{\bar{M}}^k \bar{\bar{Q}}^k = \bar{\bar{D}} \qquad \text{(Eq. F-24)}$$

Where:

$$\bar{\bar{M}}^k = \begin{pmatrix} \bar{\bar{K}}^k \\ \overline{\overline{A_t}} \end{pmatrix}, \quad \bar{\bar{Q}}^k = \begin{pmatrix} Q_1^k \\ \dots \\ Q_{N_E}^k \end{pmatrix}, \quad \bar{\bar{D}} = \begin{pmatrix} \bar{\bar{f}} \\ \bar{\bar{q}} \end{pmatrix} \qquad \text{(Eq. F-25)}$$

The matrix $\bar{\bar{M}}^k$ is square and its dimension is $(N_E,\ N_E)$ - we remind that $N_E = N_L + N_N - 1$ -, it gathers the resistances and the geometry of the system. $\bar{\bar{Q}}^k$ is the vector of flow rates. Finally, $\bar{\bar{D}}$ includes the system constraints, its expression does not change with the iterations.

The whole method is summed up in Figure F-5:

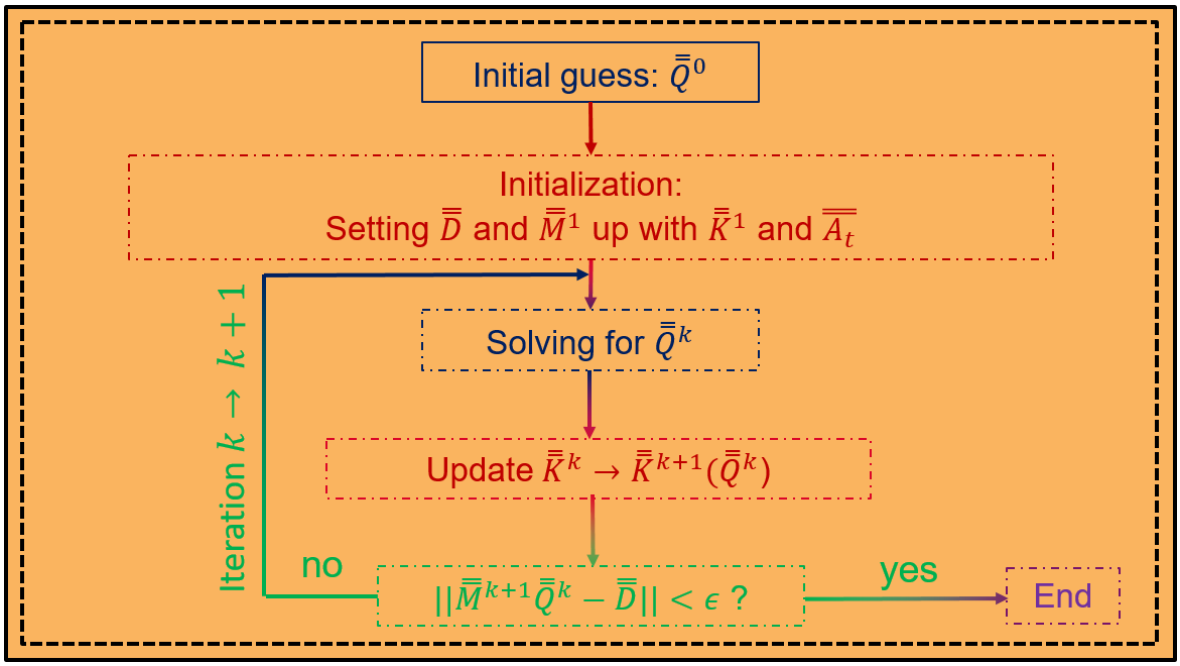

Figure F-5 - Runing a flow rate calculation with LTM

Let us make a couple of remarks.
Firstly, at iteration k, a linear system has to be solved, because $\bar{\bar{Q}}^k$ is given by:

$$\bar{\bar{Q}}^k = \bar{\bar{M}}^{k^{-1}}\bar{\bar{D}} \qquad \text{(Eq. F-26)}$$

In fact, the system (Eq. F-24) can be directly solved using a dedicated algorithm. In our case, *Phorcys* works as a Python package which leans on a couple of several other libraries. Among them we can quote *Scipy*, *Numpy* and *Matplotlib* for instance. Linear systems, put in an array form, can be solved with a dedicated *Scipy* function, which itself is a wrapper of Fortran's library LAPACK (which uses LU decomposition). For larger systems, it can be necessary to use a sparse formulation for solving. $\bar{\bar{M}}^k$ includes indeed a lot of unnecessary null values which is memory consuming. When changing the standard array format with a sparse format 'CSC', standing for *'Compressed Sparse Column'*, another dedicated solving function must be used. In this case this is a wrapper of C's library UMFPACK (which uses

Unsymmetric MultiFrontal method). In practice, experience shows that the time spent for solving sparse systems and 'standard' systems is almost the same for relatively 'large' systems (let us say N_E up to $\sim 10^3$). However, for higher N_E, the memory can quickly fills up and the calculation ends up very slow. Using the sparse format is incredibly timesaving for high N_E due to a huge amount of null values flushed out from the memory.

Secondly, as stated by Wood himself, and further explained by Nielsen [63], this method can undergo oscillations when approaching the solution. In this case, Wood recommended to use what is called an 'averaged LTM', in other words, under-relaxing the solution at iteration k with the solution obtained at iteration $k-1$ [61, 147]:

$$\bar{\bar{Q}}^k \rightarrow \frac{\bar{\bar{Q}}^k + \bar{\bar{Q}}^{k-1}}{2} \qquad \text{(Eq. F-27)}$$

This distinct improvement has been latter mathematically explained by Nielsen [63], who also recommended to use a 'full LTM' (*i.e.* without averaging) for first iteration and then 'averaged LTM' considering the convergence properties of each method on its own.

Thirdly, our systems mainly deal with fuel assemblies in a context of deformation. Hydraulically, this deformation holds in the width of the gaps surrounding the fuel assemblies. The models developed in the project depend on λ, the convergent-diffuser width between two successive grids. This parameter characterizes K_{CD} the associated hydraulic resistance of the convergent-diffuser, which is part of the numerous ones in the matrix of resistances. In other words, one must previously provide a correct distribution of λ in the system to set up $\bar{\bar{K}}^k(\lambda)$.

4. Structure and usage

1.3. Main classes and related objects

The tool is still under development, and thus is subjected to future improvements. At the moment, three main classes are essential: the nodes, the elements, and the loops (Figure F-6).

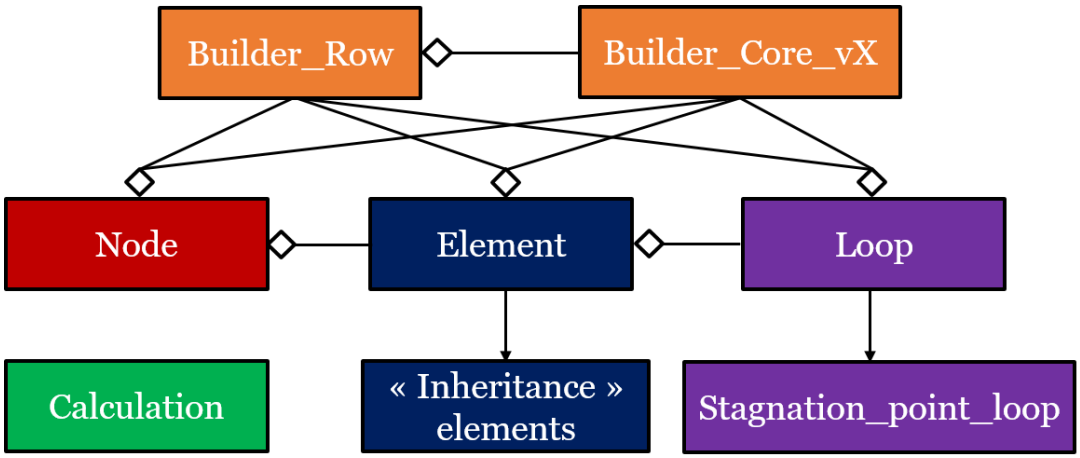

Figure F-6 - Simplified structure

The class Node is used for declaring nodes and their possible locations for further viewing.

The class Element is used for declaring elements – pipes. Each object of type Element contains physical parameters such as its cross section, or the associated hydraulic diameter. Inherited classes from Element such as 'Bypass_element' contain additional parameters like the width λ and related methods. Element objects also have information on their arrival and departure nodes to which they are bound. In return, when instancing an Element object bound to two nodes, the latter are updated with information regarding elements departing from them, and arriving to them.

The class Loop is used for declaring loops based on elements previously set up in the system. An inheritance class 'Stagnation_point_loop' is used for telling further calculation to create a modified resistance associated to certain elements within the loop. It is the case for redistributions upstream from spacer grids, where Model 2 introduces a modified resistance for both grids and convergent-diffuser. This modified resistance adds a kind of dynamic of pressure term, based on the cross section. Consequently, when building up energy equations for calculation, it is this resistance that is used.

The class Calculation mostly deals with class attributes related to the network calculation, like the criterion precision.

Some others classes exist, including the ones designed for core or row calculations, which automatically builds a network through repetitive pattern based on the other classes. We would also find methods to easily set up boundary conditions, or importing/exporting data (like a set of λ, or demands).

2.3. Illustrative example of use

Let us get back to the textbook case based on Figure F-3. This system is interesting for illustrating and verifying the tool, because it is a well-known simplistic case whose solution can be easily obtained through a Hardy Cross method[4]. We consider the parameters shown

[4] For instance, its analysis and solution are findable at https://en.wikipedia.org/wiki/Hardy_Cross_method.

in Figure F-7.

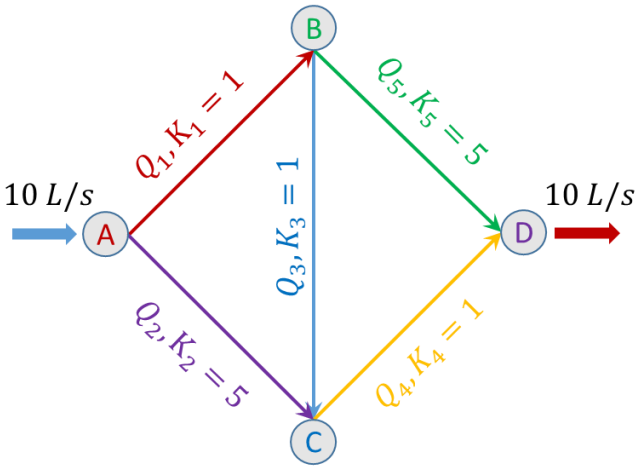

Figure F-7 - Illustrative example for usage

In Figure F-8 we can see how we handle nodes and related elements in a simple script.

```
# -*- coding: utf-8 -*-
"""
Created on Sat Oct 31

@author: Stan
"""


from Phorcys import NEL
from Phorcys import plot3dnetwork as pltn
from Phorcys import wood_ltm as fltm

Node1=NEL.Node("A")
Node2=NEL.Node("B")
Node3=NEL.Node("C")
Node4=NEL.Node("D")

Node1.set_position([0,0,0])
Node2.set_position([1,1,0])
Node3.set_position([1,-1,0])
Node4.set_position([2,0,0])

Element1=NEL.Element("Q1",Node1,Node2,1.)
Element2=NEL.Element("Q2",Node1,Node3,5.)
Element3=NEL.Element("Q3",Node2,Node3,1.)
Element4=NEL.Element("Q4",Node3,Node4,1.)
Element5=NEL.Element("Q5",Node2,Node4,5.)

pltn.plot_network()
```

Figure F-8 - Building up nodes and elements

These commands first create the nodes separately, and set up their positions. Then, we build elements based on the previous nodes to reproduce the network in Figure F-7. The network is plotted afterwards. The result of the previous commands is in Figure F-9.

```
++++++
WELCOME TO PHORCYS
++++++
```


```
*******
*******
*******
YOU ARE ACTUALLY RUNNING THE CASE : C:/Users/Stan/.spyder-py3 /simple_test.py
*******
*******
*******
```

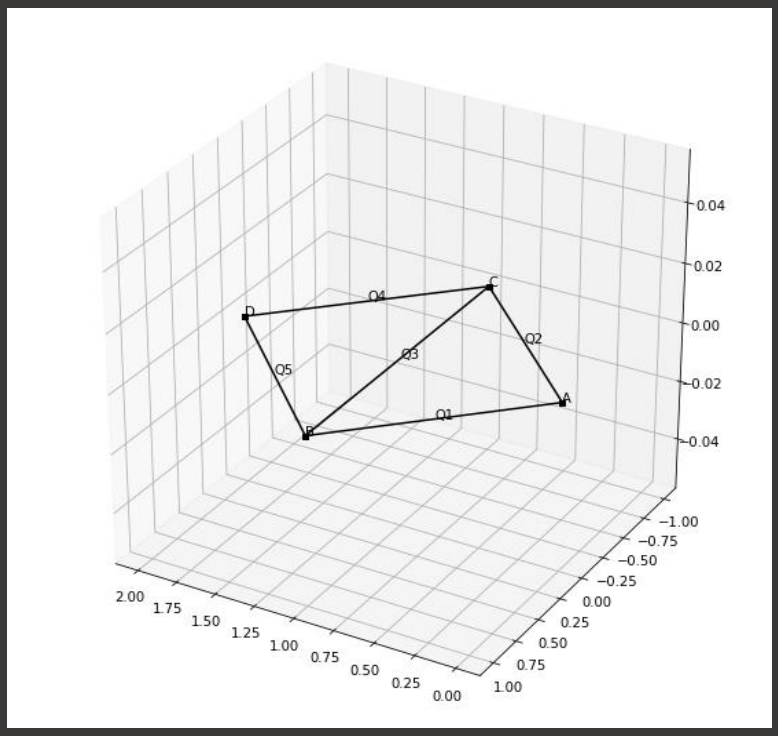

Figure F-9 - Results of first commands

```
Node1.set_new_boundary_condition(10.)
Node4.set_new_boundary_condition(-10.)

NEL.Node.check_boundary_conditions()

Loop1=NEL.Loop("loop1")
Loop1.set_new_element(Element1)
Loop1.set_new_element(Element2)
Loop1.set_new_element(Element3)


Loop2=NEL.Loop("loop2")
Loop2.set_new_element(Element3)
Loop2.set_new_element(Element4)
Loop2.set_new_element(Element5)



fltm.compute()

NEL.Element.print_all_flowrates()

NEL.calculation.print_stats()
pltn.plot_flowrates()

NEL.Element.compute_headlosses()
pltn.plot_headlosses()
```

Figure F-10 - End of the script

The second part (Figure F-10) includes the boundary conditions definition, a verification of those demands (check if the sum of entrances equals the sum of exits). Then, we define loops, compute the system, print the flow rates and statistics, and finally plot flow rates and head losses (pressure losses).

The results are shown in Figure F-11:

All good, mass conservation is ok
During iteration 1, norm of the linear system is 17.560609328835945
[...]
During iteration 27, norm of the linear system is 8.462232874405907e-08
System converged towards the demanded error
Flow rates associated to each element :
Q5 : 3.333333314292961
Q2 : 3.3333333142929606
Q3 : 3.3333333192600145
Q1 : 6.666666626102394
Q4 : 6.666666626102394
wood_ltm calculation, iterations number : 27, time of calculation : 0.033991575241088887 s, Matrix dimension : 5x5

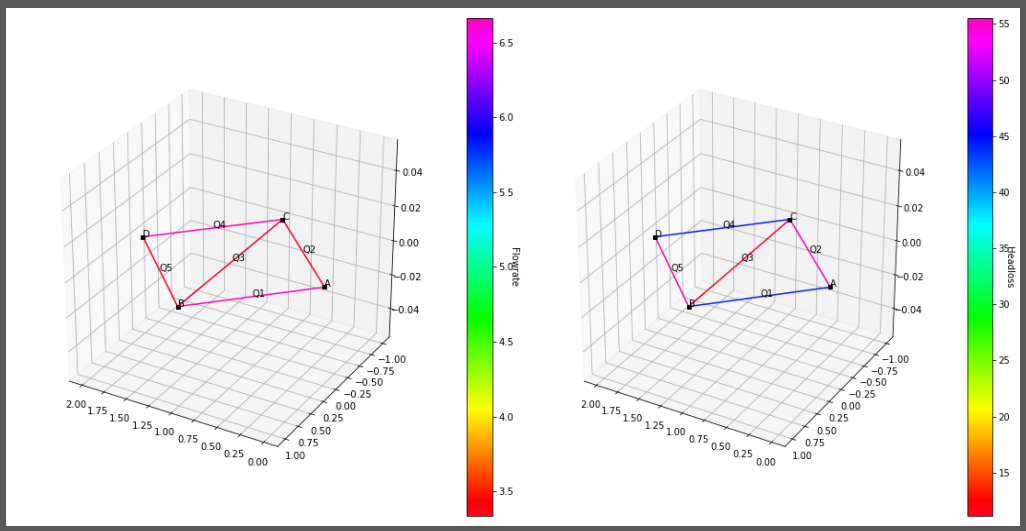

Figure F-11 - Results of the end of the script

As one can see, the flow rates are in agreement with the analytical results of the system[4]: $Q_1 = \frac{10}{3} L.s^{-1}$, $Q_2 = \frac{10}{3} L.s^{-1}$, $Q_3 = \frac{20}{3} L.s^{-1}$, $Q_4 = \frac{20}{3} L.s^{-1}$, $Q_5 = \frac{10}{3} L.s^{-1}$.

From now on, we will explain how we can pull forces out of the calculation.

5. Evaluate hydraulic forces from a network calculation

1.3. An elementary mesh to evaluate the forces

As widely explained above, the network calculation gives a distribution of flow rates and, *a fortiori*, the pressure losses in the system through a simple operation. The question is then how can we value the different forces from such a flow rate distribution.

To do so, we need to define what is called internally in Phorcys an "elementary mesh" from which all classic forces can be drawn up (Figure F-12).

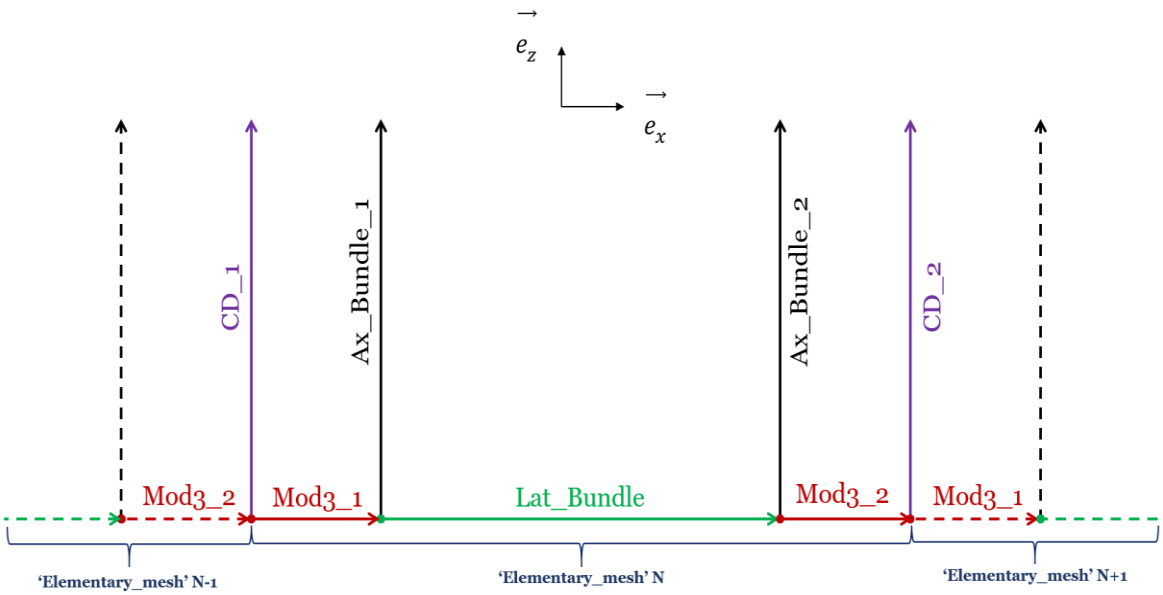

Figure F-12 - Illustration of an elementary mesh to calculate forces

The elementary mesh is built upon two convergent-diffusers (named CD_1 and CD_2), two axial elements (named Ax_Bundle_1 and A_xBundle_2), and three lateral elements : two outer elements from Model 3 (named Mod_3_1 and Mod_3_2) and one inner lateral bundle element (named Lat_Bundle).

2.3. Forces inventory in the elementary mesh

From here on we describe every force which can be set up from the data in one elementary mesh. In what follows, S_i stands for the entrance cross-section of element i, Q_i the flow rate in element i, and ΔP_i the positive pressure loss in element i.

<u>Axial forces</u>

The axial force drawn up from axial elements in one assembly's span, namely F_Z, is given below :

$$\overrightarrow{F_Z} = \Delta P_{Ax\_Bundle\_1}\, S_{Ax\_Bundle\_1} \frac{Q_{Ax\_Bundle\_1}}{|\, Q_{Ax\_Bundle\_1}|}\, \overrightarrow{e_z} + \Delta P_{Ax\_Bundle\_2}\, S_{Ax\_Bundle\_2} \frac{Q_{Ax\_Bundle\_2}}{|\, Q_{Ax\_Bundle\_2}|}\, \overrightarrow{e_z} \qquad \text{(Eq. F-28)}$$

Lateral forces exerting on the bundle

Two forces, respectively F_{Mod3_1} and F_{Mod3_2} are generated by the ΔP_{tot} pressure losses terms (sum of ΔP_l and ΔP_c, see (Eq. 2-29) in chapter 2) through $Mod3\_1$ and $Mod3\_2$ elements occurring within a h_l height upstream from the grid:

$$\overrightarrow{F_{M3\_1}} = \frac{1}{2}\rho \left(\left(\frac{Q_{Ax\_Bundle\_1}}{S_{Ax\_Bundle\_1}} \right)^2 - \left(\frac{Q_{CD\_1}}{S_{CD\_1}} \right)^2 + \Delta P_{l,Mod3\_1} \frac{Q_{Mod3\_1}}{|\, Q_{Mod3\_1}|} \right) h_L L\, \overrightarrow{e_x} \qquad \text{(Eq. F-29)}$$

$$\overrightarrow{F_{M3\_2}} = \frac{1}{2}\rho \left(\left(\frac{Q_{Ax\_Bundle\_2}}{S_{Ax\_Bundle\_2}} \right)^2 - \left(\frac{Q_{CD\_2}}{S_{CD\_2}} \right)^2 + \Delta P_{l,Mod3\_2} \frac{Q_{Mod3\_2}}{|\, Q_{Mod3\_2}|} \right) h_L L\, \overrightarrow{e_x} \qquad \text{(Eq. F-30)}$$

In (Eq. F-29) and (Eq. F-30), we note that the forces are made of velocities coming from ΔP_l and the pressure loss within h_l, ΔP_l (Eq. 2-29).

And one force is induced by the inner bundle located below a grid, named F_{Bu}:

$$\overrightarrow{F_{Bu}} = \Delta P_{Lat\_Bundle} S_{Lat\_Bundle} \frac{Q_{Lat\_Bundle}}{|\, Q_{Lat\_Bundle}|}\, \overrightarrow{e_x} \qquad \text{(Eq. F-31)}$$

Lateral forces exerting on the grid due to coolant put in the upright position

This force, F_{UP}, has already been described in chapter 1. Knowing that we have access with the network to bulk velocities (let us say V_z axially and V_x laterally), we do not know the inner variations of velocity within the cross-sections. Considering that axially, the velocity component equals V_z in each point, we can reuse the equation found out in Appendix A. As a reminder, the general equation giving F_{UP} is the following:

$$F_{UP} = \rho S_g \langle v_x v_z \rangle_{S_g} = \rho S_g V_z \langle v_x \rangle_{S_g} \qquad \text{(Eq. F-32)}$$

Where $\langle v_x \rangle_{S_g}$ is the mean of the lateral component on S_g. Again, we only have access to the inlet bulk velocity V_x. As a first approach it is a reasonable hypothesis thinking that v_x equals either V_x or βV_X (where β is the pitch to diameter ratio) accordingly to whether we consider a position between rods or not (see Figure F-13).

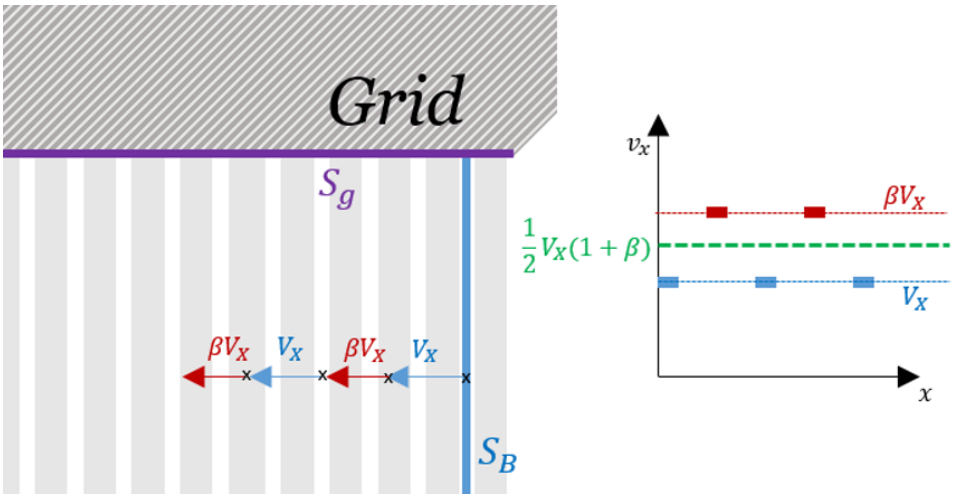

Figure F-13 - Illustration of the lateral velocity variation in the bundle

Consequently $\langle v_x \rangle_{S_g} \sim \frac{1}{2} V_X(1+\beta)$. Injecting the latter expression in (Eq. F-32), all happens as if F_{UP} was the average of two forces (the one for the maximal value of lateral bulk velocity and the one for its minimal value) of the form 'perfect fluid' or 'constant velocity':

$$F_{UP} = \frac{1}{2} \rho \sin(2\theta)\, S_g\, v_\infty^2 \qquad \text{(Eq. F-33)}$$

Where ρ is the fluid density ($kg.m^{-3}$), θ is the angle between the inclined flow entering the grid and the normal to the surface (rad), S_g is the coolant cross-section upstream from the grid (m^2), v_∞ is the norm of the velocity upsteam from the grid ($m.s^{-1}$).

As said previously, F_{UP} may put up with non-trivial oscillations along the grid width, indeed the lateral component of the velocity vary successively from V_X to βV_X in the bundle, and thus θ and v_∞ too. The two couples of variables giving the two extreme forces are:

$$\begin{cases} (\theta_1, \theta_2) = \left(\tan^{-1}\left(\dfrac{S_{Ax\_Bundle} \left| Q_{Lat\_Bundle} \right|}{S_{Lat\_Bundle} \left| Q_{Ax\_Bundle} \right|} \right), \tan^{-1}\left(\beta \dfrac{S_{Ax\_Bundle} \left| Q_{Lat\_Bundle} \right|}{S_{Lat\_Bundle} \left| Q_{Ax\_Bundle} \right|} \right) \right) \\ (v_{\infty_1}, v_{\infty_2}) = \left(\sqrt{\left(\dfrac{Q_{Ax\_Bundle}}{S_{Ax\_Bundle}} \right)^2 + \left(\dfrac{Q_{Lat\_Bundle}}{S_{Lat\_Bundle}} \right)^2}, \sqrt{\left(\dfrac{Q_{Ax\_Bundle}}{S_{Ax\_Bundle}} \right)^2 + \beta^2 \left(\dfrac{Q_{Lat\_Bundle}}{S_{Lat\_Bundle}} \right)} \right) \end{cases} \qquad \text{(Eq. F-34)}$$

With:

$$\begin{cases} Q_{Ax\_Bundle} = Q_{Ax\_Bundle\_1} & (Q_{Lat\_Bundle} > 0) \\ Q_{Ax\_Bundle} = Q_{Ax\_Bundle\_2} & (Q_{Lat\_Bundle} < 0) \end{cases} \qquad \text{(Eq. F-35)}$$

Consequently,

$$\overrightarrow{F_{UP}} = \frac{1}{2}\left(F_{UP}(\theta_1, v_{\infty_1}) + F_{UP}(\theta_2, v_{\infty_2})\right)\frac{Q_{Lat\_Bundle}}{|Q_{Lat\_Bundle}|}\overrightarrow{e_x} \qquad \text{(Eq. F-36)}$$

Lateral force exerting on the grid due to difference of pressure in the bypasses

The expression of the force F_{UP} is:

$$\overrightarrow{F_V} = \left(LL_t\Delta P_u + L\int_0^{L_t}\left(p_1(Q_{CD\_1}) - \widetilde{p_1}(Q_{CD\_2})\right)dz\right)\overrightarrow{e_x} \qquad \text{(Eq. F-37)}$$

Where $p_1(Q_{CD\_1})$ and $\widetilde{p_1}(Q_{CD\_2})$ are respectively the pressure profiles on the left and right hand sides of the grid. In practice, ΔP_u is obtained through:

$$\begin{aligned}\Delta P_u = {} & \Delta P_{Lat\_Bundle}\frac{Q_{Lat\_Bundle}}{|Q_{Lat\_Bundle}|} \\ & + \frac{1}{2}\rho\left(\left(\frac{Q_{Ax\_Bundle\_1}}{S_{Ax\_Bundle\_1}}\right)^2 - \left(\frac{Q_{CD\_1}}{S_{CD\_1}}\right)^2 - \left(\frac{Q_{Ax\_Bundle\_2}}{S_{Ax\_Bundle\_2}}\right)^2\right. \\ & \left. + \left(\frac{Q_{CD\_2}}{S_{CD\_2}}\right)^2\right) + \Delta P_{l,Mod3\_1}\frac{Q_{Mod3\_1}}{|Q_{Mod3\_1}|} + \Delta P_{l,Mod3\_2}\frac{Q_{Mod3\_2}}{|Q_{Mod3\_2}|}\end{aligned} \qquad \text{(Eq. F-38)}$$

As in (Eq. F-29) and (Eq. F-30), (Eq. F-38)ΔP_u is composed of the pressure losses ΔP_l and ΔP_c associated to $Mod3\_1$ and $Mod3\_2$ as well as the lateral pressure loss in the bundle ΔP_{Lat_Bundle}. It represents, as said in chapter 3, the lateral upstream pressure loss between two successive CDs.

3.3. Exporting data from elementary meshes

When necessary, all data can be exported to a single text file. The latter has a format illustrated in Table .

N_x	N_y	Floor	F_B	F_{UP}	F_V	F_Z
1	1	1	5	2	-4	60
1	1	2	-6	2	-6	65
…						

Table F-1 - Example of file exported

N_x and N_y stand for the position of the fuel assembly in the core, Floor is the elementary mesh number axially. F_{UP}, F_V and F_{Ax} match both definitions presented above. F_B is a bit different. It implies the sum of $F_{M3,1}$ and $F_{M3,2}$, which are located a couple of centimeters (along h_l) underneath the grid, plus the mean of F_{Bu} calculated on the considered elementary mesh and the one calculated above the grid (in the elementary mesh situated overhead). In fact, in the mechanical code used for the deformation, the sum of all lateral forces are applied on one given grid. As shown in Figure F-14, all forces exert on a surface

either on or beside the grid in one elementary mesh. F_{Bu} is quite an exception. The force is exerting on cross-sections located on the bundle right below. Averaging the two surrounding F_{Bu} might head toward a better perception of the effect perceived by the grid.

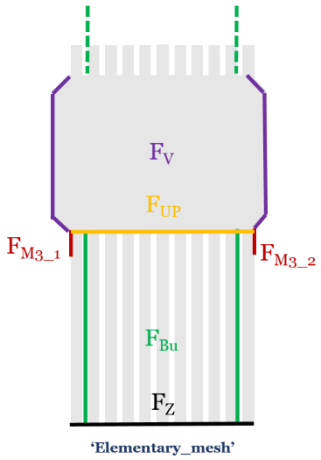

Figure F-14 - Cross-sections entailed by the forces

In practice, F_{Bu} calculated as such may underestimate the bundle a little bit (only 15 'inner' fuel rods are taken into account so does K_B calculated through the Eole correlation). A possible attempt in the future could be to include 17 fuel rods in K_B, at the risk of duplicating outer fuel rods in the vicinity of the spacer grid.

In addition, one can also keep in mind that for 3D redistributions, both forces presented in the exported data (except F_Z) would contain 2 components each, along the x- and y-axis.

References

[1] D. K. Sarkar, "Chapter 1 - General Description of Thermal Power Plants," in *Thermal Power Plant*, D. K. Sarkar, Ed., Elsevier, 2017, pp. 1-31.

[2] USNRC, "Westinghouse Technology Systems Manual," USNRC Technical Training Center, 2012.

[3] I. A. E. Agency, Review of Fuel Failures in Water Cooled Reactors, Vienna: International Atomic Energy Agency, 2010.

[4] H. Grard, Physique, fonctionnement et sûreté des REP: Le réacteur en production, EDP Sciences, 2015.

[5] N. Kerkar and P. Paulin, Exploitation des coeurs REP, EDP Sciences, 2008.

[6] S. de Lambert, G. Campioni, B. Leturcq and A. Bergeron, "Etude de l'impact de la déformation mécanique des assemblages REP sur la neutronique et des conséquences sur l'asymétrie de la nappe de puissance," Institut national des sciences et techniques nucléaires (INSTN), 2016.

[7] L. Karlsson and T. Manngard, "Modelling of PWR Fuel Assembly Deformations During Irradiation," in *Structural mechanics in reactor technology*, Seoul, 1999.

[8] A. Wanninger and et al., "Mechanical Analysis of the Creep Deformation of a Row of Fuel Assemblies in a PWR Core," in *WRFPM 2017*, Jeju Island, 2017.

[9] A. Wanninger, M. Seidl and R. Macián-Juan, "Mechanical analysis of the bow deformation of a row of fuel assemblies in a PWR core," *Nuclear Engineering and Technology*, vol. 50, pp. 297-305, 2018.

[10] P. Coppolani, La chaudière des réacteurs à eau sous pression, EDP Sciences, 2004.

[11] A. Franzén, "Evaluation of Fuel Assembly Bow Penalty Peaking Factors for Ringhals 3 Based on a Cycle Specific Core Water Gap Distribution," Uppsala universitet, 2017.

[12] R. Fernandes, "Modélisation de la déformation d'assemblages combustibles d'une centrale REP. Activité dans le cadre du projet MADRAS : Maintien Axial, Déformations, Robustesse des Assemblages combustibles sous Sollicitations thermo-hydrauliques," 2010.

[13] D.-Y. Sheng and M. Seidl, "Towards the development of a full-scale transient CFD model to simulate the static and dynamic in-core mass flux distribution in a classical german PWR," in *NURETH-16*, Chicago, 2015.

[14] Y. Fournier, C. Vurpillot and C. Béchaud, "Evaluation of fluid flow in the lower core of a PWR with Code_ Saturne," *Nuclear Engineering and Design*, vol. 237, pp. 1729-1744, 9 2007.

[15] Z. E. Karoutas, Lang, P. Joffre, E. Baglietto, E. Brewster and R. Volpenheim, "Evaluating PWR fuel performance using vessel CFD analysis," in *Proceedings of 2010 LWR Water Reactor Fuel Performance Meeting (TopFuel 2010)*, Orlando, 2010.

[16] A. Horvath and B. Dressel, "On numerical simulation of fuel assembly bow in pressurized water reactors," *Nuclear Engineering and Design*, vol. 265, pp. 814-825, 2013.

[17] Y. Xu, M. Conner, K. Yuan, M. B. Dzodzo, Z. Karoutas, S. A. Beltz, S. Ray, T. A. Bissett, C.-C. Chieng, M.-T. Kao and C.-Y. Wu, "Study of impact of the AP1000® reactor vessel upper internals design on fuel performance," *Nuclear Engineering and Design*, vol. 252, pp. 128-134, 2012.

[18] P. Mollard, P.-H. Louf, G. Gentet and G. Doix, "GAIA, assemblage de combustible de nouvelle génération," *RGN*, pp. 56-60, 11 2015.

[19] J. Li, D. Rochman, J. Herrero, A. Vasiliev, H. Ferroukhi, A. Pautz, M. Seidl and D. Janin, "UO2 fuel pin bowing effects on isotopic concentrations," *Annals of Nuclear Energy*, vol.

105, pp. 361-368, 7 2017.

[20] J. Li, D. Rochman, A. Vasiliev, H. Ferroukhi, J. Herrero, A. Pautz, M. Seidl and D. Janin, "Bowing effects on isotopic concentrations for simplified PWR assemblies and full cores," *Annals of Nuclear Energy,* vol. 110, pp. 1023-1029, 12 2017.

[21] T. Andersson, J. Almberger and L. Bjoernkvist, "A decade of assembly bow management at Ringhals," International Atomic Energy Agency (IAEA), 2005.

[22] A. Wanninger, "Mechanical Analysis of the Bow Deformation of Fuel Assemblies in a Pressurized Water Reactor Core," Technische Universität München, 2018.

[23] B. Tarride, Physique, fonctionnement et sûreté des REP: Maîtrise des situations accidentelles du systèmeme réacteur, EDP Sciences, 2013.

[24] U. Bieder and A. Rashkovan, "Baffle jetting: CFD analysis of plain jets impinging on fuel rods," *Progress in Nuclear Energy,* vol. 114, pp. 31-45, 2019.

[25] D.-Y. Sheng and M. Seidl, "Determination of the pressure loss coefficient at control-rode guide tube flow-hole for a PWR nuclear fuel assembly by using CFD and Bernoulli solutions," in *NURETH-16*, Chicago, 2015.

[26] Sheng and Seidl, "State-of-the-art hydraulic pressure drop and lift force analysis for a PWR fuel assembly by using CFD as compared to the classical one-dimensional approach," in *Conference: Computational Fluid Dynamics for Nuclear Reactor Safety Applications (CFD4NRS-6),* 2016.

[27] J. Yan, Y. Zhang, B. Yang, W. Li and Y. Zhou, "Influence of Spacer Grid Outer Strap on Fuel Assembly Thermal Hydraulic Performance," *Science and Technology of Nuclear Installations,* no. 602062 , 2014.

[28] J. Peybernès, "Evaluation of the forces generated by cross-flow on PWR fuel assembly," in *Technical meeting on structural behaviour of fuel assemblies for water cooled reactors*, Vienna, 2005.

[29] U. Bieder, A. Scoliege and Q. Feng, "Turbulent Non-axial Flow in Rod Bundles," *Notes on Numerical Fluid Mechanics and Multidisciplinary Design,* vol. 135, pp. 89-100, 1 2018.

[30] U. Bieder, "Cfd analysis of non-axial flow in fuel assemblies," in *NURETH-16*, Chicago, 2015.

[31] J. Konheiser, C. Brachem and M. Seidl, "Investigation of the effects of a variation of fuel assembly position on the ex-core neutron flux detection in a PWR," *Journal of Nuclear Science and Technology,* vol. 54, pp. 188-195, 9 2016.

[32] R. Mukin, R. Puragliesi, M. Pecchia and M. Seidl, "Subchannel modeling of single rod bowing in a bundle geometry," *Nuclear Engineering and Design,* vol. 340, pp. 347-369, 2018.

[33] G. Ricciardi, S. Bellizzi, B. Collard and B. Cochelin, "Modelling Pressurized Water Reactor cores in terms of porous media," *Journal of Fluids and Structures,* vol. 25, pp. 112-133, 2009.

[34] E. F. Relf and C. H. Powell, Tests on Smooth and Stranded Wires Inclined T the Wind Direction, and a Comparison of Results on Stranded Wires in Air and Water, H.M. Stationery Office, 1917.

[35] M. M. Zdravkovich, Flow around Circular Cylinders; Volume 2: Applications, vol. 612, O. U. P. Oxford, Ed., OUP Oxford, 2003.

[36] R. A. Smith, W. T. Moon and T. W. Kao, "Experiments on Flow About a Yawed Circular Cylinder," *Journal of Basic Engineering,* vol. 94, pp. 771-776, 12 1972.

[37] G. I. Taylor, "Analysis of the swimming of long and narrow animals," *Proceedings of the Royal Society A. Mathematical, Physical and Engineering Sciences,* vol. 214, pp. 158-183,

1952.

[38] L. Divaret, P. Moussou, J. Berland, H. Berro, O. Cadot and O. Doaré, "Forces Exerted on a Cylinder in Near-Axial Flow," *Journal of Pressure Vessel Technology,* vol. 136, no. 051306, 8 2014.

[39] L. Divaret, O. Cadot, P. Moussou and O. Doaré, "Normal forces exerted upon a long cylinder oscillating in an axial flow," *Journal of Fluid Mechanics,* vol. 752, p. 649–669, 2014.

[40] S. Ersdal and O. M. Faltinsen, "Normal forces on cylinders in near-axial flow," *Journal of Fluids and Structures,* vol. 22, pp. 1057-1077, 2006.

[41] M. P. Paidoussis and S. Suss, "Stability of a Cluster of Flexible Cylinders in Bounded Axial Flow," *Journal of Applied Mechanics,* vol. 44, pp. 401-408, 9 1977.

[42] L. Divaret, "Caractérisation des forces fluides s'exerçant sur un faisceau de cylindres oscillant latéralement en écoulement axial," ENSTA Paris, 2015.

[43] A. Joly, "Forces fluides stationnaires exercées sur un cylindre déformé en écoulement axial et confiné - application au dimensionnement sismique des assemblages combustibles," Université Paris-Saclay, 2018.

[44] EDF, "Etudes pour une spécification fonctionnelle d'un programme expérimental dédidé à la validation du modèle thermohydraulique de THYC-COEUR," 2013.

[45] Areva, "Déformations d'assemblages combustibles, IFS," 2012.

[46] G. Ricciardi and E. Boccaccio, "Modelling of the flow induced stiffness of a PWR fuel assembly," *Nuclear Engineering and Design,* vol. 282, pp. 8-14, 2 2014.

[47] S. Delafontaine, "Simulation of unsteady fluid forces on a single rod downstream of mixing grid cell," *Nuclear Engineering and Design,* vol. 332, pp. 38-58, 2018.

[48] U. Bieder, F. Falk and G. Fauchet, "LES analysis of the flow in a simplified PWR assembly with mixing grid," *Progress in Nuclear Energy,* vol. 75, pp. 15-24, 2014.

[49] U. Bieder, C. Genrault and P. Ledac, "Hydraulic forces acting on full cross section fuel assemblies with 17×17 fuel rods," *Progress in Nuclear Energy,* vol. 130, no. 103515, 2020.

[50] J. Stabel, B. Dressel and &. al., "Advanced Methodology to Predict In-Reactor Bow of PWR Fuel Assemblies for Efficient Design Optimization: Background, Validation, Examples," in *2011 Water Reactor Fuel Performance Meeting*, Chengdu, 2011.

[51] R. Puragliesi and &. al., "Comparison of computational fluid dynamics and subchannel numerical solutions of fuel assemblies characterised by bowing," in *18th International Topical Meeting on Nuclear Reactor Thermal Hydraulics (NURETH-18)*, Portland, 2019.

[52] T. Xu and &. al., "Numerical simulation on fuel assembly deformation induced by flow redistribution with CODE_SATURNE," in *18th International Topical Meeting on Nuclear Reactor Thermal Hydraulics (NURETH-18)*, Portland, 2019.

[53] S. de Lambert, J. Cardolaccia, V. Faucher, O. Thomine, B. Leturcq and G. Campioni, "Semi-analytical modeling of the flow redistribution upstream from the mixing grids in a context of nuclear fuel assembly bow," *Nuclear Engineering and Design,* no. 110940, 2021.

[54] H. Cross, Analysis of Flow in Networks of Conduits Or Conductors, University of Illinois, 1936.

[55] I. E. Idel'cik, Memento des pertes de charge, Eyrolles, 1969.

[56] M. Asker, O. Turgut and M. Coban, "A review of non iterative friction factor correlations for the calculation of pressure drop in pipes," *Bitlis Eren University Journal of Science and Technology,* vol. 4, pp. 1-8, 6 2014.

[57] D. C. Rennels and H. M. Hudson, Pipe Flow: A Practical and Comprehensive Guide, Wiley, 2012.

[58] W. K. In, D. S. Oh and T. H. Chun, "Pressure Drop Correlation for a PWR Fuel Assembly with Mixing Vane," in *Proceedings of the Korean Nuclear Society Spring Meeting*, Cheju, 2001.

[59] W. K. In, D. S. Oh and T. H. Chun, "Empirical and Computational Pressure Drop Correlations for Pressurized Water Reactor Fuel Spacer Grids," *Nuclear Technology,* vol. 139, pp. 72-79, 2002.

[60] K. Rehme, "Pressure Drop Correlations for Fuel Element Spacers," *Nuclear Technology,* vol. 17, pp. 15-23, 1973.

[61] D. Wood and C. O.A. Charles, "Hydraulic Network Analysis Using Linear Theory," *Journal of the Hydraulics Division,* vol. 98, pp. 1157-1170, 7 1972.

[62] D. Wood and A. G. Rayes, "Reliability of algorithms for pipe network analysis.," *J. HYDRAUL. DIV.: PROC. ASCE,* vol. 107, pp. 1145-1161, 1 1981.

[63] H. B. Nielsen, "Methods for Analyzing Pipe Networks," *Journal of Hydraulic Engineering,* vol. 115, pp. 139-157, 1989.

[64] P.-E. Angeli, U. Bieder and G. Fauchet, "OVERVIEW OF THE TRIOCFD CODE: MAIN FEATURES, V&V PROCEDURES AND TYPICAL APPLICATIONS TO NUCLEAR ENGINEERING," in *NURETH-16*, Chicago, 2015.

[65] F. Archambeau, N. Méchitoua and M. Sakiz, "Code Saturne: A Finite Volume Code for the computation of turbulent incompressible flows - Industrial Applications," *International Journal on Finite Volumes,* vol. 1, 2 2004.

[66] A. Ribes, A. Bruneton and A. Geay, *SALOME: an Open-Source simulation platform integrating ParaView*, 2017.

[67] J. Cardolaccia and S. de Lambert, "Investigation of the flow redistribution upstream of grid-like obstacles separated by a variable gap," *Experimental Thermal and Fluid Science,* no. 110289, 2021.

[68] F. Gaudier, "URANIE: The CEA/DEN Uncertainty and Sensitivity platform," *Procedia - Social and Behavioral Sciences,* vol. 2, pp. 7660-7661, 2010.

[69] J. Jacques, "Pratique de l'analyse de sensibilité : comment évaluer l'impact des entrées aléatoires sur la sortie d'un modèle mathématique," *Publications IRMA,* vol. 71, pp. 2-20, 2011.

[70] B. Iooss, "Revue sur l'analyse de sensibilité globale de modèles numériques," *Journal de la Société Française de Statistique,* vol. 152, pp. 1-23, 2011.

[71] M. D. McKay, R. J. Beckman and W. J. Conover, "A Comparison of Three Methods for Selecting Values of Input Variables in the Analysis of Output from a Computer Code," *Technometrics,* vol. 21, p. 239–245, 1979.

[72] J. Jacques, C. Lavergne and N. Devictor, "Sensitivity analysis in presence of model uncertainty and correlated inputs," *Reliability Engineering & System Safety,* vol. 91, pp. 1126-1134, 2006.

[73] U. Bieder, "CFD analysis of full cross section fuel assemblies," in *1st International Seminar on Fluid Structure Interaction Modelling for Nuclear Fuel Assemblies (ISFSIMNA2020)*, Aix-en-Provence, 2020.

[74] U. Bieder and C. Genrault, "CFD analysis of intra and inter fuel assembly mixing," *Annals of Nuclear Energy,* vol. 135, no. 106977, 2020.

[75] G. Ricciardi, "Fluid–structure interaction modelling of a PWR fuel assembly subjected to axial flow," *Journal of Fluids and Structures,* vol. 62, pp. 156-171, 4 2016.

[76] G. Ricciardi and E. Boccaccio, "Measurements of fluid fluctuations around an oscillating nuclear fuel assembly," *Journal of Fluids and Structures,* vol. 48, pp. 332-346, 2014.

[77] A. Combescure, A. Hoffmann and P. Pasquet, "The CASTEM finite element system," *Finite Element Systems: a Handbook,* pp. 115-125, 1982.

[78] A. Wanninger, M. Seidl and R. Macian, "Screening sensitivity analysis of a PWR fuel assembly FEM structural model," in *TopFuel 2016*, Boise, 2016.

[79] G. Ruiz Antón-Pacheco Jaime, "Study of the set up of a fluid structure coupling interface (FSI) between PWR fuel assemblies and the reactor coolant," UPV Universitat Politècnica de València, 2016.

[80] F.-K. Benra, H. Dohmen, J. Pei, S. Schuster and B. Wan, "A Comparison of One-Way and Two-Way Coupling Methods for Numerical Analysis of Fluid-Structure Interactions," *Journal of Applied Mathematics,* vol. 2011, 11 2011.

[81] C. Patricot, "Couplages multi-physiques : évaluation des impacts méthodologiques lors de simulations de couplages neutronique/thermique/mécanique.," Université Paris-Saclay, 2016.

[82] C. Lascar and &. al., "Advanced predictive tool for fuel assembly bow based on a 3D coupled FSI approach," in *TopFuel 2015 Conference Proceedings part II*, Zurich, 2015.

[83] B. Dressel, U. Staude, S. Hofbeck, C.-J. Münch and S. Kovacs, "Investigations on the FSI Characteristic of a Scaled and Integral Fuel Structure Under Axial Flow," in *ASME 2017 International Mechanical Engineering Congress and Exposition*, Tampa, 2017.

[84] D. Butterworth, "The development of a model for three-dimensional flow in tube bundles," *International Journal of Heat and Mass Transfer,* vol. 21, pp. 253-256, 1978.

[85] S. B. Beale, "Tube Banks, Crossflow over," *Thermopedia, A-to-Z Guide to Thermodynamics, Heat & Mass Transfer, and Fluid Engineering,* 2011.

[86] S. de Lambert, G. Campioni, V. Faucher, B. Leturcq and J. Cardolaccia, "Modeling the consequences of fuel assembly bowing on PWR core neutronics using a Monte-Carlo code," *Annals of Nuclear Energy,* vol. 134, pp. 330-341, 2019.

[87] R. Mukin, I. Clifford, H. Ferroukhi and M. Seidl, "THERMAL HYDRAULIC ANALYSIS OF PWR ASSEMBLY BOWING USING SUBCHANNEL CODE COBRA-TF," in *17th International Topical Meeting on Nuclear Reactor Thermal Hydraulics (NURETH-17)*, Xi'an, China, 2017.

[88] R. J. Fetterman and F. Franceschini, "Analysis of PWR assembly bow," in *International Conference on Reactor Physics, Nuclear Power : A Sustainable Resource*, Casino-Kursaal Conference Center, Interlaken, Switzerland, 2008.

[89] E. Syrjälahti, T. Ikonen and V. Tulkki, "Modeling burnup-induced fuel rod deformations and their effect on transient behavior of a VVER-440 reactor core," *Annals of Nuclear Energy,* vol. 125, pp. 121-131, 2019.

[90] L. Shishkov, S. Gorodkov, E. Mikailov and E. Sukhino-Khomenko, "Inter-assembly gap deviations in VVER-1000: Accounting for effects on engineering margin factors," *Kerntechnik,* vol. 80, pp. 408-411, 8 2015.

[91] P. Gabrielsson, D. Schrire, E. Suvdantsetseg and M. Malmerg, "Investigation of the development of fuel assembly bow in Ringhals 3 and 4," in *TopFuel 2018*, Prague, 2018.

[92] G. Kępisty, J. Cetnar and P. Stanisz, "Parametric studies of the PWR fuel assembly modeling with Monte-Carlo method," *Annals of Nuclear Energy,* vol. 94, pp. 189-207, 2016.

[93] J. Leppänen, "SERPENT - a Continuous-energy Monte Carlo Reactor Physics Burnup Calculation Code," VTT Technical Research Centre of Finland, 2013.

[94] E. Brun, F. Damian, C. M. Diop, E. Dumonteil, F. X. Hugot, C. Jouanne, Y. K. Lee, F. Malvagi, A. Mazzolo, O. Petit, J. C. Trama, T. Visonneau and A. Zoia, "TRIPOLI-4®, CEA, EDF and AREVA reference Monte Carlo code," *Annals of Nuclear Energy,* vol. 82, pp. 151-160, 2015.

[95] A. Santamarina and et al., "The JEFF-3.1.1 Nuclear Data Library," OECD/NEA, 2009.

[96] L. Patarin, Le cycle du combustible nucléaire, EDP Sciences, 2002.

[97] P. Reuss, Neutron Physics, EDP Sciences, 2008.

[98] P. Cattaneo, "Développement d'une méthodologie de modélisation multiphysique de type best-estimate d'un coeur de REP en évolution," Université Grenoble Alpes, 2020.

[99] O. Mula Hernandez, "Some contributions towards the parallel simulation of time dependent neutron transport and the integration of observed data in real time," Université Pierre et Marie Curie, 2014.

[100] Y. S. Jung and H. Joo, "Decoupled planar MOC solution for dynamic group constant generation in direct three-dimensional core calculations," in *International Conference on Mathematics, Computational Methods & Reactor Physics (M&C 2009)*, Saratoga Springs, New York, 2009.

[101] Y. Périn and K. Velkov, "CTF/DYN3D multi-scale coupled simulation of a rod ejection transient on the NURESIM platform," *Nuclear Engineering and Technology,* vol. 49, pp. 1339-1345, 2017.

[102] D. Schneider, F. Dolci, F. Gabriel, J.-M. Palau, M. Guillo, B. Pothet, P. Archier, K. Ammar, F. Auffret, R. Baron, A.-M. Baudron, P. Bellier, L. Bourhrara, L. Buiron, M. Coste-Delclaux, C. De Saint Jean, J.-M. do, B. Espinosa, E. Jamelot and I. Zmijarevic, "APOLLO3 ® : CEA/DEN DETERMINISTIC MULTI-PURPOSE CODE FOR REACTOR PHYSICS ANALYSIS," in *International Conference on Physics of Reactors (PHYSOR2016)*, Sun Valley Idaho, 2016.

[103] S. Santandrea and P. Mosca, "LINEAR SURFACE CHARACTERISTIC SCHEME FOR THE NEUTRON TRANSPORT EQUATION IN UNSTRUCTURED GEOMETRIES," in *International Conference on Physics of Reactors (PHYSOR2006)*, Vancouver, 2006.

[104] K. S. Smith, "Assembly homogenization techniques for light water reactor analysis," *Progress in Nuclear Energy,* vol. 17, pp. 303-335, 1986.

[105] A.-M. Baudron and J.-J. Lautard, "MINOS: A Simplified Pn Solver for Core Calculation," *Nuclear Science and Engineering,* vol. 155, pp. 250-263, 2007.

[106] J.-Y. Moller and J.-J. Lautard, "MINARET, A DETERMINISTIC NEUTRON TRANSPORT SOLVER FOR NUCLEAR CORE CALCULATIONS," in *Internation Conference on Mathematics and Computational Methods Applied to Nuclear Science and Engineering (M&C2011)*, Rio de Janeiro, RJ, Brazil, 2011.

[107] J. Li, "Simulation of Bowing Effects on Isotopic Inventories for Simplified Pin, Assembly and Full Core Models," École Polytechnique Fédérale de Lausanne (EPFL), 2016.

[108] J. Berger, "Impact of fuel assembly bowing on the power density distribution and its monitoring in Siemens/KWU-PWR," KTH Royal Institute of Technology, Stockholm, 2017.

[109] T. Bahadir, I. I. I. Joel D Rodes and D. G. Knott, "CMS Assembly Bow Model," Studsvik, 1997.

[110] S. Scandpower, "CASMO5 - A Fuel Assembly Burn up Program - User's Manual," 2016.

[111] A. Vidal-Ferràndiz, A. Carreño, D. Ginestar, C. Demazière and G. Verdú, "Neutronic Simulation of Fuel Assembly Vibrations in a Nuclear Reactor," *Nuclear Science and Engineering,* vol. 194, pp. 1067-1078, 2020.

[112] M. Viebach, N. Bernt, C. Lange, D. Hennig and A. Hurtado, "On the influence of dynamical fuel assembly deflections on the neutron noise level," *Progress in Nuclear Energy,* vol. 104, pp. 32-46, 2018.

[113] U. Rohde, M. Seidl, S. Kliem and Y. Bilodid, "Neutron noise observations in German KWU built PWRs and analyses with the reactor dynamics code DYN3D," *Annals of Nuclear*

Energy, vol. 112, pp. 715-734, 2018.

[114] A. Yamamoto, T. Endo, H. Nagano, Y. Ohoka and K. Yamamoto, "A simple treatment of increased gap due to fuel assembly bowing through correction of cross sections," *Journal of Nuclear Science and Technology,* vol. 56, pp. 471-478, 2019.

[115] D. Rochman, P. Mala, H. Ferroukhi, A. Vasiliev, M. Seidl, D. Janin and J. Li, "Bowing effects on power and burn-up distributions for simplified full PWR and BWR cores," in *International Conference on Mathematics & Computational Methods Applied to Nuclear Science & Engineering (M&C2017)*, Jeju, 2017.

[116] M. Reed, K. Smith and B. Forget, "“Virtual density” and traditional boundary perturbation theories: Analytic equivalence and numeric comparison," *Annals of Nuclear Energy,* vol. 112, pp. 531-548, 2018.

[117] A. YAMAMOTO, Y. KITAMURA and Y. YAMANE, "Approximate Treatment of Thermal Expansion Effect in Lattice Transport Calculations," *Journal of Nuclear Science and Technology,* vol. 41, pp. 1003-1007, 2004.

[118] M. Westlund, "Monte Carlo Simulations of Bowing Effects Using Realistic Fuel Data in Nuclear Fuel Assemblies," Uppsala universitet, 2019.

[119] A. Bruneton, *Alamos, mise en données pour la neutronique. Journée utilisateur SALOME 2014,* 2014.

[120] A. Saeed, M. A. Bakr and A. U. Saqib, "Estimation of Axial and radial in-core power peaking in PWR plant using artificial neural network technique," in *2016 International Conference on Emerging Technologies (ICET)*, 2016.

[121] W. C. Dawn, J. Ortensi, M. D. DeHart and S. P. Palmtag, "Comparison of Generation of Higher-Order Neutron Scattering Cross Sections," USDOE, 2020.

[122] F. Jeanpierre and M. Livolant, "Autoprotection des résonances dans les réacteurs nucléaires; application aux isotopes lourds," CEA, 1974.

[123] L. Lei-Mao, "Modèles d'autoprotection d'APOLLO3 : analyse et orientation technique," CEA, 2007.

[124] A. Calloo, "Développement d'une nouvelle modélisation de la loi de choc dans les codes de transport neutronique multigroupes," Université de Grenoble, 2012.

[125] P. Reuss, Précis de neutronique, EDP Sciences, 2003.

[126] B. Leturcq, "Nuclear Fuel Assembly Deformation, Reduced Mechanical Model Dedicated to FSI Simulation," in *13th World Congress on Computational Mechanics (WCCM XIII) & 2nd Pan American Congress on Computational Mechanics (PANACM II)*, New York, 2018.

[127] B. Leturcq, S. Pascal and P. Le Tallec, "Réduction de modèle viscoplastique par application de la méthode NTFA à un VER de structure," in *14ème Colloque National en Calcul des Structures (CSMA 2019)*, Giens, 2019.

[128] B. Leturcq, S. Pascal, P. Le Tallec and J. Pacull, "Reduction of a mechanical model dedicated to the study of assembly bow," in *Transactions, 25th International Conference on Structural Mechanics in Reactor Technology (SMiRT 25)*, New York, 2019.

[129] G. Kępisty, C. Patricot, D. Broc and G. Campioni, "SFR mechanical scenarios and neutron transport transients with CAST3M code," *Annals of Nuclear Energy,* vol. 101, pp. 226-236, 2017.

[130] W. R. Martin, "Challenges and prospects for whole-core Monte Carlo analysis," *Nuclear Engineering and Technology,* vol. 44, pp. 151-160, 3 2012.

[131] B. Faure and G. Marleau, "Simulation of a sodium fast core: Effect of B1 leakage models on group constant generation," *Annals of Nuclear Energy,* vol. 99, pp. 484-494, 2017.

[132] L. Cai, Y. Peneliau, J. Tommasi, J.-F. Vidal and C. M. Diop, "Leakage-corrected fast reactor

assembly calculation with Monte-Carlo code TRIPOLI4r and its validation methodology," in *International Conference on Physics of Reactors (PHYSOR2014)*, Kyoto, 2014.

[133] D. Huilier, *Fluides réels, écoulements permanents et pertes de charge,* Université de Strasbourg, 2010.

[134] J. Lemay, *Pertes de charge en conduite,* Université Laval, 2010.

[135] M. Stanislas and P. Dupont, *Cours de Mécanique des Fluides de première et deuxième Année, Tome 1.,* École centrale de Lille, 2007.

[136] T. B. Drew, Advances in Chemical Engineering, Academic Press, 1978.

[137] A. Popel, "A Model of Pressure and Flow Distribution in Branching Networks," *Journal of Applied Mechanics,* vol. 102, pp. 247-253, 6 1980.

[138] J. D. Nault, "Comparison of One-Dimensional Unsteady Flow Models for Simulating Pipeline and Pipe Network Hydraulics," in *1st International WDSA / CCWI 2018 Joint Conference*, Kingston, 2018.

[139] I. Sarbu and E. Valea, "Nodal analysis models of water supply networks," in *Proceedings of the 8th WSEAS international conference on fluid mechanics, 8th WSEAS international conference on Heat and mass transfer*, 2011.

[140] D. Stephenson, Ed., "Chapter 4 Linear Method," in *Pipeflow Analysis*, vol. 19, Elsevier, 1984, pp. 45-54.

[141] L. Debnath, "A brief historical introduction to Euler's formula for polyhedra, topology, graph theory and networks," *International Journal of Mathematical Education in Science and Technology,* vol. 41, pp. 769-785, 2010.

[142] R. Epp and A. G. Fowler, "Efficient Code for Steady-State Flows in Networks," *Journal of the Hydraulics Division,* vol. 96, pp. 43-56, 1970.

[143] U. Y. Shamir and C. D. D. Howard, "Water Distribution Systems Analysis," *Journal of the Hydraulics Division,* vol. 94, pp. 219-234, 1968.

[144] E. Todini and S. Pilati, "A Gradient Algorithm for the Analysis of Pipe Networks," in *Computer Applications in Water Supply: Vol. 1—Systems Analysis and Simulation*, GBR, Research Studies Press Ltd., 1988, p. 1–20.

[145] P. Boulos, K. Lansey and B. Karney, Comprehensive Water Distribution Systems Analysis Handbook for Engineers and Planners, 2nd edition ed., MWH Soft, 2006.

[146] R. Gupta and T. D. Prasad, "Extended Use of Linear Graph Theory for Analysis of Pipe Networks," *Journal of Hydraulic Engineering,* vol. 126, pp. 56-62, 2000.

[147] A. Ayad, H. Awad and A. Yassin, "Developed hydraulic simulation model for water pipeline networks," *Alexandria Engineering Journal,* vol. 52, pp. 43-49, 2013.

[148] A. Ayad, H. Awad and A. Yassin, "Integrated approach for the optimal design of pipeline networks," *Alexandria Engineering Journal,* vol. 57, pp. 87-96, 2018.

[149] S. Waldrip H., R. Niven, M. Abel and M. Schlegel, "Maximum Entropy Analysis of Hydraulic Pipe Flow Networks," *Journal of Hydraulic Engineering,* vol. 142, no. 04016028, 5 2016.

[150] A. El-Bahrawy, "A Spreadsheet Teaching Tool For Analysis Of Pipe Networks," *Engineering Journal of University of Qatar,* vol. 10, pp. 33-50, 1997.

[151] K. B. Adedeji, Y. Hamam, B. T. Abe and A. M. Abu-Mahfouz, "A spreadsheet tool for the analysis of flows in small-scale water piping networks," in *2017 IEEE 15th International Conference on Industrial Informatics (INDIN)*, 2017.

université PARIS-SACLAY

ÉCOLE DOCTORALE
Sciences mécaniques et énergétiques, matériaux et géosciences (SMEMAG)

Titre : Contribution à l'analyse multiphysique de la déformation d'assemblage

Mots clés : Déformation, Multiphysique, Assemblage combustible

Résumé : La déformation des assemblages en cœur est un sujet d'intérêt pour la sûreté et l'exploitation du parc électronucléaire, en raison du risque d'augmentation du temps de chute des barres de commande, de difficultés (voire de blocages) lors de la manutention des assemblages, mais aussi de déséquilibre de la nappe de puissance (tilt) ou encore d'usure locale prématurée du combustible. Les phénomènes physiques couplés à l'origine de ces mécanismes de déformation, avec des effets collectifs à l'échelle d'un cœur complet, font encore l'objet d'analyses amont pour en identifier et comprendre les éléments prépondérants.

Le présent sujet est dédié à l'étude détaillée de phénomènes multiphysiques à l'influence connue : l'interaction fluide-structure d'une part, définissant les conditions d'équilibre statique pilotant l'écoulement et la déformée de l'assemblage au premier ordre, et le couplage mécanique/neutronique d'autre part, influencé par les éléments précédents et contribuant sur des temps plus longs à l'évolution des caractéristiques du système complet (propriétés mécaniques de l'assemblage, répartition de température et de débit à l'échelle du cœur...).

Title : Contribution to the multiphysical analysis of fuel assembly bow

Keywords : Deformation, Multiphysics, Fuel assembly

Abstract: Fuel assembly bow in a nuclear core is a topic of interest for safety and performance of power plants, due to the potential increase of the drop time of rod cluster control assemblies, and potential difficulties to handle the assemblies. It may as well lead to quadrant power tilts or to early wear of the fuel rods. Some advanced analyses are still required to capture the coupled physical phenomena at the origin of theses deformations and the present thesis aims at studying in detail two classes of phenomena with a known significant influence.

Fluid-structure interaction on the one hand, setting up the first ordrer equilibrium conditions governing the fluid flow and the shape of the assemblies, and the mechanics/neutronics coupling on the other hand, influenced by the former topic and contributing on a larger time scale to the evolution of the characteristics of the whole system (mechanical properties of the assemblies, global temperature distribution and flow inside the core...).